MANAGEMENT OF OXIDATIVE STRESS IN PLANTS: DISSECTING THE DUAL ROLE OF GLUTATHIONE IN OXIDANT REDUCTION AND PROTEIN *S*-THIOLATION

Dissertation

zur

Erlangung des Doktorgrades (Dr. rer. nat.)

der

Mathematisch-Naturwissenschaftlichen Fakultät

der

Rheinischen Friedrich-Wilhelms-Universität Bonn

vorgelegt von

Finja Bohle

aus

Troisdorf

Bonn, 2023

Angefertigt mit Genehmigung der Mathematisch-Naturwissenschaftlichen Fakultät

der Rheinischen Friedrich-Wilhelms-Universität Bonn

Gutachter: Prof. Dr. Andreas Meyer

Gutachter: Prof. Dr. Peter Dörmann

Tag der Promotion: 15.06.2023

Erscheinungsjahr: 2023

THIS THESIS HAS BEEN CONDUCTED UNDER THE SUPERVISION OF:

Prof. Dr. Stefanie Müller-Schüssele

Molekulare Botanik

Fachbereich Biologie

Technische Universität Kaiserslautern

Erwin-Schrödinger-Straße 70

67663 Kaiserslautern, Germany

AND

Prof. Dr. Andreas Meyer

Chemical Signalling

Institut für Nutzpflanzenwissenschaften und Ressourcenschutz

Universität Bonn

Friedrich-Ebert-Allee 144

53113 Bonn, Germany

FIRST EXAMINER:

Prof. Dr. Andreas Meyer

SECOND EXAMINER:

Prof. Dr. Peter Dörmann

Molekulare Biotechnologie/Biochemie

Institut für Molekulare Physiologie und Biotechnologie der Pflanzen

Karlrobert-Kreiten-Str. 13

53115 Bonn, Germany

TABLE OF CONTENT

SUMMARY

The regulation of enzyme activity by post-translational modifications enables a fast acclimation at the metabolic level under changing environmental conditions. The amino acid cysteine is very susceptible to redox modifications such as *S*-glutathionylation, a reversible mixed disulfide between a cysteine thiol group and the tripeptide glutathione (GSH, *γ-Glu-Cys-Gly*). Class I glutaredoxins (GRXs) facilitate the transfer of electrons from glutathione to target proteins and can (de)glutathionylate proteins. For their efficient reduction GRXs require GSH. A high concentration of reduced GSH is maintained by the glutathione reductase (GR), which reduces oxidized glutathione (GSSG) to two GSH using NADPH as electron donor. The absence of GR leads to a less reducing glutathione redox potential (E_{GSH}). Under oxidative stress conditions, increased levels of *S*-glutathionylation are observed, potentially resulting from an altered GSH:GSSG ratio and E_{GSH}. To what extend GRX function, the GSH:GSSG ratio or changes in E_{GSH} contribute to increasing levels of protein *S*-glutathionylation is largely unknown.

To explore the evolutionary conservation of the glutathione-dependent redox network including GRX and GR in plastids, I conducted a phylogenetic analysis showing evolutionary conservation of GR and GRX clades from streptophyte algae to flowering plants. I provide an overview of known plastidial glutathionylation target proteins and the respective *S*-glutathionylation sites based on available literature.

To investigate the influence of E_{GSH} and GSH:GSSG on protein *S*-glutathionylation, I used redox-sensitive GFP (roGFP2) as glutathionylation target and exposed it to various GSH:GSSG ratios at constant E_{GSH}. GRX-mediated roGFP2 oxidation kinetics increased with higher ratios of GSH:GSSG, indicating an important function of the GSH:GSSG ratio on the glutathionylation rate. To test the *in vivo* influence of E_{GSH} on protein glutathionylation, the cytosolic glutathionylation target GAPC1-YFP (glyceraldehyde-3-phosphate dehydrogenase C1) was introduced into the Arabidopsis GR mutant *gr1-1*, displaying a less reducing E_{GSH}. I observed higher expression of GAPC1-YFP in *gr1-1*, suggesting that changes in E_{GSH} affect GAPC1 promotor activity. However, aggregate formation triggered by *S*-glutathionylation of GAPC1 was not observed.

While class I GRX have been well characterized *in vitro, in vivo* studies provided only limited information due to functional redundancy. To elucidate the *in planta* role of class I GRX, I generated viable knock-outs of the single plastid class I GRX present in *Physcomitrium*

patens (Δ*grxc5*). To date, stress treatments did not reveal phenotypic differences between Δ*grxc5* and WT, in contrast to null mutants of glutathione reductase (Δ*gr1*). I conclude that stromal GRX malfunction is not the cause for the dwarfed and stress-sensitive Δ*gr1* phenotype.

*Pp*GRXC5 showed a high oxidoreductase activity *in vitro*. Plastid-targeted roGFP2 in Δ*grxc5* revealed a complete loss of this activity observed by slower roGFP2 reduction kinetics after oxidative stress *in vivo*. I performed Western blot analyses on protein extracts of wild-type (WT) and Δ*grxc5* before and after oxidative stress and observed increased total protein *S*-glutathionylation levels in both, suggesting that *Pp*GRXC5 is not necessary for *S*-glutathionylation under these conditions.

1. Introduction

The rise of oxygen levels in the world's atmosphere to modern levels of 21% took place between 2.4 and 2.1 billion years ago, resulting in the need for anaerobic life forms to adopt more and more to the increasing oxidizing environment (Lyons *et al.* 2014). Although O_2 was toxic to the anaerobic organisms, evolution took its turn and resulted in the beneficial use of O_2 as electron acceptor in form of respiration. Enzymatically and non-enzymatically reactive oxygen species (ROS) detoxification mechanisms helped to maintain a reduced cellular environment. However, organisms not able to adopt to the changing oxidizing conditions went extinct or were forced to inhabit anaerobic niches (Halliwell 1999; Sessions *et al.* 2009). A side effect of an oxygen metabolizing system is the unavoidable production of ROS such as $^1O_2$ (singlet oxygen), $O_2^{\bullet-}$ (superoxide), H_2O_2 (hydrogen peroxide) and OH^- (hydroxyl radical) (Mittler *et al.* 2004, 2022). Maintaining a reduced environment on cellular level in the presence of ROS requires a tightly controlled redox and antioxidant defense system protecting proteins, lipids and other macromolecules like DNA from damage (Møller *et al.* 2007; Meyer 2008). ROS formation can occur when molecular oxygen acts as an electron acceptor. In addition to being generated in mitochondria within the respiratory electron transport (ETC), ROS is as well a byproduct of photosynthesis within the photosynthetic electron transport (PET). The highest amount of ROS in form of superoxide is generated at the site of photosystem I (PSI) via the Mehler reaction (Mehler 1951), whereas under stress conditions $^1O_2$ can be produced at the site of photosystem II (PSII) via the interaction of ^{3}Chl (excited chlorophyll in its triplet state) with O_2 (Dietz *et al.* 2016). Superoxide dismutase (SOD) converts $O_2^{\bullet-}$ to H_2O_2 and O_2 without the input of additional electrons. Peroxides can then be detoxified by a set of enzymes such as ascorbate peroxidases (Foyer & Noctor 2011), glutathione *S*-transferases (Ugalde, Lamig, *et al.* 2021) and peroxiredoxins (Liebthal *et al.* 2018). However, the importance of ROS as signaling molecule gained momentum (reviewed in Mittler *et al.* 2022) and its role as electron sink was further labeled as ‘essential’ for survival (Meyer *et al.* 2021).

1.1. Glutathione – a cellular electron reservoir

Reactive oxygen species are produced under physiological conditions and fulfill functions in redox signal transmission. An increased ROS formation occurs as response to abiotic and biotic stresses for example in response to drought stress (abiotic) and pathogen attack (biotic) (Apel & Hirt 2004; Mittler *et al.* 2004; Meyer 2008). Glutathione, a highly abundant tripeptide, with a cysteine thiol group, is an important electron donor involved in ROS detoxification and oxidative damage repair. It further performs a variety of functions, including detoxification of xenobiotics and heavy metals (Dixon *et al.* 1998; Jozefczak *et al.* 2012), participation in cellular processes such as cell division (Vernoux *et al.* 2000) and flowering (Ogawa *et al.* 2001), and acting as a cofactor in the coordination of iron-sulfur cluster (Berndt *et al.* 2007).

The low molecular weight thiol consists of the three amino acids glutamate, cysteine and glycine, with a specific γ-glutamyl peptide bond preventing its degradation by most peptidases (Deponte 2022). Glutathione synthesis occurs in two sequential steps and is catalyzed by the glutamate-cysteine ligase (GSH1) and glutathione synthetase (GSH2). Glutathione synthesis in plants is compartmentalized and takes place in the chloroplast and in the cytosol (Hell & Bergmann 1988; Wachter *et al.* 2004). GSH1 was shown to localize only to plastids, and GSH2 to both compartments, necessitating a transport of glutathione and γ-glutamyl cysteine (γ-EC) between the compartments (Pasternak *et al.* 2007).

Complete loss of GSH1 results in embryo lethality, further demonstrating the fundamental role of glutathione in the plant metabolism (Cairns *et al.* 2006). Mutations in the *GSH1* gene led to a massive decrease of glutathione concentration with only 5-50% of the WT glutathione level. Lower GSH levels observed in GSH1 mutants, have an impact on the regulation of genes involved in oxidative defense and heavy metal detoxification such as cadmium (Howden *et al.* 1995; Cobbett *et al.* 1998; Ball *et al.* 2004). The mutation with the biggest impact on glutathione concentration with only 40-200 µM left occurred due to a point mutation (D to N) in *GSH1*, root meristemless 1 (*rml1*), resulting in a diminished root growth and arrests in growth after germination (Vernoux *et al.* 2000). While mutations leading to a ~50% (*rax1;* Ball *et al.* 2004) or ~30% (*cad2;* Howden *et al.* 1995) reduction of the glutathione pool compared to WT level showed no growth phenotype under steady-state conditions, they showed significant differences under stress. Under non-stressed conditions, phenotypic analysis of

Arabidopsis mutants from a GSH-deficient allelic series determined the threshold for growth impairments to 25% GSH of WT-level (Bangash *et al.* 2019).

1.1.1 Glutathione homeostasis

The function of glutathione is based on thiol exchange reactions in which two molecules of reduced glutathione (GSH) are oxidized to form a glutathione disulfide (GSSG) providing two electrons (and two protons) to the respective coupled reaction partners. To maintain a reduced glutathione pool, oxidized glutathione is reduced back to two molecules of GSH by the glutathione reductase (GR) requiring NADPH. Glutathione reductase isoforms are localized to the cytosol and peroxisomes (*Arabidopsis thaliana* (*At*) *At*GR1, *Physcomitrium patens* (*Pp*) *Pp*GR2) as well as to plastids and mitochondria (*At*GR2, *Pp*GR1) and help to maintain the redox potential of the compartments (Marty *et al.* 2009; Kataya & Reumann 2010).

The glutathione redox potential (E_{GSH}) is dependent on the concentration and oxidation degree of the glutathione redox couple and determined via the Nernst equation with R = 8.315 J K^{-1} mol^{-1}, T =298.15 K, z =2, F = 96.485 C mol^{-1} and $E^{0'}$=-240 mV at pH 7 (Schafer & Buettner 2001; Meyer & Hell 2005; Meyer *et al.* 2007).

$$E' = E^{0'}{}_{(GSH)} - \frac{2.303RT}{zF} log_{10} \frac{[GSH]^2}{[GSSG]}$$

The total cellular concentration of glutathione was determined by fluorescent labeling in root tips of Arabidopsis to be around 2-3 mM (Fricker *et al.* 2000). Measurements with a GFP-based redox sensitive biosensor (roGFP) suggested only 0.002% of the glutathione pool to be oxidized under steady state conditions, leaving only nanomolar concentrations of GSSG. Already small changes in GSSG concentration or total glutathione levels can induce a severe shift in redox potential (Meyer *et al.* 2007; Schwarzländer *et al.* 2008).

The cytosolic glutathione pool of Arabidopsis is maintained at a glutathione redox potential of -320 mV at pH 7 (Meyer *et al.* 2007) with a potential GSH:GSSG ratio of 50000:1 (Schwarzländer *et al.* 2016). *At*GR2 contributes approximately 35% of total GR activity, with cytosolic activity accounting for the remaining 65% (Marty *et al.* 2009). The loss of the cytosolic glutathione reductase leads to a less reducing redox potential of -270 mV induced by higher GSSG levels in the cytosol and is partially compensated by the cytosolic thioredoxin system (Marty *et al.* 2009). In contrast, the loss of the dual targeted organellar isoform results

in embryo lethality in Arabidopsis and cannot be compensated by the plastidial thioredoxin system (Marty *et al.* 2019). Complementation studies of the *At*GR2 knock-out mutant with GR2 under the endogenous promotor either targeted to the plastids or to mitochondria pinpointed the essential GR activity to the plastids (Marty *et al.* 2019). A point mutation in an *AtGR2* exon (*miao*) resulted in a decrease of total GR activity of ~50% and showed a strong root growth phenotype (Yu *et al.* 2013). In the model moss plant *Physcomitrium patens* the GR knock-out of the plastidial and mitochondrial isoform resulted in a viable mutant, displaying a dwarfed phenotype altered in photosynthetic performance like non-photochemical quenching (NPQ). The plastidial glutathione redox potential (E_{GSH}) in *P. patens* was determined to be -311 mV, less than values measured in *Arabidopsis thaliana* epidermal plastids of -361 mV (Schwarzländer *et al.* 2008; Müller-Schüssele *et al.* 2020). In the organellar GR knock-out of *P. patens* (Δ*gr1*) the plastidial E_{GSH} showed a 33 mV shift to a less reducing E_{GSH} of -278 mV. During characterization of plastidial targeted roGFP2, a dynamically behaving plastidial E_{GSH} was observed upon light-dark changes. The function of this dynamic change is unknown so far (Müller-Schüssele *et al.* 2020).

Enzymes using glutathione as electron donor such as methionine sulfoxide reductase B1 (MSRB1), peroxiredoxin II E (PRXIIE), glutaredoxins (GRX) and dehydroascorbate reductase (DHAR) are key players in ROS scavenging and oxidative damage repair for example DHAR via the ascorbate-glutathione cycle (Noctor *et al.* 2012). Within the ascorbate-glutathione cycle H_2O_2 is reduced to H_2O by ascorbate. This reaction is catalyzed by ascorbate peroxidase, releasing monodehydroascorbate (MDH). MDH can either be directly reduced back to ascorbate by NADH–dependent monodehydroascorbate reductase (MDHAR) or two MDH molecules can disproportionate to ascorbate and dehydroascorbate (DHA). GSH provides electrons to reduce DHA via DHAR, regenerating reduced ascorbate. The produced GSSG is reduced back to two GSH molecules catalyzed by GR using NADPH as electron source (Foyer & Noctor 2011).

GRXs can further use glutathione to glutathionylate or deglutathionylate other proteins (see 1.2.1) resulting in the post-translational modification of protein thiol groups (*S*-glutathionylation; Meyer & Hell 2005; Couturier, Jacquot, *et al.* 2013).

1.2. Post-translational cysteine-based redox modifications

The proteinogenic amino acid cysteine is very susceptible to oxidation and post translational modification, due to its sulfhydryl residue (-SH). While the protonated form of the thiol group is relatively unreactive, the deprotonated form (thiolate anion; S^-) is very nucleophilic. The acid dissociation constant (pKa) can be used to determine a thiol's reactivity, which is highly specific to each cysteine (Alvarez 2022). A thiol's pKa shows the pH level at which it is 50% deprotonated and 50% protonated. Therefore, under physiological conditions with pH values ranging from pH 7.2 in the cytosol to 8 in plastid stroma (Schwarzländer *et al.* 2008) cysteines with lower pKa's rather exist in their thiolate, reactive form, while higher pKa values indicate a high amount of the protonated, unreactive thiol. While free cysteine shows a pKa of ~8.3 (Alvarez & Salinas 2022), the cysteine residue of glutathione shows a pKa of 8.7-8.9 due to the influence of the amino acid environment (Deponte 2022). An example for a plastidial protein, its pKa and its influence on activity is the glyceraldehyde-3-phosphate dehydrogenase (GAPDH, catalytic Cys 154), which shows a pKa ~6. The thiol state of GAPDH is influenced by pH changes in the plastid stroma upon light-dark induced pH changes (pH 7, dark – pH 8, light) shifting to slightly more deprotonated GAPDH in the light (Zaffagnini, Fermani, *et al.* 2019).

Protein thiolates are very susceptible to the oxidation with H_2O_2 resulting in the formation of sulfenic acid (-SOH). Shown by reaction rates in the amplitude of 10^5 - 10^8 M^{-1} s^{-1} measured for peroxidases reacting with H_2O_2 (Baker & Poole 2003; Poole *et al.* 2004; Manta *et al.* 2009; Gupta & Carroll 2014) which are faster than the uncatalyzed reaction of GSH and H_2O_2 (see Table 1). Further oxidation of the sulfenic acid with H_2O_2 leads to sulfinic ($-SO_2H$) and sulfonic ($-SO_3H$) acid (Figure 1) with reaction rates between 0.1-10^2 M^{-1} s^{-1} (Zaffagnini, Fermani, *et al.* 2019). While sulfonic acid formation is irreversible and potentially leads to protein dysfunction, in specific cases like the 2-Cys peroxiredoxins, sulfinic acid can be reduced by sulfiredoxins in the presence of ATP (Rey *et al.* 2007; Couturier, Chibani, *et al.* 2013; Figure 1).

Table 1: Reaction rates of thiols with H_2O_2

Reaction	Reaction rate	Reference
2 GSH + H_2O_2 → GSSG +2 H_2O	0.9 $M^{-1}s^{-1}$	Gupta & Carroll 2014
HSA(SOH) + GSH → HSA(SSG) + H_2O	2.9 $M^{-1}s^{-1}$	Deponte 2017, Turell *et al.* 2008
$GAPDH_{red}$ + H_2O_2 → $GAPDH_{ox}$ + H_2O	2–11×10^2 $M^{-1}s^{-1}$	Deponte 2017, Little & O'brien 1969
PRX_{red} + H_2O_2 → PRX_{ox} + H_2O	10^8 $M^{-1}s^{-1}$	Deponte 2017, Manta *et al.* 2009

Sulfenic acids are energetically less stable, due to the oxidation state of the sulfur atom and rather display an intermediate oxidation state of the thiol prior to further modification or formation of a disulfide (Reddie & Carroll 2008). In a recent study of Huang *et al.* (2019) 1,394 proteins in Arabidopsis protein extracts were identified as target of *S*-sulfenylation. Protein *S*-sulfenylation occurred at positions involved in metal binding or catalytic sites of the protein. Due to the instability of the sulfhydryl group, proteins identified as *S*-sulfenylated might occur as *S*-glutathionylated (see 1.2.1) *in vivo* in the presence of GSH (Zaffagnini, Bedhomme, Marchand, Morisse, *et al.* 2012; Couturier, Chibani, *et al.* 2013). For example oxidized human serum albumin (HSA(SOH)) showed a reaction rate of 2.9 $M^{-1}s^{-1}$ when reacting with GSH to glutathionylated HSA (HSA(SSG)) and H_2O (Little & O'brien 1969, see Table 1).

Redox modifications can contribute to protein activity regulation, protection from overoxidation, or signaling via a thiol switching mechanism (Buchanan & Balmer 2005). This redox regulation of thiols is catalyzed by a large set of enzymes belonging to the thioredoxin (TRX) superfamily, which includes thioredoxins (TRX; Gelhaye *et al.* 2005; Buchanan & Balmer 2005), peroxiredoxins (PRX; Dietz 2003) protein disulfide isomerases (PDI; Frand *et al.* 2000) and glutaredoxins (GRX; Li 2014).

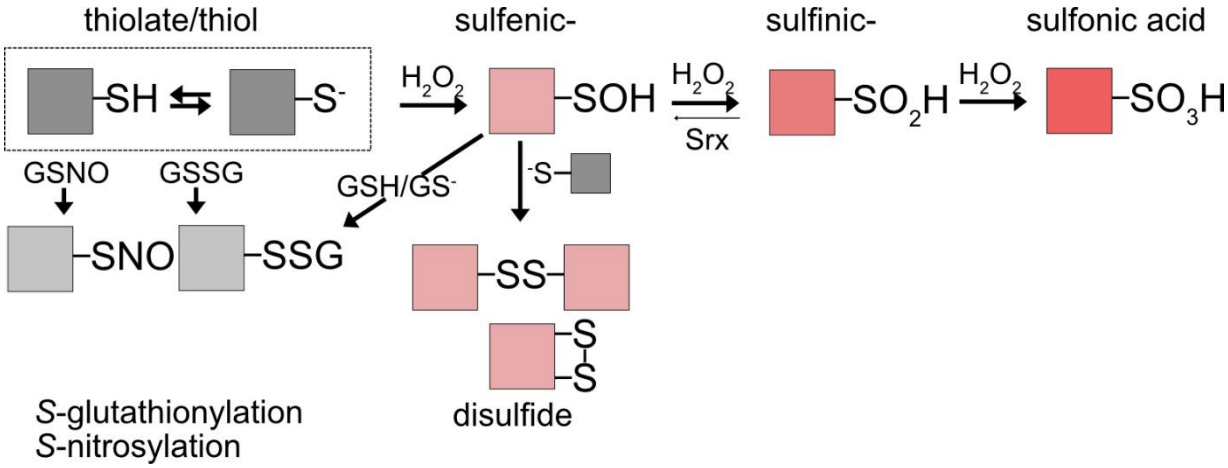

Figure 1: Post-translational thiol modifications of cysteines

Simplified schematic overview of cysteine modifications and cysteine oxidation with H_2O_2 resulting in the formation of sulfenic, -sulfinic or -sulfonic acid. For specific proteins, oxidation o sulfenic acid to sulfinic acid is partially reversible e.g. via sulfiredoxins (Srx) for example for the 2-Cys peroxiredoxin Tsa1 (Biteau *et al.* 2003) The sulfenic acid group can be further oxidized to sulfinic or sulfonic acid or lead to the formation of *S*-glutathionylation in the presence of glutathione. Oxidation of the thiolate with GSSG or GSNO results as well the formation of PTM's like *S*-nitrosylation or *S*-glutathionylation (Modified from Couturier, Chibani, *et al.* 2013 and Alvarez & Salinas 2022)

1.2.1 Reversible protein *S*-glutathionylation

The formation of a disulfide between a protein cysteine residue and glutathione is termed *S*-glutathionylation. The reduction of such a mixed disulfide is catalyzed by oxidoreductases belonging to class I of GRXs (see 1.3 Glutaredoxins). While *S*-glutathionylation has been studied extensively in animals and humans where glutathionylation was indicated to play a role in human diseases like cancer (Mieyal *et al.* 2008; Dalle-Donne *et al.* 2009; Zaffagnini, Bedhomme, Marchand, Morisse, *et al.* 2012), less is known about the importance and function of protein *S*-glutathionylation in plants. However, it is hypothesized to fulfill a function in protection of proteins from overoxidation and is involved in regulation of protein activity (Zaffagnini, Bedhomme, Marchand, Morisse, *et al.* 2012).

Possible pathways of protein glutathionylation involve the interaction of GSSG with a protein thiol, the reduction of a disulfide bond with GSH and the reaction of an activated thiol such as a sulfenic acid (-SOH) with GSH (Dixon, Skipsey, *et al.* 2005; Gao *et al.* 2009; Zaffagnini, Bedhomme, Marchand, Morisse, *et al.* 2012). The reaction rate of a GRX (mammalian GRX1) with GSSG was determined to be 7.1×10^5 $M^{-1}s^{-1}$ (Rabenstein & Millis 1995; Deponte 2017). The reaction of a sulfenic acid group with GSH also results in the formation of *S*-glutathionylation but showed a slower reaction rate of 2.9 $M^{-1}s^{-1}$ (Turell *et al.* 2008, Table 1).

For a detailed review of protein *S*-glutathionylation and reaction constants of competing pathways refer to Deponte 2017.

In vitro studies showed that glutathionylation increased in the presence of GSH and an oxidant rather than GSSG alone (Michelet *et al.* 2005). The plastidial thioredoxin *At*TRXf was efficiently glutathionylated in the presence of H_2O_2 and GSH and revealed a decrease in activity when TRXf was glutathionylated (Michelet *et al.* 2005). Similar results were observed for *At*GAPDH, which was incubated with GSH and H_2O_2. Subsequently after glutathionylation the protein formed insoluble aggregates, concomitant with a decrease in GAPDH-activity (Zaffagnini, Marchand, *et al.* 2019). Although *S*-glutathionylation can happen spontaneously, it can also be catalyzed by oxidoreductases including GRX. *S*-glutathionylation was detected for bovine 1-Cys-PRX extracted from rats catalyzed by a glutathione-*S*-transferase (πGST) (Manevich *et al.* 2004). *S*-glutathionylation activity was proposed for serval GRXs including human GRX1 and GRX2 (Gao *et al.* 2009). TRXs and PDIs were able to deglutathionylate proteins but showed only minor glutathionylation activity compared to class I type GRXs (Peltoniemi *et al.* 2006; Rouhier *et al.* 2008). Until today, the exact mechanism of *in vivo* protein *S*-glutathionylation remains unresolved, while the deglutathionylation is known to be mainly catalyzed by GRX and additional by TRX and PDIs (Peltoniemi *et al.* 2006; Rouhier *et al.* 2008).

1.2.1.1 *In vivo* target proteins of *S*-glutathionylation

Several methods were established for detection of *S*-glutathionylated proteins in animals and plants. The radioactive labeling of the glutathione pool with the sulfur isotope ^{35}S requires the short-time inhibition of protein biosynthesis and application of an oxidant like diamide or H_2O_2. In the presence of diamide, this method allowed the identification of 25 target proteins in *Chlamydomonas reinhardtii* (Michelet *et al.* 2008). However, the impact of protein biosynthesis disruption and oxidative stress treatment in influencing the *in vivo* state of protein *S*-glutathionylation as well as the specificity towards identifying only glutathionylated groups is under discussion (Gao *et al.* 2009). Another approach uses biotin tagged glutathione and offers serval detection methods such as immunodetection or affinity-based purification. By using biotinylated glutathione, the method is very specific for glutathionylation and does not require disruption of protein synthesis (Gao *et al.* 2009). In Dixon, Skipsey, *et al.* 2005 oxidized biotinylated glutathione was used to identify *in vitro* and *in vivo* targets of glutathionylation following oxidative stress treatment in Arabidopsis. Additionally,

glutathionylation targets in general can be identified via immunodetection with an anti-glutathione antibody or via a GRX-mediated deglutathionylation and subsequent thiol labeling with biotinylated NEM (*N*-ethylmaleimide) (Gao *et al.* 2009).

Depending on the position of the glutathionylated cysteine, protein *S*-glutathionylation can influence the proteins activity in a positive or negative manner or show no impact on activity at all. An inactivation upon *S*-glutathionylation of its cysteine residues was detected for the protein tyrosine phosphatase (PTP) of soybean by Dixon *et al.* in 2005. Furthermore, *S*-glutathionylation of enzymes involved in carbon fixation such as phosphoribulokinase (PRK) decreased enzyme activity (Zaffagnini, Bedhomme, Groni, *et al.* 2012).The Isocitrate lyase (ICL) of *C. reinhardtii,* an enzyme of the glyoxylate cycle, is reversibly inhibited upon its glutathionylation and was shown to be deglutathionylated by poplar GRXS12 (Bedhomme *et al.* 2009; Zaffagnini, Bedhomme, Marchand, Couturier, *et al.* 2012). However, *S*-glutathionylation can also influence structural properties such as aggregation as seen for cytosolic GAPDH (*in vitro*; Zaffagnini, Marchand, *et al.* 2019) or dissociation of poplar 1-Cys D-PRX homodimers into monomers (Noguera-Mazon *et al.* 2006).

_S_-glutathionylation target: glyceraldehyde-3 phosphate dehydrogenase (GAPDH)

GAPDH is a very abundant glycolytic enzyme and highly conserved between species. The two cytosolic isoforms of GAPDH in *Arabidopsis thaliana* (GAPC1, At3g04120; GAPC2, At1g13440) are glutathionylated under oxidative stress induced by tert-butylhydroperoxide (BHP) (Dixon, Skipsey, *et al.* 2005). The cysteine residue Cys 149 (referred to the sequence of GAPDH of *Bacillus stearothermophilus,* Biesecker *et al.* 1977) with a pKa of 5.7 was identified as highly susceptible to oxidation via H_2O_2 and further post-translational modification (Hancock *et al.* 2005; Bedhomme *et al.* 2012). In the absence of GSH, H_2O_2 treatment led to the irreversible inactivation of GAPC1 *in vitro*. However, in the presence of GSH, GAPC1 activity could be restored after reduction with DTT. This observation led to the conclusion that glutathionylation of Cys 149 protects GAPC1 from irreversible inactivation of the protein by overoxidation (Bedhomme *et al.* 2012). In animals, GAPDH fulfills functions outside of the glycolytic pathway, such as (post)transcriptional gene regulation (reviewed in Sirover 2011). Moonlighting functions were also proposed for plant isoforms of GAPDH under oxidative stress conditions due to accumulation and nucleus translocation upon cadmium treatment (Vescovi *et al.* 2013). Plastidial monomeric isoforms of GAPDH (A_4-GAPDH) are as well as the

cytosolic GAPDH very susceptible to oxidation via H_2O_2 and subsequent *S*-glutathionylation (Zaffagnini, Bedhomme, Groni, *et al.* 2012; Zaffagnini, Marchand, *et al.* 2019). Mixed disulfide formation between A_4-GAPDH and GSH was shown by MALDI-TOF mass spectrometry. Oxidation and glutathionylation of Cys 149 lead to the loss of enzyme activity, which was reversible in the case of glutathionylation or in the presence of only low levels of H_2O_2 (Zaffagnini *et al.* 2007). Interestingly, heterooligomers of plastidial GAPDH consisting of A and B subunits (A_nB_n -GAPDH) were less sensitive to glutathionylation most likely due to Cys 149 protection by subunit B (Zaffagnini *et al.* 2007; Marotta *et al.* 2022). This AB-isoform of GAPDH is light-regulated by forming high molecular weight oligomers in the dark and low molecular weight oligomers in the light. This process is directly regulated by the interaction of the cysteines in the C-terminal extension of subunit B (Cys-349 and Cys-358) with TRXf (Sparla *et al.* 2002). As mentioned above, TRXf has been identified as plastidial target protein of glutathionylation, that impacts its activity. Thus the glutathionylation is further influencing also the regulation of TRXf target proteins like GAPDH (Michelet *et al.* 2005).

_S_-glutathionylation target: thioredoxins

Thioredoxins are small thiol oxidoreductases with a molecular weight of ~12 kDa and a canonical CxxC/CxxS active site motif. They are members of the TRX superfamily sharing a similar tertiary structure termed TRX-fold. This TRX-fold is characterized by a four stranded ß-sheet with three flanking α helices and an active site motif consisting of one or two cysteinyl residues (Eklund *et al.* 1984; Martin 1995). While only two types of thioredoxins are present in animals and bacteria, multiple ones are present in different compartments of plants (Schürmann & Jacquot 2000). With the N-terminal cysteine in their active site (WC(G/P)PC) thioredoxins can perform a nucleophilic attack on a protein disulfide and serve as an electron donor to their specific target proteins (Arnér & Holmgren 2000; Michelet *et al.* 2005). Target proteins of the plastidial f- type thioredoxins are the name giving fructose 1.6 bisphosphatase (Soulie *et al.* 1981; Geck *et al.* 1996) and other proteins of the Carbon Benson cycle such as sedoheptulose 1,7-bisphosphatase (SBPase), phosphoribulokinase (PRK), NADP-dependent malate dehydrogenase (NADP-MDH) and glucose 6-phosphate dehydrogenase (G6PDH) (Schürmann & Jacquot 2000). Thioredoxins are reduced by thioredoxin reductases, which obtain their reducing power either via NADPH (e.g. cytosolic NADPH-dependent thioredoxin reductase, NTR) or via the photosynthetic electron transport to ferredoxin (ferredoxin dependent thioredoxin reductase, FTR)(Gao *et al.* 2009). Noteworthy, when an additional

cysteine outside of the active site (Cys 60) of TRXf in *Arabidopsis thaliana* is glutathionylated, decreased activity of the target proteins such as GAPDH was observed. This was explained by less efficient reduction of TRXf via the FTR system (Michelet *et al.* 2005). Thus, glutathionylation and its role in CBC related protein regulation should be further investigated. *In vitro* experiments of Bedhomme *et al.* 2012 showed that mitochondrial poplar h-type thioredoxins were able to deglutathionylate and reactivate GAPDH only being ~two times slower that the tested class I GRX.

1.3. Glutaredoxins

Glutaredoxins are ubiquitous proteins present in all kingdoms of life and are also members of the TRX superfamily. Based on the primary structure and the amino acid sequence of the active sites, GRXs were classified into four classes. Class I consist of GRXs with a CXXC or CXXS motif, whereas class II members share a highly conserved CGFS active site motif. Class III GRXs are exclusively found in plants and harbor a CCXC/S type motif while class IV are found in specific algae (Couturier, Jacquot, *et al.* 2009, 2013). Depending on their specific biochemical features glutaredoxins are involved in iron sulfur cluster coordination (class II) and are electron transmitters via deglutathionylation and reduction of thiols (class I) (Liedgens *et al.* 2020; Trnka *et al.* 2020). Several putative GRX-interacting (poplar GRXC4-C30S) enzymes like peroxiredoxin (e.g *At*PRXIIE and *At*PRXIIF) and ascorbate peroxidase have been identified among 92 other proteins by Rouhier *et al.* 2005. Depending on the glutaredoxin, the deglutathionylation occurs via a mono- or dithiol mechanism which is influence by the presence of a second cysteine close to the active site of the GRX (Rouhier *et al.* 2008; Gao *et al.* 2009, Figure 2). The mixed disulfide between the cysteine of the protein and glutathione is resolved by a nucleophilic attack of the thiolate of the catalytic cysteine of GRX resulting in the glutathionylation of the GRX (GRX-SSG) and the release of the reduced protein. In the monothiol mechanism, a second GSH moiety reduces the GRX-SSG, which leads to the release of a GSSG and the reduced GRX. GSSG will subsequently get reduced back to GSH via the NADPH-dependent glutathione reductase. GRXs performing the dithiol mechanism are able to form an intramolecular disulfide upon glutathionylation and can be reduced for example by the thioredoxins system or two molecules of GSH (Couturier, Jacquot, *et al.* 2013). However, also GRXs with a dithiol active site (such as WCSYC, *At*GRXC5) are able to reduce disulfides via the monothiol mechanism and concomitantly get reduced via GSH (Couturier *et al.* 2011;

Zimmermann *et al.* 2020). Studies based on monocysteinic active site mutants pin-pointed the important function in deglutathionylation to the N-terminal cysteine residue (Rouhier *et al.* 2002; Johansson *et al.* 2004; Gao *et al.* 2009). In addition, it was shown in yeast that a monocysteinic variant can functionally replace dithiol GRXs (Zimmermann *et al.* 2020).

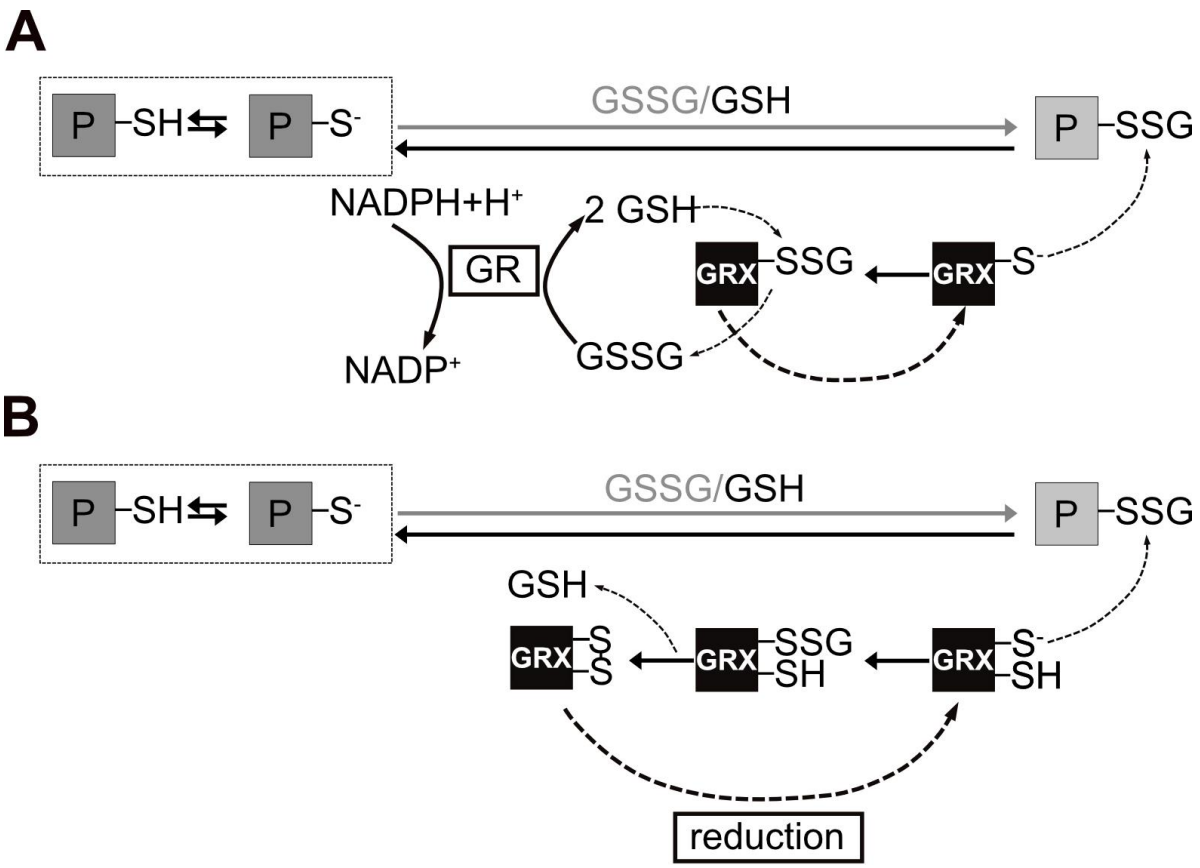

Figure 2. Protein deglutathionylation catalyzed by GRX

Mechanism of the monothiol (**A**) or dithiol (**B**) deglutathionylation of a glutathionylated target protein. The reaction starts with a nucleophilic attack of the N-terminal active site cysteine of GRX on the mixed disulfide between the protein and glutathione. Subsequently the reduced, deglutathionylated target protein is released, while GRX becomes glutathionylated. The deglutathionylation of GRX depends on the type of GRX. In the monothiol mechanism, a free GSH attacks the mixed disulfide between GRX and glutathione. GSSG and the reduced GRX are released. The produced GSSG will get reduced by the glutathione reductase. In the dithiol mechanism, glutathionylation of the GRX is released by forming an intramolecular disulfide bridge between a second cysteine present near to the active site. Reduction of the formed disulfide can be further reduced by e.g the thioredoxin system (FTR, NTR) (modified from Zaffagnini, Bedhomme, Marchand, Morisse, *et al.* 2012).

1.3.1 Class I GRX

Class I GRX are characterized by their C[P/G/S]Y[C/S] motif and their oxidoreductase activity. The class I forms three clades, which can be further subdivided into 3 subclades: GRXC1 and GRXC2, GRXC3 and GRXC4, and GRXC5 and GRXS12. *At*GRXC1 and *At*GRXC2 both showed cytosolic localization (Riondet *et al.* 2012), while *At*GRXC3 and *At*GRXC4 are targeted to the secretory pathway (Belin *et al.* 2015). *At*GRXC5 and *At*GRXS12 localize to the plastids (Couturier *et al.* 2011). Phylogenetic analysis from streptophyte algae to seed plants revealed conserved clades of the cytosolic, plastidial and secretory isoforms (Müller-Schüssele, Bohle, *et al.* 2021; Figure 3). *At*GRXC1, with an active site motif of the CGYC type and deglutathionylation activity, has been found to form a homodimer containing an iron sulfur cluster (Fe-S)(Riondet *et al.* 2012). The coordination of an Fe-S cluster was already previously observed for another class I GRX *in vitro*: for *At*GRXC5 with a WCSYC active site (Couturier *et al.* 2011). For GRXC1 the function of coordination of a Fe-S cluster was pin-pointed to the presence of a guanin (G) in the active site motif (Rouhier *et al.* 2007; Riondet *et al.* 2012). Upon mutation of the guanin to a proline the ability of iron sulfur coordination was lost. This observation was supported by GRXC2 (CPYC) only showing oxidoreductase activity and no Fe S cluster coordination.

The single mutants of the cytosolic localized GRXs (GRXC1 and GRXC2) in Arabidopsis did not reveal a phenotype (Riondet *et al.* 2012). However, the double knock-out *grxc1grxc2* is reported to be lethal, suggesting a redundant function of GRXC1 and GRXC2 rather pointing towards an essential function of GRX reduction activity (Riondet *et al.* 2012). Potential knock-outs of Arabidopsis *grxc3* and *grxc4* showed significant differences in the hypocotyl length compared to WT grown in elevated temperatures (Dard *et al.* 2022). In other model organisms like yeast, a double knock-out of both enzymatic active, cytosolic GRX isoforms GRX1 and GRX2 was viable and only resulted in lethality when concomitantly knocking-out all cytosolic TRX isoforms (Draculic *et al.* 2000). Yet, single and double mutants of yeast GRX1 and GRX2 revealed sensitivity to oxidants like H_2O_2 (Luikenhuis *et al.* 1998). Regarding the plastidial GRXC5 or GRXS12 no null mutants are described yet. Hence, *in vivo* data on the function of class I GRX and their impact under physiological conditions in plants remains still scarce.

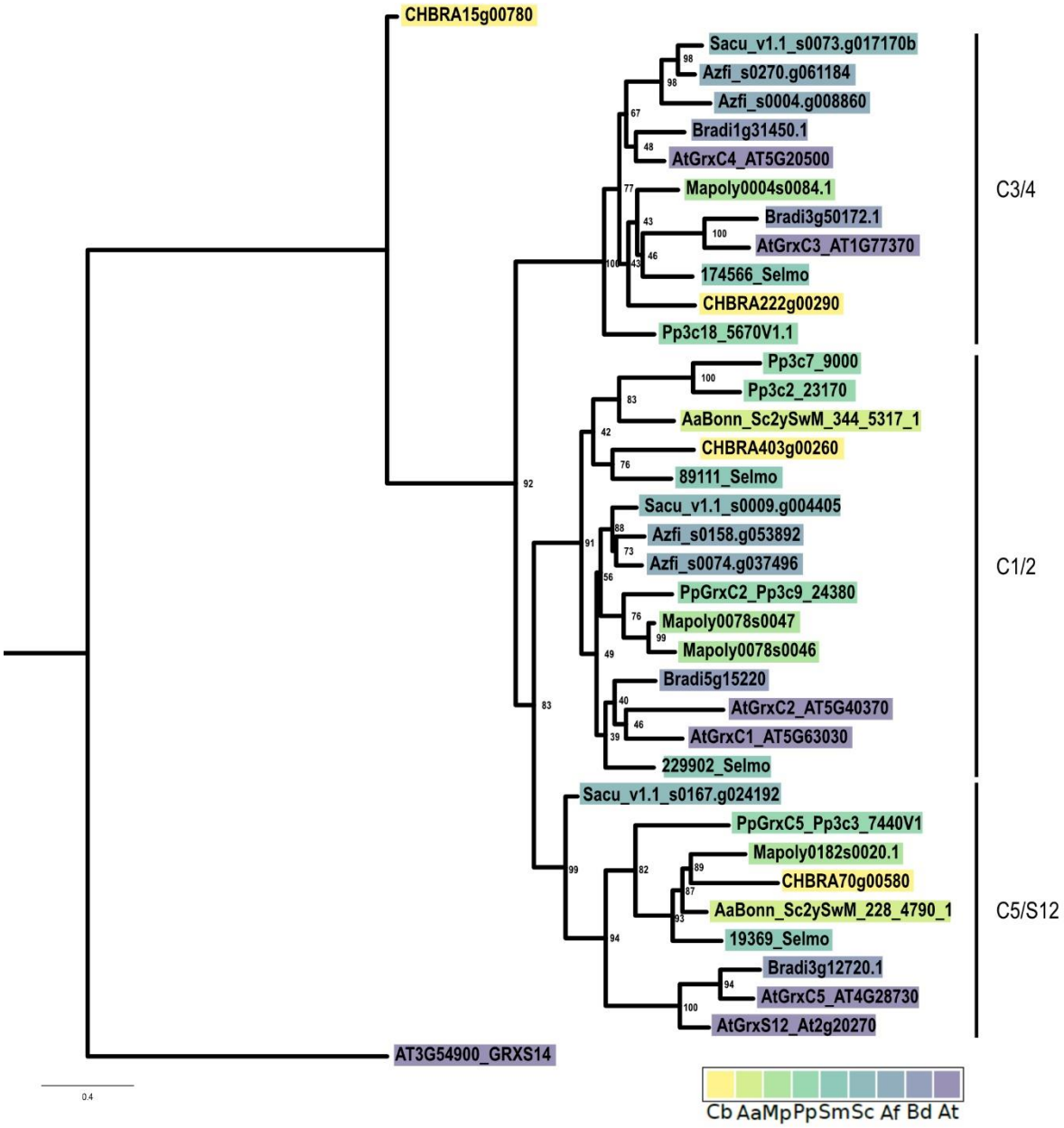

Figure 3: Phylogenetic tree of class I GRX

Phylogenetic analysis of class I GRX from streptophyte algae to seed plants revealing defined subclades of class I GRX. Gene identifiers referring to gene models for *Chara braunii* (CHBRA), *Anthoceros agrestis* strain Bonn (AaBonn), Marchantia polymorpha (Mapoly), *Physcomitrium patens* (Pp), *Selaginella moellendorffii* (Selmo), *Salvinia cucullata* (Sacu), *Azolla filiculoides* (Azfi), *Brachypodium distachyon* (Bradi) and *Arabidopsis thaliana* (At) and are color-coded (right corner). The class I GRX alignment for tree generation with IQ web tree (Trifinopoulos *et al.* 2016) was retrieved from Müller-Schüssele, Bohle, *et al.* 2021.

1.3.1.1 Plastidial class I GRX

Many identified protein *S*-glutathionylation targets are found to be plastid localized (Zaffagnini, Bedhomme, Groni, *et al.* 2012). Therefore, plastidial isoforms of class I GRX are very important to understand plastidial redox regulations via post translational modification. The plastidial isoforms of class I GRX include GRXC5 and GRXS12. GRXC5 and GRXS12 share 70% of sequence identity, however they differ in their active site motif with GRXC5 showing the typical dithiol motif 'WCSYC', whereas GRXS12 has a WCSYS active site motif. According to Couturier *et al.* 2011 deglutathionylation with monomeric *At*GRXC5 is occurring over the monothiol mechanism, followed by the reduction of GRX-SSG with a GSH molecule. In its homo dimer form *At*GRXC5 is able to coordinate a [2Fe-2S] cluster with its crystal structure being resolved (Couturier *et al.* 2011; 3RHC). Regarding *At*GRXS12, a clear plastidial localization was shown by a GFP-fusion construct expressed in tobacco leaves. In Couturier, Koh, *et al.* 2009 biochemical properties of poplar GRXS12 were determined revealing *in vitro* reductase activities with HED, DHA and A_4-GAPDH as substrate. The involved catalytic cysteine at positions 29 showed a low pKa with 2.8, sensitive to post translational modification (Couturier, Koh, *et al.* 2009). Under physiological conditions, *At*GRXS12 might as well catalyze protein glutathionylation as seen for example for a cytosolic GRX2 of Chlamydomonas (Roret *et al.* 2021; de Bont *et al.* 2022). Further sequence analysis revealed that the tryptophane (W) in the active site motif is highly conserved in GRXC5 and GRXS12 isoforms, but not observed for other GRX groups (Couturier, Koh, *et al.* 2009).

1.3.1.2 Determining GRX activity

Generally, class I GRXs show a thiol reduction activity which is classically tested with bis(2-hydroxyethyl) disulfide (HED) deglutathionylation. GRX activity is determined indirectly over GSSG reduction via GR, leading to a decrease in NADPH and its absorbance at 340 nm (Begas *et al.* 2015). Activities of several class I GRXs were determined within the HED assay such as $5.50 \times 103\ M^{-1}s^{-1}$ for *At*GRXC1 and $0.06 \times 10^5\ M^{-1}s^{-1}$ for *At*GRXC5 (Couturier, Koh, *et al.* 2009; Couturier *et al.* 2011; Riondet *et al.* 2012; Trnka *et al.* 2020). Another method to detect the oxidoreductase activity of GRXs is the use of the artificial protein called roGFP2 (reduction-oxidation sensitive GFP).

1.4. Redox-sensitive green fluorescent protein (GFP)

The green fluorescent protein (GFP) of the jelly fish *Aequorea victoria* was engineered to obtain two redox sensitive cysteinyl residues (Cys 147, Cys 204) on the surface of two adjacent ß-strands (strand 7 and 10). Oxidation of the cysteines of the roGFP results in the formation of a disulfide bridge between Cys 147 and 204. Oxidation-dependent structural changes influence the protonation state of the chromophore, allowing a fluorescence-based ratiometric read-out of the cysteine redox state (Figure 4). GRX activity can be assed with the ratiometric biosensor roGFP2, which was developed from EGFP and a S65T mutation leading to an excitation maximum at 480 nm (reduced state) and 405 nm (oxidized state) (Hanson *et al.* 2004; Aller *et al.* 2013).

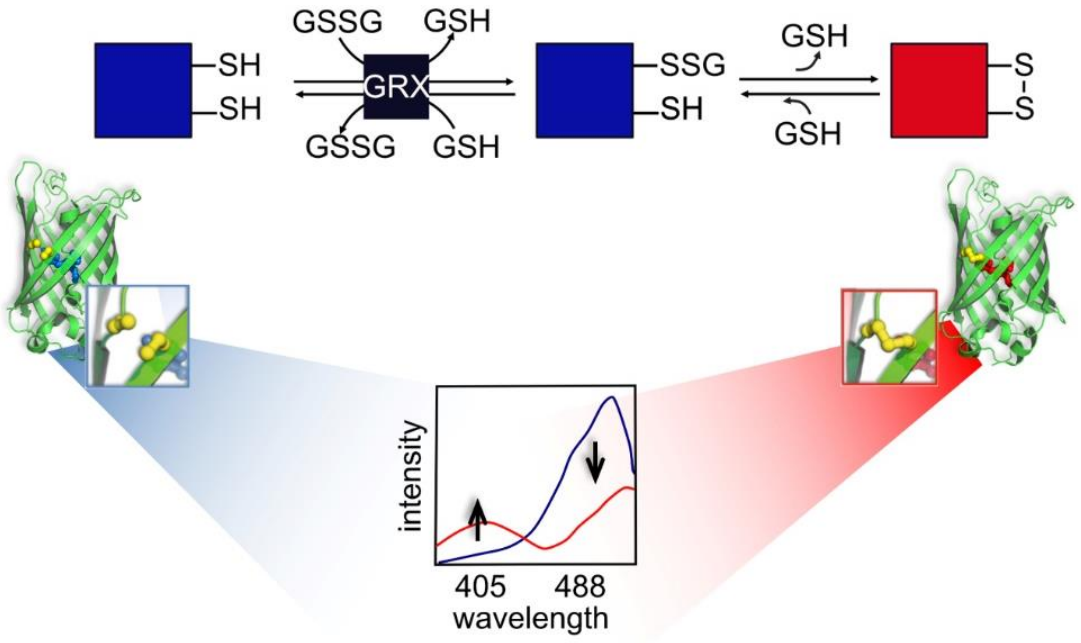

Figure 4: Structural changes of reduced and oxidized roGFP2

The roGFP2 oxidation occurs via an intermediate step of *S*-glutathionylation catalyzed by GRX. Structural changes upon oxidation or reduction are due to the formation of an intramolecular disulfide formation of Cys 147 and Cys 204. Formation of the disulfide bridge leads to conformational changes in the protein barrel further influencing the protonation state of the GFP. The protonated form of roGFP2 shows an excitation maximum at 405 nm while the deprotonated form shows an excitation maximum at 488 nm allowing a ratiometric sensor read-out. Reduced and glutathionylated roGFP2 are indicated with a blue color, while oxidized roGFP2 is depicted with a red color. Sulfur atoms are depicted as yellow. Modified from Morgan & Schwarzländer 2016.

roGFP2 oxidation occurs via a glutathionylated intermediate of roGFP2 and is catalyzed by GRX, therefore making roGFP2 a unique tool to test for GRX enzymatic properties with the ability to determine the oxidation capacity of GRXs (Meyer *et al.* 2007). In addition to these

bidirectional measurements, another advantage is also the direct readout of glutathionylation or deglutathionylation based on the changes in fluorescence emission of reduced or oxidized roGFP2, respectively. Examples of GRX activities measured with roGFP2 are *At*GRXC1, human Grx2 and Grx5 published in Trnka *et al.* 2020.

1.4.1 The *in vivo* use of the genetically encoded biosensor roGFP2

The application of genetically encoded redox sensors and their targeting to cellular compartments allowed a deeper investigation of physiological redox dynamics (Aller *et al.* 2013; Nietzel *et al.* 2018; Elsässer *et al.* 2020; Müller-Schüssele, Schwarzländer, *et al.* 2021; Ugalde, Fuchs, *et al.* 2021; Ugalde, Schlößer, *et al.* 2021; Ugalde *et al.* 2022). *In planta*, in the presence of GRX, roGFP2 equilibrates rapidly with the glutathione redox potential (E_{GSH}), therefore allowing the determination of compartment-specific E_{GSH} (Gutscher *et al.* 2008). In contrast to other fluorescent proteins like YFP (a yellow fluorescent protein) GFP is insensitive to changes in pH ranging from 5.5-8.5.

To overcome the problem of compartments lacking or showing less GRX activity, a fusion construct of human GRX1 and roGFP2 was engineered (GRX1-roGFP2) which guarantees rapid equilibration of roGFP2 with the respective E_{GSH} independent of cellular GRX concentration (Gutscher *et al.* 2008; Schwarzländer *et al.* 2016). Several roGFP variants exist displaying differences in their midpoint potential for the optimal application in various compartments (Meyer & Dick 2010). The fusion of other redox-sensitive enzymes to roGFP2 changes the specificity of the sensor response. For example, the fusion of a yeast peroxidase oxidant receptor peroxidase-1 (ORP1) to roGFP2 led to the development of a probe specific for oxidation via H_2O_2 (roGFP2-ORP1), while the sensor is reduced via the glutathione redox system (Nietzel *et al.* 2018).

1.5. *Arabidopsis thaliana, Physcomitrium patens*, and *Hordeum vulgare* as model species and their advantages

Arabidopsis thaliana belongs to the family of *Brassicaceae* with a short reproductive cycle of 6 - 8 weeks. Since 2000, the Arabidopsis genome is fully sequenced (The Arabidopsis Genome Initiative 2000). Arabidopsis is genetically accessible e.g. via chemical mutagenesis or *A. tumefaciens* mediated transformation and multiple knock-out lines are commercially available. Up until today, Arabidopsis is one of the major model organisms in plant biology (Koornneef & Meinke 2010).

Physcomitrium patens is a moss and belongs to the bryophytes and gained momentum in evolutionary research based on its basal position between algae and higher land plants (Rensing *et al.* 2008). The haploid gametophore is the dominant generation of *P. patens*. The moss shows a high rate of homologous recombination, which is a DNA repair mechanism and used in reverse genetic approaches to specifically target genes (Falz & Müller-Schüssele 2019). The genome of *P. patens* was fully sequenced in 2008 (Rensing *et al.* 2008).

Hordeum vulgare is a model crop plant belonging to the family of *Poaceae*. It is a self-pollinating wheat with a fully sequenced genome (Mascher *et al.* 2017). Barley is genetically accessible via embryo transformation (Amanda *et al.* 2022). It is often used as model organism to study the effects of drought and climate change on yield of crops (Dawson *et al.* 2015).

1.6. Objectives of this study

To analyze available data on *S*-glutathionylation targets and evolutionary conservation of the plastidial GSH-dependent redox network

Many enzymes can be redox-regulated by post-translational modifications of cysteines via thiol switching systems like the GSH-GRX or TRX system. This allows for a more rapid adaptation of metabolism to environmental conditions through the regulation of enzyme activity (Zaffagnini, Bedhomme, Marchand, Morisse, *et al.* 2012). However, the evolution of the glutathione-dependent network in plastids of land plants as well as the conservation of *S*-glutathionylated cysteines on the other hand, has not been studied, yet.

The publicly accessible genomes of *Chara braunii* , *Anthoceros agrestis, Salvinia cucullata, Azolla filiculoides, Physcomitrium patens, Marchantia polymorpha* , *Selaginella moellendorfii*, *Brachypodium distachyon* and *Arabidopsis thaliana* allow to study the evolutionary context of enzymes belonging to the GSH-dependent plastidial redox network via phylogenetic analysis. To gain information on the evolutionary conservation of *S*-glutathionylation sites, known positions of *S*-glutathionylation in the different plant species will be identified and summarized via literature screening and compared within the 9 plant species.

To elucidate the influence of E_{GSH} and GSH:GSSG on protein *S*-glutathionylation

Protein *S*-glutathionylation has been shown to occur increasingly under oxidative stress conditions (Michelet *et al.* 2005; Zaffagnini, Bedhomme, Marchand, Morisse, *et al.* 2012). However, if *S*-glutathionylation was induced through a change in E_{GSH} or by the increase of GSSG resulting in GSH:GSSG ratio changes remains unknown so far.

- **To investigate the influence of changes in E_{GSH} on target proteins of *S*-glutathionylation**

  Crossing GAPC-YFP into the *gr1-1* background

To further investigate the influence of a less reducing E_{GSH} on protein *S*-glutathionylation, the cytosolic *S*-glutathionylation target GAPDH (Bedhomme *et al.* 2012; Zaffagnini, Marchand, *et al.* 2019) fused to a YFP tag (Vescovi *et al.* 2013) is crossed into the cytosolic and peroxisomal glutathione reductase mutant of Arabidopsis (*gr1-1,* (Marty *et al.* 2009)) which showed a less reducing E_{GSH} under control conditions. GAPDH was shown to accumulate upon *S*-glutathionylation forming insoluble, inactive aggregates (Zaffagnini, Marchand, *et al.*

2019).The GAPDH-YFP x *gr1-1* lines will be analyzed regarding its GAPDH-YFP expression level and localization under less reducing E_{GSH}.

Tracking E_{GSH} in the crop plant *H. vulgare*

With the goal of providing a first tool to assess the *in vivo* glutathione redox dynamics in crop plants the genetically encoded biosensor roGFP2 is introduced in *H. vulgare.* First measurements will be done providing information of the suitability of the redox sensor GRX1-roGFP2 in barley.

- **To investigate *in vitro* the influence of GSH:GSSG ratio on protein glutathionylation under constant E_{GSH}**

The E_{GSH} is determined by the Nernst equation and is dependent on the exact concentrations of $[GSH]^2$ and [GSSG]. Different GSH:GSSG ratios can result in the same redox potential depending on the assumed total glutathione concentration, and vice versa. In the oxidation mechanism of roGFP2 with GSSG in the presence of GRX one molecule of GSH is bound to one of the active site cysteines of roGFP2 (glutathionylation intermediate state). The second active site cysteine resolves the glutathionylation leading to the formation of an intramolecular disulfide bridge and the release of the other GSH molecule. Thus, roGFP2 equilibrates rapidly with the E_{GSH} in the presence of GRX.

Kinetic differences in roGFP2 oxidation with varying GSH:GSSG ratio

In cooperation with Paolo Trost, Mirko Zaffagnini and Jacopo Rossi (University of Bologna, Italy) the hypothesis was formed that the glutathionylation of GRXC1 and roGFP2 is dependent on the ratio of GSH:GSSG (1 molecule of GSSG consumed, 1 molecule GSH released), whereas the endpoint of roGFP2 oxidation is dependent on the E_{GSH} (1 molecule GSSG consumed, 2 molecules GSH released). Here I investigate the roGFP2 oxidation kinetics in buffer solutions with a constant E_{GSH} and varying GSH:GSSG ratios.

***S*-glutathionylation of monothiol vs. dithiol proteins upon GSH:GSSG ratio changes**

Based on the assumption of roGFP2 oxidation levels rather depending on the E_{GSH} than the GSH:GSSG ratio, different *S*-glutathionylation states are expected for a monothiol protein, without the ability to release the *S*-glutathionylation by disulfide formation. A cysteine mutant of roGFP2 (roGFP2-C204S) will be used in oxidation assays with varying GSH:GSSG ratios and

constant E_{GSH}. An SDS-PAGE-based size-shift assay will be established as read-out method to analyze for differences in levels of *S*-glutathionylation in different GSH:GSSG ratios.

To explore *in planta* functions of plastidial class I GRX

Class I GRX catalyze the (de)glutathionylation of proteins (Couturier, Jacquot, *et al.* 2013). Two plastidial class I GRX isoforms are known (GRXC5 and GRXS12) and have been studied in *A. thaliana* (Couturier, Koh, *et al.* 2009; Couturier *et al.* 2011). However, *in vivo* knock-out studies of class I GRX remain scarce, with only a few studies showing redundant functions of other GRX within one compartment (Draculic *et al.* 2000; Riondet *et al.* 2012; Dard *et al.* 2022). The precise function and impact of class I GRXs on plastid redox processes *in vivo*, remains largely unknown.

To unravel the *in vivo* function of class I GRX and its active role in *S*-glutathionylation, a *P. patens* knock-out of the single class I GRX in plastids (Δ*grxc5*) will be generated and analyzed regarding its phenotype and biochemical features. Within Δ*grxc5* we generate a mutant completely lacking class I GRX activity in one compartment.

2. Material & Methods

2.1. Consumables and laboratory equipment

2.1.1 Laboratory equipment

ÄKTA Prime Plus chromatography (GE Healthcare, Germany, Solingen)

Airstream LHG-F8 horizontal, 1,8 m Faust Lab Science GmbH

Airstream® Class II Biological Safety (ESCO, Singapore)

Beckman Centrifuge Avanti® J-26-XP (Beckman Coulter GmbH, Germany, Krefeld)

Rotor JA-10 and JA-25.50 (Beckman Coulter GmbH, Germany, Krefeld)

Eppendorf BioPhotometer Plus (Eppendorf, Germany, Hamburg)

Eppendorf Centrifuge 5424 R (Eppendorf, Germany, Hamburg)

Eppendorf Centrifuge 5430 (Eppendorf, Germany, Hamburg)

Eppendorf Thermomixer™ Comfort (Eppendorf, Germany, Hamburg)

Incubators Ecotron Typ ET25-TA-RC (INFORS, Swiss, Bottmingen)

Incubators C Ecotron Typ ET25-TA-00 (INFORS, Swiss, Bottmingen)

ECL ChemoStar imaging system (INTAS, Germany, Göttingen)

Labculture® Vertical laminar flow cabinet (ESCO, Singapore)

M165FC stereomicroscope and DCF245C Camera (Leica, Germany, Wetzlar)

M205 FCA stereomicroscope (Leica, Germany, Wetzlar)

Mini Trans-Blot® cell (Bio-Rad, Germany, Feldkirchen)

Mini-PROTEAN® Tetra cell (Bio-Rad, Germany, Feldkirchen)

Nanodrop 2000 c (Thermo Scientific™, USA, Waltham)

Platereader CLARIOstar® (BMG Labtech, Germany, Ortenberg)

TissueLyser II (Qiagen, Germany, Hilden)

LSM 780 (Zeiss, Germany, Jena)

LSM 880 (Zeiss, Germany, Jena)

2.1.2 Antibiotics

Table 2: Antibiotic working concentrations

Antibiotic	concentration [µg/mL]
Ampicillin	100
Kanamycin	50
Hygromycin	12.5-25
Rifampicin	100
Spectinomycin	100
G418 (Neomycin)	12.5

2.1.3 Frequently used enzymes, kits and chemicals

Kits:

NucleoSpin® Plasmid (Macherey-Nagel, Germany, Düren)

NucleoSpin® RNA (Macherey-Nagel, Germany, Düren)

NucleoSpin® Gel and PCR Clean-up (Macherey-Nagel, Germany, Düren)

RevertAid First Strand cDNA Synthesis (Thermo Scientific™, USA, Waltham)

Zeba™ Spin Desalting Columns (Thermo Scientific™, USA, Waltham)

Enzymes:

*Bsp*Q1 (New England Biolabs, USA, Ipswich)

BP clonase II enzyme mix (Invitrogen™, USA, Waltham)

*Eco*RV (New England Biolabs, USA, Ipswich)

LR clonase II enzyme mix (Invitrogen™, USA, Waltham)

Proteinase K Invitrogen™ (Invitrogen™, USA, Waltham)

Phusion® High-Fidelity DNA Polymerase (Thermo Scientific™, USA, Waltham)

T4 DNA Ligase (Thermo Scientific™, USA, Waltham)

Taq™ DNA Polymerase (New England Biolabs, USA, Ipswich)

Chemicals:

Dithiothreitol, DTT (Carl Roth GmbH, Deutschland, Karlsruhe)

2,2-dithiopyridylsulfide, DPS (Sigma, Japan, Kawasaki)

Hydrogen peroxide 30%, H_2O_2 (Carl Roth GmbH, Deutschland, Karlsruhe)

Glutathione, reduced, GSH (Carl Roth GmbH, Deutschland, Karlsruhe)

Glutathione disulfide, GSSG (Carl Roth GmbH, Deutschland, Karlsruhe)

N-etyhlmaleimide, NEM (Sigma, Japan, Kawasaki)

Methoxypolyethylene glycol maleimide, MPEG-Mal, (Sigma, Japan, Kawasaki)

2.2. Molecular Methods

2.2.1 Polymerase chain reaction

Polymerase chain reaction (PCR) was performed to amplify specific DNA fragments. A standard protocol using the *Taq*-Polymerase (NEB) is shown in Table 3 used for colony and genotyping PCR. Annealing temperature was chosen depending on the oligonucleotide combination. Elongation time was adjusted to the fragment length and dependent on the type of polymerase. For cloning the high fidelity Phusion® polymerase was used (NEB). For colony PCR, a bacteria colony was picked with a pipette tip and mixed into the PCR mix. Transgenic lines of Arabidopsis and Physcomitrium were identified with genotyping PCR. Primers either bound to the wild type allele or within the transformed construct. For genotyping 1 µL of resuspended DNA was used as template. A standard PCR program and primers used in standard PCR reactions are shown in Table 3 and Table 4.

Table 3: Polymerase chain reaction standard protocol.

	[c]	[µL]			
Primer f/r	10 µM	0.5	Initial denaturation	95°C	1 min
H_2O		19.875	Denaturation	95°C	30 s
dNTPs	10 mM	0.5	Annealing	X C	30 s
Polymerase [NEB Taq]	0.5 U	0.125	Elongation	68°C	X s
10x NEB reaction buffer	1x	2.5	Final elongation	68°C	~ 6 min
DNA template	~1 ng	~1	Repetition of step 2 to 4 for 30 cycles		

Table 4: Primer sequences

Name	Sequence	Construct
PTA1_NosT_Seq_R	CGGCAACAGGATTCAATCTTAAG	Screening PTA1/2 vector
Act5_seq_F	TCCACATGGCTACAGCTG	Screening Act5 promotor
pETG10-A_F	GTGAGCGGATAACAATTCCCC	Screening T7 promotor
M13_R	CCAACGTCAAAGGGCGAAAA	Screening M13 terminator
LBb1	GACCGCTTGCTGCAACTCTCTCAGG	Left boarder T-DNA
GR1_F	TCGTCTATGGAGCTACTTACGGTGG	*GR1* locus
GR1_R	CGCAAAAATATCCAATCTACTGAGCAC	*GR1* locus
EF1α F	CGACGCCCCTGGACATC	Amplify EF1α transcript
EF1α R	CATGTTGTCACCCTCGAACC	Amplify EF1α transcript
CROST2 R	CCGAGGCTGTAGCCGAC	CROST2 screening
35S_F	GCAAGTGGATTGATGTGATATC	Screening 35 S promotor

2.2.2 cDNA synthesis and semiquantitative RT-PCR

For transcription of single stranded RNA to cDNA the reverse transcriptase kit of ThermoFisher was used as described in the manufacturer's protocol. For this, 1 µg previously extracted RNA (see 2.2.6) was mixed with 1 µL of 100 µM oligo dT_{18} primer in a total volume of 12 µL. Samples were handled on ice and buffer, RNAse inhibitor, dNTPs and RevertAid M-MulV reverse transcriptase were added according to the manual. Negative controls were done by adding water instead of MulV reverse transcriptase. After incubation for 1 h at 42°C the enzyme was deactivated at 70°C for 5 min. cDNA was used for semiquantitative PCR analysing the gene expression level of GRXC5 using gene specific primers. The *Ef1*α transcript was amplified as RNA/cDNA control.

2.2.3 Agarose gel electrophoresis

Agarose gel electrophoresis was performed on PCR products and plasmid purifications to analyze and separate DNA fragments. Loading buffer (0.05% (w/v) bromophenol blue, 0.05% (w/v) xylene cyanole and 8% (v/v) glycerol) was added to the samples prior to gel loading. For the agarose gel, 0.8-2% of agarose was dissolved in 1x TAE buffer (40 mM TRIS-HCL pH 7.6, 20 mM acetic acid, 1 mM Ethylenediaminetetraacetic acid (EDTA). The gel was supplemented with 4 µL/100 mL of HDGreen Plus (Intas). The gene ruler mix (ThermoFisher) was used as size standard. The gel was run at 80-120 V for 30 - 60 min depending on the size of the gel and DNA fragment, respectively. Images were taken with the INTAS ECL ChemoStar imaging system (Intas).

2.2.4 Gateway® cloning

For Gateway® cloning, cloning DNA sequences (CDS) were amplified including the flanking sites (*attB*1/*attB*2) via PCR. The 'attB1_sequence of interest_attB2' construct was cloned into an entry vector via BP-reaction using the Gateway® BP clonase II enzyme mix, following the manufacturer's instructions. *E. coli* DH5α were transformed with the reaction mix and positive colonies were selected on LB plates (Lysogeny Broth: 1% (w/v) tryptone, 0.5% (w/v) yeast extract, 1% (w/v) NaCl, pH 7 with NaOH, 2% (w/v) agar; Bertani 1951) supplemented with the respective antibiotics. Colonies were verified via PCR and plasmids of positive colonies were sent for sequencing. LR reaction was performed using the Gateway® LR clonase II enzyme mix to clone the gene of interest into the destination vector. The LR reaction was used for transformation of *E. coli* DH5α. Plasmids of positive colonies were purified for transformation of the destination organism (plant/bacteria).

Table 5: Gateway vectors

Plasmid	Selection marker (on plasmid)	Target organism	Usage
pDONR207	Kan	*E. coli*	entry vector
pETG-10A	Amp	*E. coli*	protein expression
pSS02	Kan	*A. thaliana*	plant expression
PTA2_Act5_NosT_GW	Amp	P. patens	plant expression

Table 6: Gateway constructs generated or analyzed in this study

Construct	Destination vector	Target organism	Usage
TKTP-roGFP2	PTA2_Act5_NosT_GW	*P. patens*	roGFP2 in plastids of Δ*grxc5* + WT
ΔA120-GRXC5	pETG10-A	*E. coli*	protein characterization
CROST2	PTA2_Act5_NosT_GW	*P. patens*	thioredoxin sensor in plastids

Table 7: Gateway primer sequences

Name	Sequence	Construct
attB1-TKTP f	GGGGACAAGTTTGTACAAAAAAGCAGGCTATGGCGTCTTCTTCTTCTCT	TKTP-roGFP2
TKTP-roGFP2 r	CCTCGCCCTTGCTCACCAGCGCAGTCTCAGTT	TKTP-roGFP2
TKTP-roGFP2 f	ACTGAGACTGCGCTGGTGAGCAAGGGCGAGGAG	TKTP-roGFP2
roGFP2-attB2 r	GGGGACCACTTTGTACAAGAAAGCTGGGTCTTACTTGTACAGCTCGTCCATG	TKTP-roGFP2
F_N_CROST_attB1	GGGGACAAGTTTGTACAAAAAAGCAGGCTTAATGGATTCACAGCTAGTCTTGT	CROST2
R_N_CROST_attB2_stop	GGGGACCACTTTGTACAAGAAAGCTGGGTTTCATTCGATATTATGACGAATCTTA	CROST2
PpGRXC5_A120 F	GGGGACAAGTTTGTACAAAAAAGCAGGCTTAGCAGCAGGTTCGGGG	ΔA120-Grxc5
PpGRXC5_r	GGGGACCACTTTGTACAAGAAAGCTGGGTGTCAACTCCTGTTTGCACCAG	ΔA120-Grxc5

2.2.4.1 Δ120A_GRXC5

P. patens WT cDNA was used as PCR template to amplify GRXC5 lacking the first 120 amino acids (cDNA synthesis see 2.2.2). 5’ and 3’ primer sequences (PpGRXC5_A120 F and PpGRXC5_r, Table 7) contained Gateway recombination sites B (attB). The PCR product was verified via its size of 361 bp on an agarose gel and cut out for gel elution. The gel eluted product was further used for cloning into the pDNOR207 entry vector via BP reaction and further recombined into the pETG-10A expression vector via LR reaction (see Table 5). The final A120_GRXC5_pETG-10A construct was sequenced and used for transformation of the *E. coli* expression strain Rosetta2 and its correct transformation verified by colony PCR. This construct was generated in a cooperation with Jacopo Rossi (University of Bologna, Italy).

2.2.4.2 TKTP-roGFP2

The construct of plastidial targeted roGFP2 was generated by overlap PCR. For this, two DNA templates were generated in separate PCR reactions. First, the plastidial target sequence of *N. tabacum* was amplified using TKTP forward (attB1-TKTP f) and TKTP-roGFP2 reverse (TKTP-roGFP2 r) primers using the plasmid of TKTP-cpcpYFP as template (Stefanie Müller-Schüssele, University of Kaiserslautern, Germany). The forward primer contained the Gateway recombination site B in its 5’ end, while the reverse primer created an overlap to the 5’ roGFP2 sequence. Similarly, roGFP2 was amplified with TKTP-roGFP2 f and roGFP2-attB2 r to create a 5’ TKTP sequence overlap and an attached gateway recombination site at the 3’ end (primers

see Table 7). The construct was cloned via the Gateway system into the pDONR207 entry vector and verified via colony PCR and send for sequencing. The plasmid preparation of BP-clone (#4) was used for LR reaction into the PTA2_Act5_GW destination vector. The construct TKTP-roGFP2_PTA2_Act5_GW was transformed into DH5α and concomitant verified by sequencing. For transformation into *P. patens* protoplasts, the construct of LR clone #1 was digested with *Bsp*Q1.

2.2.4.3 CROST2

CROST2 was cloned into the PTA2_Act5_GW Gateway destination vector for further transformation into *P. patens* protoplasts. The CROST2_pRI201_AN template was obtained from Prof. Tori Hisabori (Sugiura *et al.* 2019). Primers adding 5' and 3' Gateway recombination sites (F_N_CROST_attB1, R_N_CROST_attB2_stop, Table 7) were used. The PCR product was analyzed over an agarose gel and used for BP cloning into pDONR207 and transformation into DH5α. Clones were verified via sequencing and clone #1 further used for LR reaction into PTA2-Act5_GW. After transformation of the LR-construct into DH5α, the product was sequenced and used for further transformation of *P. patens* digested with *Bsp*Q1.

2.2.5 DNA extraction from plant material

Plant material (not frozen, 10-30 mg) was pulverized using the TissueLyser II (Qiagen) with two metal beads or via plastic pestles. 400 µL of Edwards buffer (200 mM Tris-HCL pH 7.5, 250 mM NaCl, 25 mM EDTA, 0.5% SDS (w/v)(Edwards *et al.* 1991) were added. Samples were vortexed and centrifuged for 5 min at 20,000 *g*. 300 µL of the supernatant was transferred into a new 1.5 mL Eppendorf tube and 300 µL isopropanol was added. Tubes were inverted carefully and centrifuged for 10 min at 20,000 *g* rpm. Resulting pellets were washed with 700 µL 70% (v/v) EtOH and centrifuged again for 3 min at 20,000 *g* rpm. EtOH was discarded and the pellet was air dried for 30 min before resuspension in 50 µL H_2O. Concentrations were measured photometrically with the Nanodrop 2000 c (Thermo Scientific™, see 2.2.7).

2.2.6 RNA extraction from plant material

Plant material was frozen in liquid nitrogen and pulverized using the TissueLyser II (Quiagen) at 30 Hz for 1.5 min. This step was repeated until all samples were pulverized. RNA was

extracted using the NucleoSpin RNA isolation kit (Macherey-Nagel) following the manufacturer's instructions. Resuspension was done in 20 µL RNAse free H_2O.

2.2.7 Quantification of nucleic acid concentrations

Concentrations of DNA and RNA samples were measured using the Nanodrop 2000c spectrophotometer.

2.3. Protein methods

2.3.1 Recombinant protein extraction and affinity-based purification

Recombinant proteins containing an N-terminal His_6-tag were expressed in *E. coli* BL21 (DE3), Rosetta2 or Origami. 2 x 500 mL LB media with the respective antibiotics were inoculated with 1 mL over-night culture of *E. coli* and grown at 37°C. At OD_{600} = 0.6-0.8, isopropyl-D-1-thiogalactopyranoside (IPTG) was added to a concentration of 0.5 -1 mM and the bacteria were further grown for 24 h at 21°C. Cells were centrifuged at 8000 *g* for 10 min. The cell pellet was resuspended in 50 mL buffer A (20 mM Tris, 150 mM NaCl, 20 mM Imidazole pH 7.4) containing protease inhibitors (100 µL Phenylmethylsulfonylfluoride (PMSF), cOmplete™ Protease Inhibitor Cocktail (Merck, Germany)). After complete resuspension, 100 µL 1 mg/mL lysozyme was added. The solution was sonicated 5 x for 1 min at 50% power, while the falcon was cooled in ice. Sonicated cells were centrifuged at 25.000 *g* for 20 min at 4 °C. The supernatant was filtered (0.45 µm) and loaded onto a HisTrap (Ni-NTA, GE Healthcare) column using a peristaltic pump. The column was equilibrated with binding buffer A prior to column loading. Protein purification was done using the Äkta Prime. The protein was eluted by increasing the concentration of imidazole by adding buffer B (20 mM Tris-HCL, 150 mM NaCl, 500 mM Imidazole, pH 7.4) while collection 1 mL samples. Fractions were collected and loaded on an SDS-PAGE. Pure fractions were combined to one sample and re-buffered in 100 mM Tris-HCL pH 7 using PD-10 desalting columns packed with Sephadex G25 resin (Cytiva, GE17-0851-01). Protein concentrations were determined (see 2.2.7). Fractions were further concentrated if needed using Vivaspin centrifugal concentrators (Sartorius ST-2717).

2.3.2 Methanol-chloroform based extraction of plant protein for immunodetection of protein bound glutathione

Frozen plant material was pulverized using the TissueLyserII (Qiagen). Protein thiol groups were blocked by addition of a final concentration of freshly balanced 20 mM *N*-ethylmaleimide (NEM, Sigma 128-53-0) directly added to the lysis buffer. 100 µL lysis buffer (7.5 M urea, 2.5 M thiourea, 12.5% (v/v) glycerol, 62.5 mM Tris-HCL pH 8, 0.1% (v/v) Sigma plant protease inhibitor cocktail (P9599)) was added per 10 mg plant material. Samples were vortexed and incubated for 10 min at room temperature (RT, 22°-25°C). Subsequently, samples were centrifuged at 20000 *g* for 1 h. Supernatant was transferred into a new tube and three volumes methanol (RT) and one volume chloroform was added. Samples were vortexed before and after addition of four volumes H_2O and centrifuged again for 15 min at 20000 *g* at 0°C. The upper phase of the sample was discarded. The proteins accumulated at the interface. Four volumes of cold methanol were added to the remaining sample (interface and lower phase) and mixed gently. Samples were incubated for >1 h at -20 °C. For pelleting the protein, the samples were centrifuged for 15 min at 20000 *g* at 0°C. The supernatant was discarded and the protein pellet left to airdry for around 15 min. Protein pellets were dissolved in 50-100 µL protein resuspension buffer (50 mM Tris-HCL, 8 M urea, pH 7.5-8) unless stated otherwise. Protein concentration was determined using Bradford solution (see 2.3.2).

2.3.3 Determination of protein concentration

For measuring protein concentration, bovine serum albumin (BSA) was set as standard (0.1-0.7 mg/mL or 10-100 µg/mL). Protein samples were diluted to fit in the range of the standard curve. 10 µL of diluted sample was added to 1:5 diluted Roti®Quant (Carl Roth GmbH, K015.1) solution in a total volume of 220 µL in a 96-well plate and incubated for 5 min before monitoring the absorbance at 595 nm in 96 well plate using a plate reader (CLARIOstar, BMG Labtech). For proteins used in immunoblot analysis in section 4.1.5.4 quantification was done following Roti®Quant (Roth, K015.1) instructions.

2.3.4 SDS-PAGE and staining

For a reducing, denaturing SDS-PAGE samples were prepared by mixing the sample with 1x Laemmli buffer (2% (w/v) SDS, 50 mM Tris-HCl pH 6.8, 0.002% (w/v) bromophenol blue, 5% (v/v) ß-mercaptoethanol, 10% (v/v) glycerol) and heated for 15 min at 60°C. Samples for a

non-reducing, non-denaturing SDS-PAGE were prepared without reductants in the Laemmli buffer and not heated prior to loading (except when especially mentioned otherwise). Mini-PROTEAN® precast gels (Bio-Rad) were purchased for gel electrophoresis in different gel percentages (4-20%, 10%). Gel electrophoretic separation of proteins was performed in SDS-running buffer (25 mM Tris-HCL pH 8.3, 192 mM glycine, 0.1% (w/v) SDS) at 80-200 V for 30 - 90 min until the running front reached the end of the gel. PageRuler™ Prestained Protein Ladder (ThermoFisher, 26616, 5 µL) was loaded as molecular size standard. Gels were stained for >1 h in PageBlue ™ protein staining solution (ThermoFisher). Protein gels were destained in H_2O for serval hours until the gel background appeared clear. Gels loaded with roGPF2 and roGFP2-C204S were imaged under UV-light with the INTAS ECL ChemoStar imaging system (Intas) without further staining unless stated otherwise.

2.3.5 Labelling of reduced thiol groups of roGFP2 and roGFP2-C204S

2.5 µM roGFP2 or roGFP2-C204S was treated with 1 mM DTT for 30 min to obtain a fully reduced control. For a fully oxidized control, 1 mM H_2O_2 was incubated with 2.5 µM of roGFP2 or roGFP2-C20S. GSH:GSSG ratios were calculated for a constant E_{GSH} (see 2.4.2.1, Table 16) and GSH and GSSG concentrations were pipetted accordingly to the respective wells of a 96 well plate. 1 µM of GRXC1 was added to the wells of varying GSH:GSSG concentrations. As additional control, 40 µM GSSG together with 1 µM GRXC1 was added into a well. roGFP2 or roGFP2-C204S were added last to prevent oxidation of roGFP2 prior to plate reader measurements. Fluorescence intensity of roGFP2 was followed until an oxidation plateau was reached (see oxidation assay 2.4.2.1, GSH:GSSG ratios). Subsequently after assay stop, 2.5 µM of roGFP2 or roGFP2-C204S (1.4 µg) were treated with either 50 mM *N*-ethylmaleimide (Sigma, 128-53-0) or 5 mM of methoxy-polyethylene glycol M_n 5000 (MPEG-Mal, Sigma: 63187; PEG average M_n 5,000) dissolved in 0.1 M potassium phosphate buffer pH 7.4 and 1 mM EDTA and left shaking in the dark at 25°C for 2 h. Samples were mixed with 1x non-reducing Laemmli buffer and run on an SDS-PAGE (see 2.3.4). A more detailed protocol can be found in Bohle *et al.* 2023 (see Appendix).

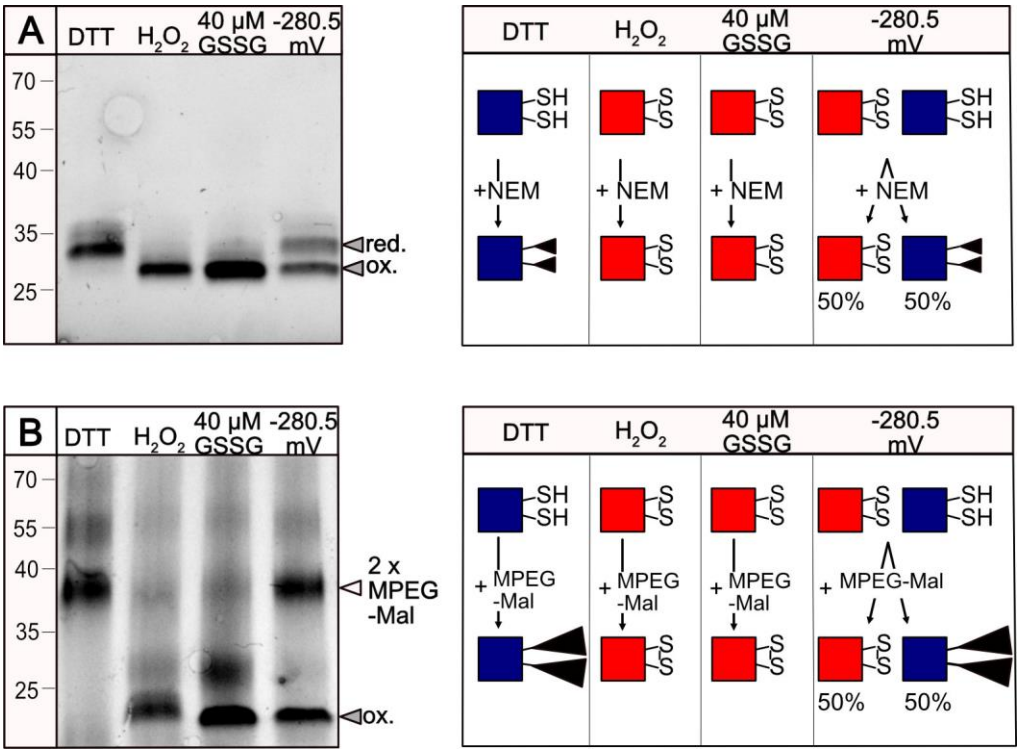

Figure 5: roGFP2 size shift assay

Example of roGFP2 gel- after oxidation assay. **A** Left: roGFP2 was pre-reduced with 10 mM DTT before oxidation with 40 µM GSSG +1 µM GRXC1 (40 µM GSSG) or 6.6 mM GSH + 40 µM GSSG + 1 µM GRXC1 (glutathione buffer with E_{GSH} ~ -280 mV at pH 7.4). Reduced cysteines were blocked with 20 mM NEM before the gel run to avoid reoxidation. 2.1 µg roGFP2 (M_w =28 kDa) (5 µL of 3 µM roGFP2) were loaded on a 10% SDS-PAGE. Right panel: schematic overview of redox states in A. **B** Left panel: Free cysteines were labelled with 5 mM MPEG-Mal (adding c. 5 kDa for each reduced cysteine). 2.1 µg roGFP2 were loaded on a 10% SDS-PAGE. Right panel: schematic overview of redox states in **B** (Figure and legend of Bohle *et al.* 2023).

2.3.6 Immunoblot analysis

Unstained SDS-PAGEs were transferred to a PVDF membrane (Immobilon-P, Millipore Corporation, Billerica, MA, USA) via semi-dry Western blotting. The membrane containing the proteins was blocked in 5% (w/v) milk powder (dissolved in TBS-T (20 mM Tris pH 7.6, 137 mM NaCl, 0.1% (v/v) Tween20)) for 1 h at 25°C or overnight at 4°C before labelling with primary antibodies in 2.5% (w/v) milk powder (dissolved in TBS-T). Membranes were washed with TBS-T after the primary antibody but washed with TBS (20 mM Tris pH 7.6, 137 mM NaCl) after the secondary antibody incubation. For immunodetection the Agrisera ECL kit (Super Bright, AS16 ECL-SN) was used according to the recommendations of the supplier. Western blots were imaged using the INTAS ECL ChemoStar imaging system (Intas).

Table 8: Antibodies

Name	Against	Supplier
Glutathione Monoclonal Antibody (D8) from mouse	Glutathione	www.ThermoFisher.de MA1-7620
Goat anti-Mouse IgG (H&L)	Mouse	www.Agrisera.com AS11 1772

2.3.7 Glutaredoxin activity assay (HED)

Prior to the HED assay, the concentration of the respective GRX was determined via a Bradford assay. To ensure a correct concentration of NADPH, a 20 mM stock was prepared and concentration was verified via absorption measurements using the NADPH extinction coefficient of 6.23 L/mmol/cm. To test for the GRX concentration in which the GRX shows a linear activity, HED assays were performed as described below using 1 mM GSH and 0.7 mM HED (see Table 9), varying the concentration of the GRX from 10-50 nM. The HED assay, with GSH as tested substrate, was performed by preparing a 1 mL cuvette containing 0.5-4 mM GSH and 0.7 mM hydroxyethyl disulfide (HED). With HED as tested substrate, GSH concentration was kept constant at 1 mM, while HED concentrations varied from 0.3 mM to 1.5 mM. To the HED and GSH mixture 200 µM NADPH and 100 mM Tris-HCL, 1 mM EDTA pH 7.9 were added (volumes are displayed in Table 9). After exactly 3 min of incubation, GR (final concentration of 6 µg/mL) and GRXC5 (final concentration 30 nM) were added to the cuvette adding up to a final volume of 1 mL. For each concentration of varying GSH or HED, a background activity was determined. A background activity measurement was performed by adding the same volume of buffer instead of GRX. The absorbance decrease at 340 nm was followed for 1 min using the Nanodrop 2000c spectrophotometer. For a detailed protocol refer to appendix section 7.1)

Table 9: Example of the HED-assay mix

Stock	Final concentration	Volume [µL]
10 mM NADPH	0.2 mM	20
100 mM Tris 1 mM EDTA pH 7.9	100 mM Tris	926
60 mM GSH	1 mM	16.6
100 mM HED	0.7 mM	7
3 min incubation before adding		
0.3 mg/mL GR	6 µg/mL	20
3 µM GRXC5	30 nM	10

2.4. Plate reader-based fluorimetry

Plate reader assays were done using the CLARIOstar® plate reader (BMG) plate reader. 96-well plates (flat base, transparent) were purchased from Sarstedt.

2.4.1 Excitation scans

Excitation and emission scans were done on plants expressing biosensors and on recombinant proteins using the CLARIOstar® plate reader. 96-well plates were filled up with 100 -200 µL imaging buffer (10 mM MES, 5 mM KCL, 10 mM $CaCl_2$, 10 mM $MgCl_2$ pH 5.8). Plant material was transferred to the wells with soft tweezers. Control wells were supplemented with 10 mM H_2O_2, 5 mM DPS or 10 mM DTT to obtain total reduction and oxidation of the sensors. Recombinant proteins were imaged in potassium phosphate buffer and 1 mM EDTA pH 7.4.

Table 10: Excitation or emission scan settings

Fluorophore	Excitation	Emission
TKTP-roGFP2	386 to 495 nm	535±16 nm
hGrx1-roGFP2	386 to 495 nm	530-40 nm
CROST2	365 to 466 nm	494±16 nm
	430-10 nm	459 to 542 nm

2.4.2 Fluorescence assays

Ratiometric time-course measurements for roGFP2 were done using a filter-based excitation of 400-10 nm and 482-16 nm while emission was detected at 520-10 nm. Degree of oxidation of roGFP2 was calculated as described in Aller et al. 2013. Excitation of the CP12-based thioredoxin sensor CROST2 was kept at 430-10 nm, while emission was read out at 530-20 nm and 480-10 nm.

2.4.2.1 Oxidation assay of roGFP2 and roGFP2-C204S

100 µL of 10-20 µM roGFP2 was initially reduced with 10 mM DTT for 30 min before removing the DTT by spin-desalting columns (Zeba™Spin Desalting Columns, ThermoFisher) and exchanging the solution to 100 µL 0.1 M phosphate buffer pH 7.4, 1 mM EDTA. The pre-reduced roGFP2 was added to a well of a 96-well plate in concentrations ranging from 1-10 µM depending on the experiment. To determine the maximum and minimum fluorescence intensity of roGFP2 1 mM H_2O_2 or 1 mM DTT were added to the respective roGFP2 (1-10 µM) in control wells. The assay was conducted in 0.1 M potassium phosphate buffer pH 7.4 containing 1 mM EDTA. A final concentration of 1 µM GRX was added manually from a stock of 10 µM GRX (diluted in 0.1 M phosphate buffer pH 7.4). Fluorescence was followed in the plate reader. Specifically for GRXC5 oxidation assay measurements, a final concentration of 40 µM GSSG, and for GRXC5 reduction 2 mM GSH, were added via the injection pump after 5 min of initial measurements.

When performing oxidation assays with a specific GSH:GSSG ratio, the mixed glutathione solution was added first to the well and the assay was started after manual addition of 1-10 µM of roGFP2 and 1 µM GRXC1. Stock solutions of GSH and GSSG exceeding 0.1 M were dissolved in 0.2 M potassium phosphate buffer pH 7.4. Examples of GSH:GSSG ratios at a specific E_{GSH} are shown in Table 16 section 4.1, To obtain a specific redox potential, the Nernst equation was applied with R = 8.315 J K^{-1} mol^{-1}, T =298.15 K, z =2, F = 96.485 C mol^{-1} (= 96485 J $V^{-1}mol^{-1}$) and E_0' = -251.8 mV at pH 7.4.

$$E_{GSH} = E^{0'}_{GSH} - \frac{2.303RT}{zF} log_{10} \frac{[GSH]^2}{[GSSG]}$$

The Nernst equation is adapted to the wanted E_{GSH} (e.g. -280.5 mV) and solved for the concentration of GSH (unit: Molar)

$$-280.5\,mV = -251\,mV - \frac{2.303RT}{zF}\,log_{10}\frac{[GSH]^2}{[GSSG]}$$

$$-280.5\,mV = -251\,mV - 29.5\,mV \times log_{10}\frac{[GSH]^2}{[GSSG]}$$

$$-29.5\,\mathrm{mV} = -29.5\,\mathrm{mV} \times log_{10}\frac{[GSH]^2}{[GSSG]}$$

$$log_{10}\frac{[GSH]^2}{[GSSG]} = 1$$

$$10 = \frac{[GSH]^2}{[GSSG]}$$

$$[GSH] = \sqrt{10 * [GSSG]}$$

(see Bohle *et al.* 2023)

Limiting factors in feasible GSH:GSSG ratios were stock concentrations of GSH: 100 g/L (= 320 mM) (Roth) and GSSG: ~100 mM (Abcam), as well as volumes (error prone below 1 µL).

2.4.2.2 Reduction assay of roGFP2

For roGFP2-based reduction assays, roGFP2 was used without prior treatment. Exceptions are made for oxidized and reduced controls where 10 µM roGFP2 was treated with 10 mM DTT and 10 mM H_2O_2 30 min before the assay start. The reduced and oxidized controls were diluted 1:10 (in 100 mM potassium phosphate buffer pH 7.4) to obtain a final concentration of 1 µM in the wells. 1 µM of untreated roGFP2 was mixed with 1 µM of *At*GRXC1 or *Pp*GRXC5, 100 µM of NADPH and 1 U glutathione reductase (GR, *Saccharomyces cerevisiae*, Sigma) in 100 µL assay mix to keep the glutathione redox potential of the assay reduced. After measuring for 10 cycles, a final concentration of 2 mM GSH was added automatically by the injection needles of the plate reader into the respective wells. Fluorescence was followed until roGFP2 ratio stabilized.

2.4.2.3 Recovery of roGFP2 in *P. patens* protonema culture after peroxide treatment

The protonema culture of *P. patens* expressing TKTP-roGFP2 was mixed and transferred to fresh KNOP-ME pH 5.8 media one week prior to measurements. 200 µL of protonema culture was pipetted with a wide cut pipette tip into wells of a 96-well plate. Cultivation media was taken up after the moss settled to the bottom of the plate and substituted by 200 µL of

imaging buffer (10 mM MES, 5 mM KCL, 10 mM $CaCl_2$, 10 mM $MgCl_2$ pH 5.8). First roGFP2 measurements were done in the plate reader (CLARIOstar®; Ex. 400-10 nm, 482-16 nm; Em. 530-40 nm, LP504) to detect initial fluorescence values. After 10-15 min the 200 µL imaging buffer was removed with a 100 µL tip and substituted with the same volume of imaging buffer containing either 10 mM H_2O_2 or 10 mM DTT as respective controls. For H_2O_2 recovery experiments, H_2O_2 in concentrations ranging from 1-10 mM were added to the wells. Measurements were continued until a plateau of roGFP2 oxidation was detected. This was the case around 30 min after peroxide addition. Then, H_2O_2 containing wells, except the oxidation and reduction control wells, were buffer exchanged to imaging buffer without peroxide (by taking up the liquid with a 1000 µL pipette) to follow roGFP2 reduction after H_2O_2 treatment. The plate was transferred back to the plate reader as fast as possible and measurements were continued.

2.5. Bacteria methods

2.5.1 Bacteria strains

Table 11: Bacterial strains used in this study

Bacterial Strain	genotype information
E. coli DB3.1	F– *gyr*A462 *end*A1 Δ(sr1-*rec*A) *mcr*B *mrr hsd*S20(rB–, mB–) *sup*E44 *ara*-14 *gal*K2 *lac*Y1 *pro*A2 *rps*L20(SmR) *xyl*-5 λ– *leu mtl*1 (Invitrogen)
E. coli DH5α	F– Φ80*lac*ZΔM15 Δ(*lac*ZYA-*arg*F) U169 *rec*A1 *end*A1 *hsd*R17 (rK–, mK+) *pho*A *sup*E44 λ– *thi*-1 *gyr*A96 *rel*A1 (Stratagene)
E. coli Top10	F– mcrA Δ(mrr-hsdRMS-mcrBC) Φ80lacZΔM15 ΔlacX74 recA1 araD139 Δ(ara-leu)7697 galU galK rpsL (StrR) endA1 nupG (Invitrogen)
E. coli Rosetta2 DE3	F– ompT hsdSB(rB– mB–) gal dcm (DE3) pRARE2 (CamR) (Novagen)
E. coli BL21 DE3	F– ompT gal dcm lon hsdSB(rB–mB–) λ(DE3 [lacI lacUV5 T7p07 ind1 sam7 nin5]) [malB+]K-12(λS) (Invitrogen)
A. tumefaciens AGL-1	AGL-0 (C58 pTiBo542) recA::bla, T-region deleted Mop(+) Cb(R) (Lazo *et al.* 1991)

2.5.2 Bacterial growth conditions

Bacteria were cultivated at 28°C (*A. tumefaciens)* or 37°C (*E. coli*) in liquid LB media (1% (w/v) tryptone, 0.5% (w/v) yeast extract, 1% (w/v) NaCl, pH 7) or on agar plates (LB media supplemented with 2% (w/v) agar). The cultivation media was supplemented with the respective antibiotics in the specific working concentrations.

2.5.3 Plasmid isolation

For plasmid isolation, 5 mL *E. coli* culture was grown overnight at 120 rpm at 37°C. The cells were harvested and plasmids isolated according to the manual of the NucleoSpin Plasmid kit (Macherey-Nagel).

2.5.4 Bacteria transformation

2.5.4.1 *Agrobacterium tumefaciens* transformation

Electro-competent *A*. *tumefaciens* were transformed applying electroporation. Aliquots of 40 µL of competent cells were thawed on ice and mixed with 1 µL of plasmid DNA. The mixture was transferred into the electroporation cuvette and shocked with a pulse of 2500 V for 5 ms. Immediately after electroporation 500 µL LB media was added to the cells and the suspension further grown at 28°C 120 rpm for 1-2 h. Cells were spread onto agar plates containing the respective antibiotics.

2.5.4.2 *E. coli* transformation

Chemically competent *E. coli* were transformed via heat-shock method. Hereby 100 µL of competent cells were thawed on ice and 1 µL plasmid (~10 ng/µl) was added to the cells. After further incubation on ice for 20 min, the cells were heat shocked at 42°C for 45 s and subsequently put back on ice. 600 µL pre-heated LB was added after 2 min to the cells and further grown at 37°C shaking at 120 rpm. After 1 h cells were pelleted at 2000 *g* for 1 min and plated onto agar plates containing the selective antibiotic.

2.6. Plant methods

2.6.1 Arabidopsis thaliana

Experiments were conducted using *A. thaliana* ecotype Columbia-0 (Col-0) referred to as wild-type (WT). Other mutants and crosses used in this study are listed in Table 12 .

Table 12: *A. thaliana* lines used in this study

Name	Function	Reference
miao	point mutation in *At*3g54660	(Yu et al. 2013)
gr1-1	T-DNA insertion in *At*3g24170	SALK_105794 (Marty *et al.* 2009)
p35S-GAPDH-YFP	overexpressing YFP tagged GAPDH	Alex Costa
pgapC-GAPDH-YFP	YFP tagged GAPDH under endogenous (gapC) promoter	Alex Costa (Vescovi *et al.* 2013)
p35S-GAPDH-YFP x *gr1-1*	overexpressing YFP tagged GAPDH in *gr1-1* background	Finja Bohle
pgap*C*-GAPDH-YFP x *gr1-1*	YFP tagged GAPDH in *gr1-1* background under endogenous (gapC) promoter	Finja Bohle
CROST2	Plastid targeted thioredoxin sensor	Construct of Toru Hisabori (Sugiura *et al.* 2019), Finja Bohle
CROST2 *miao*	Plastid targeted thioredoxin sensor	Construct of Toru Hisabori (Sugiura *et al.* 2019), Finja Bohle

2.6.1.1 Growth on agar plates

Prior to plating, seeds were surface-sterilized with incubation in 70% (v/v) ethanol for 3-5 min and subsequently washed three times with sterile water. Seeds were plated onto half-strength Murashige and Skoog medium ($^1/_2$ MS basal salts including vitamins, 1 mM MES pH 5.8, 0.1% (w/v) sucrose, 1% (w/v) agar) and sealed with parafilm. The sown seeds were stratificated for 2 days in the dark at 4°C before transferring to long-day growing conditions (8 h dark, 18°C, 16 h 100 µE, 22°C) placed vertically unless stated otherwise.

2.6.1.2 Growth on soil

Plants were grown on a mixture of soil (Floradur B-seed, Oldenburg), quartz sand and perlite peligran 0-6 in a ratio of 10:1:1. For fast growth and seed harvest plants were cultivated on Jiffy-7® pellets, grown for two weeks and replanted into the soil mixture. Young seedlings or freshly sown seeds were covered with a plastic dome for one week to increase humidity. Plants were grown under long day conditions for 16 h at 22°C at 100-120 µmol photons $m^{-2}s^{1}$ and 8 h at 18°C in darkness. The relative air humidity in the growth chamber was kept constant at 50%.

2.6.1.3 Arabidopsis stable transformation by floral dip

Arabidopsis stable transformation via floral dip was based on the protocol of (Clough & Bent 1998).4–6-week-old plants with a high number of inflorescences were dipped upside down for serval seconds in a solution of *Agrobacterium tumefaciens* AGL-1 containing the designated construct. The Agrobacterium containing solution was prepared by inoculating a 400 mL bacteria culture and grown at 28°C for several hours until an OD_{600} of 0.6-0.8 was reached. Bacteria cells were harvested by centrifugation at 5000 *g* for 10 min and the pellet was washed with water before it was resolved to an OD_{600} of 1 in floral dip solution (5% sucrose (w/v), 0.02% (v/v) Silwet L-77). After dipping, the plants were kept in the dark for 24 h before placing them into standard growing conditions, using a plastic dorm to increase humidity in the first days after transformation. Seeds were harvested and screened for successful transformation by the selective marker (antibiotic, fluorescence) on ½ MS agarose plates. Plants selected after screening were transferred to soil and grown until seed harvest.

2.6.1.4 Crossing of Arabidopsis lines

The mature but closed buds of flowering Arabidopsis plants were gently fixated under a binocular. Using sharp forceps, the petals, sepals and anthers were removed carefully without injuring the stigma. Taking an open flower of another genotype, the flower with the ripe anthers is pressed upon the stigma of the first plant, covering the stigma with pollen. To prevent Arabidopsis from self-pollinating, all other buts not pollinated in the crossings were removed from the plant. When the siliques developed, they were harvested and stored at room temperature for drying before selection on antibiotics, fluorescence or via genotyping PCR.

2.6.2 *Physcomitrium patens*

Physcomitrium patens cultures were grown axenically either in liquid media or on agar plates. Experiments were conducted in the WT XI background. Lines used in this study are listed in Table 13.

Table 13: *P. patens* lines used in this study

name	Function	Source
Δ*gr1*	knock-out of GR1 (*Pp*1s13_127)	Stefanie Müller-Schüssele (Müller-Schüssele *et al.* 2020) Δ*gr1* #4
Δ*grxc5*	knock-out of GRXC5 (*Pp*1s321_10)	Stefanie Müller-Schüssele, Alexa Brox, Finja Bohle Δ*grxc5* #54 IMSC-Nr. 40954 Δ*grxc5* #64 IMSC-Nr. 40956 Δ*grxc5* #249 IMSC-Nr. 40955
TKTP-roGFP2	plastid targeted roGFP2 in WT	Finja Bohle WT #20, IMSC-Nr. 40959
TKTP-roGFP2 in Δ*grxc5*	plastid targeted roGFP2 in Δ*grxc5* #54	Finja Bohle Δ*grxc5* #17, IMSC-Nr. 40957 Δ*grxc5* #21, IMSC-Nr. 40958
CROST2	plastid targeted CROST2 in WT	Stefanie Müller-Schüssele, Alexa Brox, Finja Bohle
CROST2 in Δ*gr1*	plastid targeted CROST2 in Δ*gr1*	Stefanie Müller-Schüssele, Alexa Brox, Finja Bohle
Δ*gr1* in Δ*grxc5*	double knock-out of plastidial GR (*Pp*1s13_127) and plastidial glutaredoxin C5 (*Pp*1s321_10)	Finja Bohle, Sadia S. Tamanna Stefanie Müller-Schüssele

2.6.2.1 Growth on agar plates

Moss colonies were plated on KNOP-ME medium (250 mg/L KH_2PO_4, 250 mg/L KCl, 250 mg/L $MgSO_4$ 7 x H_2O, 1 g/ L 1 $Ca(NO_3)_2$ x 4 H_2O, 12.5 mg/L $FeSO_4$ x 7 H_2O, and microelements H_3BO_3, $MnSO_4$, $ZnSO_4$, KI,Na_2MoO_4 x 2 H_2O, $CuSO_4$, $Co(NO_3)_2$) as described in (Reski & Abel 1985) supplemented with 12 g/L purified agar (Oxoid™ agar, ThermoFisher). Moss plates were sealed with $^1/_3$ micropore $^2/_3$ parafilm and grown horizontally under long day conditions for

16 h at 22°C in 100 µE/m^2 s and 8 h in the dark. For specific experimental set-ups like selection after transformation, moss was cultivated on cellophane discs placed on KNOP-ME agar plates.

2.6.2.2 Growth in liquid culture

Moss protonema cultures were grown in 250 mL Erlenmeyer flasks containing KNOP-ME media. The moss was transferred to new medium at regular intervals (weekly) and homogenised using a dispersion tool (Ultraturrax T25, IKA-Werke GmbH) to promote new protonema growth. Sterile controls were taken regularly on TSAG plates (15 g/L casein peptone, 5 g/L soya peptone, 5 g/L NaCl, 10 g/L glucose, 15 g/L agar, pH ~7.3). Liquid cultures were grown on rotary shakers ~100 rpm under long day conditions (16 h, 22°C 100 µE/m^2 s /8 h dark) in growth cabinets.

2.6.2.3 *Δgrxc5 P. patens* knock-out generation

Cloning steps and generation of the DNA construct were performed by Stefanie Müller-Schüssele (University of Kaiserslautern, Germany) and Alexa Brox (University of Bonn, Germany). The construct for generating GRXC5 knock-outs in *P. patens* was generated by the exchange of the complete *GRXC5* coding sequence (Pp1s321_10V6.1, Pp3c3_7440_V1) with a nptII resistance cassette under the Nos promotor and terminator. The resistance cassette was amplified from the pBSNNN plasmid (Horstmann *et al.* 2004) with primers (GrxC5ko_npt_F and R) creating a 5’ and 3’ overhang of homologous regions (HR) upstream and downstream of the genomic *GRXC5* sequence. Next, two PCRs were conducted on the *P. patens* genomic DNA to amplify the 5’ (PpGrxC5ko_5PHR P1+P2) or the 3’ (PpGrxC5ko_3PHR P3+P4) homologous region 602 bp upstream or 621 bp downstream of *GRXC5* with a respective overhang of the *nptI* sequence obtained from the pBSNNN plasmid. The flanking primers (PpGRXC5ko_5PHR P1 and PpGrxC5ko_5PHR P4) contain an additional *Eco*RV restriction site. For further information, primers used to design the DNA fragments are listed in Table 14. A PCR was conducted with the three DNA templates obtained from the steps described above: 5’ HR of *GRXC5* (20 ng), 3’ HR of *GRXC5* (20 ng) and the *nptII* cassette (50 ng) using the flanking primers PpGrxC5ko_5PHR P1 and PpGrxC5ko_5PHR P4. The PCR was verified by an agarose gel and the expected band was cut out and eluted in 30 µL H_2O via the NucleoSpin® Gel and PCR Clean-up kit (Macherey-Nagel). The obtained *GRXC5* knock-out construct was further cloned into the pJet1.2 vector (Thermo Scientific) using a 1:1 ratio of insert and the with *Eco*RV

linearized vector and the concomitant ligation with a T4 DNA ligase (Thermo Scientific). The GRXC5ko_pjet was verified by sequencing and used for plasmid amplification via transformation into *E. coli*. To proceed with the transformation of GRXC5ko into *P. patens* protoplasts (see 2.6.2.4) the construct was digested with *Eco*RV and analyzed over an agarose gel. Furthermore, the digest was precipitated by adding 0.1 volumes of 3 M sodium acetate pH 5.2. After mixing, 2.5 volumes of 95% (v/v) EtOH were added and the mixture was incubated for 2 h at -20°C. The sample was centrifuged at 20,000 *g* for 30 min and the supernatant was discarded. The precipitated DNA was washed with 1 mL of 70% (v/v) EtOH and centrifuged for 10 min at 20,000 *g.* To obtain a sterile DNA sample, the supernatant was taken up under the sterile bench and the pellet was dried for 10 min before resuspension in 103 µL of sterile H_2O.

Table 14: Primer sequences for generating *P. patens* knock-out

Primer	Sequence	construct
Triple template PCR		
PpGrxC5ko_5PHR P1	ATCACAGGAAGCTATGGAAGGCA	Δ*grxc5, npt*
PpGrxC5ko_5PHR P2	TTGACAGGATCCGATAATCCCCACTTAGCACCAGG	Δ*grxc5, npt*
PpGrxC5ko_3PHR P3	ATCGGGCCTCCTGTCATGCCATCACATACGGAACT	Δ*grxc5, npt*
PpGrxC5ko_3PHR P4	ATCTTCAGCTCCTCAGTTCCTCG	Δ*grxc5, npt*
GrxC5ko_npt_F	TGCTAAGTGGGGATTATCGGATCCTGTCAAACACTG	Npt resistance
GrxC5ko_npt_R	CGTATGTGATGGCATGACAGGAGGCCCGATCTAGTA	Npt resistance
RT-PCR		
PpGrxC5ko__RT_F	TTAATCGGCAGGTGTGTGGA	cDNA Δ*grxc5*
PpGrxC5ko__RT_R	AAAAGCTTCTTCACGCGCAT	cDNA Δ*grxc5*
PpEF1a_RT_F	CGACGCCCCTGGACATC	cDNA control
PpEF1a_RT_R	CCTGCGAGGTTCCCGTAA	cDNA control
PpGR1ko_scr_F	GCCCGGGGATTTTGGTAGTA	5'HR GR1
PpGR1ko_scr_R	CAGTTGGGCCGCAATGAAAT	3'HR GR1

2.6.2.4 *Physcomitrium patens* transient and stable transformation

Physcomitrium patens was transformed using homologous recombination. New overexpression constructs like TKTP-roGFP2 were transformed into the PTA2 gene locus under

the expression of the *PpActin5* promoter (Müller *et al.* 2016). For generating knock-out constructs see section 2.2.4.1.

Moss was transformed via PEG4000 mediated DNA transfer in protoplasts isolated from protonema cultures. Protonema cultures were mixed and transferred 1 week before protoplastation to KNOP-ME medium at pH 4.5 and freshly transferred to new media two days before moss transformation. Moss protoplasts were isolated using driselase in a 1% (w/v) concentration for 2 h in the dark. The solution of cell debris and protoplast was filtered through a 100 µm sieve using a wide pipette and washed with 3 mL of 0.5 M medium (102.02 g mannitol/L ~ 560 mOSmol pH 5.6-5.8). The solution was filtered through a 50 µm sieve. After centrifugation (10 min, 45 *g*) the pelleted protoplasts were resuspended to a concentration of $1.2*10^6$ protoplasts/mL in 3 M medium (15 mM $MgCl_2$ x $6H_2O$, 5 mM MES, 96.07 g mannitol/L pH 5.6 ~580 mOsmol). 300,000 protoplasts were transformed with 10-30 µg DNA in 0.1 M $Ca(NO_3)_2$ by the addition of 40% (w/v) PEG4000 in 3 M medium. Knock-in constructs, not containing a selective marker, were co-transformed with a second plasmid containing an antibiotic resistance (pBsNNNev,pJEThpt). Samples were carefully diluted in 3 M medium by step-by-step addition of 1, 2, 3 and 4 mL of 3 M medium until a volume of 10.7 mL was reached. Diluted samples were centrifugated, the supernatant was carefully discarded and the protoplasts were resuspended in 3 mL of regeneration medium (50 g glucose/L, 44.1 g mannitol/L in KNOP-ME pH5.8 ~540 mOsmol). Transformed protoplasts were incubated in the dark for 2 days, if transiently transformed or transferred to standard growing conditions after 1 day. Selection of successful stable transformants was done via screening on KNOP-ME plates containing the respective antibiotic.

2.6.2.5 Hydrogen peroxide treatment of gametophore or protonema culture

3 days after subculturing of protonema culture of WT, Δ*grxc5* #54, Δ*gr1* #4, 30 mL of each culture was transferred into a fresh 50 mL falcon. 10 mL of each culture were harvested directly using a vacuum pump. The first samples were labeled as T_0 and directly frozen in liquid nitrogen and transferred to -80°C until further processing. The remaining 20 mL of each protonema culture were treated by the addition of 1 mL of 200 mM H_2O_2 resulting in a final concentration of 10 mM H_2O_2. The cultures were incubated for 30 min, shaking, under normal growth conditions. After that, 10 mL of the treated culture were harvested (labeled T_1) via the vacuum pump, flash frozen and stored at -80°C. The supernatant of the remaining 10 mL of

the cultures were taken up with a 1 mL pipette tip and discarded. The moss was resuspended in fresh KNOP-ME pH 5.8 media and incubated for 30 min shaking in standard growth conditions. Afterwards samples were harvested (T_{30}) and frozen in liquid nitrogen. From these samples, proteins were extracted using the methanol-chloroform precipitation (see 2.3.2).

Three colonies of WT, Δ*grxc5* #54, Δ*grxc5* #249 and Δ*gr1* #4 were grown on one agar plate for 4-6 weeks until gametophores had a size of min. Ø 1 cm. 1/3 of the gametophores of each genotype were gently transferred into separate 15 mL falcon tubes containing KNOP-ME medium and 2/3 of the gametophores were transferred into the respective falcons with KNOP-ME medium supplemented with 10 mM H_2O_2. After 30 min of incubation in the light (growth chambers), half of the gametophores submerged in the H_2O_2 solution were dried on a paper towel and flash frozen in liquid nitrogen, marked as samples T_1. The other half of the H_2O_2 treated gametophores were transferred into a new 15 mL falcon tube filled with KNOP-ME medium and incubated for 30 min in the growth chambers. After 30 min the remaining gametophores of the previously H_2O_2 treated samples were harvested and labeled as T_{30}. Simultaneously, the control gametophores only treated with KNOP-ME solution were harvested as well as described above and labeled as T_0. From theses samples, proteins were extracted using the methanol-chloroform precipitation (see 2.3.2).

2.6.2.6 Pulse-amplitude modulation (PAM) and gas exchange fluorescence (GFS) measurements on moss gametophores and protonema tissue

PAM and GFS measurements were performed in the lab of Ekkehard Neuhaus with the help of Frank Reinhardt at the University of Kaiserslautern, Germany. For PAM measurements 6-week-old gametophores of *P. patens* grown on agar plates were dark adapted for 15 min prior to measurements. Optimal time points for measurements of *P. patens* were determined prior to the experiments and revealed a 5 h window after turning on the light. A photosynthetically active radiation (PAR) value of 205 was set for the light curve measurements. Additionally, for oxidative challenge, moss gametophores were flooded with 10 mM H_2O_2 for 15 min afterwards the excess liquid was taken up. The moss was given 30 min (including 15 min dark adaption) to recover before light curve measurements. GFS measurements were performed with the GFS-300 (Walz). For each measurement, 3-4 mL of WT, Δ*grxc5* #54, Δ*grxc5* #249 and Δ*gr1* #4 protonema culture with a similar density (optically determined) were dropped on top of a Whatman filter paper in the size of a mini petri dish (Ø 4 mm). Excess liquid was taken off

by a 1000 µL pipette tip. CO_2 uptake was measured for 7.5 min in the dark and subsequently 7.5 min in the light (125 µE/m^2 s). As blank (zero point) with KNOP-ME medium wetted Whatman paper was used before every fourth measurement. Humidity was set to 98% at 22°C. After measurement a photo of each plate was taken, to normalize the measurements over the amount of green material per area. This was done in software ImageJ (Schneider *et al.* 2012), transforming the image into an 8 bit image and calculating the pixel percentage of green moss covered area.

Additional PAM measurements were performed by Stephanie Bethmann in the laboratory of Prof. Peter Jahns (University of Düsseldorf). For these measurements, moss colonies of WT, Δ*grxc5* #54, Δ*grxc5* #249 and Δ*gr1* #4, were grown on one agar plate in 60 µE (16 h/ 8 h) for 4 weeks. Plates were either 45 min dark incubated and measured within an IMAGING-PAM (Maxi, Heinz Walz GmbH, Germany) or treated for 1 h and 4 h with high light (450 µE) and subsequently dark incubated for 45 min before measurement.

2.7. Confocal laser scanning microscopy

Leaf disks or seedlings were imaged using a Zeiss LSM 780 confocal laser scanning microscope (CLSM) connected to an Axio Observer Z1 (Carl Zeiss Microscopy, Jena, Germany) with a 20x and 40x lens (C-Apochromat 20x/ 40x/1.2 W Korr). The respective settings are shown in Table 15.

Table 15: CLSM laser and filter settings

Organism	Construct	Excitation (nm)	Relative Laser output	Emission (nm)	info
H. vulgare	hGrx1-roGFP2	405	3%	508-535	roGFP2
		488	1.5%	508-535	roGFP2
		405	3%	430-470	autofluorescence
H. vulgare	WT	405	1.5%	449-613	MCB
		543	24	614-704	PI
P. patens	TKTP-roGFP2	405	4%	430-470	autofluorescence
				508-535	roGFP2
		488	2%	508-535	roGFP2
				680-735	chlorophyll
P. patens	CROST2	405	2%	464-490	CFP
A. thaliana				517-544	YFP
		488	2%	517-544	YFP (control)
				624-673	Chlorophyll
A. thaliana	p35s-GAPDH-YFP	488	2%	511-541	YFP fluorescence
A. thaliana	pgapc-GAPDH-YFP	488	2%	511-541	YFP fluorescence

2.7.1 Ratiometric image analysis

Microscopic images (.lsm format) were analyzed with the ratiometric analysis software (RRA). roGFP2 405/488 nm ratios were determined with the MATLAB-based software (MathWorks, Natick, MA, USA) including background subtraction and noise correction (Fricker 2016).

2.7.1.1 Stromal redox sensing time laps at dark light transitions

Liquid (gametophore and protonema mix) cultures of *P. patens* WT #20, Δ*grxc5* #17 and Δ*grxc5* #21 were incubated for at least 45 min in the dark with the avoidance of light and laser-scanning stress (no prescreening). Steady state of roGFP2 fluorescence was imaged for 1 min in the dark. After that an external light source was illuminating the sample with ~ 100 µE/m^2 s from a 90° angle for 5 min while imaging, as seen in Müller-Schüssele *et al.* 2020. roGFP2 was excited at 405 and 488 nm and emission was collected at 508-535 nm. Images were taken every 30 s for 20 min.

3. Plasticity in plastid redox networks: Evolution of glutathione-dependent redox cascades and glutathionylation sites

Chapter three of this thesis is published in BMC Plant Biology:

Müller-Schüssele, S. J., Bohle, F., Rossi, J., Trost, P., Meyer, A. J., & Zaffagnini, M. (2021). Plasticity in plastid redox networks: evolution of glutathione-dependent redox cascades and glutathionylation sites. BMC Plant Biology, 21(1), 1-20.

https://doi.org/10.1186/s12870-021-03087-2

Supplementary material is available at the BMC website including alignment files and phylogenetic tree analyses: https://doi.org/10.1186/s12870-021-03087-2#Sec26

3.1. Summary and personal contribution

The recent availability of full genome sequences for streptophyte algae such as *Chara braunii* (Nishiyama *et al.* 2018), hornworts such as *Anthoceros agrestis* (Li *et al.* 2020) and also ferns including *Salvinia cucullata* or *Azolla filiculoides* (Li *et al.* 2018) complement the repertoire of genome data for existing model species such as *Physcomitrium patens* (Rensing *et al.* 2008), *Marchantia polymorpha* (Bowman *et al.* 2017), *Selaginella moellendorfii* (Banks *et al.* 2011), *Brachypodium distachyon* (The International Brachypodium Initiative 2010) and *Arabidopsis thaliana* (The Arabidopsis Genome Initiative 2000). Together, this enabled molecular studies investigating protein evolution spanning streptophyte algae to flowering plants.

In this study, we focused on the phylogenetic analysis of proteins belonging to the glutathione redox network. We selected a set of protein candidates involved in ROS scavenging and damage repair which draw electrons from GSH and release GSSG. Additionally, due to the focus of the study on the plastid redox network, the selected candidates had to show a plastid localization, which led us to choose proteins like dehydroascorbate reductase (DHAR), glutathione *S*-transferases (GSTL, GSTI), atypical methionine sulfoxide reductase B1 (MSRB1), peroxiredoxin IIE (PRXIIE), glutaredoxins (GRXC5, GRXS12, GRXS14, GRXS16) and plastidial/mitochondrial glutathione reductase (GR). While the enzymes involved in ROS scavenging and damage repair were evolutionary less conserved, clades of plastidial isoforms

of GR (dual targeted) and GRX were evolutionary conserved within the tested species, underlining a potentially important function of these enzymes in early land plants, as well as the algal sister clade. Phylogenetic analysis of GRX class I further supported the isoform GRXC5 as the more ancestral variant (Rouhier 2010; Couturier *et al.* 2011). Relevant for this thesis is the identification of GRXC5 in *Physcomitrium patens* as the only member of class I found within the plastids, making it a highly interesting candidate to study the function of class I GRXs via knock-out experiments.

Furthermore, the study focused on reversible post-translational thiol modification by glutathione, termed *S*-glutathionylation. Class I GRX are oxidoreductases, able to (de)glutathionylate proteins (Rouhier 2010; Couturier *et al.* 2011; Couturier, Jacquot, *et al.* 2013). *S*-glutathionylated proteins have been identified via proteomic studies for example in cyanobacteria (*Synechocystis spec.*; Chardonnet *et al.* 2015) and green algae (such as *Chlamydomonas reinhardtii,* Michelet *et al.* 2008; Zaffagnini, Bedhomme, Groni, *et al.* 2012). This study provides an overview of 151 plastidial *S*-glutathionylation target sites which were identified by literature screening, but only in 26 proteins exact cysteine positions have been determined. We compared the proteins with the known glutathionylated cysteine position on the basis of multiple sequence alignment in species from cyanobacteria to angiosperms and found that 38% of those cysteine sites were completely conserved with 22% accounting for non-catalytic cysteine sites. We further focused on non-catalytic, non-conserved cysteines of e.g alpha-amylase (AMY3), thiamine thiazole synthase (THI1), apoferredoxin (FDX) and 3'phosphoadenosine 5' phosphate phosphatase (SAL1). Here, we observed evolutionary gains and losses of putative protein *S*-glutathionylation sites e.g in phosphoribulokinase (PRK), FDX and SAL1. This study provides a first insight into the conservation and occurrence of glutathionylation sites in an evolutionary context and underlines the important role of protein *S*-glutathionylation in redox regulation and oxidative stress responses. In this work, one or two representatives of lineages covering streptophyte algae, bryophytes, lycophytes, monilophytes and angiosperms were analyzed to provide a first overview of the evolution of plastidial redox networks for the selected model species.

I generated Maximum-Likelihood based trees using iQtree web (Trifinopoulos *et al.* 2016) as additional method to the Bayesian inference via MrBayes (Ronquist & Huelsenbeck 2003) generated by Stefanie Müller-Schüssele. For the proteins dehydroascorbate reductase (DHAR), glutathione-*S*-transferases Iota and lambda (GST-I/L), methionine sulfoxide reductase

B1 (MSRB1), peroxiredoxin II E (PRXIIE), glutaredoxin (GRX) class I, GRXS14/16 and glutathione reductase (GR) (Additional File 13). I also visualized the data of *S*-glutathionylation sites based on table S2 (Fig.3), by creating pie chart diagrams displaying the percentages of plastidial glutathionylation targets depicting known and unknown glutathionylation site and conservation status of the cysteine. I additionally contributed to the collection of data for table 1 to generate the overview of the 26 known glutathionylated plastidial proteins. Moreover, I collected protein sequence data for our selected model species using Phytozome v12.1 (Goodstein *et al.* 2012), Fernbase (http://www.fernbase.org), TAIR10 (www.arabidopsis.org) and Uniprot (https://www.uniprot.org) to align sequences according to the known glutathionylated cysteine manually (Additional File 10, 11) with the Jalview alignment software (www.jalview.org). Based on these data I created the graphical display of five example proteins and their non-catalytic, non-conserved cysteines (Fig 4). Finally, I contributed in writing of the first manuscript draft and was involved in the revision process.

3.2. Manuscript

Müller-Schüssele et al. BMC Plant Biology (2021) 21:322
https://doi.org/10.1186/s12870-021-03087-2

BMC Plant Biology

RESEARCH ARTICLE Open Access

Plasticity in plastid redox networks: evolution of glutathione-dependent redox cascades and glutathionylation sites

Stefanie J. Müller-Schüssele[1,2*], Finja Bohle[1], Jacopo Rossi[3], Paolo Trost[3], Andreas J. Meyer[1] and Mirko Zaffagnini[3]

Abstract

Background: Flexibility of plant metabolism is supported by redox regulation of enzymes via posttranslational modification of cysteine residues, especially in plastids. Here, the redox states of cysteine residues are partly coupled to the thioredoxin system and partly to the glutathione pool for reduction. Moreover, several plastid enzymes involved in reactive oxygen species (ROS) scavenging and damage repair draw electrons from glutathione. In addition, cysteine residues can be post-translationally modified by forming a mixed disulfide with glutathione (*S*-glutathionylation), which protects thiol groups from further oxidation and can influence protein activity. However, the evolution of the plastid glutathione-dependent redox network in land plants and the conservation of cysteine residues undergoing *S*-glutathionylation is largely unclear.

Results: We analysed the genomes of nine representative model species from streptophyte algae to angiosperms and found that the antioxidant enzymes and redox proteins belonging to the plastid glutathione-dependent redox network are largely conserved, except for lambda- and the closely related iota-glutathione *S*-transferases. Focussing on glutathione-dependent redox modifications, we screened the literature for target thiols of *S*-glutathionylation, and found that 151 plastid proteins have been identified as glutathionylation targets, while the exact cysteine residue is only known for 17% (26 proteins), with one or multiple sites per protein, resulting in 37 known *S*-glutathionylation sites for plastids. However, 38% (14) of the known sites were completely conserved in model species from green algae to flowering plants, with 22% (8) on non-catalytic cysteines. Variable conservation of the remaining sites indicates independent gains and losses of cysteines at the same position during land plant evolution.

Conclusions: We conclude that the glutathione-dependent redox network in plastids is highly conserved in streptophytes with some variability in scavenging and damage repair enzymes. Our analysis of cysteine conservation suggests that *S*-glutathionylation in plastids plays an important and yet under-investigated role in redox regulation and stress response.

Keywords: Protein *S*-glutathionylation, Redox regulation, Land plant evolution, Plastid, Cysteine, Glutathione, Glutaredoxin

* Correspondence: stefanie.mueller@uni-bonn.de
[1]Institute of Crop Science and Resource Conservation (INRES), University of Bonn, Friedrich-Ebert-Allee 144, 53113 Bonn, Germany
[2]Present Address: Department of Biology, Technische Universität Kaiserslautern, 67663 Kaiserslautern, Germany
Full list of author information is available at the end of the article

© The Author(s). 2021 **Open Access** This article is licensed under a Creative Commons Attribution 4.0 International License, which permits use, sharing, adaptation, distribution and reproduction in any medium or format, as long as you give appropriate credit to the original author(s) and the source, provide a link to the Creative Commons licence, and indicate if changes were made. The images or other third party material in this article are included in the article's Creative Commons licence, unless indicated otherwise in a credit line to the material. If material is not included in the article's Creative Commons licence and your intended use is not permitted by statutory regulation or exceeds the permitted use, you will need to obtain permission directly from the copyright holder. To view a copy of this licence, visit http://creativecommons.org/licenses/by/4.0/. The Creative Commons Public Domain Dedication waiver (http://creativecommons.org/publicdomain/zero/1.0/) applies to the data made available in this article, unless otherwise stated in a credit line to the data.

Background

Importance of redox regulation in photosynthetic eukaryotes

Plant evolution has its roots in two major endosymbiotic events, the first leading to the formation of the first eukaryotic cell and the second generating photosynthetic eukaryotes [1]. In the green lineage (Chloroplastida), land plants evolved from streptophyte algae [2]. In chloroplasts, the photosynthetic electron transport (PET) chain allows the generation of reducing equivalents (e.g. NADPH) and ATP that fuel sugar biosynthesis by the Calvin-Benson cycle (CBC). In order to balance the photosynthetic process, a tight regulation of electron flux is required to harmonise light capture with metabolic activities, as well as to prevent extensive energy or electron transfer to oxygen, generating reactive oxygen species (ROS) that can damage DNA, lipids or proteins [3, 4]. Nascent ROS and damaged molecules are addressed by high capacity scavenging and repair systems that draw electrons from either NADPH or PET coupled to stromal redox proteins [5–8].

In order to balance energy demand for metabolic processes, plant cells have a highly flexible metabolism that quickly switches between photosynthetic and non-photosynthetic modes. Moreover, cell compartments can contain metabolic enzymes with conditional or opposing activities, and regulation in time and space may avoid futile cycling of metabolites [9]. These complex regulatory processes are partly mediated by changes in the redox status of cysteine thiol groups in proteins enabling reversible modulation of protein function and structure that is influenced by the intracellular redox state.

Electron flux in redox cascades

Cysteine thiols influence protein structure and activity as their redox state may have an impact on protein folding and oligomerization, reactivity towards ROS or on substrate binding to active sites of redox-active enzymes [6, 9]. In this regard, dithiol/disulfide exchange reactions play a pivotal role in protein regulation. This redox modification allows the reversible transfer of two electrons, depending on the interaction of redox-sensitive proteins and according to the midpoint potential of involved thiol-switches. Many enzymes involved in scavenging of ROS and lipid peroxides or protein repair contain active site or regulatory cysteines that are coupled to redox cascades. However, the reactivity of the thiol group (especially the thiolate anion, $-S^-$) can also favour reactions with oxidant molecules such as hydrogen peroxide (H_2O_2) or the free radical nitric oxide (•NO) and NO-derived compounds (also referred to as reactive nitrogen species, RNS). This results in the oxidation of the thiol moiety by reversible (*S*-sulfenylation, *S*-sulfhydration, *S*-nitrosylation or *S*-glutathionylation) or even irreversible modifications (*S*-sulfonylation), that can modulate or block protein function [3].

The redox network in plants comprises several specific reductases that transfer electrons to either the cysteine-containing tripeptide glutathione (GSH) or thioredoxins (TRX). In plastids, glutathione reductase (GR) safeguards a highly reduced glutathione pool relying on NADPH as electron source, whereas ferredoxin TRX reductase (FTR) draws electrons from photosynthetic light reactions to reduce TRX. Plastids also contain a special type of TRX, namely NTRC that can be reduced by NADPH through an NTR domain fused to the TRX module [10, 11]. Thiol switches downstream of TRXs are relatively well characterised with direct evidence for 36 TRX-regulated proteins in plastids [5] whereas proteomics studies suggested a number of approximately 100 putative TRX-regulated proteins in plastids [12, 13]. In chloroplasts, redox control via TRX-dependent dithiol/disulfide exchanges allows enzyme activation under light conditions via the reduction of regulatory protein disulfides on target proteins such as CBC enzymes [6, 14]. TRXs can also transfer electrons to peroxide scavenging enzymes such as 2-Cys peroxiredoxins (PRX) [15] and glutathione peroxidase-like proteins (GPXLs) [16]. Thus, plastidial 2-Cys PRX can serve as a link between H_2O_2 scavenging and the oxidation of thiol switches on several target proteins such as *m*- and *f*-type TRXs [17–19] and glucose-6-phosphate dehydrogenase [20]. This redox interaction supports deactivation of CBC enzymes and activation of the first step of the oxidative pentose phosphate pathway, respectively, facilitating the tight regulation of plastid carbon metabolism in light to dark transitions to avoid futile cycling.

The glutathione pool in cell compartments containing a GR is highly reduced (≥50,000:1 GSH:GSSG), leaving only nM concentrations of glutathione disulfide (GSSG). This results in a highly negative glutathione redox potential (E_{GSH}) ranging from − 310 to − 360 mV [21–23]. Glutathione acts as reductant during the detoxification of potentially toxic organic electrophiles, as well as during ascorbate regeneration via the ascorbate-glutathione-cycle [24]. In addition, some enzymes involved in ROS scavenging and damage repair, such as single cysteine (atypical) methionine sulfoxide reductase B (AtMSRB1), are fully dependent on GSH for reduction [25], whereas others, such as type II peroxiredoxin E (PRXIIE), can be regenerated via GSH/glutaredoxins (GRXs) with a higher efficiency than via TRX [15, 26]. The role of GSH in MSRB1 and PRXIIE activities relies on its nucleophilic attack on sulfenylated active site cysteines formed during the catalytic cycle. This spontaneous reaction leads to the formation of a mixed disulfide (i.e. *S*-glutathionylation) that is specifically controlled by GRXs, enzymes belonging to the TRX superfamily [27]. GRXs catalyse the

removal of the glutathione moiety (i.e. deglutathionylation) allowing the regeneration to reduced and active enzymes in a mechanism involving GSH as electron donor. Thus, there is an interrelation with yet unknown biological significance between the local ROS levels, the local detoxification systems, the glutathione redox potential and protein *S*-glutathionylation.

Cross-talk between TRX and the GSH/GRX system has been evidenced in *Arabidopsis thaliana* mutants lacking the cytosolic GR1 or GR2 in mitochondria, where the TRX system can serve as a back-up system for local control of GSSG accumulation in the respective compartment [28, 29]. Vice versa, TRX redox state can be linked to the GSH/GRX system, as cytosolic TRX redox status can be rescued via the glutathione system [30], and as some TRXs such as *f*-type TRXs are *S*-glutathionylation targets [31]. However, studies in *A. thaliana* and *Physcomitrium* (formerly *Physcomitrella* [32]) *patens* have evidenced that the TRX system cannot compensate for a disturbed GSH/GRX system in plastids [29, 33], raising the question of redox cascade organisation and cross-talk in the stroma.

Evolution shapes redox regulation

In photosynthesis, light-dependent regulation of several enzymes of the CBC has evolved to coordinate active light reactions with carbon fixation in the metabolic phase. Some redox-responsive thiol-switches relying on dithiol/disulfide interchanges were already established in the cyanobacterial cell that became the endosymbiont, whereas others emerged during algal evolution [9, 34, 35]. The set of redox-regulated proteins acquired via endosymbiosis was expanded by gain of cysteines via amino acid changes or the insertion of entire cysteine-containing flexible regulatory loops [9, 34]. During plant evolution, streptophyte algae were able to colonise freshwater habitats and surrounding land, as they exhibited a set of advantageous morphological features such as apical cell growth, biplastidy and branching [2]. Early land plants possessed simple body plans but were facing a habitat with rapidly fluctuating environmental conditions such as flooding, dehydration, rapid temperature changes and high light exposure [36]. This lifestyle is mirrored in extant non-vascular land plant lineages such as mosses that are tolerant to extended submergence and contain several protection mechanisms against light stress [37, 38]. Light and temperature fluctuations as well as photoinhibitory conditions are especially challenging for metabolic regulation and ROS scavenging in chloroplasts due to large changes in electron transport rate, as well as the necessary fast adaptations in enzymatic activities to sustain growth and promote survival.

However, the evolutionary adaptations that occurred in redox cascades during land plant evolution are largely unknown. To date, genomes of streptophyte algae (*Chara braunii*), hornworts (*Anthoceros agrestis* and *Anthoceros punctatus*) and ferns (*Salvinia cucullata, Azolla filiculoides*) have become available [39–42], complementing the existing genomic information from liverworts (*Marchantia polymorpha*), mosses (*P. patens*) and lycophytes (*Selaginella moellendorffii*) model species. This unprecedented coverage of land plant lineages and their algal sister group enables the comparative investigation of redox cascade evolution in the green lineage on several levels, namely regarding the distinct reductases, redox transmitters, as well as target thiol-switches on metabolic enzymes. Based on the importance of glutathione as redox buffer and source of reducing equivalents for antioxidant enzymes, this study investigates the components of glutathione-related redox networks in plastids of streptophyte model species.

Notably, during plant evolution, several redox-relevant protein families, such as the TRX superfamily comprising both TRXs and GRXs [9, 35], have largely expanded supporting functional diversification. Moreover, in seed plants, ROS/RNS are tightly linked to biotic defence responses, e.g. via the NADPH oxidase-mediated ROS bursts at the plasma membrane or via the salicylic acid signalling pathway involving NPR1 [43]. In contrast, the organisation and significance of redox networks for metabolic regulation, ROS scavenging and development in non-seed plants are only starting to emerge [33, 44]. However, understanding the evolution of redox networks may help to reveal ancestral mechanisms in stress resilience. Studies in model organisms allowing reverse genetics show that phenotypes of mutants with defects in plastid glutathione homeostasis are diverse, suggesting modification of redox networks during plant evolution. Thus, the absence of plastid GR is embryo-lethal in *A. thaliana*, whereas *P. patens* can partially compensate this loss but becomes light-sensitive [29, 33].

In order to assess the evolution of both, the effectors and putative target cysteines of glutathione-related redox networks in plastids, we additionally investigate protein *S*-glutathionylation by creating an updated list of known target cysteines of *S*-glutathionylation and their evolutionary conservation.

Results

Phylogenetic analysis of glutathione-dependent redox-relevant plastid proteins from streptophyte algae to land plants

On the one hand, many protein families of redox cascade components have expanded during land plant evolution and underwent functional diversification [9]. On the other hand, several proteins are persistently conserved as only one isoform in a compartment, suggesting a potential essential biological function and tight

regulation of gene copy number. In order to identify plastidial glutathione-related redox components with interesting phylogenetic patterns, we first did an explorative phylogenetic analysis taking advantage of the available sequence coverage of streptophyte algae and non-seed plant lineages. We included all known scavenging and damage repair enzyme families with members that were reported to (1) localise to plastids and (2) use GSH and produce GSSG: dehydroascorbate reductase (DHAR), glutathione *S*-transferases lambda and iota (GSTL, GSTI), atypical methionine sulfoxide reductase B1 (MSRB1), peroxiredoxin IIE (PRXIIE), glutaredoxins (GRXs), as well as glutathione reductase (GR), which is responsible for reduction of GSSG. All used protein sequences and gene accessions are listed in Table S1 (Additional file 1).

Dehydroascorbate reductases

DHARs belong to the GST superfamily and catalyse the reduction of dehydroascorbate to ascorbate using GSH as electron donor. By maintaining a reduced ascorbate pool, DHARs indirectly assist in the detoxification of H_2O_2 catalysed by ascorbate peroxidases (APXs). The phylogenetic tree of plant DHARs (Additional file 2) shows several independent gene duplications resulting in a number of one to three paralogs per species. Targeting predictions (TargetP [45, 46], LOCALIZER [47] and PredAlgo [48], Additional file 1 Table S1) as well as the presence or absence of N-terminal sequence extensions suggest a high variability in subcellular targeting. Notably, only a single DHAR gene is present in *C. braunii* and two bryophyte species (*M. polymorpha*, *A. agrestis*) (Fig. 1, Additional file 2). Whereas the *C. braunii* ortholog is putatively cytosolic, both *M. polymorpha* and *A. agrestis* orthologs possess an N-terminal extension and are predicted to be targeted to plastids. This indicates that a stromal DHAR occurred early in land plant evolution. DHAR1 from *P. patens* (Pp3c22_5470V3) [49] is predicted to be targeted to plastids but proteomic evidence also indicates its presence in mitochondria [49], which may suggest dual-targeting to plastids and mitochondria. All land plant model species except *S. moellendorffii* have at least one DHAR isoform with N-terminal extension and/or a plastid targeting prediction (Fig. 2 and Additional file 2). In *S. moellendorffii*, the situation remains unclear, as at least one gene model is incomplete at the N-terminus.

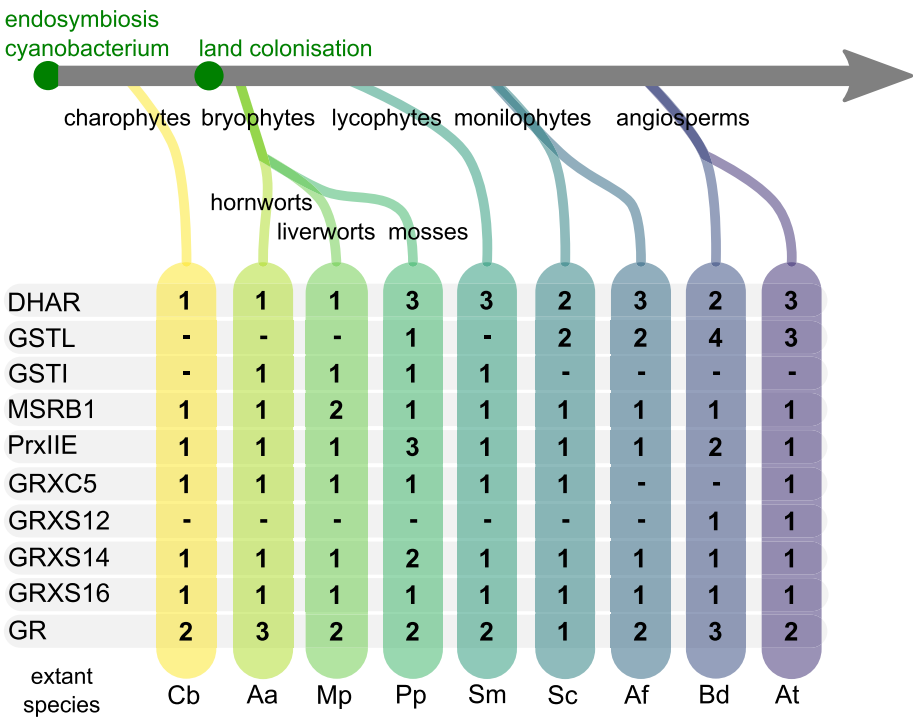

Fig. 1 Evolution of protein families related to plastid GSH-dependent redox balance. Numbers indicate the number of isoforms present in the genome. DHAR, dehydroascorbate reductase; GST, glutathione *S*-transferase, L: Lambda, I: Iota; MSRB1, methionine sulfoxide reductase B1 (1 Cys); PRX, peroxiredoxin; GRX, glutatredoxin; GR, glutathione reductase. Model species names are abbreviated: Cb = *Chara braunii*; Aa = *Anthoceros agrestis*; Mp = *Marchantia polymorpha*; Pp = *Physcomitrium patens*; Sm = *Selaginella moellendorffii*; Sc = *Salvinia cucullata*; Af = *Azolla filiculoides*; Bd = *Brachypodium distachyon*; At = *Arabidopsis thaliana*

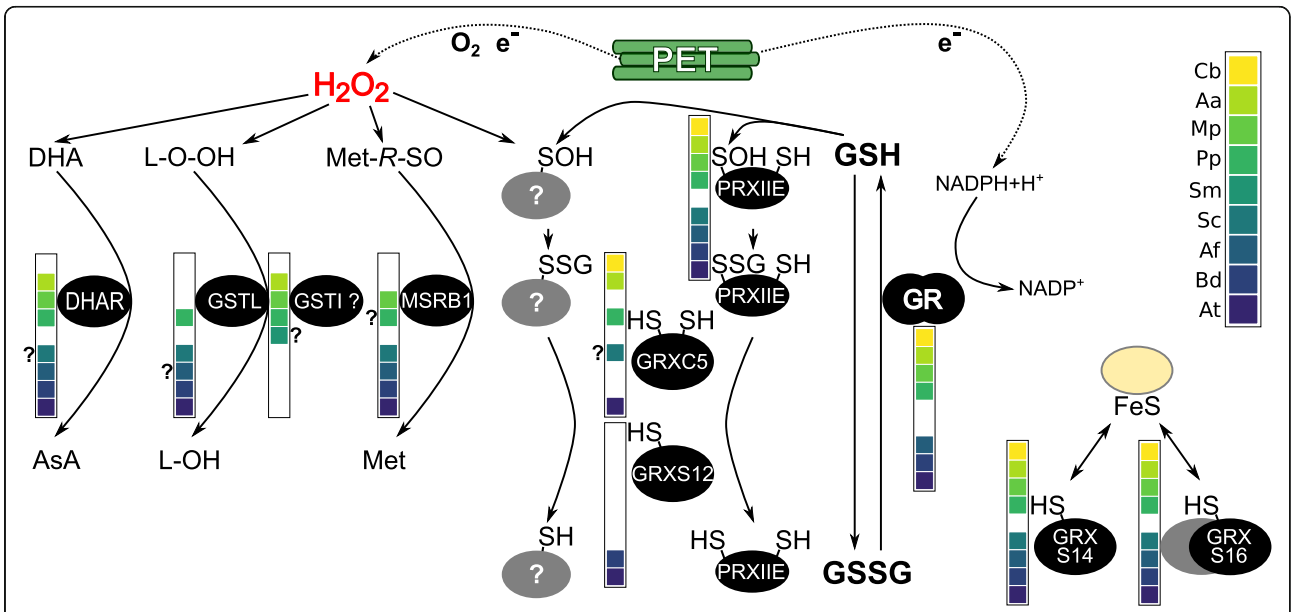

Fig. 2 Overview of evolution of plastid glutathione-related redox networks in land plants and streptophyte algae. Schematic overview of the plastid GSH-dependent redox network in land plant model species and the streptophyte alga *C. braunii*. Electrons from photosynthetic electron transport (PET) contribute to ROS generation and at the same time to ROS scavenging, damage repair and redox homeostasis. H_2O_2 leads to lipid peroxidation (L-O-O-H) as well as oxidation of protein methionine (Met-*R*-SO), of ascorbic acid (AsA) to dehydroascorbate (DHA) or protein thiol oxidation to the respective sulfenic acid (RS-OH) that can react with GSH to form an *S*-glutathionylated adduct (RS-SG). Glutaredoxins (GRX) can (de) glutathionylate proteins. The balance between the reduced tripeptide glutathione (GSH) and glutathione disulfide (GSSG) is influenced by GSSG generation via enzymes involved in ROS/RNS scavenging or protein as well as lipid repair, such as dehydroascorbate reductase (DHAR), atypical (1 Cys) methionine sulfoxide reductases B1 (MSRB1), lambda and iota-type (?, function not confirmed in vitro) glutathione *S*-transferases and type II peroxiredoxins (PRX). Glutathione reductase (GR, NADPH-dependent) safeguards a highly reduced GSH-pool. The presence of at least one plastid-targeted isoform of a protein in a model species (assessed by presence of an N-terminal extension and targeting predictions, see Additional files 1, 2, 3, 4, 5, 6, 7, 8) is represented by a coloured box in the species legend next to the protein. A coloured box with question mark means the potential presence of an isoform as targeting prediction is unclear, but N-terminal extension indicating a targeting peptide is present (see Additional files 1, 2, 3, 4, 5, 6, 7, 8). Absence of a box can either mean absence of homologs from that species (see Fig. 1), or that all homologs do not have N-terminal extensions or that gene models are fragmentary (see Additional files 1, 2, 3, 4, 5, 6, 7, 8). Species legend: *Chara braunii* (Cb), *Anthoceros agrestis* (Aa), *Marchantia polymorpha* (Mp), *Physcomitrium patens* (Pp), *Selaginella moellendorffii* (Sm), *Salvinia cucullata* (Sc), *Azolla filiculoides* (Af), *Brachypodium distachyon* (Bd) and *Arabidopsis thaliana* (At)

Iota (I)- and lambda (L)-type glutathione S-transferases

In addition to DHARs, plastid-targeting has also been reported within the lambda-subclass of GSTs (GSTL) [50]. While canonical GSTs conjugate GSH with electrophilic compounds, the subclasses theta, phi and tau have also been shown to act as GSH-dependent peroxidases that release GSSG [50, 51]. Because a similar reductive activity towards DHA or hydroperoxides has also been reported for plastid-localised PpGSTL1, we investigated isoforms of this subclass [50]. We did not identify any GSTL homologs in *C. braunii*, *A. agrestis*, *M. polymorpha* and *S. moellendorffii* but several homologs with variable N-terminal extensions and predicted targeting to plastids are present in the seed plant models (Additional file 3). On the contrary, the closely related subfamily of iota-type GSTs (GSTI) contains homologs from *A. agrestis*, *M. polymorpha* and *S. moellendorffii*, but is absent in the fern and seed plant models (Fig. 1). The function of GSTIs is yet unclear [50] while our analysis indicates that they may also be targeted to plastids where they might fulfil similar functions to their sister clade GSTL (Additional file 3, Fig. 2). We did not identify a *C. braunii* GSTI, but a *C. reinhardtii* GSTI has been reported [50], suggesting that the GSTI subfamily is present in chlorophytes.

Atypical methionine sulfoxide reductase B

Methionine sulfoxide reductases (MSR) catalyse the reduction of methionine sulfoxide (MetSO), repairing ROS-induced damage to proteins (Fig. 2). Oxidation of methionine can generate two diastereomeres that are reduced by two different non-related enzyme families, namely MSRA (reducing methionine-*S*-sulfoxide) and MSRB (reducing methionine-*R*-sulfoxide) [52]. MSRA and MSRB proteins containing two cysteines are dependent on TRX for regeneration, while atypical MSRBs such as plastid-targeted AtMSRB1 (AT1G53670), depend on GSH/GRX for regeneration [53]. In AtMSRB1, the second cysteine is replaced by a threonine (Thr132). Investigating AtMSRB1 homologs

(Additional file 4a, c, d), we find a complete conservation of the isoform containing one cysteine as the well-supported MSRB1(1Cys) clade contains *C. braunii*, bryophyte, lycophyte and fern isoforms. The conservation of plastid targeting is unclear but likely variable, based on TargetP [45, 46], LOCALIZER (L) [47] and PredAlgo (P) [48] predictions (Additional file 1 Table S1) and the presence and absence of N-terminal extensions (Additional file 4b, Fig. 2). Notably, *M. polymorpha* does not possess a MSRB2 homolog while the MSRB1 gene was duplicated and the emerging two isoforms show differing N-terminal extensions and targeting predictions (Additional file 4).

Peroxiredoxin II E

PRXs are antioxidant enzymes that catalyze the reduction of hydroperoxides into alcohols using a strictly conserved cysteine (i.e. peroxidatic cysteine). Plastids contain canonical 2-Cys PRXs having two active site cysteines (peroxidatic and resolving cysteine), and an atypical 2-Cys PRX named PRXIIE (reviewed in [15]). Whereas the regeneration of canonical 2-Cys PRX is controlled by the plastidial TRX system via a dithiol/disulfide exchange, the recycling of oxidised poplar PRXIIE was demonstrated to be more efficiently catalysed by GRXS12 in vitro [26]. GRXS12 can restore the reduced PRXIIE as the peroxidatic cysteine undergoes glutathionylation during the catalytic cycle, highlighting the dependence of this PRXII subfamily on the GSH/GRX system for functional recycling (Fig. 2).

PRXIIE homologs are evolutionary conserved [54] and our analysis confirms a single highly supported clade of PRXIIE homologs from charophytes to flowering plants (Additional file 5). Most organisms investigated possess a single PRXIIE isoform and all complete protein models confirm an N-terminal extension that is largely predicted to confer targeting to plastids (Fig. 2, Additional file 1 Table S1, Additional file 5). The *S. moellendorffii* homolog did not allow a targeting analysis as the N-terminus of the protein model was fragmentary. We found gene duplications in *B. distachyon* with two isoforms and *P. patens* with three isoforms, all with conserved plastid targeting. Based on the phylogenetic analysis (Additional file 5), plastid GRX-dependent PRXIIE homologs are likely present in all analysed organisms.

Glutaredoxins

GRXs are oxidoreductases belonging to the TRX family, which is largely involved in the control of protein redox state. In photosynthetic eukaryotes, the GRX family comprises four classes that are localised in various subcellular compartments and distinguished by their active site signature and domain organization [3]. The nomenclature of the members of these GRX classes is based on the presence of a cysteine or a serine at the last position of the active site signature (CXXC/S) with a limited number of exceptions containing a residue differing from cysteine or serine [3]. In the model plant *A. thaliana*, GRXs are represented by six class I, four class II, and two class IV isoforms, while class III GRXs (also referred to as CC-type GRX or ROXY proteins) have largely expanded and comprise 21 members with multiple functions. One example of class III GRX function is the interaction with bZIP TGA transcription factors, influencing plant development and flowering [55, 56]. Plastids typically contain GRX members belonging to class I and II, namely class I GRXS12 and the close paralog GRXC5 (in *A. thaliana*) and class II GRXS14 and GRXS16 [57–59].

Class I GRX

GRXC5 and GRXS12 contain a single GRX domain with an active site signature (YCPYC and WCSYS, respectively) that differs slightly from the typical YC [P/S/G][Y/F] C motif of class I GRXs. Both GRX isoforms are redox-active being involved in the control of protein glutathionylation of plastidial proteins and in the recycling of antioxidant enzymes such as MSRB1 and PRXIIE (see above). The analysis of the phylogenetic tree for the redox-active class I GRXs revealed several evolutionary ancient clades corresponding to isoforms targeted to plastids (C5/S12 clade), the cytosol (C1/C2 clade), and the secretory pathway (C3/C4 clade) (Additional file 6). We found that only in the two angiosperm model species investigated, the second cysteine of the active site was replaced by a serine, giving rise to the GRXS12 isoform. This substitution can increase protein activity because formation of an internal disulfide that would block the active site can be avoided [58, 60]. The relevance of this mutation is emphasized by the fact that GRXS12 homologs became predominant in several angiosperms [61]. While the GRXC5 gene models from *S. moellendorffii* and *M. polymorpha* may be fragmentary and thus not contain the N-terminal targeting sequence, we did not identify any C5/S12 isoform clustering with the highly conserved GRXC5/S12 clade in the fern *A. filiculoides* (Additional file 6, Fig. 2).

Class II GRX

Class II GRXS14 and S16 contain a CGFS active site motif that is typically conserved in all other class II GRX members. As observed for plastidial class I GRXs, GRXS14 is formed by a single GRX domain whereas GRXS16 has a modular organization possessing an N-terminal domain (GIY–YIG endonuclease fold) fused to one GRX domain [3, 62, 63]. Class II GRXs are mainly thought to be involved in the coordination and transfer of iron-sulfur clusters [64, 65] (Fig. 2), but may also

become redox-active after loss of iron-sulfur coordination in response to an oxidative signal [66]. Our phylogenetic analysis showed that GRXS14 and GRXS16 homologs are conserved in all investigated model species, with only one duplicated isoform of GRXS14 in *P. patens* (Additional file 7). As far as complete gene models are available, N-terminal extensions and predicted plastid targeting confirm the very high conservation of a single plastid-targeted isoform in these class II GRX subfamilies (Additional file 1 Table S1, Additional file 7, Fig. 2).

Glutathione reductase

GRs perform the highly efficient NADPH-dependent recovery of GSH from enzymatically or non-enzymatically generated GSSG (Fig. 2), keeping GSSG as low as nanomolar amounts [21]. The resulting highly negative E_{GSH} in the plant cytosol, peroxisomes, plastids and mitochondria is based on the activity of two isoforms exhibiting dual targeting to either cytosol and peroxisomes (e.g. AtGR1, AT3G24170) or plastids and mitochondria (e.g. AtGR2, AT3G54660) [28, 29]. These two isoforms were already shown to be evolutionary conserved, including the dual-targeting of one isoform to plastids and mitochondria in *P. patens* [67]. We inferred a phylogeny using our set of model species and found the same conservation of two clades, representing the two GR isoforms, suggesting that these isoforms were established before the emergence of land plants (Additional file 8, Fig. 2). The *S. moellendorffii* gene model for the mitochondria/plastid GR clade was potentially fragmentary at the N-terminus, not allowing for a targeting prediction. We did not identify an isoform in the mitochondria/plastid GR clade for *S. cucullata* nor for *A. agrestis* (Bonn). A BLASTN search revealed a possible locus for *S. cucullata* on scaffold s0092, however without a gene model present. The presence of a plastidial/mitochondrial isoform in *A. agrestis* (Oxford) suggests that the respective gene is present but not correctly predicted for *A. agrestis* (Bonn). Except for *B. distachyon*, that possesses two plastidial/mitochondrial GR isoforms, each investigated species has a single isoform in each clade. Notably, one *A. agrestis* isoform (Sc2ySwM_228.5258.1) did show higher sequence similarity to bacterial than plant GRs. We identified similar isoforms in the other sequenced Anthoceros species and strains, namely *A. agrestis* (Oxford) and *A. punctatus* [40] (Additional file 8), suggesting a horizontal gene transfer (HGT) that occurred before the split of these species. Notably, these isoforms possess N-terminal extensions compared to bacterial sequences (Additional file 8b).

Evolutionary conservation of putative glutathionylation sites on plastid proteins

Many target thiol switches on cyanobacterial or plastidial proteins were acquired early in evolution, while others were reported to have evolved regulatory cysteines later. For example, the C-terminal extension in the plastidial glyceraldehyde-3-phosphate dehydrogenase isoform B (GAPB) evolved in streptophytes and the N-terminal cysteine pair of the plastidial NADPH-dependent malate dehydrogenase in land plants [9, 14, 68].

The vast majority of these enzymes are regulated by TRX through dithiol/disulfide interchanges that induce conformational changes either negatively or positively modulating protein activity [5, 6]. Besides TRX-dependent regulation, *S*-glutathionylation has recently emerged as an important regulatory mechanism in plants. It is involved in the recycling of antioxidant enzymes, but it can also protect protein cysteines from irreversible oxidation and modulate protein function/activity [3, 60, 69]. Many glutathionylation target proteins and the exact Cys that undergo *S*-glutathionylation remain unknown (Fig. 2). *S*-glutathionylation is not routinely detected in proteomics experiments in which cysteines are usually reduced, removing reversible modifications such as *S*-glutathionylation, and subsequently treated with Cys-blocking agents as a standard modification for MS/MS. However, several proteomic studies have developed specific protocols to detect *S*-glutathionylation and identified hundreds of putative target proteins highlighting the role of *S*-glutathionylation as thiol switching regulatory mechanism in eukaryotic oxygenic phototrophs [3] (and references therein). A BioGSSG-based (biotinylated glutathione disulfide) proteomic study was carried out in the cyanobacterium *Synechocystis* PCC 6803 and 383 proteins were identified as putative *S*-glutathionylated targets [70]. This study underpins the hypothesis that *S*-glutathionylation might have a regulatory role in all oxygenic phototrophs. Due to the importance of this post-translational redox modification, we decided to examine its relevance for plastidial proteins by analysing data from proteomic studies that used different methodologies, i.e. biotinylated GSH (biotinylated GSH ethyl ester (BioGEE)) [71], biotinylated GSSG (BioGSSG) [72, 73], anti-GSH antibodies [74] or radiolabelling of the glutathione pool using ^{35}S-cysteine [75]. In order to obtain an exhaustive and complete list of *S*-glutathionylated proteins, we also considered research studies carried out on purified proteins in vitro [71, 76–93] (see Additional file 9 Table S2). Combining all these studies, we compiled a list of 364 proteins known to undergo *S*-glutathionylation in green eukaryotes (Additional file 9 Table S2, Fig. 3).

We determined the subcellular localisation of glutathionylated proteins based on biological function and

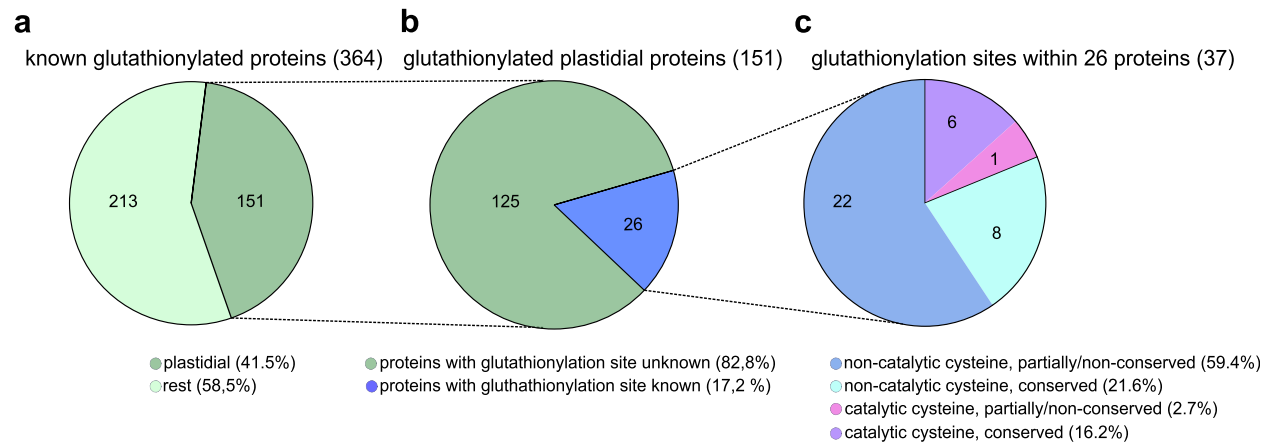

Fig. 3 Overview of glutathionylation target proteins. **a** Overview of all known glutathionylated proteins in green eukaryotes with the plastidial glutathionylation target proteins highlighted. **b** Overview of all known plastidial glutathionylation target proteins with known glutathionylation sites highlighted. **c** Overview of all known plastidial glutathionylation sites with classification in evolutionary conserved and non–/partially conserved cysteine sites and subdivision in catalytic and non-catalytic function (for accessions, annotation and references, see Additional file 9 Table S2)

prediction tools such as TargetP [45, 46] and SUBA (Subcellular Localisation Database for *Arabidopsis thaliana* [94]). Among the 364 proteins, 151 proteins are localised to plastids (Additional file 9 Table S2, Fig. 3), corresponding to c. 41% of the known plant glutathionylome. Subsequently, we explored for which plastidial proteins the exact site of *S*-glutathionylation was determined. One proteomic work in the chlorophyte *C. reinhardtii* combined the identification of glutathionylated targets with streptavidin enrichment using biotinylated-tagged peptides [73]. This approach allows establishing the exact *S*-glutathionylation sites if the identified peptide contains only one Cys residue. To further extent the analysis, we also considered studies on recombinant plastidial proteins in which the cysteine residues undergoing *S*-glutathionylation were identified by in vitro oxidant treatments coupled to mass spectrometry analysis [76–82]. Among 151 plastidial proteins, we found 37 glutathionylation sites with known target Cys within 26 different proteins (Table 1 and Additional file 9 Table S2), representing c. 17% of the known plastidial glutathionylome (Fig. 3).

The number of sites exceeds the number of proteins as several glutathionylated proteins contain multiple *S*-glutathionylation sites (Table 1 and Additional file 9 Table S2). More precisely, seven proteins contain two glutathionylated Cys and two proteins contain three glutathionylated Cys (Table 1 and Additional file 9 Table S2). The proteins with identified *S*-glutathionylation sites are putatively involved in diverse cellular processes such as photosynthesis, carbohydrate metabolism, biosynthetic pathways, redox regulation, signalling and protein homeostasis (Table 1).

To assess the evolutionary conservation of Cys undergoing glutathionylation, we constructed multiple sequence alignments of the 26 plastidial proteins (Additional file 10) from all analysed plant model species. We found that among the 37 known *S*-glutathionylation sites seven sites were involved in catalytic activity, of which six sites were fully conserved from green algae to flowering plants (Fig. 3, Additional file 9 Table S2, Additional file 10). Thirty glutathionylation sites were identified on non-catalytic cysteines (Fig. 3) of which eight Cys were nevertheless fully conserved in all investigated model species. The remaining 22 Cys were not or only partially conserved (Additional file 10), exhibiting different patterns of evolutionary gains and losses (Fig. 3 and Additional file 9 Table S2).

Five examples of interesting gains and losses of putative *S*-glutathionylation sites are illustrated in Fig. 4. In alpha-Amylase 3 (AMY3) and SAL1 (3′-phosphoadenosine 5′-phosphate phosphatase) two *S*-glutathionylation sites were identified in each of the *A. thaliana* homologs. Cys499 in AMY3 is only present in the investigated angiosperm models. An additional sequence alignment incorporating basal angiosperm sequences (see Additional file 11) revealed the presence of Cys 499 in *Amborella trichopoda* and *Ananas comosus* AMY3 homologs. Cys119 of AtSAL1 is only conserved in about a third of eudicots and few monocots [76] and we do not identify any Cys at the homologous position in any non-flowering model plant. These data suggest an origin of cysteines at the Cys499 position in AMY3 and Cys119 position in SAL1 at the latest in early angiosperm evolution. In contrast, Cys106 of thiamine thiazole synthase (THI1) is present in *C. reinhardtii* and all homologs of investigated land plant models, except for *A. thaliana*, suggesting a late loss in land plant evolution. Several of

Table 1 Overview of glutathionylation sites on plastid proteins and evolutionary conservation

	Protein name	Cys	Org.	Cat.	Ref.
Redox regulation	2-Cys peroxiredoxin	172	Ps	yes	Calderón et al. 2017 [92]
	Glutaredoxin S12 (GRXS12)	29	Pt	yes	Zaffagnini et al. 2012 [73]
	Thioredoxin f (TRX-f)	60	At	no	Michelet et al. 2005 [31]
Photosynthesis	Ferredoxin 1	48	Cr	no	Zaffagnini et al. 2012 [73]
		69	Cr	yes	Zaffagnini et al. 2012 [73]
	Fructose-1,6-bisphosphatase	109	Cr	no	Zaffagnini et al. 2012 [73]
	Fructose-1,6-bisphosphate aldolase	58	Cr	no	Zaffagnini et al. 2012 [73]
	Glyceraldehyde-3-phosphate dehydrogenase, A subunit (GAPA)	156	At	yes	Zaffagnini et al. 2007 [93]
	Plastocyanin	130	Cr	yes	Zaffagnini et al. 2012 [73]
	Phosphoglycerate kinase	159	Cr	no	Zaffagnini et al. 2012 [73]
		412	Cr	no	Zaffagnini et al. 2012 [73]
	Phosphoribulokinase	47	Cr	no	Zaffagnini et al. 2012 [73]
		274	Cr	no	Zaffagnini et al. 2012 [73]
	Photosystem II (PSII) core phosphatase (PBCP)	168	Os	no	Liu et al. 2019 [79]
		176	Os	no	Liu et al. 2019 [79]
		195	Os	no	Liu et al. 2019 [79]
	Ribulose bisphosphate carboxylase large chain	172	Cr	no	Zaffagnini et al. 2012 [73]
		247	Cr	no	Zaffagnini et al. 2012 [73]
		427	Cr	no	Zaffagnini et al. 2012 [73]
	Transketolase	84	Cr	no	Zaffagnini et al. 2012 [73]
	Triose phosphate isomerase (chloro TPI)	15	At	no	López-Castillo et al. 2016 [80]
Carbohydrate metabolism	ADP-glucose pyrophosphorylase large subunit	112	Cr	no	Zaffagnini et al. 2012 [73]
	Alpha-amylase 3 (AMY3)	499	At	yes	Gurrieri et al. 2019 [77]
		587	At	yes	Gurrieri et al. 2019 [77]
	Beta-amylase 3 (BAM3)	433	At	no	Storm et al. 2018 [78]
Biosynthesis	Acetohydroxy acid isomeroreductase	439	Cr	no	Zaffagnini et al. 2012 [73]
	Full-length thiazole biosynthetic enzyme	106	Cr	no	Zaffagnini et al. 2012 [73]
	Isopropylmalate dehydratase, large subunit	444	Cr	no	Zaffagnini et al. 2012 [73]
	Magnesium-chelatase subunit chlI	184	Cr	no	Zaffagnini et al. 2012 [73]
others	3′-phosphoadenosine 5′-phosphate phosphatase SAL1	119	At	no	Chan et al. 2016 [76]
		190	At	no	Chan et al. 2016 [76]
	Chaperonin 60B2	249	Cr	no	Zaffagnini et al. 2012 [73]
		537	Cr	no	Zaffagnini et al. 2012 [73]
	Heat shock protein 70B (HSP70B)	349	Cr	no	Michelet et al. 2008 [75]
	Phosphorylase	171	Cr	no	Zaffagnini et al. 2012 [73]
	Protein tyrosine phosphatases (PTP)	78	At	no	Dixon et al. 2005 [72]
		176	At	no	Dixon et al. 2005 [72]

Protein names and putative functions were partly assigned on sequence similarity and/or phylogenetic trees; please refer to the cited literature and references therein. *Cys* position of identified cysteine, *Org* organism, *Cat* catalytic cysteine, *Ref* literature reference, *At Arabidopsis thaliana*, *Cr Chlamydomonas reinhardtii*, *Os Oryza sativa*, *Ps Pisum sativum*, *Pt Populus trichocarpa*

the putative *S*-glutathionylation sites show variable conservation patterns that suggest several independent gains and losses in land plant lineages, such as Cys190 of SAL1, Cys159 and Cys412 in phosphoglycerate kinase (PGK) and Cys48 in ferredoxin.

Discussion

The plastid glutathione-dependent redox network is largely conserved

In a redox cascade, the steady-state redox status of an individual protein cysteine is influenced by the input of

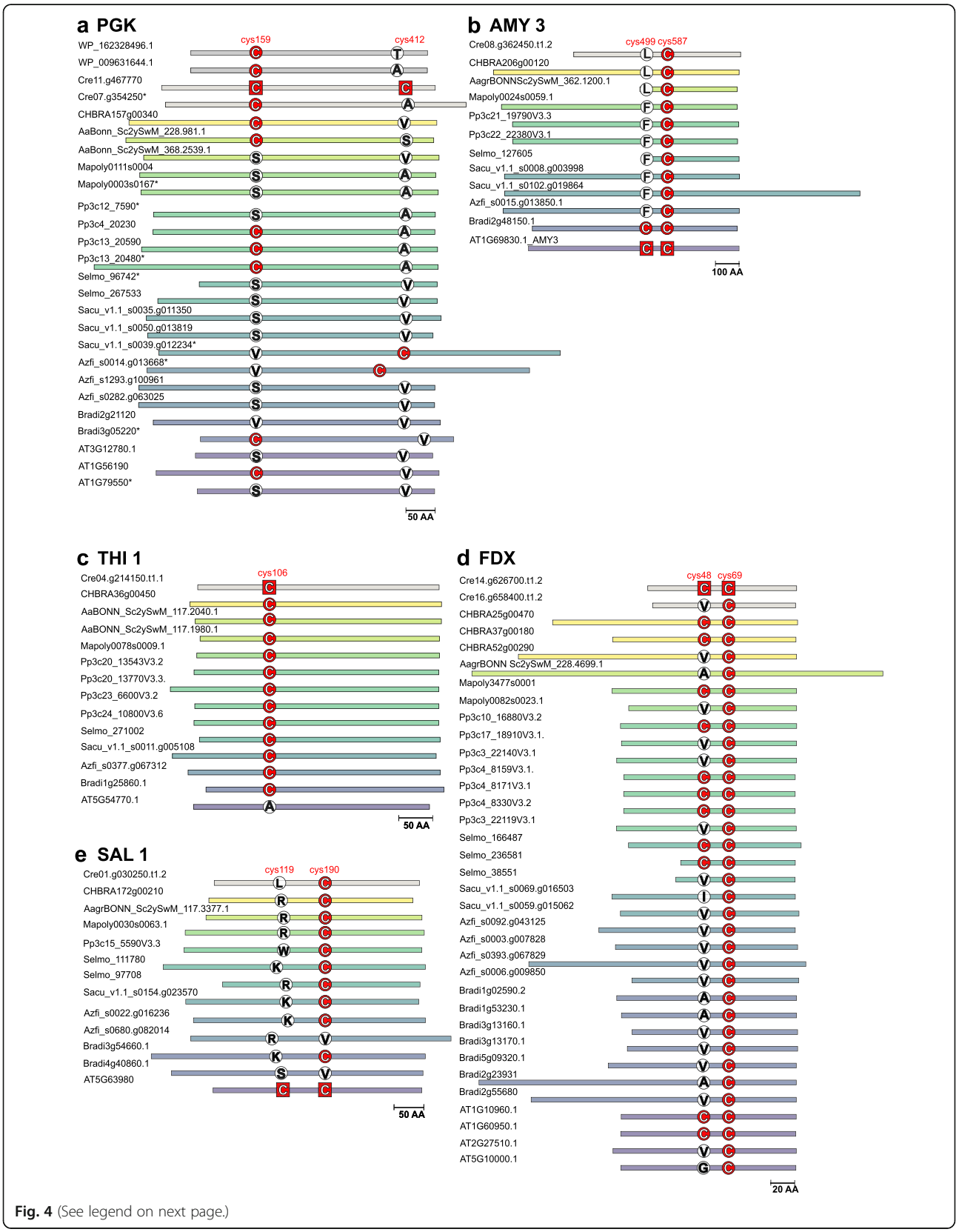

Fig. 4 (See legend on next page.)

(See figure on previous page.)

Fig. 4 Evolutionary conservation of known *S*-glutathionylation sites on non-catalytic cysteines. Schematic representation of five target proteins with non-conserved and non-catalytic cysteines showing interesting patterns of evolutionary conservation regarding *S*-glutathionylation sites (see Additional file 10 for alignments). To generate the alignments BlastP results were filtered manually by clades based on phylogenetic trees and additionally length of the N-terminus and TargetP [45, 46] predictions to identify the organellar isoforms of phosphoglycerate kinase (**a**), alpha-amylase (AMY3) (**b**), thiamine thiazole synthase (THI1) (**c**), apoferredoxin (FDX) (**d**) and 3′phosphoadenosine 5′ phosphate phosphatase (SAL1) (**e**). The bars indicate the total length of the proteins and are aligned with the position of the glutathionylated cysteine. In the case of two cysteine positions, the proteins were aligned to the cysteine that is conserved in more species. Gaps in the alignments are not indicated in this graph. The known glutathionylated cysteine sites are marked with a red square in the respective organism. Asterisks indicate putative cytosolic isoforms (TargetP [45, 46] predictions) regarding PGK. *Synechocystis sp. (WP), Chara braunii (Chbra), Anthoceros agrestis (Aa), Marchantia polymorpha (Mapoly), Physcomitrium patens (Pp), Selaginella moellendorffii (Selmo), Salvinia cucullata (Sacu), Azolla filiculoides (Azfi), Brachypodium distachyon (Bradi)* and *Arabidopsis thaliana (At)*

electrons from nucleophiles (i.e. electron donors), as well as the presence of proteins or molecules that interact and behave as electrophiles (i.e. electron acceptors). In cell compartments, thiol-switching networks can thus be limited by kinetic and thermodynamic parameters, such as the composition of the proteome, the ability of the present proteins to interact and the respective midpoint potentials of involved disulfides, as well as the reactivity of individual cysteine residues towards ROS/RNS. Glutathione-dependent reactions can be disturbed by mutants of either GSH biosynthesis enzymes [95, 96] or by mutants of GR, shifting the glutathione redox potential to less reducing values [29, 33]. The reported phenotypes of mutants lacking a stromal GR differed in *A. thaliana* and *P. patens*, as embryo development is aborted in *A. thaliana* but is completed in *P. patens*. Evolutionary changes could in theory either affect the composition and activity of redox-active proteins present, the presence and position of target thiols on metabolic enzymes, or signalling cascades linked to plastid glutathione redox balance. We compiled a list of protein members in the glutathione-dependent plastid redox network in representative streptophyte model species (Fig. 1) and their network relationships and evolution (Fig. 2). We found that plastid targeting of several GSSG-producing enzymes was already established before the transition to land and that no large expansions occurred in the gene families of DHAR, GSTL, GSTI, PRXIIE or class I and class II GRX during land plant evolution. However, several enzymes of ROS scavenging and damage repair families (DHAR, GSTL, GSTI, MRSB1) do not currently have an identified plastid-targeted isoform in the streptophyte alga *C. braunii*. However, as targeting predictions via algorithms for evolutionary distant species are prone to result in false positives and negatives [48, 97], we used three different predictors, namely the two most recently improved tools based on the largest plant training sets TargetP2.0 [46] and LOCALISER [47], as well as PredAlgo, that was trained on *C. reinhardtii* sequences. However, we still likely underestimate the number of plastid-targeted proteins, due to (1) false predictions and (2) fragmentary gene models that do not predict N-terminal sequences correctly. Localisation predictions often yielded different results (Additional file 1 Table S1, sheet2) and differed from experimentally determined localisations (e.g. AtMSRB1). Thus, we additionally screened for the presence of N-terminal extensions to determine the presence or absence of a putative targeting peptide (Additional files 2, 3, 4, 5, 6, 7, 8). However, incorrect or fragmentary gene models, can still lead to misinterpretation of the available data. Thus, the available *S. moellendorffii* protein models do often not allow one to predict N-terminal targeting signals or draw conclusions on presence or absence of N-terminal extensions due to incompleteness (Fig. 2).

In some of the investigated gene families, we found variable targeting to organelles and presence or absence of N-terminal extensions across land plant evolution, whereas others showed very consistent targeting. Thus, we observed variable targeting in the GST subfamilies DHAR, GSTL and GSTI. DHAR couples the regeneration of dehydroascorbate to the glutathione pool in the ascorbate/glutathione cycle, while monodehydroascorbate reductase regenerates ascorbate at the expense of NADH [24]. In *A. thaliana*, stromal DHAR is not necessary for growth, but takes a role in the high light response [98]. Variability in DHAR targeting would indicate evolutionary variability in the coupling of the ascorbate redox state to the E_{GSH} in different compartments, which could affect signalling responses. Regarding GSTL and GSTI, targeting may be variable, but these GST subfamilies show a nearly complementary distribution in land plant lineages, with GSTI being present in bryophytes and GSTL in the moss *P. patens*, ferns and seed plants. The function of GSTI has not been established in vitro, but is suspected to be similar to GSTL, acting on the detoxification of peroxides [50]. In plastids, several pathways for hydrogen peroxide and lipid peroxide detoxification co-exist (ascorbate peroxidases [8], TRX-dependent GPXL [99] and PRXs (PRXQ, 2-Cys PRX, PRXIIE [15]), suggesting that redundancy might be a reason for independent gains and losses in the investigated protein families during land plant evolution.

Similarly, regarding the repair of oxidised methionine (methionine-*R*-sulfoxide), atypical MSRB with one cysteine (AtMSRB1 homologs) as well as with two cysteines (AtMSRB2 homologs) act redundantly with the difference of regeneration being powered from a different redox cascade (i.e. GSH/GRX and TRX, respectively). Thus, if species are lacking a plastidial 1-Cys MSRB1 homolog, the 2-Cys MSRB2 may compensate and still allow for repair of the *R* diastereomer of MetSO. The biological significance of the variable composition of scavenging and repair enzymes in plastids during streptophyte evolution is yet unclear but raises the question if the only reason is functional redundancy, or if parallel redox cascades with coupling to different electron donors are important for processes such as stress signalling or relate to differences between tissues or light conditions.

On the contrary, PRXIIE, GRXC5/S12, GRXS14, GRXS16 homologs are present as a single plastid isoform in the majority of species, suggesting conserved plastid-specific functions and tight control of gene copy number. Although peroxide detoxification is linked to TRX via several PRXs (PRXQ and 2-Cys PRX, [15]) the plastid isoform PRXIIE that can be more efficiently regenerated via GSH/GRX is likely fully conserved in streptophytes (Fig. 2). The strict conservation of PRXIIE isoforms suggests an important specific biological function, although the abundance of PRXIIE is substantially lower than that of plastid 2-Cys PRX [15]. Its specific properties include that PRXIIE is the only PRX not associated with thylakoids, that it is coupled to GRX for reduction and that it has been linked to RNS signalling [15, 100].

PRXIIE and MSRB1 are regenerated via the action of class I GRX. Besides, GRXC5 can bind a [2Fe-S] cluster that might act in a regulatory mechanism under oxidative stress conditions [66]. We found a conserved clade containing plastid-targeted GRXC5/S12 homologs. As an exception, we did not identify a GRXC5 nor GRXS12 isoform in the fern *A. filiculoides*. However, isoforms in the C1/C2 (Azfi_s0158.g053892; Azfi_s0074.g037496) as well as the C3/C4 (Azfi_s0270.g061184; Azfi_s0004.g008860) clades underwent duplication and are candidates for re-targeting to plastids to compensate for the loss of the plastid-targeted class I isoform. In *C. braunii* and non-seed plants, only one isoform with a CPYC active site is present (GRXC5), indicating that CPYC is the ancestral active site motif of this GRX isoform, while the GRXS12 variant only appeared in angiosperm evolution.

Class II GRX isoforms are involved in the coordination and transfer of Fe-S cluster on target proteins [64, 65] and become only redox-active after loss of the coordinated Fe-S cluster. Without Fe-S cluster, they are able to catalyze *S*-glutathionylation in vitro in the presence of GSSG, but fail to deglutathionylate target proteins such as redox-sensitive GFP [65]. In vivo evidence revealed that GRXS14 levels correlate with tolerance to abiotic stress conditions in either Arabidopsis [62, 101] or tomato [102]. In addition, GRXS14 along with GRXS16 are necessary for functional photosynthesis and chlorophyll biosynthesis [62]. In *C. reinhardtii*, class II GRX3, a GRXS14 homolog, was found to catalyse deglutathionylation of photosynthetic GAPDH from *Arabidopsis thaliana* (AtGAPA) using electrons from PSI-reduced ferredoxin [103]. However, an analogous function was not shown for land plant GRXS14 homologs to date. Our analysis confirmed the strict conservation of one GRXS14 and GRXS16 homolog in plastids in all model organisms, except for *P. patens* with two GRXS14 isoforms. However, the functional and physiological relevance of class II GRX redox-activity remains unclear.

Reduction of class I GRXs is driven by glutathione, while GR maintains a highly reducing E_{GSH} in the plastid stroma, re-reducing the generated GSSG. We confirmed two GR clades in streptophytes likely containing the dual-targeted isoform to cytosol/peroxisomes and mitochondria/plastids. At least one isoform of the mitochondrial/plastidial GR clade and one of the cytosolic/peroxisomal clade is conserved in all land plant model species, while one additional isoform originating from horizontal gene transfer (HGT) is present in *Anthoceros* species. The most closely related bacterial sequence in Uniprot [104] is from the cyanobacterium *Nostoc* spec. (Uniprot ID P48638), suggesting that this GR isoform was acquired from cyanobacteria, which are known to colonise hornworts [40, 42]. The presence of putative N-terminal extensions in the GRs originating from HGT is interesting (Additional file 8), as they might confer targeting to organelles, raising the question of the biological function of the additional GR in the investigated hornworts.

Non-catalytic cysteines sensitive to *S*-glutathionylation are evolutionary conserved

Cysteines are central for the structural integrity and catalytic activity of many proteins, and post-translational modifications of Cys residues control major steps in plant signalling and metabolism [105, 106]. The biological role of *S*-glutathionylation is only resolved for a few exemplary target proteins and ranges from reaction intermediates on active site Cys of scavenging/repair enzymes over protection from Cys overoxidation to regulation of protein activity [3, 60, 69].

To date, 151 different plastid proteins were identified as targets for *S*-glutathionylation by various experimental approaches in different plant systems, suggesting that this post-translational redox modification might be quite

common in plastids. However, the exact number of proteins in plastids that are glutathionylated at a given time point in a given organism remains unknown and is potentially rather low, for a number of reasons.

Firstly, high-throughput methods used to identify *S*-glutathionylation partly use reaction conditions that are non-physiological. For instance, BioGSSG is used to induce protein *S*-glutathionylation. However, this mechanism is unlikely as (i) GSSG concentration is physiologically in the nanomolar range while a millimolar concentration of BioGSSG is used in vitro and (ii) most proteins have a K_{ox} of around 1 meaning that equimolar concentration of GSH and GSSG are required to reach 50% of glutathionylated protein [107, 108]. GSSG can react with a cysteine in its thiolate state ($-S^-$) via a thiol-disulfide exchange reaction. However, the GSSG-dependent mechanism is known to be thermodynamically disadvantageous because of the high in vivo GSH/GSSG ratio, and only some protein species have been shown to be able to undergo *S*-glutathionylation via this pathway [60, 109]. Some proteins undergo *S*-glutathionylation following exposure to the nitrosylated counterpart of glutathione known as *S*-nitrosoglutathione (GSNO). While GSNO is a nitrosylating agent [110], it has been observed to induce *S*-glutathionylation on certain protein species probably depending on the microenvironment of their cysteine [60, 111–113]. Another physiologically likely pathway to *S*-glutathionylation occurs via nucleophilic attack of glutathione on *S*-sulfenylation sites that are formed by the reaction of protein thiols with H_2O_2. Using exogenous application of 0.1–20 mM H_2O_2, between 68 and 132 different plastid proteins were identified as prone to *S*-sulfenylation [114–116]. How many proteins undergo *S*-sulfenylation and potentially subsequent *S*-glutathionylation under physiologically relevant H_2O_2 concentrations in plastids remains unclear.

Secondly, many proteins are potentially rapidly deglutathionylated in vivo. In plastids, the deglutathionylation would require interaction with the plastid class I GRXC5/S12 isoforms (Fig. 2). Based on experimental evidence, there is no functional redundancy between TRXs and GRXs despite their structural similarity, and they are specifically dedicated to the redox control of protein disulfides and *S*-glutathionylation, respectively. To date, the reduction of glutathionylated cytosolic glyceraldehyde-3-phosphate dehydrogenase from *Arabidopsis thaliana* (AtGAPC) constitutes the sole exception since both enzymes can efficiently catalyse its deglutathionylation [87, 117]. Increased GSSG levels and/or less reducing stromal glutathione redox potential might influence the level of *S*-glutathionylation on proteins in vivo, e.g. via decreased rates of de-glutathionylation. As we identified a dynamic oxidative response of the stromal glutathione redox potential to a transition from light to dark [33], future studies need to investigate the biological relevance of these redox dynamics and a putative influence on *S*-glutathionylation levels on proteins.

Unfortunately, the exact position of only 37 Cys (on 26 different plastid proteins) susceptible to *S*-glutathionylation is known, representing c. 17% of the different identified glutathionylated proteins in plastids. Catalytic Cys were fully conserved with the exception of Cys499 in AMY3 (Fig. 4, Additional file 9: Table S2). Here, the annotation as catalytic Cys is based on a mutant protein in *A. thaliana* that largely lacks catalytic activity [118]. However, the mechanism is unknown and Cys499 might not be strictly necessary for catalytic activity in other organisms, based on our analysis. Notably, c. 22% of the known sites on non-catalytic Cys were fully conserved from green algae to flowering plants. This suggests an important regulatory role of these Cys, including the potential for modification via *S*-glutathionylation.

Distinct conservation patterns of putative glutathionylation sites

Our evolutionary analysis on conservation of Cys undergoing *S*-glutathionylation in at least one species revealed that several regulatory Cys are re-appearing in land plant evolution suggesting independent gains and losses of these sites (Fig. 4, FDX, PGK, SAL1).

Regarding phosphoglycerate kinase (PGK), we found a decreasingly complex regulation during evolution. In the green alga *C. reinhardtii* two *S*-glutathionylation sites (CrPGK1 Cys159 and Cys412) were identified and *S*-glutathionylation confirmed in vitro [73]. Interestingly, Cys412 is conserved in human and mouse [75] but not in most land plants, although it forms a regulatory disulfide with Cys278 in CrPGK1 [81]. Cys159 is partially conserved in some land plant homologs. Most investigated species encode for several isoforms of which at least one contains Cys159, except for *M. polymorpha* and the fern model species. In *A. thaliana*, the function of the different isoforms is known, with AtPGK3 (AT1G79550) serving as the cytosolic glycolytic isoform, AtPGK1 (AT3G12780) as the photosynthetic isoform, and AtPGK2 (AT1G56190) as the plastidial glycolytic isoform [119]. AtPGK1 and AtPGK2 are thus participating in the Calvin-Benson cycle and plastidial glycolysis, respectively, but catalysing the inverse reaction. Cys159 is only conserved in the plastidial glycolytic isoform in *A. thaliana*. It is tempting to speculate that *S*-glutathionylation is contributing to differential regulation between photosynthetic and glycolytic isoforms in plastids.

Similarly, a highly conserved Cys is not present in the *A. thaliana* ortholog of thiamine thiazole synthase (THI1) (Fig. 4c). THI1 is synthetizing the thiazole

moiety of thiamine (vitamin B1). It is a suicide enzyme undergoing a single catalytic turnover, as the sulfide is transferred from a conserved Cys [120] (corresponding to AtTHI1 Cys216). The Cys of one *S*-glutathionylation site (Cys106 identified in *C. reinhardtii*) is strictly conserved, except for *A. thaliana* (A98). The position of Cys106 is in the alpha 2 helix [121] within a highly conserved motif of unknown function. However, the meaning of a potential redox regulation in single-turnover enzymes remains unclear.

In contrast, the redox regulation of alpha-amylase 3 (AMY3) seems to be increasingly complex in evolution. Whereas two *S*-glutathionylation sites were identified in *A. thaliana*, only one Cys (Cys587) is strictly conserved. The second Cys (Cys499) is only present in the investigated angiosperm models. It was already shown that AtAMY3 is more active in its reduced form [118], with a midpoint redox potential of − 329 mV (pH 7.9) and that it is most efficiently reduced by TRX f, m and y. Whereas the single Cys mutant C587S was retaining activity under oxidising conditions, the Cys499 mutant was nearly inactive [118]. AMY3 plays a role in starch metabolism associated with stomatal opening and is involved in the response to stress [122]. In the presence of H_2O_2 it undergoes a partial irreversible inactivation due to the oxidation of cysteines, which is prevented by *S*-glutathionylation on at least three different Cys, including Cys499 and Cys587. Once glutathionylated, the enzyme can be reverted to its active state via GRXs or TRX, if the *S*-glutathionylation is resolved by formation of an intramolecular disulfide [77].

Similarly, two *S*-glutathionylation sites were identified in the *A. thaliana* ortholog of the 3′-phosphoadenosine 5′-phosphate phosphatase SAL1 of which only Cys190 is conserved in at least one homolog of all investigated model species. Cys119 is only present in *A. thaliana* with positively charged AA residue being present in most other species at the equivalent position. SAL1 has an important evolutionarily conserved function in the regulation of PAP levels and thereby in plastid to nucleus retrograde signalling [123] (Zhao et al., 2019). A "moonlighting" signalling function by secondary redox sensing was already described for SAL1 [76] via the fully conserved Cys167 that forms a cross beta-strand disulfide bond with Cys190. Cys119 or Cys190 are required for deactivation under oxidising conditions in *A. thaliana* with Cys119 being involved in intermolecular disulfide and dimer formation, facilitating the cross beta-strand disulfide bridge Cys167-Cys190 [76]. The redox-regulatory mechanism in *A. thaliana* consists of first dimerization and subsequent oxidative inactivation. Alternatively, *S*-glutathionylation on Cys119 or Cys190 did decrease the activity in monomer or dimer (midpoint redox potential − 308 mV monomer, pH 7.5).

Finally, we found variable conservation of putative *S*-glutathionylation sites, with potentially several independent gains and losses in ferredoxins (FDX). While Cys69, that is one of four 2Fe-2S coordinating cysteines, is strictly conserved, there is variable conservation of Cys48. Cys48 *S*-glutathionylation was identified in *C. reinhardtii* and this residue is present in *A. thaliana* leaf-type ferredoxins (FDX1 (AT1G10960) and FDX2 (AT1G60950)), but not in root-type ferredoxin FDX3 (AT2G27510) and FDX4 (AT5G10000) [124]. It is possible that there is a different redox regulation of leaf-type FDX that are reduced by PSI, compared to root-type FDXs, that are reduced by FNR and are more efficient electron donors to sulphite reductase [124]. However, Cys48 is conserved in none of the FDX sequences from fern model species and the monocot model *B. distachyon*. This suggests either independent losses of Cys48 in these plant lineages, or the independent re-appearance of a regulatory Cys at the same position during land plant evolution.

Conclusions

By analysing enzymes drawing electrons from the glutathione pool and producing GSSG we found that GR and GRX isoforms are largely conserved between streptophyte algae and land plant model species, identifying them as central players of plastid glutathione-dependent redox cascades. Here, GRXC5 is the ancestral isoform likely involved in protein de-glutathionylation. The composition of scavenging and damage repair enzymes in plastids was evolutionary less conserved except for PRXIIE. This indicates variability of ROS-scavenging and damage repair between different species and highlights that PRXIIE might be necessary for plastid redox regulation. As we found evolutionary conservation of many known *S*-glutathionylation sites on plastid proteins, including non-catalytic cysteines, we conclude that protein *S*-glutathionylation in plastids plays an important and yet under-investigated role in redox regulation and stress response. Future challenges are to determine (i) new targets of *S*-glutathionylation, (ii) the exact position of *S*-glutathionylation in more target proteins, (iii) the in vivo dynamics of protein *S*-glutathionylation and the resulting steady-state level of the *S*-glutathionylated fraction of target proteins and (iv) the biological relevance of this modification for plastid function.

Methods

Sequence retrieval and alignment

To reconstruct gene diversification of components of plastid and mitochondrial redox cascades, protein sequences were retrieved from OrcAE for *Chara braunii* (http://www.bioinformatics.psb.ugent.be/orcae/overview/Chbra), Phytozome v12.1 [125] for *Chlamydomonas*

reinhardtii, *Marchantia polymorpha*, *Physcomitrium* (*Physcomitrella*) *patens*, *Selaginella moellendorffii* and *Brachypodium distachyon*, Fernbase (http://www.fernbase.org) for *Salvinia cucullata* and *Azolla filiculoides*, and TAIR10 (www.arabidopsis.org) for *Arabidopsis thaliana*. Additionally, protein sequences encoded by organellar genomes were retrieved from Uniprot [104]. BLAST access to *Anthoceros agrestis* and *Anthoceros punctatus* genomes [42] was provided by Prof. Peter Szövenyi. Alignments were constructed using JalView [126] and the Muscle algorithm with default settings.

Construction of phylogenetic trees

Phylogenetic trees were generated from manually curated alignments (see Additional file 12) using Bayesian inference with MrBayes (run parameters: mixed protein models, rates = invgamma, number of generations: $2*10^6$, burnin = 20%, end split frequencies< 0.01) [127]. As complementary method, Maximum Likelihood-based trees (see Additional file 13) were generated using iQtree web [128] (run parameters: 1000 bootstrap, standard settings).

Graphical representations of phylogenetic trees were created using the Figtree software (v1.4.2, A. Rambaut, http://tree.bio.ed.ac.uk/software/figtree/).

Compiling the list of glutathionylated plastid proteins

Proteins found to be glutathionylated in different proteomic and in vitro studies [31, 60, 71–93] were retrieved from the literature and used to assemble a list (Additional file 9: Table S2, sheet1). NCBI reference sequences (www.ncbi.nlm.nih.gov) and TAIR (www.arabidopsis.org) accession numbers were used to unambiguously identify proteins.

Arabidopsis homologs of every protein were identified using the BLASTP tool from NCBI (https://blast.ncbi.nlm.nih.gov/Blast.cgi). The presumed subcellular localization of Arabidopsis homologs was retrieved from SUBA (Subcellular Localisation Database for *A. thaliana*) [94] using the SUBAcon algorithm in order to identify plastidial proteins.

Identification of catalytic cysteine sites

Catalytic cysteines were identified among those found to be glutathionylated and belonging to plastid proteins (Additional file 9 Table S2, sheet2) using Uniprot [104] and the information found within the individual publications cited.

Abbreviations

ROS: reactive oxygen species; CBC: Calvin-Benson cycle; RNS: reactive nitrogen species; GSH: glutathione; TRX: thioredoxin; GR: glutathione reductase; FTR: ferredoxin-thioredoxin reductase; NTR: NADPH-dependent thioredoxin reductase; PRX: peroxiredoxin; GPXL: glutathione peroxidase-like protein; GSSG: glutathione disulfide; E_{GSH} : glutathione redox potential; MSR: methionine sulfoxide reductase; GRX: glutaredoxin; NPR1: nonexpressor of pathogenesis-related genes 1; DHAR: dehydroascorbate reductase; GST: glutathione *S*-transferase; APX: ascorbate peroxidase; Cb: *Chara braunii*; Aa: *Anthoceros agrestis*; Mp: *Marchantia polymorpha*; Pp: *Physcomitrium patens*; Sm: *Selaginella moellendorffii*; Sc: *Salvinia cucullata*; Af: *Azolla filiculoides*; Bd: *Brachypodium distachyon*; At: *Arabidopsis thaliana*; MetSO: methionine sulfoxide; PET: photosynthetic electron transport; AsA: ascorbic acid; GAP: glyceraldehyde-3-phosphate dehydrogenase; MS/MS: tandem mass spectrometry; BioGEE: biotinylated GSH ethyl ester; BioGSSG: biotinylated glutathione disulfide; AMY: alpha-amylase; THI: thiamine thiazole synthase; PGK: phosphoglycerate kinase; FDX: ferredoxin; HGT: horizontal gene transfer; GSNO: *S*-nitrosoglutathione

Supplementary Information

The online version contains supplementary material available at https://doi.org/10.1186/s12870-021-03087-2 .

Additional file 1: Table S1. containing protein model information and targeting.

Additional file 2: Fig. S2. Phylogenetic tree of DHAR. (a) Phylogenetic tree of DHAR isoforms (*P. patens* nomenclature according to Liu et al. (2013) [50]) constructed using MrBayes, node values and line weights depict posterior probabilities (run parameters: mixed protein models, rates = invgamma, number of generations: $2*10^6$, burnin = 20%, split frequencies< 0.01). [1]*P. patens* DHAR1 was identified and quantified in mitochondrial and plastid proteomes [49] and is putatively dual targeted. TargetP2.0 (T) [46], LOCALIZER (L) [47] and PredAlgo (P) [48] predictions (Additional file 1 Table S1) indicate highly variable targeting of the multiple DHAR paralogs (M, mitochondria; P, plastid; O, other; S, secretory). The presence (check mark) or absence (X) of an N-terminal extension (ext. N) in the sequence is indicated; NA: not assessed as sequence potentially incomplete. Gene identifiers are given according to the used gene models for *Chara braunii* (CHBRA), *Anthoceros agrestis* strain Bonn (AaBonn), *Marchantia polymorpha* (Mapoly), *Physcomitrium patens* (Pp), *Selaginella moellendorffii* (Selmo), *Salvinia cucullata* (Sacu), *Azolla filiculoides* (Azfi), *Brachypodium distachyon* (Bradi) and *Arabidopsis thaliana* (At) and are additionally color-coded as in Fig. 1. Colour legend: Cb = *Chara braunii*; Aa = *Anthoceros agrestis*; Mp = *Marchantia polymorpha*; Pp = *Physcomitrium patens*; Sm = *Selaginella moellendorffii*; Sc = *Salvinia cucullata*; Af = *Azolla filiculoides*; Bd = *Brachypodium distachyon*; At = *Arabidopsis thaliana*. (b) N-terminal part of protein alignment (Jalview) showing the presence or absence of N-terminal extensions indicative of putative N-terminal targeting peptides. Colour-scheme: ClustalX.

Additional file 3: Fig. S3. Phylogenetic tree of lambda and iota-type GSTs. (a) Phylogenetic tree of lambda- and iota-type glutathione *S*-transferase isoforms (*P. patens* nomenclature according to Liu et al. (2013) [50]) constructed using MrBayes, node values and line weights depict posterior probabilities (run parameters: mixed protein models, rates = invgamma, number of generations: $2*10^6$, burnin = 20%, split frequencies< 0.01). TargetP2.0 (T) [46], LOCALIZER (L) [47] and PredAlgo (P) [48] predictions (Additional file 1 Table S1) indicate variable targeting of GSTL and GSTI isoforms to plastids (M, mitochondria; P, plastid; O, other; S, secretory). The presence (check mark) or absence (X) of an N-terminal extension (ext. N) in the sequence is indicated; NA: not assessed as sequence potentially incomplete. Gene identifiers are given according to the used gene models for *Chlamydomonas reinhardtii* (Cre), *Chara braunii* (CHBRA), *Anthoceros agrestis* strain Bonn (AaBonn), *Marchantia polymorpha* (Mapoly), *Physcomitrium patens* (Pp), *Selaginella moellendorffii* (Selmo), *Salvinia cucullata* (Sacu), *Azolla filiculoides* (Azfi), *Brachypodium distachyon* (Bradi) and *Arabidopsis thaliana* (At) and are additionally color-coded as in Fig. 1. Colour legend: Cb = *Chara braunii*; Aa = *Anthoceros agrestis*; Mp = *Marchantia polymorpha*; Pp = *Physcomitrium patens*; Sm = *Selaginella moellendorffii*; Sc = *Salvinia cucullata*; Af = *Azolla filiculoides*; Bd = *Brachypodium distachyon*; At = *Arabidopsis thaliana*. (b) N-terminal part of protein alignment (Jalview) showing the presence or absence of N-terminal extensions indicative of putative N-terminal targeting peptides. Colour-scheme: ClustalX.

Additional file 4: Fig. S4. Phylogenetic tree of methionine sulfoxide reductases B. (a) Phylogenetic tree of methionine sulfoxide reductase B

(MSRB) isoforms constructed using MrBayes, node values and line weights depict posterior probabilities (run parameters: mixed protein models, rates = invgamma, number of generations: $2*10^6$, burnin = 20%, split frequencies< 0.01). TargetP2.0 (T) [46], LOCALIZER (L) [47] and PredAlgo (P) [48] predictions (Additional file 1 Table S1) indicate variable targeting of MSRB1 isoforms to plastids (M, mitochondria; P, plastid; O, other; S, secretory). The presence (check mark) or absence (X) of an N-terminal extension (ext. N) in the sequence is indicated; NA: not assessed as sequence potentially incomplete. Gene identifiers are given according to the used gene models for *Chlamydomonas reinhardtii* (Cre), *Chara braunii* (CHBRA), *Anthoceros agrestis* strain Bonn (AaBonn), *Marchantia polymorpha* (Mapoly), *Physcomitrium patens* (Pp), *Selaginella moellendorffii* (Selmo), *Salvinia cucullata* (Sacu), *Azolla filiculoides* (Azfi), *Brachypodium distachyon* (Bradi) and *Arabidopsis thaliana* (At) and are additionally color-coded as in Fig. 1. Colour legend: Cb = *Chara braunii*; Aa = *Anthoceros agrestis*; Mp = *Marchantia polymorpha*; Pp = *Physcomitrium patens*; Sm = *Selaginella moellendorffii*; Sc = *Salvinia cucullata*; Af = *Azolla filiculoides*; Bd = *Brachypodium distachyon*; At = *Arabidopsis thaliana*. (b) N-terminal part of protein alignment (Jalview) showing the presence or absence of N-terminal extensions indicative of putative N-terminal targeting peptides. Colour-scheme: ClustalX. (c) In the presence of H_2O_2, methionine can be oxidised, a modification that can be resolved by MSRB regarding methionine-*R*-sulfoxide. The GRX-dependent reaction mechanism in atypical (1Cys) MSRB operates via an *S*-glutathionylation intermediate [53]. The GRX-dependent mechanism generates GSSG that in turn requires GR for reduction. (PDF 156 kb). (d) Conservation of threonine in the relative position to AtMSRB1 Thr132 (red arrow). Colour-scheme: ClustalX.

Additional file 5: Fig. S5. Phylogenetic tree of peroxiredoxin II E. (a) Phylogenetic tree of peroxiredoxin IIE (PRXIIE) isoforms constructed using MrBayes, node values and line weights depict posterior probabilities (run parameters: mixed protein models, rates = invgamma, number of generations: $2*10^6$, burnin = 20%, split frequencies< 0.01). TargetP2.0 (T) [46] predictions indicate conserved targeting of PRXIIE isoforms to plastids, while LOCALIZER (L) [47] and PredAlgo (P) [48] predictions vary (M, mitochondria; P, plastid; O, other; S, secretory) (Additional file 1 Table S1). The presence (check mark) or absence (X) of an N-terminal extension (ext. N) in the sequence is indicated; NA: not assessed as sequence potentially incomplete. Gene identifiers are given according to the used gene models for *Chara braunii* (CHBRA), *Anthoceros agrestis* strain Bonn (AaBonn), *Marchantia polymorpha* (Mapoly), *Physcomitrium patens* (Pp), *Selaginella moellendorffii* (Selmo), *Salvinia cucullata* (Sacu), *Azolla filiculoides* (Azfi), *Brachypodium distachyon* (Bradi) and *Arabidopsis thaliana* (At) and are additionally color-coded as in Fig. 1. Colour legend: Cb = *Chara braunii*; Aa = *Anthoceros agrestis*; Mp = *Marchantia polymorpha*; Pp = *Physcomitrium patens*; Sm = *Selaginella moellendorffii*; Sc = *Salvinia cucullata*; Af = *Azolla filiculoides*; Bd = *Brachypodium distachyon*; At = *Arabidopsis thaliana*. (b) N-terminal part of protein alignment (Jalview) showing the presence or absence of N-terminal extensions indicative of putative N-terminal targeting peptides. Colour-scheme: ClustalX.

Additional file 6: Fig. S6. Phylogenetic tree of class I GRX. (a) Phylogenetic tree of class I glutaredoxin (GRX) isoforms constructed using MrBayes, node values and line weights depict posterior probabilities; nodes with lower support than 50% are collapsed (run parameters: mixed protein models, rates = invgamma, number of generations: $4*10^6$, burnin = 20%, split frequencies< 0.01). TargetP2.0 (T) [46], LOCALIZER (L) [47] and PredAlgo (P) [48] targeting predictions (Additional file 1 Table S1) are indicated (M, mitochondria; P, plastid; O, other; S, secretory). The presence (check mark) or absence (X) of an N-terminal extension (ext. N) in the sequence is indicated; NA: not assessed as sequence potentially incomplete. Gene identifiers are given according to the used gene models for *Chara braunii* (CHBRA), *Anthoceros agrestis* strain Bonn (AaBonn), *Marchantia polymorpha* (Mapoly), *Physcomitrium patens* (Pp), *Selaginella moellendorffii* (Selmo), *Salvinia cucullata* (Sacu), *Azolla filiculoides* (Azfi), *Brachypodium distachyon* (Bradi) and *Arabidopsis thaliana* (At) and are additionally color-coded as in Fig. 1. Colour legend: Cb = *Chara braunii*; Aa = *Anthoceros agrestis*; Mp = *Marchantia polymorpha*; Pp = *Physcomitrium patens*; Sm = *Selaginella moellendorffii*; Sc = *Salvinia cucullata*; Af = *Azolla filiculoides*; Bd = *Brachypodium distachyon*; At = *Arabidopsis thaliana*. (b) N-terminal part of protein alignment (Jalview) showing the presence or absence of N-terminal extensions indicative of putative N-terminal targeting peptides. Colour-scheme: ClustalX.

Additional file 7: Fig. S7. Phylogenetic tree of plastid-targeted class II GRX. (a) Phylogenetic tree of the plastid class II glutaredoxin (GRX) S14 and S16 isoforms constructed using MrBayes, node values and line weights depict posterior probabilities; nodes with lower support than 50% are collapsed (run parameters: mixed protein models, rates = invgamma, number of generations: $2*10^6$, burnin = 20%, split frequencies< 0.01). TargetP2.0 (T) [46] predictions indicate conserved targeting of GRXS14 and GRXS16 isoforms to plastids, while LOCALIZER (L) [47] and PredAlgo (P) [48] predictions vary (M, mitochondria; P, plastid; O, other; S, secretory) (Additional file 1 Table S1). The presence (check mark) or absence (X) of an N-terminal extension (ext. N) in the sequence is indicated; NA: not assessed as sequence potentially incomplete. Gene identifiers are given according to the used gene models for *Chara braunii* (CHBRA), *Anthoceros agrestis* strain Bonn (AaBonn), *Marchantia polymorpha* (Mapoly), *Physcomitrium patens* (Pp), *Selaginella moellendorffii* (Selmo), *Salvinia cucullata* (Sacu), *Azolla filiculoides* (Azfi), *Brachypodium distachyon* (Bradi) and *Arabidopsis thaliana* (At) and are additionally color-coded as in Fig. 1. Colour legend: Cb = *Chara braunii*; Aa = *Anthoceros agrestis*; Mp = *Marchantia polymorpha*; Pp = *Physcomitrium patens*; Sm = *Selaginella moellendorffii*; Sc = *Salvinia cucullata*; Af = *Azolla filiculoides*; Bd = *Brachypodium distachyon*; At = *Arabidopsis thaliana*. (b) N-terminal part of GRXS14 protein alignment (Jalview) showing the presence or absence of N-terminal extensions indicative of putative N-terminal targeting peptides. Colour-scheme: ClustalX. (c) N-terminal part of GRXS16 protein alignment (Jalview) showing the presence or absence of N-terminal extensions indicative of putative N-terminal targeting peptides. Colour-scheme: ClustalX.

Additional file 8: Fig. S8. Phylogenetic tree of glutathione reductases (GR). (a) Phylogenetic tree of glutathione reductase isoforms constructed using MrBayes, node values and line weights depict posterior probabilities; nodes with lower support than 50% are collapsed (run parameters: mixed protein models, rates = invgamma, number of generations: $0.5*10^6$, burnin = 20%, split frequencies< 0.01). TargetP2.0 (T) [46], LOCALIZER (L) [47] and PredAlgo (P) [48] targeting predictions (Additional file 1 Table S1) are indicated (M, mitochondria; P, plastid; O, other; S, secretory); experimental evidence for conserved dual targeting of GR2 isoforms:[1] [67], [2] [29]. The presence (check mark) or absence (X) of an N-terminal extension (ext. N) in the sequence is indicated. Gene identifiers are given according to the used gene models for *Chlamydomonas reinhardtii* (Cre), *Chara braunii* (CHBRA), *Anthoceros agrestis* strain Bonn (AaBonn), *Marchantia polymorpha* (Mapoly), *Physcomitrium patens* (Pp), *Selaginella moellendorffii* (Selmo), *Salvinia cucullata* (Sacu), *Azolla filiculoides* (Azfi), *Brachypodium distachyon* (Bradi) and *Arabidopsis thaliana* (At) and are additionally color-coded as in Fig. 1. Additional species: NOSS: *Nostoc* spec.; *Anthoceros agrestis* Oxford (AaOxford), *Anthoceros punctatus* (Ap), [40]. Colour legend: Cb = *Chara braunii*; Aa = *Anthoceros agrestis*; Mp = *Marchantia polymorpha*; Pp = *Physcomitrium patens*; Sm = *Selaginella moellendorffii*; Sc = *Salvinia cucullata*; Af = *Azolla filiculoides*; Bd = *Brachypodium distachyon*; At = *Arabidopsis thaliana*. (b) N-terminal part of GR protein alignment (Jalview) showing the presence or absence of N-terminal extensions indicative of putative N-terminal targeting peptides. Red bar marks prominent example of sequence lacking in bacterial and Anthoceros GRs, supporting an origin by horizontal gene transfer (HGT). GRs acquired by HGT possess putative N-terminal extensions, compared to bacterial GRs. Colour-scheme: ClustalX.

Additional file 9: Table S2. Lists of *S*-glutathionylation sites and organisms.

Additional file 10 Word-file containing all alignments used to assess conservation of known *S*-glutathionylation sites on plastid proteins in fasta format.

Additional file 11. Word-file containing AMY3 alignment with additional angiosperm sequences.

Additional file 12. Word-file containing all alignments used to build phylogenetic trees in FASTA format.

Additional file 13. Word-file containing phylogenetic trees generated with alternative method (Maximum Likelihood).

Acknowledgements
We thank Prof. Peter Szövenyi for providing advice and BLAST-access to the *Anthoceros agrestis* genomes.

Authors' contributions
SJM-S and MZ conceived the study. FB, JR and SJM-S analysed data and prepared figures. FB, JR, PT, AJM, MZ and SJM-S discussed data and wrote the article. All authors read and approved the final manuscript.

Funding
This research was partially funded via the Joint Mobility Program between the DAAD (PPP Italy 57397466) and the MIUR (Prog. n. 34433). We are grateful for support by the Deutsche Forschungsgemeinschaft (DFG) through the Research Training Group GRK 2064 "Water use efficiency and drought stress responses: From Arabidopsis to Barley" (A.J.M.; F.B.; S.J.M.-S.). These funding bodies had no role in the design of the study and collection, analysis, and interpretation of data, nor in writing the manuscript. Open Access funding enabled and organized by Projekt DEAL.

Availability of data and materials
All data generated or analysed during this study are included in this published article and its supplementary information files. The used databases are publicly accessible and available online: https://bioinformatics.psb.ugent.be/orcae/, https://phytozome.jgi.doe.gov/pz/portal.html, https://www.fernbase.org, https://www.arabidopsis.org, https://www.uniprot.org/, https://suba.live/, https://www.ncbi.nlm.nih.gov/.

Declarations

Ethics approval and consent to participate
not applicable.

Consent for publication
not applicable.

Competing interests
The authors declare that they have no competing interests.

Author details
[1]Institute of Crop Science and Resource Conservation (INRES), University of Bonn, Friedrich-Ebert-Allee 144, 53113 Bonn, Germany. [2]Present Address: Department of Biology, Technische Universität Kaiserslautern, 67663 Kaiserslautern, Germany. [3]Department of Pharmacy and Biotechnology, University of Bologna, 40126 Bologna, Italy.

Received: 10 November 2020 Accepted: 8 June 2021
Published online: 05 July 2021

References

1. Dyall SD, Brown MT, Johnson PJ. Ancient invasions: from endosymbionts to organelles. Science. 2004;304:253–7.
2. de Vries J, Archibald JM. Plant evolution: landmarks on the path to terrestrial life. New Phytol. 2018;217(4):1428–34. https://doi.org/10.1111/nph.14975 .
3. Zaffagnini M, Fermani S, Marchand CH, Costa A, Sparla F, Rouhier N, et al. Redox homeostasis in photosynthetic organisms: novel and established thiol-based molecular mechanisms. Antioxid Redox Signal. 2019;31(3):155–210. https://doi.org/10.1089/ars.2018.7617 .
4. Waszczak C, Carmody M, Kangasjärvi J. Reactive oxygen species in plant signaling. Annu Rev Plant Biol. 2018;69(1):209–36. https://doi.org/10.1146/annurev-arplant-042817-040322 .
5. Geigenberger P, Thormählen I, Daloso DM, Fernie AR. The unprecedented versatility of the plant thioredoxin system. Trends Plant Sci. 2017;22:249–62.
6. Buchanan BB, Balmer Y. Redox Regulation: A broadening horizon. Annu Rev Plant Biol. 2005;56(1):187–220. https://doi.org/10.1146/annurev.arplant.56.032604.144246 .
7. Dietz K-J, Hell R. Thiol switches in redox regulation of chloroplasts: balancing redox state, metabolism and oxidative stress. Biol Chem. 2015;396(5):483–94. https://doi.org/10.1515/hsz-2014-0281 .
8. Dietz K-J. Thiol-based peroxidases and ascorbate peroxidases: why plants rely on multiple peroxidase systems in the photosynthesizing chloroplast? Mol Cells. 2016;39(1):20–5. https://doi.org/10.14348/molcells.2016.2324.
9. Gütle DD, Roret T, Hecker A, Reski R, Jacquot J-P. Dithiol disulphide exchange in redox regulation of chloroplast enzymes in response to evolutionary and structural constraints. Plant Sci. 2017;255:1–11. https://doi.org/10.1016/j.plantsci.2016.11.003 .
10. Yoshida K, Hisabori T. Two distinct redox cascades cooperatively regulate chloroplast functions and sustain plant viability. Proc Natl Acad Sci U S A. 2016;113(27):E3967–76. https://doi.org/10.1073/pnas.1604101113 .
11. Pérez-Ruiz JM, Cejudo FJ. A proposed reaction mechanism for rice NADPH thioredoxin reductase C, an enzyme with protein disulfide reductase activity. FEBS Lett. 2009;583:1399–402.
12. Lemaire SD, Michelet L, Zaffagnini M, Massot V, Issakidis-Bourguet E. Thioredoxins in chloroplasts. Curr Genet. 2007;51:343–65.
13. Hall M, Mata-Cabana A, Åkerlund H-E, Florencio FJ, Schröder WP, Lindahl M, et al. Thioredoxin targets of the plant chloroplast lumen and their implications for plastid function. Proteomics. 2010;10(5):987–1001. https://doi.org/10.1002/pmic.200900654.
14. Michelet L, Zaffagnini M, Morisse S, Sparla F, Pérez-Pérez ME, Francia F, et al. Redox regulation of the Calvin–Benson cycle: something old, something new. Front Plant Sci. 2013;4:470.
15. Dietz K-J. Peroxiredoxins in plants and cyanobacteria. Antioxid Redox Signal. 2011;15:1129–59.
16. Navrot N, Collin V, Gualberto J, Gelhaye E, Hirasawa M, Rey P, et al. Plant glutathione peroxidases are functional peroxiredoxins distributed in several subcellular compartments and regulated during biotic and abiotic stresses. Plant Physiol. 2006;142(4):1364–79. https://doi.org/10.1104/pp.106.089458 .
17. Pérez-Ruiz JM, Naranjo B, Ojeda V, Guinea M, Cejudo FJ. NTRC-dependent redox balance of 2-Cys peroxiredoxins is needed for optimal function of the photosynthetic apparatus. Proc Natl Acad Sci U S A. 2017;114(45):12069–74. https://doi.org/10.1073/pnas.1706003114 .
18. Vaseghi M-J, Chibani K, Telman W, Liebthal MF, Gerken M, Schnitzer H, et al. The chloroplast 2-cysteine peroxiredoxin functions as thioredoxin oxidase in redox regulation of chloroplast metabolism. eLife. 2018;7:38194.
19. Yoshida K, Hara A, Sugiura K, Fukaya Y, Hisabori T. Thioredoxin-like2/2-Cys peroxiredoxin redox cascade supports oxidative thiol modulation in chloroplasts. Proc Natl Acad Sci U S A. 2018;115:E8296–304.
20. Yoshida K, Uchikoshi E, Hara S, Hisabori T. Thioredoxin-like2/2-Cys peroxiredoxin redox cascade acts as oxidative activator of glucose-6-phosphate dehydrogenase in chloroplasts. Biochem J. 2019;476:1781–90.
21. Schwarzländer M, Dick TP, Meyer AJ, Morgan B. Dissecting redox biology using fluorescent protein sensors. Antioxid Redox Signal. 2016;24(13):680–712. https://doi.org/10.1089/ars.2015.6266 .
22. Schwarzländer M, Fricker MD, MüLler C, Marty L, Brach T, Novak J, et al. Confocal imaging of glutathione redox potential in living plant cells. J Microsc. 2008;231:299–316.
23. Meyer AJ, Brach T, Marty L, Kreye S, Rouhier N, Jacquot J-P, et al. Redox-sensitive GFP in *Arabidopsis thaliana* is a quantitative biosensor for the redox potential of the cellular glutathione redox buffer. Plant J. 2007;52:973–86.
24. Foyer CH, Noctor G. Ascorbate and glutathione: the heart of the redox hub. Plant Physiol. 2011;155:2–18.
25. Rey P, Tarrago L. Physiological roles of plant methionine sulfoxide reductases in redox homeostasis and signaling. Antioxid Basel Switz. 2018;7:114.
26. Gama F, Bréhélin C, Gelhaye E, Meyer Y, Jacquot J-P, Rey P, et al. Functional analysis and expression characteristics of chloroplastic Prx IIE. Physiol Plant. 2008;133(3):599–610. https://doi.org/10.1111/j.1399-3054.2008.01097.x .
27. Fernandes AP, Holmgren A. Glutaredoxins: glutathione-dependent redox enzymes with functions far beyond a simple thioredoxin backup system. Antioxid Redox Signal. 2004;6:63–74.
28. Marty L, Siala W, Schwarzlander M, Fricker MD, Wirtz M, Sweetlove LJ, et al. The NADPH-dependent thioredoxin system constitutes a functional backup for cytosolic glutathione reductase in Arabidopsis. Proc Natl Acad Sci. 2009;106(22):9109–14. https://doi.org/10.1073/pnas.0900206106 .
29. Marty L, Bausewein D, Müller C, Bangash SAK, Moseler A, Schwarzländer M, et al. Arabidopsis glutathione reductase 2 is indispensable in plastids, while mitochondrial glutathione is safeguarded by additional reduction and transport systems. New Phytol. 2019;224(4):1569–84. https://doi.org/10.1111/nph.16086 .
30. Reichheld J-P, Khafif M, Riondet C, Droux M, Bonnard G, Meyer Y. Inactivation of thioredoxin reductases reveals a complex interplay between

thioredoxin and glutathione pathways in Arabidopsis development. Plant Cell. 2007;19(6):1851–65. https://doi.org/10.1105/tpc.107.050849 .
31. Michelet L, Zaffagnini M, Marchand C, Collin V, Decottignies P, Tsan P, et al. Glutathionylation of chloroplast thioredoxin f is a redox signaling mechanism in plants. Proc Natl Acad Sci U S A. 2005;102(45):16478–83. https://doi.org/10.1073/pnas.0507498102 .
32. Rensing SA, Goffinet B, Meyberg R, Wu S-Z, Bezanilla M. The Moss *Physcomitrium* (*Physcomitrella*) *patens*: a model organism for non-seed plants. Plant Cell. 2020;32:1361–76.
33. Müller-Schüssele SJ, Wang R, Gütle DD, Romer J, Rodriguez-Franco M, Scholz M, et al. Chloroplasts require glutathione reductase to balance reactive oxygen species and maintain efficient photosynthesis. Plant J. 2020; 103:1140–54.
34. Woehle C, Dagan T, Landan G, Vardi A, Rosenwasser S. Expansion of the redox-sensitive proteome coincides with the plastid endosymbiosis. Nat Plants. 2017;3:17066.
35. Balsera M, Uberegui E, Schürmann P, Buchanan BB. Evolutionary development of redox regulation in chloroplasts. Antioxid Redox Signal. 2014;21:1327–55.
36. Rensing SA. Great moments in evolution: the conquest of land by plants. Curr Opin Plant Biol. 2018;42:49–54. https://doi.org/10.1016/j.pbi.2018.02.006 .
37. Yasumura Y, Pierik R, Fricker MD, Voesenek LACJ, Harberd NP. Studies of *Physcomitrella patens* reveal that ethylene-mediated submergence responses arose relatively early in land-plant evolution. Plant J Cell Mol Biol. 2012;72:947–59.
38. Alboresi A, Storti M, Morosinotto T. Balancing protection and efficiency in the regulation of photosynthetic electron transport across plant evolution. New Phytol. 2019;221:105–9.
39. Nishiyama T, Sakayama H, de Vries J, Buschmann H, Saint-Marcoux D, Ullrich KK, et al. The Chara Genome: Secondary Complexity and Implications for Plant Terrestrialization. Cell. 2018;174:448–464.e24.
40. Li F-W, Nishiyama T, Waller M, Frangedakis E, Keller J, Li Z, et al. Anthoceros genomes illuminate the origin of land plants and the unique biology of hornworts. Nat Plants. 2020;6(3):259–72. https://doi.org/10.1038/s41477-020-0618-2 .
41. Li F-W, Brouwer P, Carretero-Paulet L, Cheng S, de Vries J, Delaux P-M, et al. Fern genomes elucidate land plant evolution and cyanobacterial symbioses. Nat Plants. 2018;4(7):460–72. https://doi.org/10.1038/s41477-018-0188-8 .
42. Zhang J, Fu X-X, Li R-Q, Zhao X, Liu Y, Li M-H, et al. The hornwort genome and early land plant evolution. Nat Plants. 2020;6(2):107–18. https://doi.org/10.1038/s41477-019-0588-4 .
43. Noctor G, Reichheld J-P, Foyer CH. ROS-related redox regulation and signaling in plants. Semin Cell Dev Biol. 2018;80:3–12. https://doi.org/10.1016/j.semcdb.2017.07.013 .
44. Busch A, Deckena M, Almeida-Trapp M, Kopischke S, Kock C, Schüssler E, et al. MpTCP1 controls cell proliferation and redox processes in *Marchantia polymorpha*. New Phytol. 2019;224(4):1627–41. https://doi.org/10.1111/nph.16132 .
45. Emanuelsson O, Brunak S, von Heijne G, Nielsen H. Locating proteins in the cell using TargetP, SignalP and related tools. Nat Protoc. 2007;2(4):953–71. https://doi.org/10.1038/nprot.2007.131 .
46. Almagro Armenteros JJ, Salvatore M, Emanuelsson O, Winther O, von Heijne G, Elofsson A, et al. Detecting sequence signals in targeting peptides using deep learning. Life Sci Alliance. 2019;2:e201900429.
47. Sperschneider J, Catanzariti A-M, DeBoer K, Petre B, Gardiner DM, Singh KB, et al. Localizer: subcellular localization prediction of both plant and effector proteins in the plant cell. Sci Rep. 2017;7(1):44598. https://doi.org/10.1038/srep44598.
48. Tardif M, Atteia A, Specht M, Cogne G, Rolland N, Brugière S, et al. PredAlgo: a new subcellular localization prediction tool dedicated to green algae. Mol Biol Evol. 2012;29:3625–39.
49. Mueller SJ, Lang D, Hoernstein SNW, Lang EGE, Schuessele C, Schmidt A, et al. Quantitative analysis of the mitochondrial and plastid proteomes of the moss *Physcomitrella patens* reveals protein macrocompartmentation and microcompartmentation. Plant Physiol. 2014;164(4):2081–95. https://doi.org/10.1104/pp.114.235754.
50. Liu Y-J, Han X-M, Ren L-L, Yang H-L, Zeng Q-Y. Functional divergence of the glutathione *S*-transferase supergene family in *Physcomitrella patens* reveals complex patterns of large gene family evolution in land plants. Plant Physiol. 2013;161(2):773–86. https://doi.org/10.1104/pp.112.205815.
51. Dixon DP, Edwards R. Glutathione transferases. Arab Book. 2010;8:e0131.
52. Rouhier N. Vieira dos Santos C, Tarrago L, Rey P. plant methionine sulfoxide reductase a and B multigenic families. Photosynth Res. 2006;89(2-3):247–62. https://doi.org/10.1007/s11120-006-9097-1 .
53. Tarrago L, Laugier E, Zaffagnini M, Marchand C, Le Maréchal P, Rouhier N, et al. Regeneration mechanisms of *Arabidopsis thaliana* methionine sulfoxide reductases B by glutaredoxins and thioredoxins. J Biol Chem. 2009; 284(28):18963–71. https://doi.org/10.1074/jbc.M109.015487 .
54. Pitsch NT, Witsch B, Baier M. Comparison of the chloroplast peroxidase system in the chlorophyte *Chlamydomonas reinhardtii*, the bryophyte *Physcomitrella patens*, the lycophyte *Selaginella moellendorffii* and the seed plant *Arabidopsis thaliana*. BMC Plant Biol. 2010;10(1):133. https://doi.org/10.1186/1471-2229-10-133.
55. Xing S, Lauri A, Zachgo S. Redox regulation and flower development: a novel function for glutaredoxins. Plant Biol Stuttg Ger. 2006;8:547–55.
56. Gutsche N, Holtmannspötter M, Maß L, O'Donoghue M, Busch A, Lauri A, et al. Conserved redox-dependent DNA binding of ROXY glutaredoxins with TGA transcription factors. Plant Direct. 2017;1:e00030.
57. Couturier J, Koh CS, Zaffagnini M, Winger AM, Gualberto JM, Corbier C, et al. Structure-function relationship of the chloroplastic glutaredoxin S12 with an atypical WCSYS active site. J Biol Chem. 2009;284:9299–310.
58. Couturier J, Ströher E, Albetel A-N, Roret T, Muthuramalingam M, Tarrago L, et al. Arabidopsis chloroplastic glutaredoxin C5 as a model to explore molecular determinants for iron-sulfur cluster binding into glutaredoxins. J Biol Chem. 2011;286(31):27515–27. https://doi.org/10.1074/jbc.M111.228726 .
59. Bandyopadhyay S, Gama F, Molina-Navarro MM, Gualberto JM, Claxton R, Naik SG, et al. Chloroplast monothiol glutaredoxins as scaffold proteins for the assembly and delivery of [2Fe-2S] clusters. EMBO J. 2008;27:1122–33.
60. Zaffagnini M, Bedhomme M, Marchand CH, Morisse S, Trost P, Lemaire SD. Redox regulation in photosynthetic organisms: focus on glutathionylation. Antioxid Redox Signal. 2012;16(6):567–86. https://doi.org/10.1089/ars.2011.4255 .
61. Rouhier N. Plant glutaredoxins: pivotal players in redox biology and iron-sulphur centre assembly. New Phytol. 2010;186:365–72.
62. Rey P, Becuwe N, Tourrette S, Rouhier N. Involvement of Arabidopsis glutaredoxin S14 in the maintenance of chlorophyll content. Plant Cell Environ. 2017;40:2319–32.
63. Liu X, Liu S, Feng Y, Liu J-Z, Chen Y, Pham K, et al. Structural insights into the N-terminal GIY–YIG endonuclease activity of Arabidopsis glutaredoxin AtGRXS16 in chloroplasts. Proc Natl Acad Sci. 2013;110(23):9565–70. https://doi.org/10.1073/pnas.1306899110 .
64. Moseler A, Aller I, Wagner S, Nietzel T, Przybyla-Toscano J, Mühlenhoff U, et al. The mitochondrial monothiol glutaredoxin S15 is essential for iron-sulfur protein maturation in *Arabidopsis thaliana*. Proc Natl Acad Sci U S A. 2015;112:13735–40.
65. Trnka D, Engelke AD, Gellert M, Moseler A, Hossain MF, Lindenberg TT, et al. Molecular basis for the distinct functions of redox-active and FeS-transfering glutaredoxins. Nat Commun. 2020;11(1):3445. https://doi.org/10.1038/s41467-020-17323-0 .
66. Couturier J, Przybyla-Toscano J, Roret T, Didierjean C, Rouhier N. The roles of glutaredoxins ligating Fe-S clusters: sensing, transfer or repair functions? Biochim Biophys Acta. 1853;2015:1513–27.
67. Xu L, Carrie C, Law SR, Murcha MW, Whelan J. Acquisition, conservation, and loss of dual-targeted proteins in land plants. Plant Physiol. 2013;161(2):644–62. https://doi.org/10.1104/pp.112.210997 .
68. Petersen J, Teich R, Becker B, Cerff R, Brinkmann H. The GapA/B gene duplication Marks the origin of streptophyta (charophytes and land plants). Mol Biol Evol. 2006;23:1109–18.
69. Zaffagnini M, Bedhomme M, Lemaire SD, Trost P. The emerging roles of protein glutathionylation in chloroplasts. Plant Sci. 2012;185–186:86–96.
70. Chardonnet S, Sakr S, Cassier-Chauvat C, Le Maréchal P, Chauvat F, Lemaire SD, et al. First proteomic study of *S*-glutathionylation in cyanobacteria. J Proteome Res. 2015;14(1):59–71. https://doi.org/10.1021/pr500625a .
71. Ito H, Iwabuchi M, Ogawa K. The sugar-metabolic enzymes aldolase and triose-phosphate isomerase are targets of glutathionylation in *Arabidopsis thaliana*: detection using biotinylated glutathione. Plant Cell Physiol. 2003; 44(7):655–60. https://doi.org/10.1093/pcp/pcg098.
72. Dixon DP, Skipsey M, Grundy NM, Edwards R. Stress-induced protein *S*-glutathionylation in Arabidopsis. Plant Physiol. 2005;138(4):2233–44. https://doi.org/10.1104/pp.104.058917 .

73. Zaffagnini M, Bedhomme M, Groni H, Marchand CH, Puppo C, Gontero B, et al. Glutathionylation in the photosynthetic model organism *Chlamydomonas reinhardtii*: a proteomic survey. Mol Cell Proteomics MCP. 2012;11:M111.014142.
74. Gietler M, Nykiel M, Orzechowski S, Fettke J, Zagdańska B. Proteomic analysis of *S*-nitrosylated and *S*-glutathionylated proteins in wheat seedlings with different dehydration tolerances. Plant Physiol Biochem PPB. 2016;108:507–18. https://doi.org/10.1016/j.plaphy.2016.08.017 .
75. Michelet L, Zaffagnini M, Vanacker H, Le Maréchal P, Marchand C, Schroda M, et al. In vivo targets of *S*-thiolation in *Chlamydomonas reinhardtii*. J Biol Chem. 2008;283(31):21571–8. https://doi.org/10.1074/jbc.M802331200 .
76. Chan KX, Mabbitt PD, Phua SY, Mueller JW, Nisar N, Gigolashvili T, et al. Sensing and signaling of oxidative stress in chloroplasts by inactivation of the SAL1 phosphoadenosine phosphatase. Proc Natl Acad Sci. 2016;113:E4567–76.
77. Gurrieri L, Distefano L, Pirone C, Horrer D, Seung D, Zaffagnini M, et al. The thioredoxin-regulated α-amylase 3 of *Arabidopsis thaliana* is a target of *S*-glutathionylation. Front Plant Sci. 2019;10:993.
78. Storm AR, Kohler MR, Berndsen CE, Monroe JD. Glutathionylation inhibits the catalytic activity of Arabidopsis β-amylase3 but not that of paralog β-amylase1. Biochemistry. 2018;57:711–21.
79. Liu X, Chai J, Ou X, Li M, Liu Z. Structural insights into substrate selectivity, catalytic mechanism, and redox regulation of rice photosystem II core phosphatase. Mol Plant. 2019;12:86–98.
80. López-Castillo LM, Jiménez-Sandoval P, Baruch-Torres N, Trasviña-Arenas CH, Díaz-Quezada C, Lara-González S, et al. Structural basis for redox regulation of cytoplasmic and chloroplastic triosephosphate isomerases from *Arabidopsis thaliana*. Front Plant Sci. 2016;7:1817.
81. Morisse S, Michelet L, Bedhomme M, Marchand CH, Calvaresi M, Trost P, et al. Thioredoxin-dependent redox regulation of chloroplastic phosphoglycerate kinase from *Chlamydomonas reinhardtii*. J Biol Chem. 2014;289(43):30012–24. https://doi.org/10.1074/jbc.M114.597997 .
82. Marri L, Thieulin-Pardo G, Lebrun R, Puppo R, Zaffagnini M, Trost P, et al. CP12-mediated protection of Calvin-Benson cycle enzymes from oxidative stress. Biochimie. 2014;97:228–37.
83. Datta R, Kumar D, Sultana A, Hazra S, Bhattacharyya D, Chattopadhyay S. Glutathione regulates 1-aminocyclopropane-1-carboxylate synthase transcription via WRKY33 and 1-aminocyclopropane-1-carboxylate oxidase by modulating messenger RNA stability to induce ethylene synthesis during stress. Plant Physiol. 2015;169:2963–81.
84. Noguera-Mazon V, Lemoine J, Walker O, Rouhier N, Salvador A, Jacquot J-P, et al. Glutathionylation induces the dissociation of 1-Cys D-peroxiredoxin non-covalent homodimer. J Biol Chem. 2006;281(42):31736–42. https://doi.org/10.1016/S0021-9258(19)84088-7 .
85. Søgaard M, Andersen JS, Roepstorff P, Svensson B. Electrospray mass spectrometry characterization of post-translational modifications of barley alpha-amylase 1 produced in yeast. Biotechnol Nat Publ Co. 1993;11:1162–5.
86. Castella C, Mirtziou I, Seassau A, Boscari A, Montrichard F, Papadopoulou K, et al. Post-translational modifications of *Medicago truncatula* glutathione peroxidase 1 induced by nitric oxide. Nitric Oxide Biol Chem. 2017;68:125–36. https://doi.org/10.1016/j.niox.2017.02.004 .
87. Bedhomme M, Adamo M, Marchand CH, Couturier J, Rouhier N, Lemaire SD, et al. Glutathionylation of cytosolic glyceraldehyde-3-phosphate dehydrogenase from the model plant *Arabidopsis thaliana* is reversed by both glutaredoxins and thioredoxins in vitro. Biochem J. 2012;445(3):337–47. https://doi.org/10.1042/BJ20120505 .
88. Palmieri MC, Lindermayr C, Bauwe H, Steinhauser C, Durner J. Regulation of plant glycine decarboxylase by s-nitrosylation and glutathionylation. Plant Physiol. 2010;152(3):1514–28. https://doi.org/10.1104/pp.109.152579 .
89. Leferink NGH, van Duijn E, Barendregt A, Heck AJR, van Berkel WJH. Galactonolactone dehydrogenase requires a redox-sensitive thiol for optimal production of vitamin C. Plant Physiol. 2009;150:596–605.
90. Ma T, Yoo M-J, Zhang T, Liu L, Koh J, Song W-Y, et al. Characterization of thiol-based redox modifications of *Brassica napus* SNF1-related protein kinase 2.6-2C. FEBS Open Bio. 2018;8:628–45.
91. Iglesias MJ, Terrile MC, Correa-Aragunde N, Colman SL, Izquierdo-Álvarez A, Fiol DF, et al. Regulation of SCFTIR1/AFBs E3 ligase assembly by *S*-nitrosylation of Arabidopsis SKP1-like1 impacts on auxin signaling. Redox Biol. 2018;18:200–10. https://doi.org/10.1016/j.redox.2018.07.003 .
92. Calderón A, Lázaro-Payo A, Iglesias-Baena I, Camejo D, Lázaro JJ, Sevilla F, et al. Glutathionylation of pea chloroplast 2-Cys Prx and mitochondrial Prx IIF affects their structure and peroxidase activity and sulfiredoxin deglutathionylates only the 2-Cys Prx. Front Plant Sci. 2017;8:118.
93. Zaffagnini M, Michelet L, Marchand C, Sparla F, Decottignies P, Le Maréchal P, et al. The thioredoxin-independent isoform of chloroplastic glyceraldehyde-3-phosphate dehydrogenase is selectively regulated by glutathionylation. FEBS J. 2007;274:212–26.
94. Tanz SK, Castleden I, Hooper CM, Vacher M, Small I, Millar HA. SUBA3: a database for integrating experimentation and prediction to define the SUBcellular location of proteins in Arabidopsis. Nucleic Acids Res. 2013;41(Database issue):D1185–91.
95. Cairns NG, Pasternak M, Wachter A, Cobbett CS, Meyer AJ. Maturation of Arabidopsis seeds is dependent on glutathione biosynthesis within the embryo. Plant Physiol. 2006;141:446–55.
96. Pasternak M, Lim B, Wirtz M, Hell R, Cobbett CS, Meyer AJ. Restricting glutathione biosynthesis to the cytosol is sufficient for normal plant development. Plant J Cell Mol Biol. 2008;53:999–1012.
97. Fuss J, Liegmann O, Krause K, Rensing SA. Green targeting predictor and ambiguous targeting predictor 2: the pitfalls of plant protein targeting prediction and of transient protein expression in heterologous systems. New Phytol. 2013;200(4):1022–33. https://doi.org/10.1111/nph.12433 .
98. Noshi M, Hatanaka R, Tanabe N, Terai Y, Maruta T, Shigeoka S. Redox regulation of ascorbate and glutathione by a chloroplastic dehydroascorbate reductase is required for high-light stress tolerance in Arabidopsis. Biosci Biotechnol Biochem. 2016;80(5):870–7. https://doi.org/10.1080/09168451.2015.1135042 .
99. Attacha S, Solbach D, Bela K, Moseler A, Wagner S, Schwarzländer M, et al. Glutathione peroxidase-like enzymes cover five distinct cell compartments and membrane surfaces in *Arabidopsis thaliana*: subcellular localization of GPXLs in Arabidopsis. Plant Cell Environ. 2017;40:1281–95.
100. Romero-Puertas MC, Laxa M, Mattè A, Zaninotto F, Finkemeier I, Jones AME, et al. *S*-nitrosylation of peroxiredoxin II E promotes peroxynitrite-mediated tyrosine nitration. Plant Cell. 2007;19:4120–30.
101. Cheng N-H, Liu J-Z, Brock A, Nelson RS, Hirschi KD. AtGRXcp, an Arabidopsis chloroplastic glutaredoxin, is critical for protection against protein oxidative damage. J Biol Chem. 2006;281:26280–8.
102. Guo Y, Huang C, Xie Y, Song F, Zhou X. A tomato glutaredoxin gene SlGRX1 regulates plant responses to oxidative, drought and salt stresses. Planta. 2010;232:1499–509.
103. Zaffagnini M, Michelet L, Massot V, Trost P, Lemaire SD. Biochemical characterization of glutaredoxins from *Chlamydomonas reinhardtii* reveals the unique properties of a chloroplastic CGFS-type glutaredoxin. J Biol Chem. 2008;283(14):8868–76. https://doi.org/10.1074/jbc.M709567200.
104. The UniProt Consortium. UniProt: a worldwide hub of protein knowledge. Nucleic Acids Res. 2019;47:D506–15.
105. Akter S, Huang J, Waszczak C, Jacques S, Gevaert K, Van Breusegem F, et al. Cysteines under ROS attack in plants: a proteomics view. J Exp Bot. 2015;66:2935–44.
106. Zagorchev L, Seal C, Kranner I, Odjakova M. A central role for thiols in plant tolerance to abiotic stress. Int J Mol Sci. 2013;14(4):7405–32. https://doi.org/10.3390/ijms14047405 .
107. Gallogly MM, Starke DW, Mieyal JJ. Mechanistic and kinetic details of catalysis of thiol-disulfide exchange by glutaredoxins and potential mechanisms of regulation. Antioxid Redox Signal. 2009;11:1059–81.
108. Gilbert HF. Thiol/disulfide exchange equilibria and disulfide bond stability. Methods Enzymol. 1995;251:8–28.
109. Michelet L, Zaffagnini M, Massot V, Keryer E, Vanacker H, Miginiac-Maslow M, et al. Thioredoxins, glutaredoxins, and glutathionylation: new crosstalks to explore. Photosynth Res. 2006;89:225–45.
110. Lindermayr C. Crosstalk between reactive oxygen species and nitric oxide in plants: key role of *S*-nitrosoglutathione reductase. Free Radic Biol Med. 2018;122:110–5. https://doi.org/10.1016/j.freeradbiomed.2017.11.027 .
111. Giustarini D, Milzani A, Aldini G, Carini M, Rossi R, Dalle-Donne I. *S*-nitrosation versus *S*-glutathionylation of protein sulfhydryl groups by *S*-nitrosoglutathione. Antioxid Redox Signal. 2005;7(7-8):930–9. https://doi.org/10.1089/ars.2005.7.930.
112. Niazi AK, Bariat L, Riondet C, Carapito C, Mhamdi A, Noctor G, et al. Cytosolic Isocitrate dehydrogenase from *Arabidopsis thaliana* is regulated by glutathionylation. Antioxidants. 2019;8(1):16. https://doi.org/10.3390/antiox8010016.

113. Zaffagnini M, De Mia M, Morisse S, Di Giacinto N, Marchand CH, Maes A, et al. Protein *S*-nitrosylation in photosynthetic organisms: a comprehensive overview with future perspectives. Biochim Biophys Acta BBA - Proteins Proteomics. 1864;2016:952–66.
114. De Smet B, Willems P, Fernandez-Fernandez AD, Alseekh S, Fernie AR, Messens J, et al. *In vivo* detection of protein cysteine sulfenylation in plastids. Plant J Cell Mol Biol. 2019;97:765–78.
115. Huang J, Willems P, Wei B, Tian C, Ferreira RB, Bodra N, et al. Mining for protein *S*-sulfenylation in Arabidopsis uncovers redox-sensitive sites. Proc Natl Acad Sci. 2019;116(42):21256–61. https://doi.org/10.1073/pnas.1906768116 .
116. Akter S, Huang J, Bodra N, De Smet B, Wahni K, Rombaut D, et al. DYn-2 based identification of Arabidopsis sulfenomes. Mol Cell Proteomics. 2015;14(5):1183–200. https://doi.org/10.1074/mcp.M114.046896.
117. Zaffagnini M, Marchand CH, Malferrari M, Murail S, Bonacchi S, Genovese D, et al. Glutathionylation primes soluble glyceraldehyde-3-phosphate dehydrogenase for late collapse into insoluble aggregates. Proc Natl Acad Sci. 2019;116(51):26057–65. https://doi.org/10.1073/pnas.1914484116 .
118. Seung D, Thalmann M, Sparla F, Abou Hachem M, Lee SK, Issakidis-Bourguet E, et al. *Arabidopsis thaliana* AMY3 is a unique redox-regulated chloroplastic α-amylase. J Biol Chem. 2013;288:33620–33.
119. Rosa-Téllez S, Anoman AD, Flores-Tornero M, Toujani W, Alseek S, Fernie AR, et al. Phosphoglycerate kinases are co-regulated to adjust metabolism and to optimize growth. Plant Physiol. 2018;176:1182–98.
120. Chatterjee A, Abeydeera ND, Bale S, Pai P-J, Dorrestein PC, Russell DH, et al. *Saccharomyces cerevisiae* THI4p is a suicide thiamine thiazole synthase. Nature. 2011;478:542–6.
121. Godoi PHC, Galhardo RS, Luche DD, Van Sluys M-A, Menck CFM, Oliva G. Structure of the thiazole biosynthetic enzyme THI1 from *Arabidopsis thaliana*. J Biol Chem. 2006;281(41):30957–66. https://doi.org/10.1074/jbc.M604469200 .
122. Thalmann M, Pazmino D, Seung D, Horrer D, Nigro A, Meier T, et al. Regulation of leaf starch degradation by abscisic acid is important for osmotic stress tolerance in plants. Plant Cell. 2016;28(8):1860–78. https://doi.org/10.1105/tpc.16.00143 .
123. Zhao C, Wang Y, Chan KX, Marchant DB, Franks PJ, Randall D, et al. Evolution of chloroplast retrograde signaling facilitates green plant adaptation to land. Proc Natl Acad Sci U S A. 2019;116(11):5015–20. https://doi.org/10.1073/pnas.1812092116 .
124. Hanke GT, Kimata-Ariga Y, Taniguchi I, Hase T. A post genomic characterization of Arabidopsis ferredoxins. Plant Physiol. 2004;134(1):255–64. https://doi.org/10.1104/pp.103.032755 .
125. Goodstein DM, Shu S, Howson R, Neupane R, Hayes RD, Fazo J, et al. Phytozome: a comparative platform for green plant genomics. Nucleic Acids Res. 2012;40(Database issue):D1178–86. https://doi.org/10.1093/nar/gkr944 .
126. Waterhouse AM, Procter JB, Martin DMA, Clamp M, Barton GJ. Jalview version 2--a multiple sequence alignment editor and analysis workbench. Bioinformatics. 2009;25(9):1189–91. https://doi.org/10.1093/bioinformatics/btp033 .
127. Ronquist F, Huelsenbeck JP. MrBayes 3: Bayesian phylogenetic inference under mixed models. Bioinformatics. 2003;19(12):1572–4. https://doi.org/10.1093/bioinformatics/btg180 .
128. Trifinopoulos J, Nguyen L-T, von Haeseler A, Minh BQ. W-IQ-TREE: a fast online phylogenetic tool for maximum likelihood analysis. Nucleic Acids Res. 2016;44(W1):W232–5. https://doi.org/10.1093/nar/gkw256.

Publisher's Note

Springer Nature remains neutral with regard to jurisdictional claims in published maps and institutional affiliations.

Ready to submit your research? Choose BMC and benefit from:

- fast, convenient online submission
- thorough peer review by experienced researchers in your field
- rapid publication on acceptance
- support for research data, including large and complex data types
- gold Open Access which fosters wider collaboration and increased citations
- maximum visibility for your research: over 100M website views per year

At BMC, research is always in progress.

Learn more biomedcentral.com/submissions

4. Biochemical insights in the mechanism of protein S-glutathionylation *in vivo* and *in vitro*

4.1. Results

4.1.1 Protein *S*-glutathionylation and its dependency on glutathione ratio or redox potential

The redox sensor roGFP2 equilibrates with the glutathione redox couple (2GSH/GSSG) and allows a direct read-out of the redox potential of glutathione (E_{GSH}) (Meyer *et al.* 2007; Gutscher *et al.* 2008; Schwarzländer *et al.* 2008; Aller *et al.* 2013) (Figure 6). The assumption of a total glutathione concentration of for example 2-3 mM *in vivo* (Fricker *et al.* 2000), allows the determination of GSH and GSSG concentrations through the Nernst Equation. However, for *in vitro* experiments, concentrations of GSH and GSSG with an exact known total glutathione concentration can be calculated precisely to generate a desired redox potential following the Nernst Equation:

$$E' = E'^{0}_{(GSH)} - \frac{2.303RT}{zF} log_{10} \frac{[GSH]^2}{[GSSG]}$$

with R = 8.315 J K^{-1} mol^{-1}, T =298.15 K, z =2, F = 96.485 C mol^{-1} and E'^{0}=-240 mV at pH 7. Several concentrations of GSH and GSSG can result in the same redox potential (further described in Bohle *et al.* 2023). Calculated GSH:GSSG ratios and absolute glutathione concentrations are displayed in Table 16. To simplify, the relation of absolute concentration of GSH or GSSG [c] will be called hereinafter, GSH:GSSG ratio. When discussing redox potential, I refer to the Nernst equation and represent it (GSH^2/GSSG) as E_{GSH}. Based on the knowledge that roGFP2 is oxidized via a GRX-catalyzed *S*-glutathionylation step (Figure 6), the following theory was established in collaboration with Paolo Trost, Mirko Zaffagnini and Jacopo Rossi (University of Bologna, Italy) to investigate the dependency of *S*-glutathionylation on GSH:GSSG ratio or E_{GSH}. The glutathionylation of the thiol group of GRXC1 (Figure 6, k_{-4}) and the transfer of the glutathionylated group to roGFP2 (Figure 6, k_{-3}) may dependent on the GSH:GSSG ratio, influencing the velocity of the reaction. The second reaction of releasing the glutathionylation group of roGFP2 by disulfide formation (Figure 6, k_{-1}) might rather depend on the E_{GSH} (see

Figure 6). To assess if the ratio of GSH:GSSG is the key factor for glutathionylation of GRXC1 and roGFP2, while the endpoint of roGFP2 oxidation is dependent on E_{GSH}, roGPF2 oxidation assays were performed under constant E_{GSH} while varying GSH:GSSG ratios.

Table 16: Glutathione redox potentials and ratios

E_{GSH}	Ratio (GSH/GSSG)	final [GSH]	final [GSSG]	Total [GSH+GSSG]
-232 mV	5.25	42 mM	8 mM	50 mM
	10.5	20 mM	1.9 mM	21.9 mM
	72.5	2.9 mM	0.04 mM	2.94 mM
-280 mV	158.1	63.24 mM	0.4 mM	63.64 mM
	500.6	19.97 mM	0.0399 mM	20.0099 mM
	1500.7	6.663 mM	0.00444 mM	6.667 mM
	2000	5 mM	0.0025 mM	5.0025 mN
-220 mV	30	3 mM	0.1 mM	3.1 mM
	3000	0.03 mM	0.00001 mM	0.03001 mM
	20	4.5 mM	0.225 mM	4.725 mM
	134	0.67 mM	0.005 mM	0.675 mM

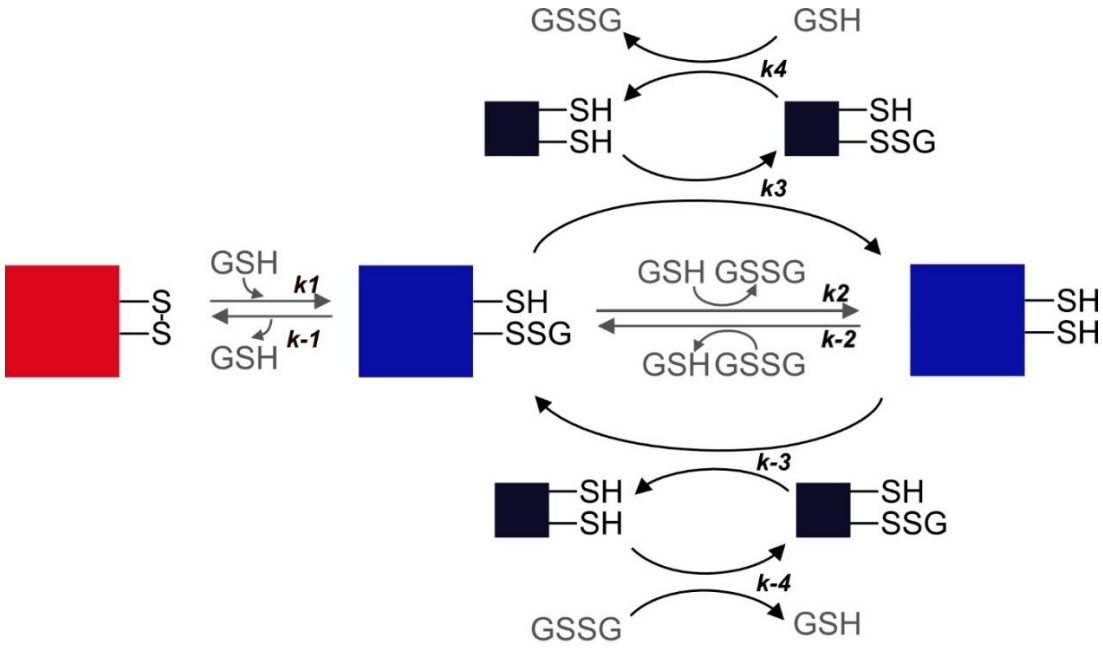

Figure 6: roGFP2 oxidation/reduction via glutathionylation catalysed by GRX

Schematic overview of roGFP2 oxidation via glutathionylation catalysed by GRX and glutathione (GSH/GSSG). Oxidized roGFP2 = red, reduced or glutathionylated roGFP2= blue, GRX = black. Modified from Prof. Andreas Meyer (University of Bonn).

4.1.1.1 At constant E_{GSH}, roGFP2 oxidation kinetics depend on GSH:GSSG

To obtain further insights in the molecular mechanism and dependency of protein *S*-glutathionylation on the E_{GSH} or molar ratio of GSH to GSSG, we calculated three GSH:GSSG ratios of 5.25, 10.5 and 72.5 resulting in a similar E_{GSH} of -232 mV and a final sensor oxidation of 98% at pH 7.4 (Table 16, Schwarzländer *et al.* 2008; Aller *et al.* 2013). The influence of the molar ratio of the GSH:GSSG redox pair on roGFP2 oxidation was tested by performing roGFP2 oxidation assays at a constant redox potential (mV) and varying the molar ratio of GSH to GSSG (Figure 7). In three tested ratios (5.25, 72.5, 10.5), sensor oxidation reached >90% after 70 min of equilibration. Differences in the GSH:GSSG ratio had an impact on the velocity of roGFP2 oxidation, nevertheless the endpoint of oxidation was the same for the three ratios. For better comparison the increase in sensor oxidation in % per min was calculated within the first 10 minutes of the assay. A sensor oxidation of 2.59% min^{-1} was obtained for the lowest GSH:GSSG ratio with 5.25, 4.85% min^{-1} for 10.5 and 7.29% min^{-1} was obtained for a 72.5 ratio, showing the fastest oxidation kinetic for the highest GSH:GSSG ratio in the presence of *At*GRXC1 (Figure 7 A). Inverse behavior of roGFP2 oxidation kinetics was observed in the absence of GRX ('-*At*GRXC1': 5.25=1.74% min^{-1}; 10.5 = 1.63% min^{-1}; 72.5= 0.76% min^{-1}). However, all tested ratios led to >90% of sensor oxidation after 180 min (5.25, 10.5) and 900 min (72.5) showing no significant difference in the endpoint of sensor oxidation (Figure 7 B). The initial oxidation degree of roGFP2 varied between the ratios with 5.25 revealing a sensor oxidation of ~40%, while 10.5 started with ~25% and 72.5 with close to 0% of sensor oxidation. Variances in the sensor oxidation at the start of the assay were due to a time gap between the addition of *At*GRXC1 or buffer and fluorescence measurement in the plate reader.

I hypothesized that in the presence of GRX, high amounts of reduced glutathione in the lower ratio (5.25) may shift the reaction towards reduction of roGFP2. To asses if the backreaction of glutathionylated *At*GRXC1 with GSH is limiting the reaction (k_4, Figure 6), I repeated the oxidation assay with *At*GRXS15 (Figure 7 C). The monothiol *At*GRXS15 is able to oxidize but unable to efficiently reduce roGFP2. Using *At*GRXS15 should minimize the GRX catalyzed reaction of glutathionylated roGFP2 to reduced roGFP2 (Figure 6, k_3; Moseler *et al.* 2015; Begas *et al.* 2017). As seen for *At*GRXC1, roGFP2 showed similar oxidation kinetics in the presence of *At*GRXS15 (Figure 7 C) with the highest ratio (72.5) resulting in the fastest roGFP2 oxidation. Due to faster roGFP2 oxidation, slopes were calculated within 5 min after *At*GRXS15 (6 µM) addition and resulted in 8.93% of roGFP2 oxidation per min for 5.25, 9.15% min^{-1} for

10.5 and 14.32% min^{-1} for 72.5. 40 µM GSSG was used as an additional positive control for successful sensor oxidation. To verify for GRX activity, roGFP2 oxidation was measured in the absence of *At*GRXS15 (Figure 7 C). Without *At*GRXS15 slopes were supporting the data obtained without *At*GRXC1 (see Figure 7A; *At*GRXS15: 5.25 = 2.46% min^{-1}; 10.5 = 1.75% min^{-1}; 72.5 = 0.29% min^{-1}).

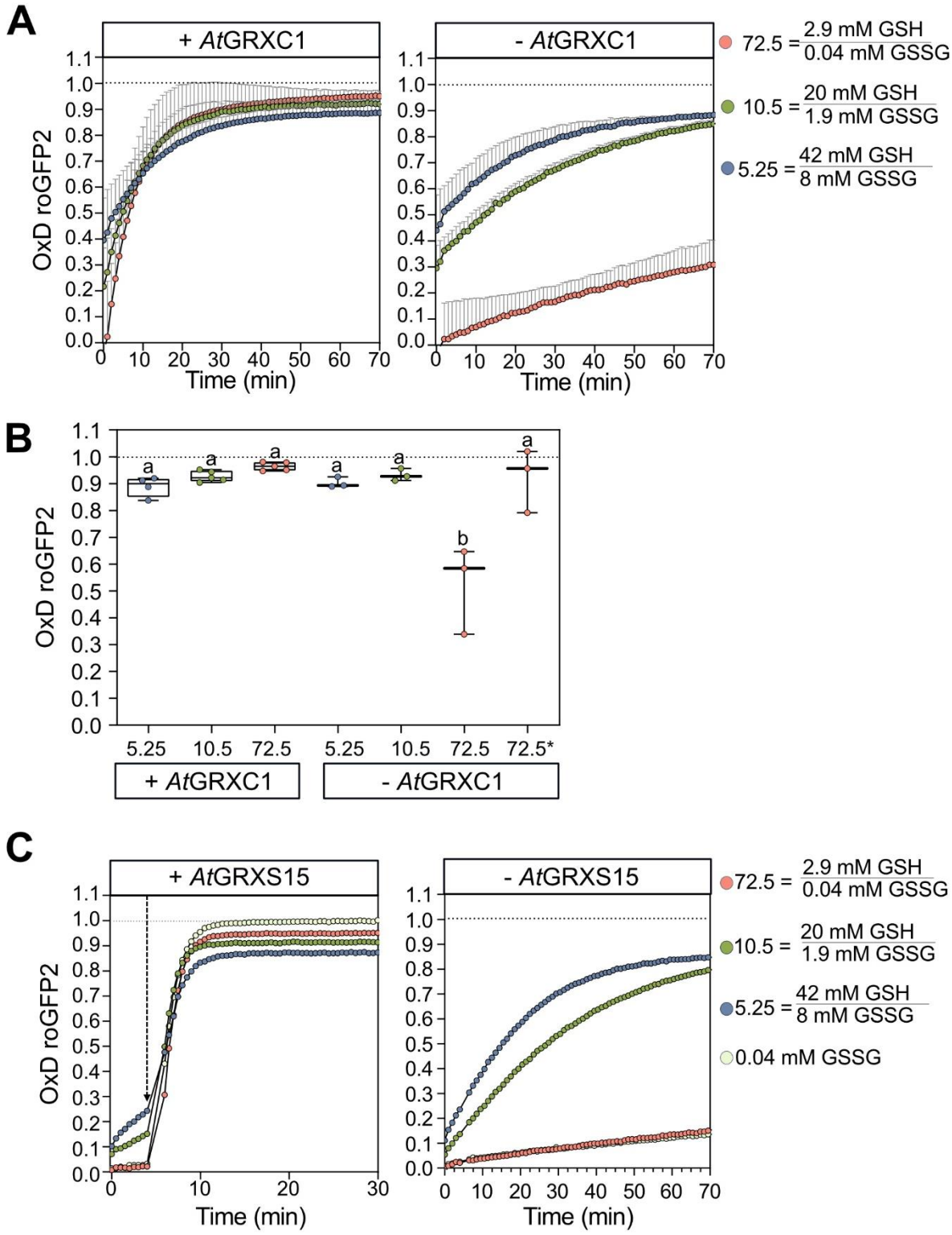

Figure 7: roGFP2 oxidation kinetics at -232 mV in different GSH:GSSG ratios

A Degree of roGFP2 (1 µM) oxidation at -232 mV pH 7.4 in GSH:GSSG ratios of 5.25, 10.5 and 72.5 in the presence (+) and absence (-) of 1 µM AtGRXC1. Full oxidation (dotted line) and reduction of roGFP2 was determined by addition of 10 mM H_2O_2 and 10 mM of DTT in control wells (n = 4-5). Oxidation degree of roGFP2 was calculated as described in Schwarzländer et al. 2008. GRXC1 was added prior to fluorescence detection in the plate reader **B** Degree of roGFP2

oxidation after 180 min of oxidation assay (data of assay shown in **A).** 72.5***** shows the endpoint of roGFP2 oxidation after 900 min of assay time. Two-way ANOVA ($p<0.0001$) with Tukey's multiple comparison test was conducted to test for significant differences. Differing lowercase letters depict significant differences. **C** Degree of roGFP2 (1 µM) oxidation at -232 mV pH 7.4 in GSH:GSSG ratios of 5.25, 10.5 and 72.5 in the presence (+) and absence (-) of 6 µM AtGRXS15 added 4 min after measurement start. 40 µM GSSG was used as oxidation control.

4.1.1.2 Degree of protein *S*-glutathionylation within various GSH:GSSG ratios at constant E_{GSH}: making use of the single cysteine mutant roGFP2-C204S

After glutathionylation of roGFP2, the nucleophilic attack by the second cysteine of roGFP2 on the glutathionylated group initiates the release of a GSH molecule and formation of an intramolecular disulfide bond (Meyer & Dick 2010; Trnka *et al.* 2020). In a currently available mutant of roGFP2 lacking the cysteine required to release the glutathionylation via disulfide formation (roGFP2-C204S, provided by Tobias Dick), the glutathionylation of roGFP2 is trapped resulting in a stable glutathionylation of the second active site cysteine at position 147 (Trnka *et al.* 2020). During the reaction of roGFP2-C204S with glutathione one GSSG molecule is consumed and one of the two GS-moieties is released as GSH. The other GS-moiety stays bound to the roGFP2-C204S since no internal disulfide formation as seen for roGFP2 releases the glutathionylation. Dimerization of roGFP2-C204S upon glutathionylation can rather be excluded under the tested conditions (examples in Figure 8, Figure 9), however an intermolecular disulfide formation between two roGFP2-C204S cannot be completely excluded. Unlike the dithiol roGFP2, whose oxidation is dependent on E_{GSH}, the monothiol roGFP2's oxidation is more likely to be dependent on the GSH:GSSG ratio. Monothiol roGFP2-C204S in its reduced and oxidized form shows no difference in fluorescence after excitation with 405 nm or 488 nm (Trnka *et al.* 2020). We therefore developed a redox state dependent read-out of roGFP2-C204S via maleimide (MPEG-Mal) labelling of the non-glutathionylated cysteine, resulting in a 5 kDa size difference per labeled thiol.

Additional to staining protein gels with Coomassie (PageBlue™), we visualized and localized roGFP2 in a non-reducing SDS-PAGE under UV-light exposure. To first asses for specific roGFP2 signal, reduced (DTT), oxidized (H_2O_2) and untreated roGFP2-C204S were loaded on a non-reducing SDS-PAGE and a first read-out under UV-light was performed (Figure 8 A) before staining with PageBlue™ (Figure 8 B).

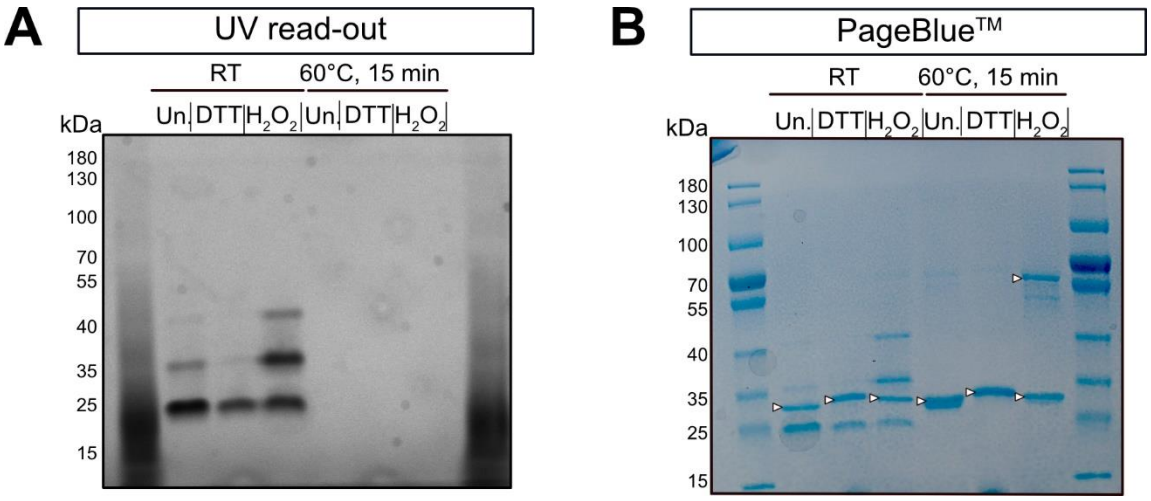

Figure 8: roGFP2-C204S SDS-PAGE read-out via UV-light

Non-reducing SDS-PAGE of roGFP2-C204S (4.8 µg/lane) non-denatured (RT, room temperature 22°C-25°C) and denatured (60°C, 15 min) after treatment with 10 mM DTT or 10 mM H_2O_2 or untreated (Un., isolated from bacteria). All samples were labeled with 10 mM NEM after DTT/H_2O_2 treatment. **A** SDS-PAGE imaged under UV-light (ChemoStar ECL, nm) **B** SDS-PAGE shown in A stained with PageBlue™. Denaturated bands marked with a white arrow and are not visible under UV light (A).

Only non-denatured roGFP2-C204S (band sizes ~25 kDa, 35 kDa and 40 kDa) was visible in the UV-light shown by lack of bands in samples treated with 60°C for 15 min before gel loading (Figure 8 A). roGFP2-C204S stained with Coomassie showed a partially overlapping band pattern as seen in Figure 8 A with detectable roGFP2-C204S bands at ~30 kDa in denaturated samples treated with 60 °C prior to loading (Figure 8 B).

Oxidation kinetics and endpoints of roGFP2 under varying ratios and constant E_{GSH} has been already assessed in Figure 7. To gain deeper insights on the *S*-glutathionylation behavior of a monothiol target protein, such as roGFP2-C204S, the oxidation assay was performed as seen in Figure 7. Samples were subsequently labeled with NEM to block free thiols or labeled with MPEG-Mal to induce a 5 kDa size shift per labeled cysteine. Samples were loaded onto the SDS-PAGE and read-out via UV light. We performed MPEG-Mal size-shift assay to identify differences between reduced and *S*-glutathionylated roGFP2-C204S fractions. Thiol groups labelled with MPEG-Mal indicate previously available, free thiol groups. The fractions of non-shifted roGFP2-C204S therefor response to potentially glutathionylated roGFP2.

We performed the experiments concurrently with roGFP2 to validate the working assay using the fluorescence read-out of roGFP2. roGFP2 revealing a typical band pattern with the reduced protein (+ DTT) showing a slower (apparent Mw of 35 kDa) and the oxidized protein (+ H_2O_2) showing a higher mobility (apparent Mw of ~28 kDa) (Figure 9). For reduced roGFP2

treated with MPEG-Mal we obtained a band shift of ~10 kDa (from ~35 kDa to~45 kDa) (Figure 9). No size shift was observed in the ratios of 10.5 and 72.5 after MPEG-Mal labeling, indicating complete oxidation of roGFP2 (no reduced thiol groups available for labelling). For NEM labelled roGFP2-C204S we observed two bands occurring at ~25 kDa and ~37 kDa in each of the treatments (DTT, H_2O_2, GSSG, 10.5, 72.5) with the intensity of the ~37 kDa increasing in the H_2O_2 treated sample (Figure 8, Figure 9). For MPEG-Mal treated reduced roGFP2-C204S (DTT) we obtained two to three bands at ~25 kDa, ~35 kDa and ~37 kDa.

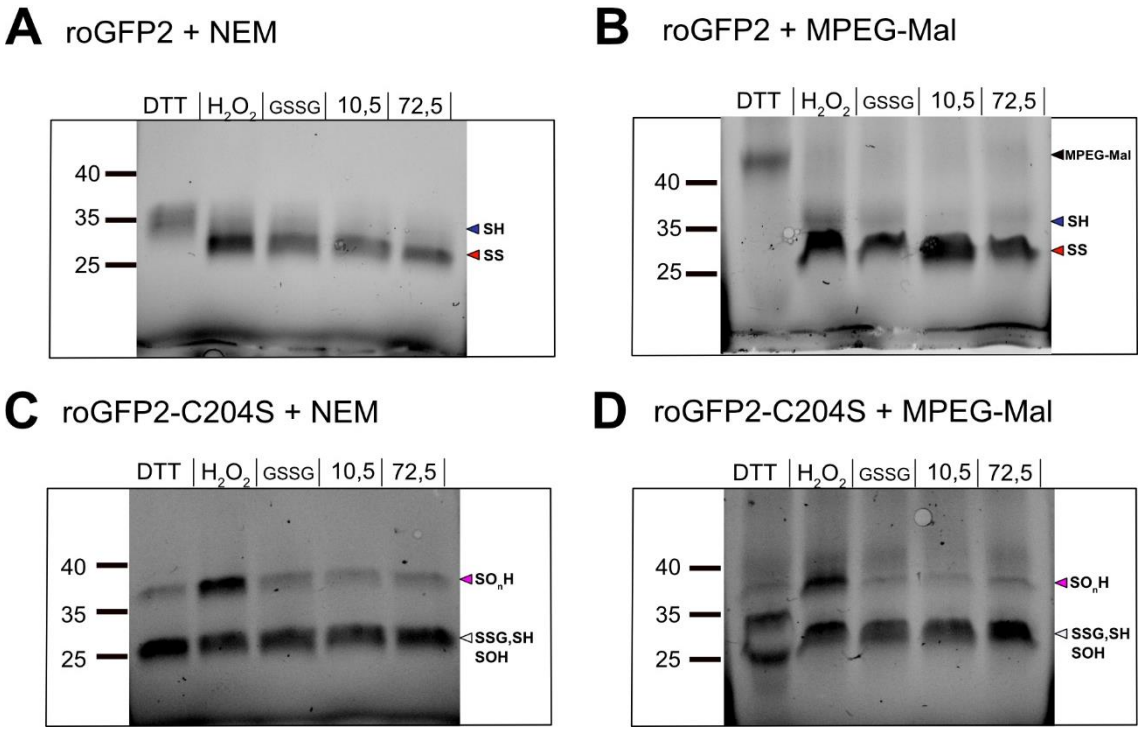

Figure 9 SDS-PAGE of roGFP2 and roGFP2-C204S after oxidation assay with 10.5 and 72.5 GSH:GSSG ratios at -232 mV

SDS-PAGE loaded with 2.5 µM (=1.4 µg) roGFP2 (**A**,**B**) and roGFP2-C204S (**C**,**D**), treated with DTT (1 mM), H_2O_2 (10 mM), 40 µM GSSG or ratios of GSH:GSSG (10.5/72.5) incubated with either 50 mM NEM (**A**,**C**) or 5 mM MPEG (**B**,**D**). In the samples 40 µM GSSG, 10.5 and 72.5 (GSH:GSSG) 1 µM of *At*GRXC1 was added. **A** roGFP2 samples were incubated with NEM to block free thiols. **B** roGFP2 incubated with MPEG-Mal to label not glutathionylated/oxidized cysteines **C** roGFP2-C204S treated with NEM to block not glutathionylated, free thiols. **D** roGFP2-C204S incubated with MPEG-Mal to label not glutathionylated/oxidized cysteines. SDS-PAGE was imaged under UV-light exposure. Bands corresponding to the potential thiol redox state are marked at the site of the gel (SH = reduced thiol, SS = intramolecular disulfide between Cys 147 and Cys 204, SSG = glutathionylated thiol, SOH/SO_nH = oxidized thiol (sulfenic, sulfinic, sulfonic acid) thiol)

However, the app. ~35 kDa band disappeared in later experiments (Figure 11, Figure 12, Figure 13), which were performed with a new roGFP2-C204S purification. The app.~37 kDa band showed increased intensity in the H_2O_2 sample. To link the thiol modifications in the various treatments to the gel running behavior, mass spectrometry was performed. Gel pieces of the

control treatments of roGFP2-C204S were excised from the gel and dispatched to the laboratory of Michael Schroda (Technical University Kaiserslautern, Germany) (Figure 10 A). A tryptic digestion of the proteins and desalting of the samples was done and MS/MS was performed as described in Spaniol *et al.* 2022. The analysis was performed and evaluated by Dr. Frederik Sommer (Prof. M. Schroda, Technical University Kaiserslautern, Germany) using the MaxQuant software (1.6.0.1., Cox & Mann 2008) or ProteinPilot V5 (ABSciex, Darmstadt). Extracted ion chromatograms (XIC) of roGFP2-C204S peptide sequences (LEYNYNCHNVYIMADK and LEYNYNCHNVYIMADKQK) with respective modifications were divided over the XIC of a reference sequence of roGFP2-C204S not containing any cysteine residues (514: GIDFKEDGNILGHK) in the same run of MS/MS analysis (Figure 10 B). The thiol modification detected with the highest XIC intensity ratio (I/I_{514}) in each run was set as maximum. The other modifications were normalized over its XIC (I_{max}). Highest abundance of NEM bound roGFP2-C204S was obtained in the DTT-reduced sample (Figure 10; 'Run 1'), but also observed for roGFP2-C204S treated with 40 µM of GSSG in the presence of *At*GRXC1 (Figure 10; Run 3, GSSG+GRX). The highest abundance of glutathionylated roGFP2-C204S was detected in the same sample (Figure 10; Run 3), but proportionally in much lower amount than the NEM-modified roGFP2-C204S (Figure 10; Run 3, GSSG+GRX). Sulfonylated roGFP2-C204S (SO_3H) was the most detected in the samples of roGFP2-C204S treated with H_2O_2 and showed an apparent molecular weight of ~25 and 37 kDa (Figure 10; Run 2+4). We detected larger amounts of glutathionylated roGFP2-C204S in run 3 with GSSG+GRX treatment than in the other conditions (Supplemental Figure 1). However, overall high abundance of reduced and NEM labeled roGFP2-C204S was detected in the run 3.

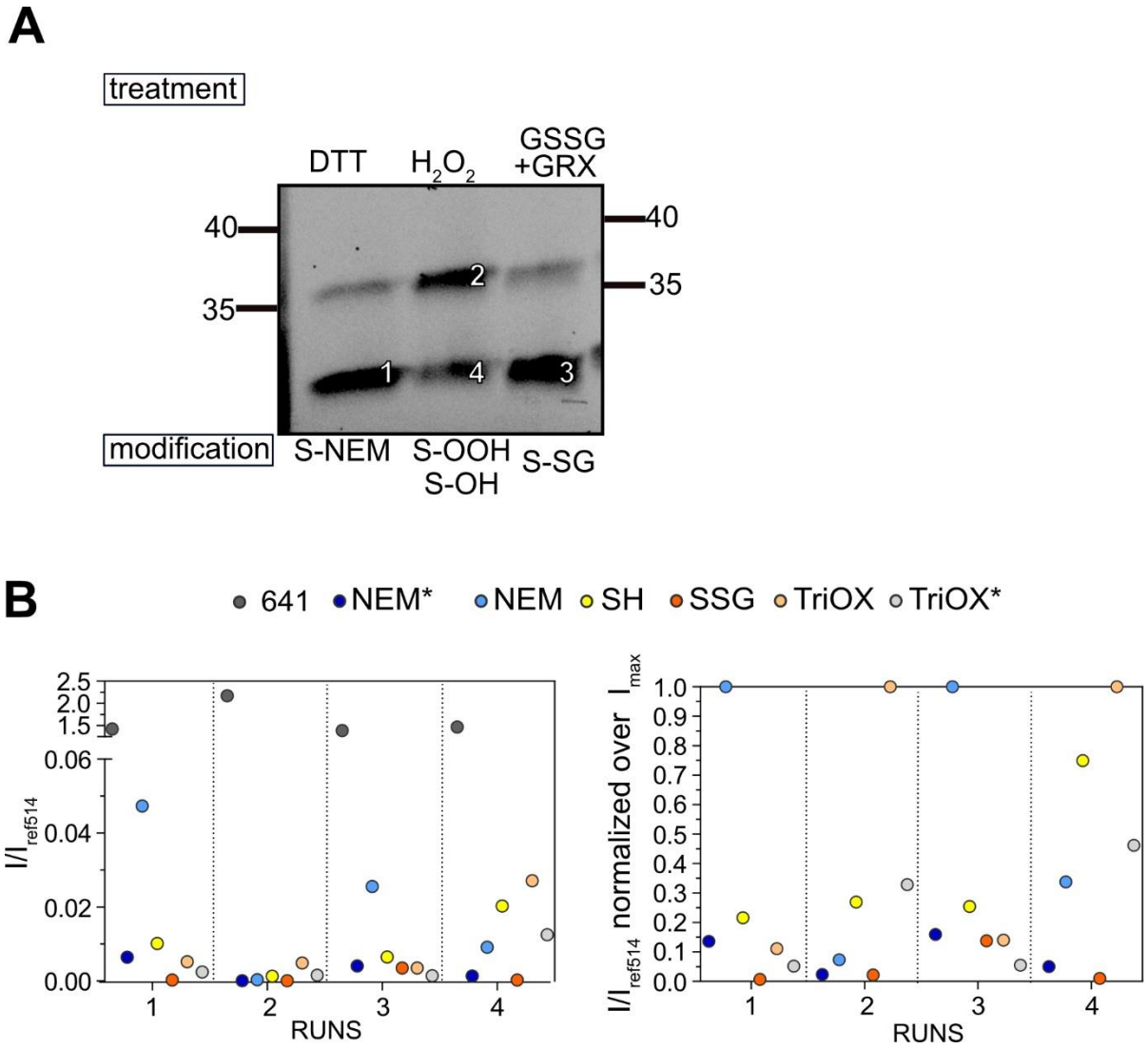

Figure 10: MS/MS analysis of roGFP2 oxidation assay samples

A SDS-PAGE and sample numbers (1-4) of roGFP2-C204S treated and incubated with NEM and send for MS/MS analysis. Samples 1, 2, 3, 4 with expected modifications of the cysteine thiol (NEM, S-OOH, S-OH, S-SG) **B** Intensities of each modification detected in the MS/MS in the peptide sequence LEYNYNCHNVYIMADK and LEYNYNCHNVYIMADKQK (missed lysin (K) cleavage (*)) was normalized over a reference sequence of roGFP2-C204S (514: GIDFKEDGNILGHK). As control for the reference peptide 514 another reference sequence of roGFP2 (641: SAMPEGYVQER) was used. Intensity detected in each run were plotted in the left panel). Intensities normalized over the maximum intensity after normalization over the reference intensity (514) of each run are depicted in the right panel.

Since no difference in MPEG-Mal labeling was detectable in the tested GSH:GSSG ratios with roGFP2-C204S (Figure 9 D), we wanted to try a different redox potential resulting in different GSH:GSSG ratios to visualize a possible small difference in glutathionylation. Due to the redox potential of -232 mV we expect a nearly complete sensor oxidation (98%) leaving only 2% of sensor able to interact with MPEG-Mal. To intensify the visibility of the MPEG-Mal shifted band, further ratio experiments were performed at the midpoint potential of roGFP2.

At -280 mV, 50% of roGPF2 will be oxidized allowing the other 50% of roGFP2 to be labelled with MPEG-Mal leading to an increased band intensity of the MPEG-Mal labeled roGFP2 or roGFP2-C204S.

For an E_{GSH} of -280 mV, ratios were calculated with GSH:GSSG concentrations of 5 mM GSH to 0.002 mM GSSG (ratio 2000) and 6.66 mM GSH to 0.004 mM GSSG (ratio 1500) (see Table 16). Full roGFP2 oxidation and reduction was detected in the roGFP2 H_2O_2 and DTT samples labeled with NEM, seen by the difference in gel mobility. Treatments with 40 µM GSSG resulted in complete sensor oxidation and the appearance of the oxidized roGFP2 at app. 28 kDa, as observed for H_2O_2-treated roGFP2 (Figure 11 B). The sensor was 50% reduced in both the ratios 1500 and 2000, as seen by two bands of equal intensity at the height of the oxidized (H_2O_2) and reduced (DTT) roGFP2. Labeling the sensor with MPEG-Mal induced a size shift of the reduced roGFP2 from ~35 kDa to ~45 kDa in the DTT treated sample and in the ratios 1500 and 2000 (Figure 11 C). The NEM labeled roGFP2-C204S of samples at -280 mV revealed an identical band pattern as seen before in Figure 9 C (Figure 11 D). The app. 25 kDa band showed a high intensity while the app. 35 kDa band intensified after H_2O_2 treatment. No differences in band heights were observed between the ratio 1500 and 2000. Labeling the reduced roGFP2-C204S (DTT) with MPEG-Mal did not lead to a 100% gel shift as observed for roGFP2 (Figure 11 E). The ~25 kDa band detected in the NEM labeled gel was still the most intense band appearing in all samples of roGFP2-C204S labeled with MPEG-Mal. However, a cloudy band appeared at ~40 kDa in the roGFP2-C204S samples treated with DTT, 40 µM GSSG, and the ratio samples (1500, 2000).

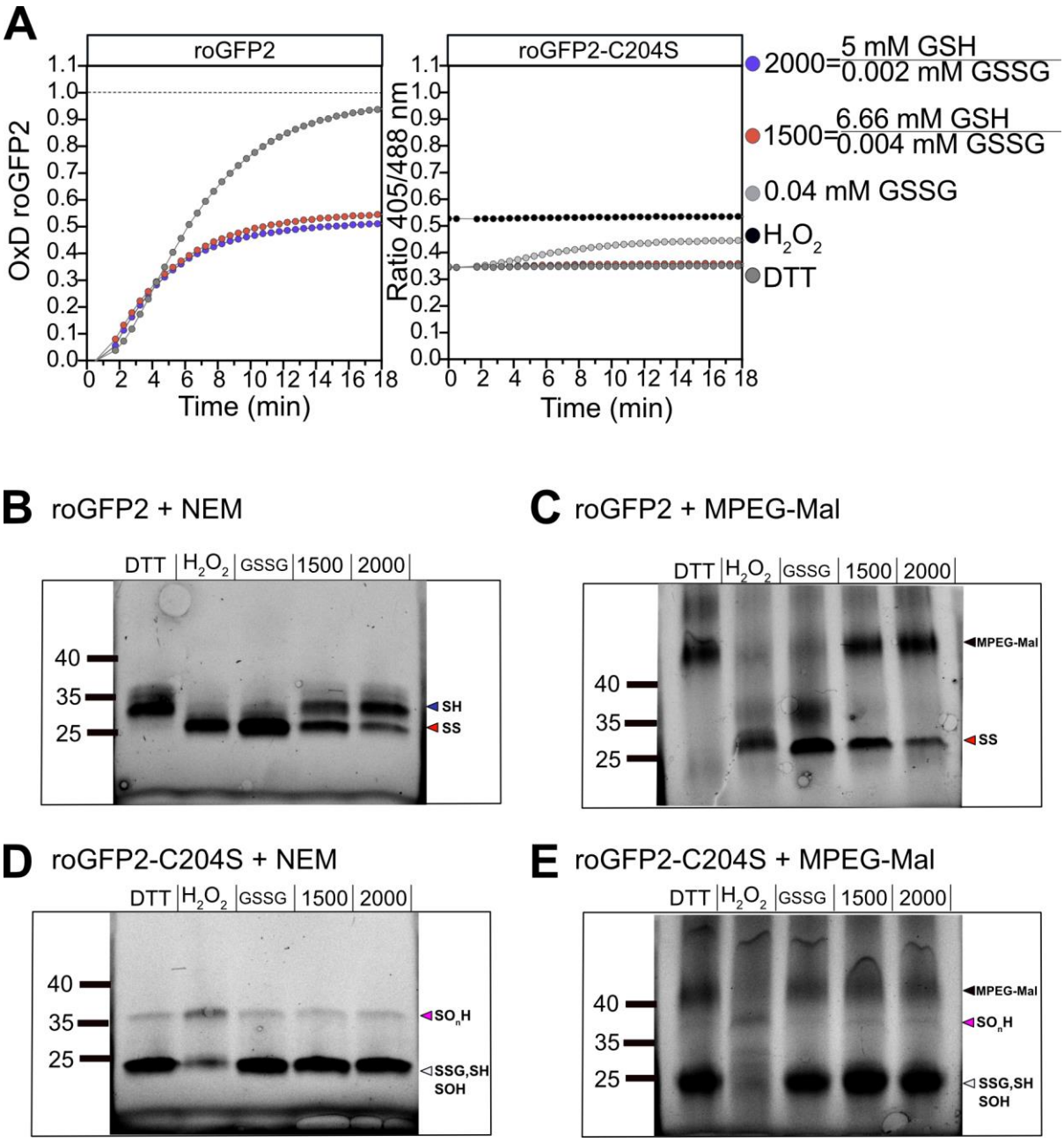

Figure 11: roGFP2 and roGFP2-C204S oxidation at -280 mV in 1500 and 2000 GSH:GSSG ratio catalysed by *At*GRXC1.

A Degree of roGFP2 oxidation and 405 nm/ 488 nm ratio of roGFP2-C204S at -280 mV and 1500 or 2000 GSH:GSSG ratio (see Table 16) within 20 min after addition of *At*GRXC1(t_1). Dotted lines indicate 100% oxidation of the sensor by H_2O_2. Oxidation degree of roGFP2 was calculated as described in Schwarzländer et al. 2008. Ox. Samples of this run were further labelled with NEM and MPEG-Mal and analyzed via SDS-PAGE. **B-E** SDS-PAGE with 1.4 µg roGFP2 (**B**,**C**) and roGFP2-C204S (**D**,**E**), treated with DTT (1 mM), H_2O_2 (10 mM), 40 µM GSSG or ratios of GSH:GSSG (1500/2000) incubated with either 50 mM NEM (**B**,**D**) or 5 mM MPEG-Mal (**C**,**E**). **B** roGFP2 samples were incubated with NEM to block free thiols. **C** roGFP2 incubated with MPEG-Mal to label not glutathionylated/oxidized cysteines. **D** roGFP2-C204S treated with NEM to block not glutathionylated, free thiols. **E** roGFP2-C204S treated with MPEG-Mal to label not glutathionylated, free thiols. Arrows in blue and red indicate bands of reduced and oxidized roGFP2, white and pink arrows indicate the height of glutathionylated, reduced or oxidized roGFP2-C204S and sulfinic or sulfonic acid. MPEG-Mal labelled protein bands are labelled with a black arrow.

To ensure that DTT treatment completely reduced roGFP2-C204S, we also tested TCEP (tris(2-carboxyethyl)phosphine, Bond-Breaker™, Thermo Fisher) as an alternative reducing agent. NEM and MPEG-Mal labeling of roGFP2 and roGFP2-C204S reduced via DTT or TCEP showed no difference in band heights within the respective treatment (Figure 12). MPEG-Mal bands of roGFP2-C204S were observed at ~40 kDa as seen in Figure 11 E, also showing a band of high signal intensity at ~25 kDa. Assuming a complete reduction of roGFP2C204S, no difference in MPEG-Mal-binding was detected between the ratios 10.5 and 72.5 (-232 mV) as well as 1500 and 2000 ratio (-280 mV; Figure 9, Figure 11).

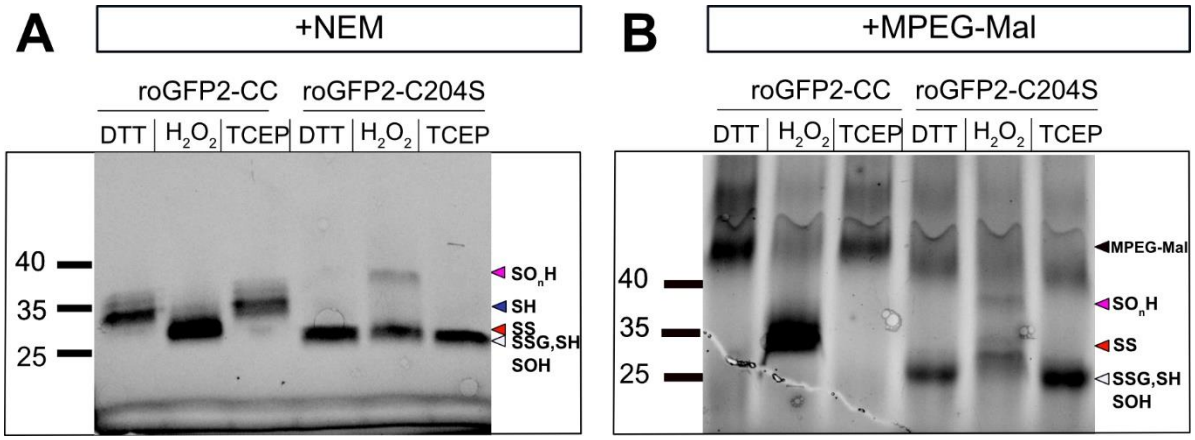

Figure 12: roGFP2 and roGFP2-C204S after reduction with DTT and TCEP

SDS-PAGE of roGFP2 and roGFP2-C204S reduced with 10 mM DTT or 10 mM TCEP for 20 min before labelling with 50 mM NEM (A) or 5 mM MPEG-Mal (B). Arrows in blue and red indicate bands of reduced and oxidized roGFP2, white and pink arrows indicate the height of glutathionylated, reduced or oxidized roGFP2-C204S and sulfinic or sulfonic acid modification. MPEG-Mal labelled protein bands (B) are labelled with a black arrow.

The tested ratios of 10.5 and 72.5 (at -220 mV) and 1500 and 2000 (at -280 mV) showed a 6.9-fold and 1.3-fold difference, respectively. Since the ratios may be too close to detect a difference in roGFP2-C204S between MPEG-Mal labeled, reduced roGFP2-C204S and unlabeled *S*-glutathionylated roGFP2-C204S, the experiment was repeated with the largest possible ratio difference. We chose a GSH:GSSG ratio of 30 and 3000 to increase the difference between the ratios to 100-fold (Table 16). Limited by solubility of stock concentrations of GSH and GSSG, these ratios were feasible at -220 mV estimated with the Nernst equation to result in 100% of sensor oxidation. Further, we increased the 40 µM GSSG control to 2 mM GSSG to push roGFP2-C204S to its glutathionylated form (Figure 6, k_{-3}) and compared *At*GRXC1 and *At*GRXS15 as catalysts in the gel-based read-out. roGFP2 in the presence of 2 mM GSSG and either *At*GRXC1 or *At*GRXS15 led to ~100% of sensor oxidation (Figure 13 A). Aside from the controls of H_2O_2 and 2 mM GSSG, the only condition that led to 100% sensor oxidation was

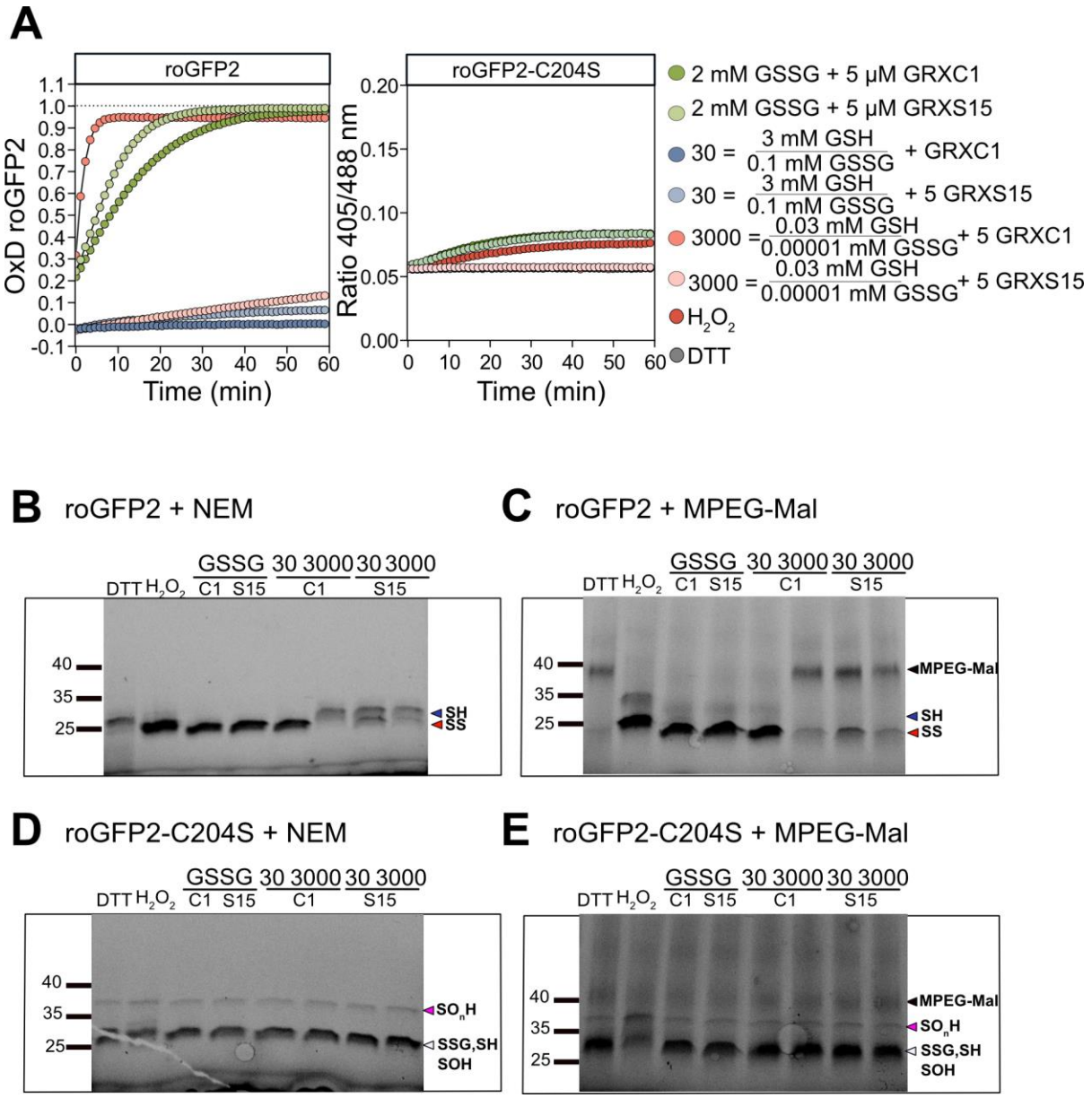

Figure 13: roGFP2 and roGFP2-C204S kinetics in 30 and 3000 ratios of GSH:GSSG at -220 mV catalyzed by *At*GRXC1 or *At*GRXS15.

A Degree of roGFP2 oxidation and 405 nm/ 488 nm ratio of roGFP2-C204S at -220 mV and 30 and 3000 GSH:GSSG ratio (see Table 16) after addition of 5 µM *At*GRXC1 or *At*GRXS15. Dotted lines indicate 100% oxidation of the sensor by H_2O_2. Oxidation degree of roGFP2 was calculated as described in Schwarzländer et al. 2008. Samples of this run were further labelled with NEM and MPEG-Mal and analyzed via SDS-PAGE. **B-E** SDS-PAGE with 1.4 µg roGFP2 (**B**,**C**) and roGFP2-C204S (**D**,**E**), treated with DTT (1 mM), H_2O_2 (10 mM), 2 mM GSSG or ratios of GSH:GSSG (30/3000) incubated with either 50 mM NEM (**B**,**D**) or 5 mM MPEG-Mal (**C**,**E**). **B** roGFP2 samples were incubated with NEM to block free thiols. **C** roGFP2 incubated with MPEG-Mal to label not glutathionylated/oxidized cysteines. **D** roGFP2-C204S treated with NEM to block not glutathionylated, free thiols. **E** roGFP2-C204S treated with MPEG-Mal to label not glutathionylated, free thiols. Arrows in blue and red indicate bands of reduced and oxidized roGFP2, white and pink arrows indicate the height of glutathionylated, reduced or oxidized roGFP2-C204S and sulfinic or sulfonic acid. MPEG-Mal labelled protein bands are labelled with a black arrow

the ratio 30 with *At*GRXC1 present as a catalyst. roGFP2 showed a shift after MPEG-Mal labeling in the GSH:GSSG ratio of 3000 + *At*GRXC1, and 30 and 3000 in the presence of *At*GRXS15, since only 10% of sensor oxidation was detected via intensity read-out (Figure 13). roGFP2-C204S displayed unchanged band patterns under all conditions, regardless of the presence of *At*GRXC1 or *At*GRXS15. The 3000 GSH:GSSG ratio with 0.03 mM GSH and 0.00001 mM GSSG contained less GSSG amounts than roGFP2 present in the sample. Thus, under the experimental conditions, complete oxidation of 5 µM roGFP2 would not have been possible with 0.01 µM GSSG.

To further optimize the experimental set-up new GSH:GSSG ratios were tested which fulfilled the following requirements: (1) the GSSG amount of the ratio had to be higher or equal to 5 µM due to the concentration of roGFP2 in the assay. If the concentration would be lower than 5 µM full oxidation of roGFP2 via GSSG is not possible. (2) The GSH amount had to be lower than the final MPEG-Mal concentration (5 mM). GSH contains a cysteine group which is accessible to MPEG-Mal. If the concentration of GSH is higher than the concentration of MPEG-Mal, less to no MPEG-Mal is available for the labeling of roGFP2. (3) Conversion of GSSG to GSH during the assay reaction should not result in a significant shift in E_{GSH}. The ratios 20 (4.5 mM GSH; 0.225 mM GSSG) and 134 (0.67 mM GSH; 0.005 mM) met these criteria and demonstrated a maximum difference of 6.7-fold at -220 mV. 100% of roGFP2 oxidation was detected in the ratio of 20 and 134 20 min after *At*GRXC1 addition (Figure 14 A), which was further shown by the band pattern in the SDS-PAGE of the NEM and MPEG-Mal labeled roGFP2, only showing a ~10 kDa MPEG-Mal shift after DTT treatment (Figure 14 B,C). The roGFP2-C204S showed the same band pattern after NEM labeling as already observed for different redox potentials and ratios as shown in Figure 9, Figure 11 and Figure 13. After MPEG-Mal labelling no intense band at app. 40 kDa was detected for neither the DTT treated nor for the ratio samples (Figure 14 D, E).

Summarizing this set of experiments, roGFP2-C204S could either not be completely reduced or the labelling with MPEG-Mal was inefficient (Figure 6, Figure 7, Figure 8, Figure 9, Figure 11, Figure 12, Figure 13, Figure 14). Even in the reduced (DTT) sample, where 100% labelling of roGFP2-C204S was expected, no 100% MPEG-Mal induced size shift was observed for roGFP2-C204S. In the roGFP2 samples, reduction, oxidation and labeling worked as expected, which rather excludes the conditions such as pH, concentrations of MPEG-Mal or DTT as causes for the failed positive control for roGFP2-C204S.

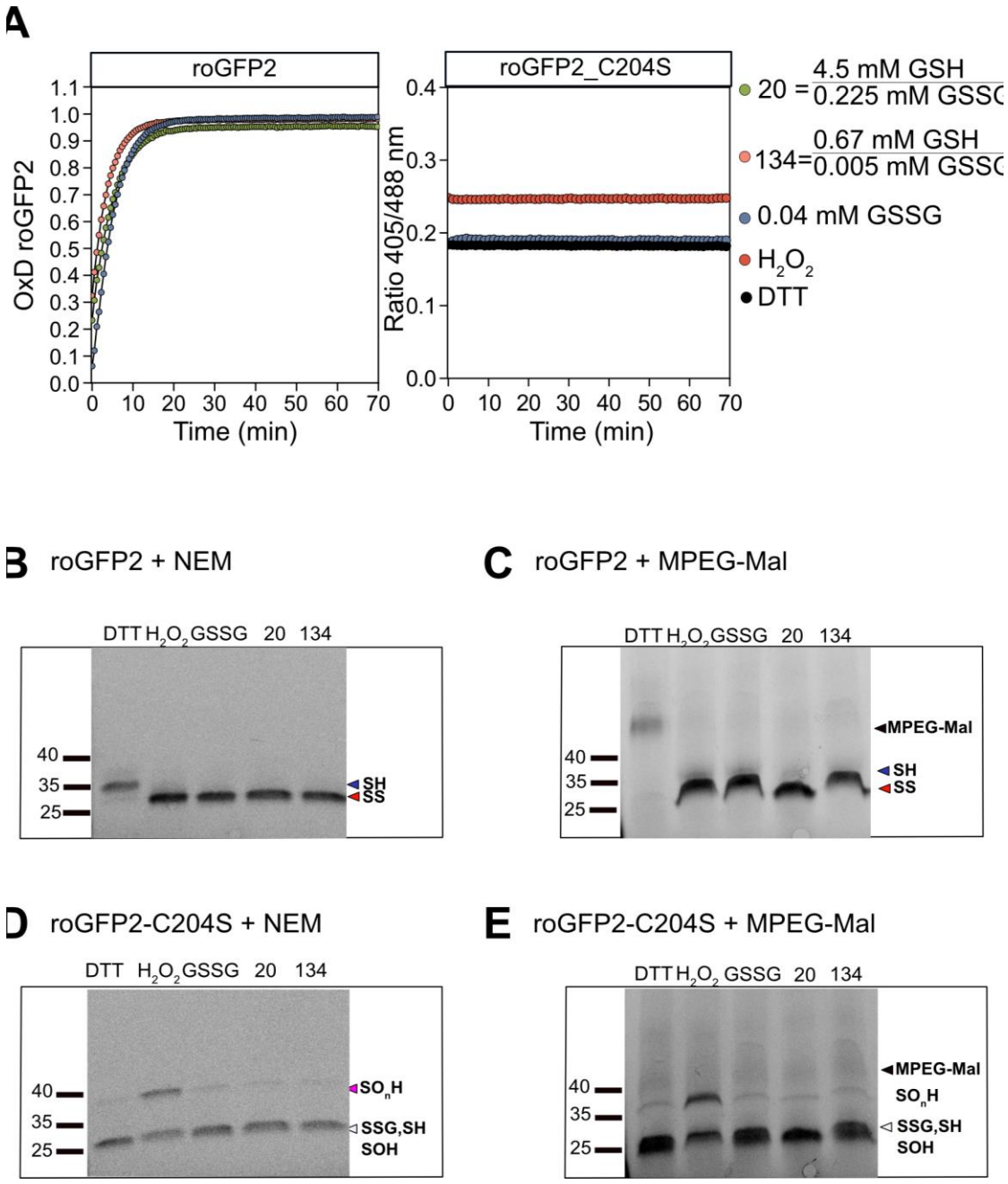

Figure 14: roGFP2 oxidation in GSH:GSSG ratios of 20 and 134 at -220 mV

A Degree of roGFP2 oxidation and 405 nm/ 488nm ratio of roGFP2-C204S oxidation at -220 mV and 20 and 134 GSH:GSSG ratio (see Table 16) after addition of 1 µM *At*GRXC1. Dotted lines indicate 100% oxidation of the sensor by H_2O_2. Oxidation degree of roGFP2 was calculated as described in Schwarzländer et al. 2008. Oxidation degree of roGFP2-C204S was calculated by roGFP2-C204S DTT and H_2O_2 controls. Samples of this run were further labelled with NEM and MPEG-Mal and analyzed via SDS-PAGE. **B-E** SDS-PAGE with 1.4 µg roGFP2 (**B**,**C**) and roGFP2-C204S (**D**,**E**), treated with DTT (1 mM), H_2O_2 (10 mM), 40 µM GSSG or ratios of GSH:GSSG (20/134) incubated with either 50 mM NEM (**B**,**D**) or 5 mM MPEG-Mal (**C**,**E**). **B** roGFP2 samples were incubated with NEM to block free thiols. **C** roGFP2 incubated with MPEG-Mal to label not glutathionylated/oxidized cysteines. **D** roGFP2-C204S treated with NEM to block not glutathionylated, free thiols. **E** roGFP2-C204S treated with MPEG-Mal to label not glutathionylated, free thiols. Arrows in blue and red indicate bands of reduced and oxidized roGFP2, white and pink arrows indicate the height of glutathionylated, reduced or oxidized roGFP2-C204S and sulfinic or sulfonic acid. MPEG-Mal labelled protein bands are labelled with a black arrow

After the oxidation assay with 20 and 134 GSH:GSSG ratios at -220 mV, a Western blot with a primary anti-glutathione antibody was performed to obtain a more sensitive detection of glutathionylated roGFP2-C204S (Figure 15). The glutathionylated roGFP2-C204S appeared at ~35 kDa and slightly below ~25 kDa in all the samples including the reduced (DTT) and oxidized (H_2O_2) control to which no external glutathione was added. The two bands of ~25 kDa and ~35 kDa are also visible in the PageBlue™ stained SDS-PAGE, but only one band at ~25 kDa is visible under UV-exposure except for the H_2O_2 sample. In the H_2O_2 sample the second band appeared at ~37 kDa as seen before, identified as sulfenylated roGFP2-C204S (Figure 10-14). No glutathionylated protein was detected at ~40 kDa in the H_2O_2 treated roGFP2-C204S. As additional control, roGFP2 was analyzed via immunoblot, expecting no glutathionylation for oxidized roGFP2. roGFP2 showed a band appearing at ~35 kDa in the sample of roGFP2 treated with DTT. The band was also visible under UV-light and after PageBlue™ staining. In samples where 100% roGFP2 oxidation is expected (H_2O_2, 40 µM GSSG, 20 and 134) no roGFP2-bound glutathione was detected.

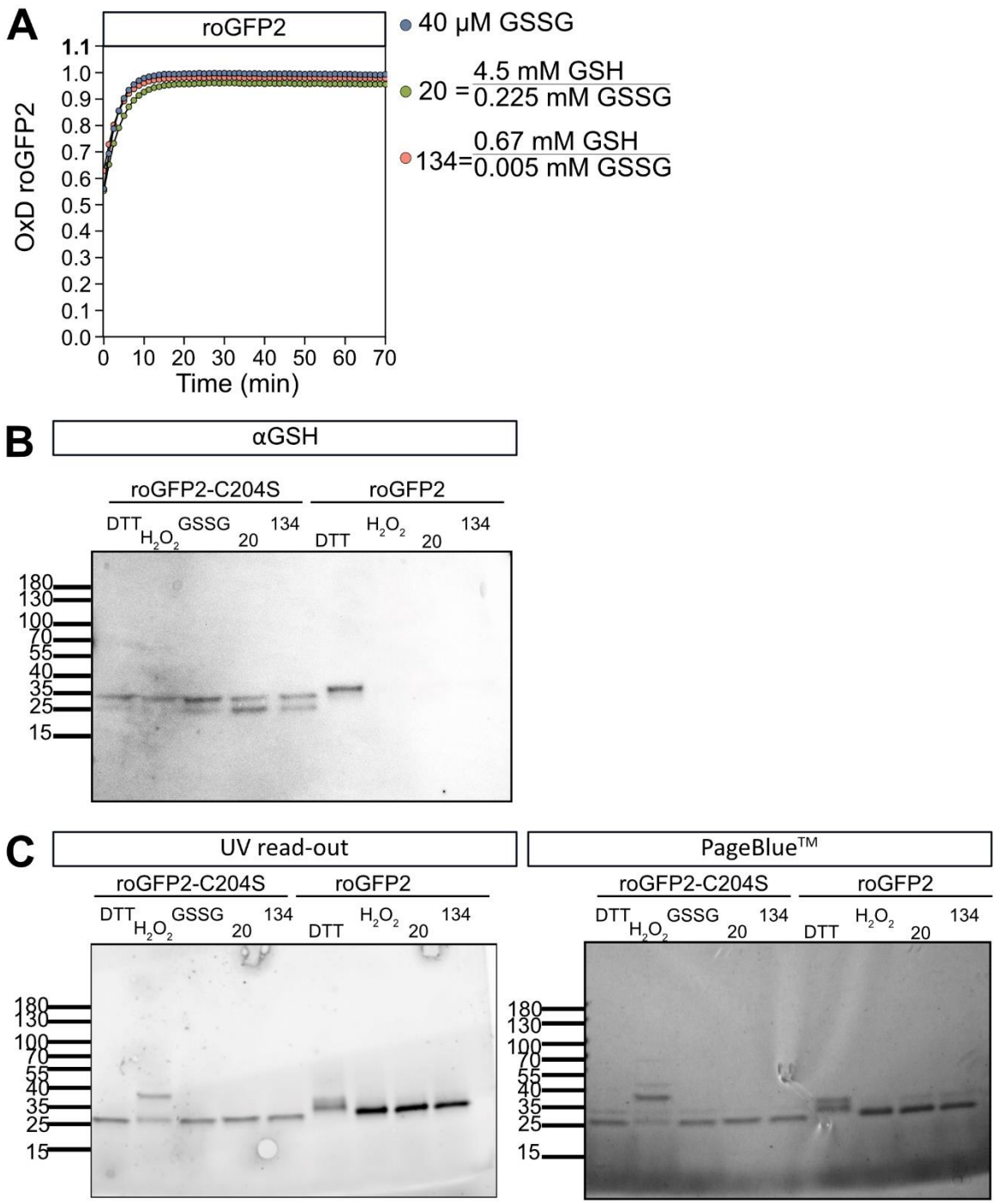

Figure 15: Detection of glutathionylated roGFP2-C204S via immunodetection

A Oxidation degree of roGFP2 at -220 mV with GSH:GSSG ratios of 20 (GSH:4.5; GSSG 0.225 mM) and 134 (GSH: 0.67 mM; GSSG: 0.005 mM) as seen in Figure 14. **B** Western blot of roGFP2-C204S and roGFP2 after roGFP2 oxidation assay seen in A. 1.75 µg of roGFP2 or roGFP2-C204S was loaded in each line. Primary antibody αGSH (ThermoFisher) was used in a 1:1000 dilution with a secondary αMouse antibody (Agrisera) in a 1:2500 dilution. **C** SDS-PAGE loaded with 1.75 µg of roGFP2-C204S and roGFP2 and imaged with UV-light **D** SDS-PAGE loaded with 1.75 µg of roGFP2-C204S and roGFP2 and stained with PageBlue™.

4.1.2 Behavior of cytosolic glyceraldehyde-3-phosphate dehydrogenase C1 (GAPC1) as target protein of S-glutathionylation under less reducing glutathione redox potential using a YFP fusion construct

To investigate the influence of the E_{GSH} on the behavior of *in vivo S*-glutathionylation target proteins, the cytosolic GAPC1 was further studied in the cytosolic and peroxisomal glutathione reductase knock-out *gr1-1* (Marty *et al.* 2009) of *A. thaliana.* Seeds of Arabidopsis plants expressing YFP tagged GAPC1 (GAPC-YFP) under the *2xCaMV35S* promotor or the endogenous *GAPC1* promotor were obtained from Alex Costa (University of Milan, Department of Bioscience, Italy; Vescovi *et al.* 2013). Constructs were crossed into the *gr1-1* background. Homozygous GAPC-YFP expressing plants were used as pollen donor for crossing with homozygous *gr1-1* plants. Seeds generated from the crossing were screened for YFP fluorescence and transferred to soil for seed generation of the progeny (F_2). The F_2 generation was screened via PCR for T-DNA insertion at the *GR1* locus and the presence of the fluorescence construct (LB-*GR1*) (Figure 16). Nine plants were identified as homozygous knock-outs of *GR1* expressing *p35S*-GAPC-YFP labelled as #8, #9, #10, #14, #20, #29, #32, #33, #40. Four plants were identified as *GR1* knock-outs expressing *pGAPC*-GAPC-YFP labelled as B#1, B#4, B#7 and A #14 (A and B labelling indicate different crossings).

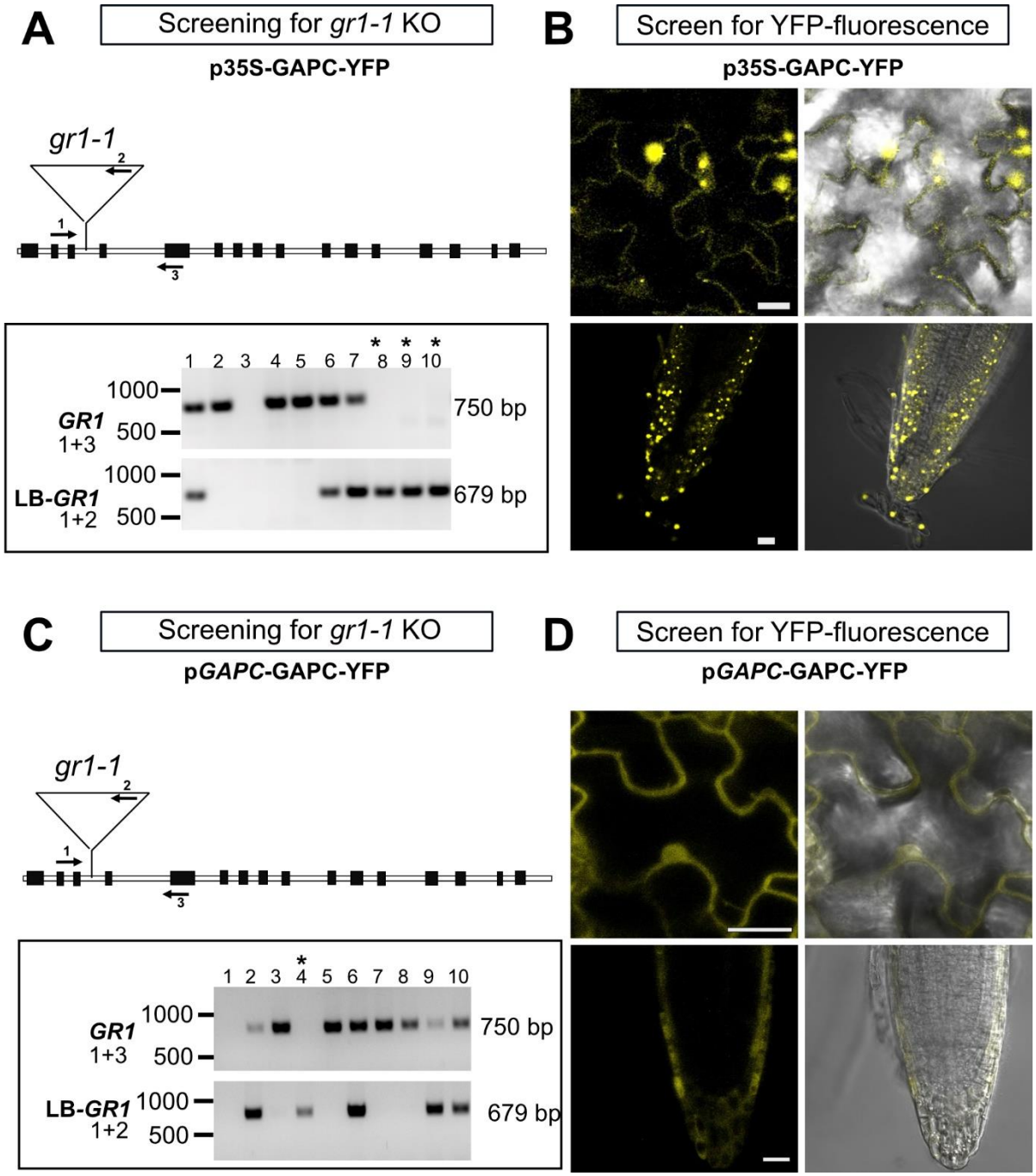

Figure 16: Genotyping of GAPC-YFP x *gr1-1* and YFP- fluorescence screening

A+B Genotyping PCR was done on crossings of *p35S*-GAPC-YFP x *gr1-1* lines (example #1-10) and YFP fluorescence screening using the CLSM (Ex. 488 nm; Em. 511-541 nm). A schematic overview over T-DNA insertion site of *gr1-1* was modified from Marty *et al.* 2009. **C+D** Genotyping PCR on crossings of p*GAPC*-GAPC-YFP x *gr1-1* lines (example #1-10) and YFP fluorescence screening using the CLSM. Primers 1 and 3 amplify a sequence of the genomic *GR1* locus ('GR1'), primer combination 1 and 2 can only be amplified if the T-DNA is present at the respective *GR1* site ('LB-*GR1*'). Primer sequences are depicted in Table 4. Scale bar =20 µm. Asterisk on top of numbers label plants with T-DNA integration at the *GR1* locus and no amplification of the WT *GR1* locus.

4.1.2.1 Translocation and aggregation of GAPC1 under less reducing E_{GSH} in root elongation zone of *gr1-1* under the 2x*CaMV35S* promotor

WT and *gr1-1* expressing *p35S*-GAPC-YFP were grown on ½ MS-plates pre-screened for YFP fluorescence and imaged via the CLSM. Due to previous results of GAPC-YFP in Arabidopsis roots (Vescovi *et al.* 2013) the focus was set on the root tip and elongation zone (zone 1, Figure 17). GAPC-YFP accumulated in clusters in the root tip in both genotypes with the tendency of more GAPC-YFP accumulations in the *gr1-1* background. In the elongation zone GAPC-YFP signal was less intense in both genotypes with a clear nuclear and cytosolic localization of the sensor seen by an overlap of signal with nuclei detected in the transmitted light.

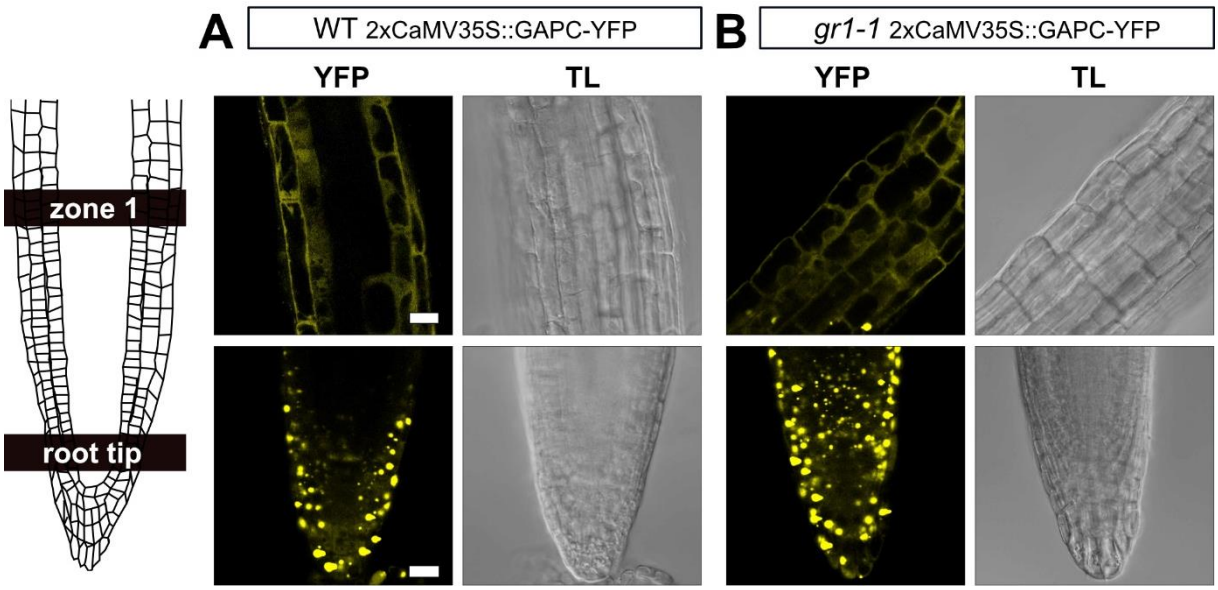

Figure 17: p35S-GAPC-YFP signal in different root zones of WT and *gr1-1*

7-day old WT (**A**) and *gr1-1* (**B**) seedlings expressing *p35S*-GAPC-YFP grown on ½ MS plates were imaged using the CLSM. Fluorescence signal of root tip and elongation zone (zone 1) are compared between WT (A) and *gr1-1* (B) expressing GAPC-YFP. YFP = Ex. 488 nm; Em. 511-541 nm; TL = transmitted light. Scale bare = 20 µm

In Vescovi *et al.* 2013, the treatment of p*GAPC*-GAPC-YFP expressing plants with 0.1 mM cadmium (cad) showed a translocation of the sensor signal to the nucleus and higher accumulation of GAPC-YFP in root tips compared to control conditions. Cadmium is a common soil pollutant, known to induce oxidative stress and can interact with the glutathione pool (Cuypers *et al.* 2010). To investigate the effect of 0.1 mM cad on GAPC as cytosolic target protein of glutathionylation in WT and *gr1-1*, four-day old Arabidopsis seedlings expressing *p35S*-GAPC-YFP were transferred to ½ MS plates containing 0.1 mM cad and further grown for 72 h. Nuclei of root cells were imaged using the CLSM and analyzed for translocation of

GAPC-YFP signal from cytosol to nucleus by extraction of nuclear specific or cytosolic signal using ICY (de Chaumont *et al.* 2012). The fluorescence signal showed a significantly higher cytosolic and nuclear signal in *gr1-1* compared to WT under control conditions (Figure 18). Treatment of the seedlings with 0.1 mM cad led to the increase of WT cytosolic and nuclear signal to the level of *gr1-1* fluorescence. To normalize for differences in expression levels of *p35S*-GAPC-YFP between plants, the ratio of nuclear to cytosolic signal was calculated and log transformed (Figure 18 E) revealing no significant difference between WT and *gr1-1* under control conditions but showed a significant difference for cadmium treated WT and *gr1-1*.

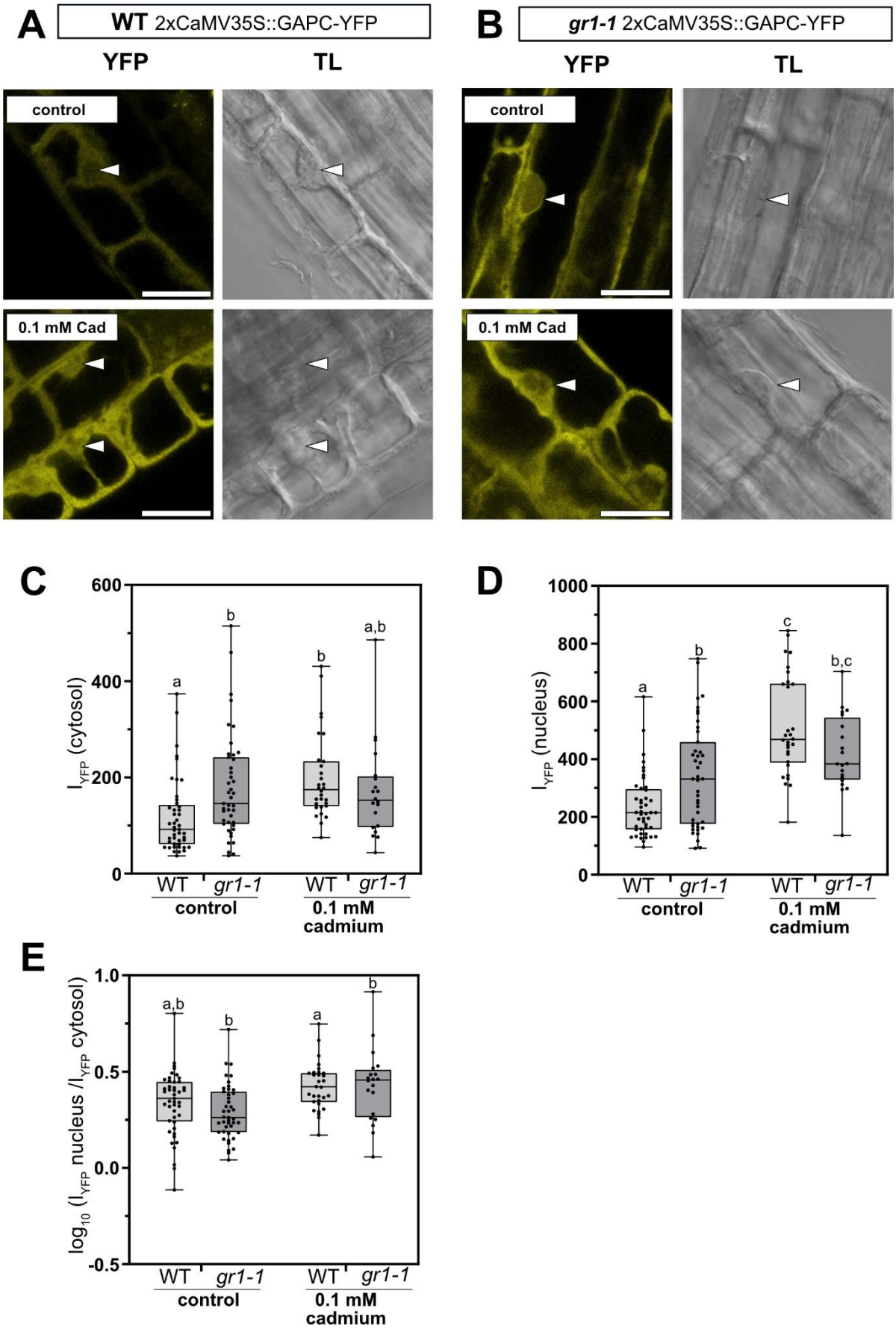

Figure 18: GAPC-YFP signal in nucleus and cytosol of Arabidopsis root cells after 72 h of 0.1 mM cadmium treatment

7-day old Arabidopsis seedlings w ere prior to imaging stressed for 72 h on 0.1 mM cadmium plates or transferred as control group to ½ MS plates. CLSM images were taken of WT (**A**) and *gr1-1* (**B**) overexpressing GAPC-YFP under control (upper panel) and cadmium treatment (lower panel). Cells in the transition zone of the root were used for analysis. White arrows indicate nuclei used for imaging analysis. Scale bars = 20 µm. Image brightness was adjusted only for this figure while intensity quantifications (mean pixel intensity/ area) were done on raw data. **C** Cytosolic YFP intensities were extracted using the region of interest tool of ICY (de Chaumont *et al.* 2012). Cytosol signal excludes the nucleus signal within the cell. **D** YFP intensities located in the nucleus were extracted using ICY. Only nuclei were taken showing a clear nucleus shape in the transmitted light. **E** Cytosolic and nucleus intensity values were log transformed and the ratio was formed. Data consist of two repetitions of the experiment with 5-7 roots analyzed per experiment per line and treatment. **C,D,E** A two-way ANOVA was done with Šidák's multiple comparison analysis to test for significant differences between treatment and genotype ($p<0.036$). Whiskers display min to max values with boxes indicating 25-75 percentiles. The median is depicted as horizontal line. YFP = Ex. 488 nm; Em. 511-541 nm; TL = transmitted light

4.1.2.2 Fluorescence intensity of *pGAPC*-GAPC1-YFP in less reducing E_{GSH} of root tips and elongation zones in *gr1-1*

The intensity change of the YFP signal can only be compared in a limited range between WT and *gr1-1* due to overexpression (with a high intensity signal) of the *p35S*-GAPC-YFP construct. Therefore, the GAPC-YFP sensor under the endogenous promoter was used to investigate the effect of a less reduced E_{GSH} (in *gr1-1*) on the expression and accumulation level of GAPC.

GAPC-YFP expressed under the endogenous promotor showed under control conditions a maximal ~240% increase of YFP intensity in the root tip area in *gr1-1* compared to WT (Figure 19 A, C). Significance of YFP increase was verified by a two-way ANOVA. After 72 h of 0.1 mM cad treatment, root morphology was altered in WT and *gr1-1* (Figure 19 B, transmitted light) as seen in Vescovi *et al.* (2013). The induction of the *GAPC1* promotor after cadmium treatment was observed by the accumulation of YFP signal in WT root tips (Figure 19 B). YFP fluorescence detected in *gr1-1* upon 72 h of cadmium treatment did not lead to an increase of cytosolic YFP signal compared to WT intensity. A two-way ANOVA was performed to test for significant differences between WT and *gr1-1* after 0.1 mM cad treatment and did not reveal a significant difference.

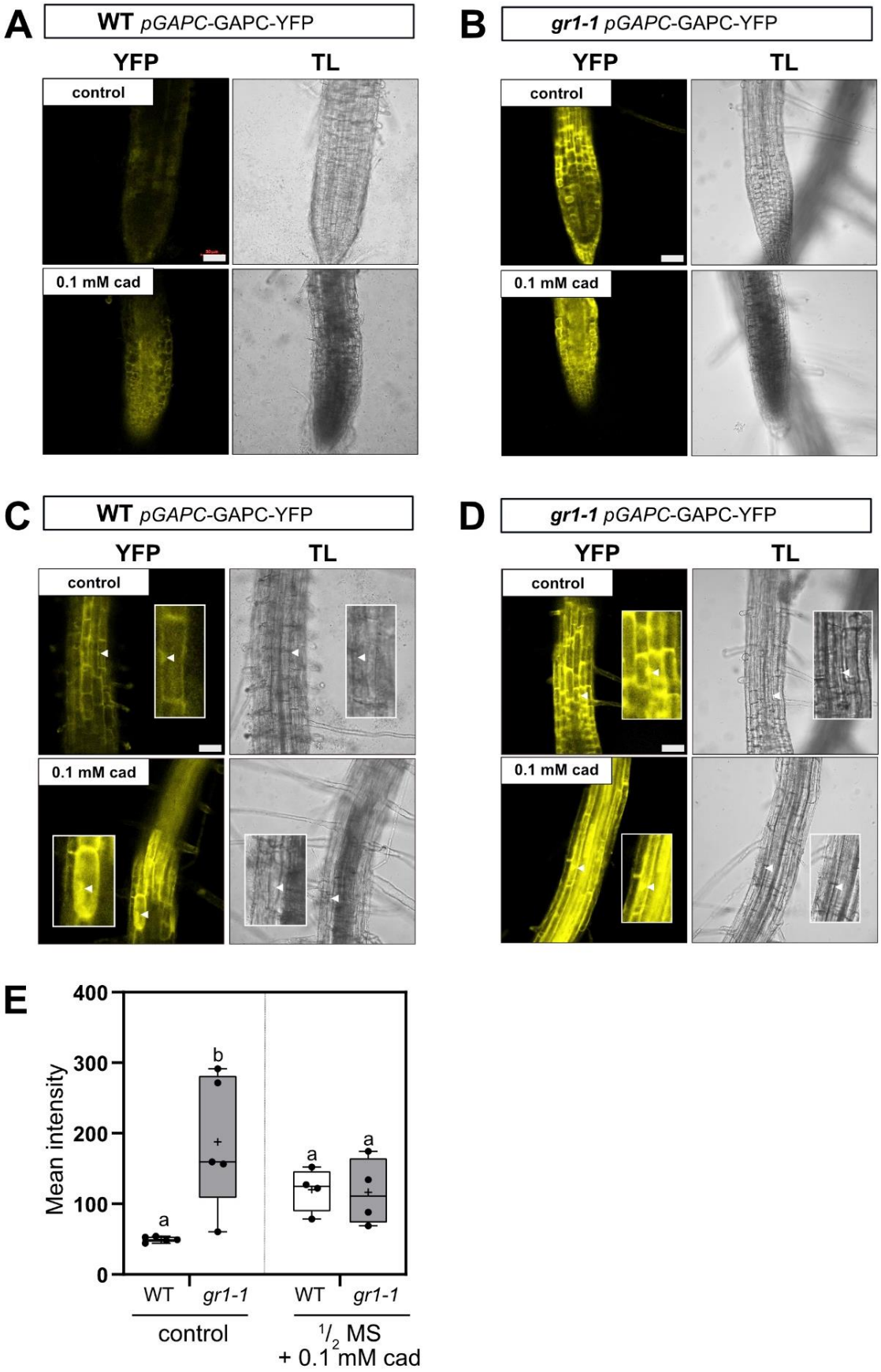

Figure 19:*pGAPC*-GAPC-YFP signal in Arabidopsis root cells of WT and *gr1-1* after 72 h of 0.1 mM cad treatment

7-day old Arabidopsis seedlings were prior to imaging stressed for 72 h on 0.1 mM cad plates or transferred as control group to ½ MS plates. CLSM images were taken of WT (**A,C**) and *gr1-1* (line B7) (**B, D**) expressing GAPC-YFP under control of the endogenous promotor. Root tips (**A, B**) and regions shortly above the root tip (**C, D**) were imaged. CLSM settings were kept constant between images. Scale bar = 50 µm. White arrow heads mark potential nuclei, visible in the transmitted light. Image brightness was adjusted only for this figure. **E** Mean YFP intensities were extracted of the total images of root tips as seen in A and B using ICY. 4-5 roots were analyzed per genotype and treatment. A two-way ANOVA with Tukey's multiple comparison test was conducted (p=0.0087). Differing lowercase letters depict significant differences. Whiskers display min to max values with boxes indicating 25-75 percentiles. The median is depicted as horizontal line and the mean shown as '+'.

4.1.3 Biochemical characterisation of the plastidial glutaredoxin C5 of *P. patens*

Based on the phylogenetic analysis shown in Chapter 3, GRXC5 was identified as single plastidial targeted class I GRX in *P. patens*. Before further functional characterization of *Pp*GRXC5 *in vivo* (see 4.1.4), *Pp*GRXC5 was analyzed regarding its *in vitro* (de-)glutathionylation abilities. For this purpose, the coding sequence of *Pp*GRXC5 without the plastidial target sequence was cloned into a bacterial expression vector (pETG-10A) and the recombinant protein was purified.

4.1.3.1 Identifying *P. patens* GRXC5 transit peptide by sequence alignment

The targeting peptide of *Pp*GRXC5 was identified by sequence alignment with the plastidial class I GRX of Arabidopsis: *At*GRXC5 (AT4G28730.1) and *At*GRXS12 (AT2G20270.2) (Figure 20). *Pp*GRXC5 showed an N-terminal extension, which is often observed for plastid targeted proteins (Glaser & Soll 2004; Couturier *et al.* 2011). By sequence comparison, the start of the N-terminal *At*GRXC5 protein sequence at 'SFGSRM' (Couturier *et al.* 2011) supposes a beginning of the *Pp*GRXC5 protein coding sequence close to the position of Alanine 120 (red asterisk, Figure 20). *Pp*GRXC5 lacking the first 120 amino acids (*Δ*A120_*Pp*GRXC5, A121 starting position) was cloned via the Gateway system into the pETG-10-A bacterial expression vector (EMBL-made vector by Arie Geerlof, Heidelberg) and transformed into *E. coli* DH5α. Transformed bacteria were checked via colony-PCR for the correct insert (Figure 21 A). The plasmid was isolated and used for transformation of *E. coli* (Rosetta2, Novagen). Expressed proteins were harvested and purified via an N-terminal His-tag and obtained protein fractions were checked for purity (Figure 21 B). We further characterized the oxidation and reduction ability of the recombinant *Pp*GRXC5.

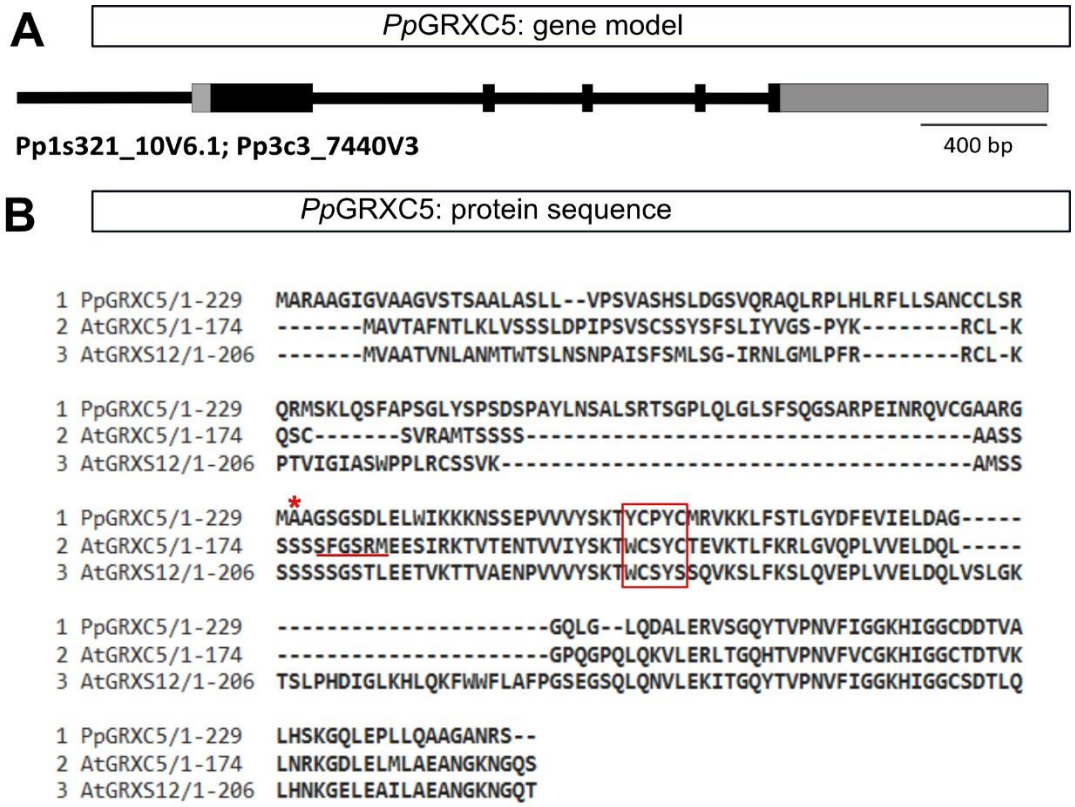

Figure 20: Schematic overview of the *Pp*GRXC5 gene model and its protein sequence alignment

A Schematic overview of *P. patens* GRXC5 gene structure. Exons are shown as a black box, 5' and 3' UTR as a grey box. Information was retrieved from (Phytozome 1.3, gene-ID: Pp1s321_10V6.1) **B** Alignment of 1. *Pp*GRXC5(Pp1s321_10V6.1), 2. *At*GRXC5(AT4G28730.1) and 3. *At*GRXS12 (AT2G20270.2) in Jalview (2.11.0) using the Muscle-alignment tool. Alignment was displayed using Mview (https://www.ebi.ac.uk/Tools/msa/mview). Alanine 120 of *Pp*GRXC5 is marked with a red asterisk. The active site motif containing one or two cysteines (Y/W,C,P/S,Y,C/S) is highlighted with a red box.

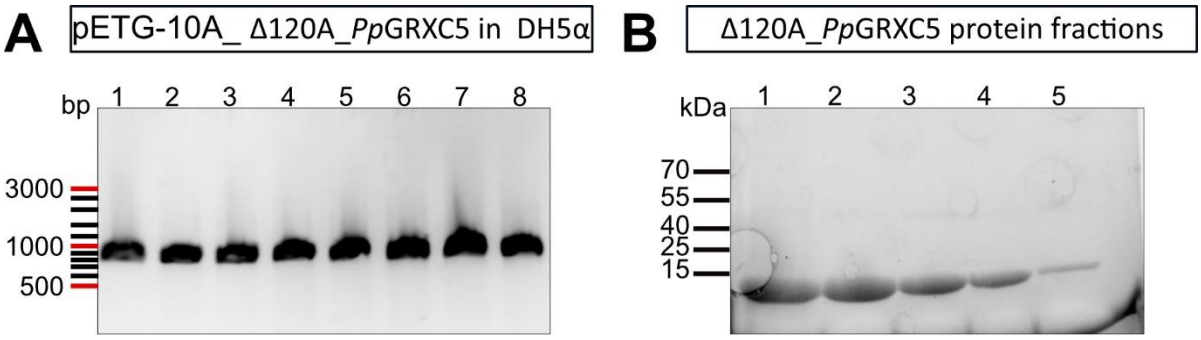

Figure 21: Δ120A_*Pp*GRXC5 expression and protein purification

A Agarose gel electrophoresis of the colony PCR of Δ120A_*Pp*GRXC5 in pETG-10A via screening primers (pETG-10A_F, M23_R, Table 4) expecting a product of 930 bp. Colony 1 and 2 were verified by sequencing. **B** Reducing SDS-PAGE of fractions of Δ120A_*Pp*GRXC5 protein purification. Δ120A_*Pp*GRXC5 was expressed in Rosetta2 and purified using the Äkta-system. 10 µL of each purification fraction was loaded.

4.1.3.2 *Pp*GRXC5 catalyzes the glutathionylation and deglutathionylation of roGFP2

roGFP2 oxidation and reduction via glutathione is catalyzed by class I GRX (Meyer *et al.* 2007; Gutscher *et al.* 2008). An example of disulfide reduction via an *S*-glutathionylation intermediate and its reduction catalyzed by GRX, is the intramolecular disulfide formed in the oxidized roGFP2 between Cys 147 and Cys 204 (Meyer *et al.* 2007; Trnka *et al.* 2020). To obtain information about the oxidoreductase activity, we tested the oxidation and reduction of roGFP2 in the presence of *Pp*GRXC5 (Figure 22). For complete oxidation and reduction controls, roGFP2 was incubated with 10 mM DTT and 10 mM H_2O_2. Efficient reduction of oxidized roGFP2 was obtained in the presence of *Pp*GRXC5 after 2 mM GSH injection. Complete oxidation of reduced roGFP2 was achieved with the addition of 40 µM GSSG. The corresponding plateaus in the oxidation and reduction assays were reached faster in the presence of *Pp*GRXC5 than in the presence of cytosolic class I *At*GRXC1, purified on the same day and under the same conditions as *Pp*GRXC5

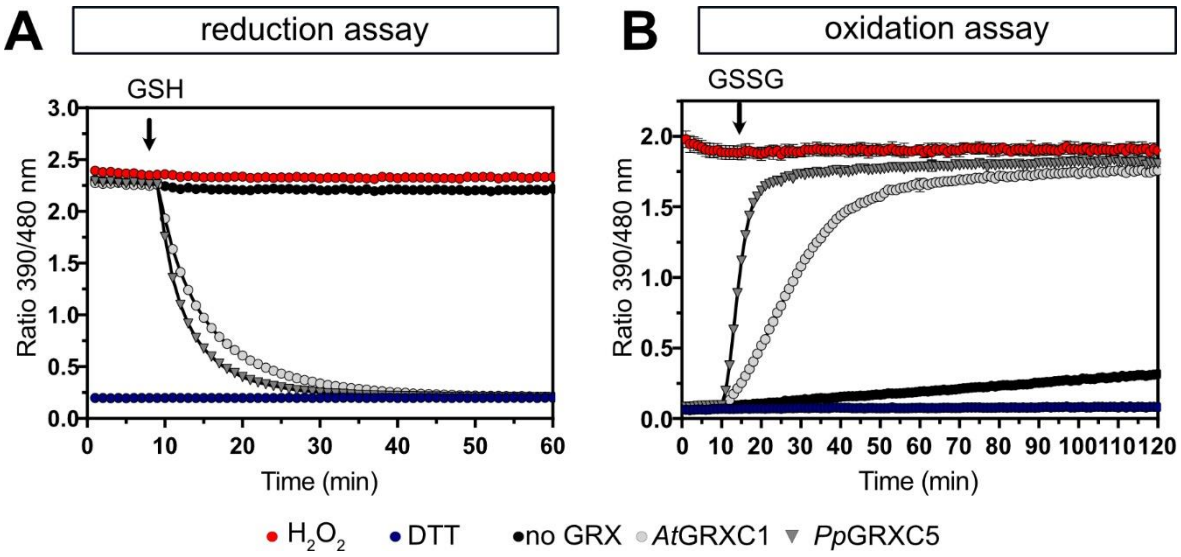

Figure 22: roGFP2 oxidation and reduction mediated by *Pp*GRXC5 and *At*GRXC1

A 1 µM of *Pp*GRXC5 or 1 µM *At*GRXC1 are incubated with 1 µM of oxidized roGFP2 in 0.1 M KPE pH 7.8. As oxidation and reduction control, 1 µM of roGPF2 was treated with 10 mM of DTT or 10 mM H_2O_2. Arrows indicate the time point of addition of 2 mM GSH. **B** 1 µM of *Pp*GRXC5 or 1 µM *At*GRXC1 are incubated with 1 µM of pre-reduced roGFP2. As oxidation and reduction control, 1 µM of roGPF2 was treated with 10 mM DTT or 10 mM H_2O_2. Arrows indicate the time point of addition of 40 µM GSSG. Fluorescence intensities were collected with the plate reader with excitation at 390-10 nm and 480-10 nm and emission at 530-10 nm. Shown in A and B are the means(+SD) of three technical replicates (SD are within the size of the symbols).

4.1.3.3 Michaelis Menten constants of *Pp*GRXC5 and *At*GRXC1

GRX activity is generally determined in assays of disulfide reduction spectrophotometrically, following the absorption of a compound. An exemplary substrate for disulfide reduction catalyzed by GRX is bis(2 hydroxyethyl) disulfide (HED) (Equation 1). HED initially interacts with GSH resulting in a mixed disulfide (ßME(SSG)). This mixed disulfide is reduced via GRX. GSH re-reduces GRX yielding GSSG, which is regenerated by GR consuming NADPH. NADPH consumption is then followed at 340 nm (Begas *et al.* 2015).

Equation 1: Reaction of HED with GSH in the presence of GRX (modified after Deponte 2017; Trnka *et al.* 2020)

$$\mathrm{HED} + \mathrm{GSH} \rightleftharpoons \mathrm{ßME(SSG)} + \mathrm{GSH}$$

$$\mathrm{ßME(SSG)} + \mathrm{GRX(SH)} \rightleftharpoons [\mathrm{ES}] \rightarrow \mathrm{ßME} + \mathrm{GRX(SSG)}$$

$$\mathrm{GRX(SSG)} + \mathrm{GSH} \rightleftharpoons [\mathrm{ES}] \rightarrow \mathrm{GRX} + \mathrm{GSSG}$$

Due to the fast dissociation of the enzyme-substrate complexes [ES] of GRX with ßME(SSG) or GSH, K_m and k_{cat} values of GRX can be considered infinite and will not lead to a steady state of substrate saturation (Deponte 2017). However due to limitation of one substrate an apparent saturation is possible (Deponte 2017). Here, only apparent enzyme constants (^{app}) were determined.

HED reduction activity of *Pp*GRXC5 was tested and compared to *At*GRXC1, which was determined in previous studies for HED reduction activity (Riondet *et al.* 2012) and repeated in the lab of Andreas Meyer by Michelle Schlösser under the same conditions as in this work (unpublished data). K_m^{app} (apparent) and k_{cat}^{app} were calculated from the obtained GRX activities shown in Table 17, with varying GSH or HED substrate concentration. GRXC5 concentration was chosen according to the linear activity of the GRXC5 (30 nM).

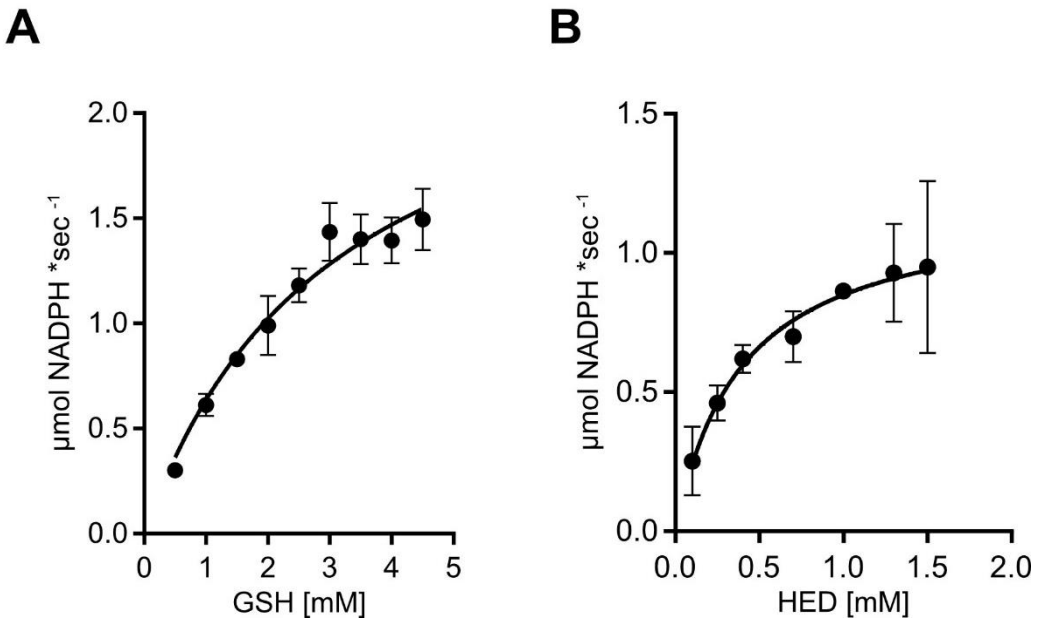

Figure 23 GRXC5 activity via HED-deglutathionylation assay

*Pp*GRXC5 [30 nM] was added to a cuvette containing GSH [0.5-4 mM], HED [0.3-1.5 mM], NADPH [200 µM], GR [6 µg/mL] (Saccharomyces cerevisiae, Sigma) in 100 mM Tris 1 mM EDTA pH 7.9. Decrease in absorbance at 340 nm was followed for 1 min(n=3+SD). **A** Varying concentration of GSH [0.5-4 mM] and a constant HED concentration of 0.7 mM was used**. B** Varying concentrations of HED and a concentration of 1 mM GSH was used. Non-linear regression was fitted using GraphPad (Prism 9) (n=4, mean + SD depicted).

k_{cat} ^{app}/K_m ^{app} values were calculated to compare *Pp*GRXC5 with other GRX apparent catalytic activities. *Pp*GRXC5 compared to cytosolic *At*GRXC1 and *At*GRXC2 measured under similar conditions showed a higher catalytic HED reduction activity of $1*10^5$ $M^{-1}s^{-1}$ compared to *At*GRXC1 with $0.83*10^5$ and *At*GRXC2 with $0.95*10^5$ $M^{-1}s^{-1}$ (Michelle Schlösser, Bonn, unpublished).

Table 17: Plastidial *Pp*GRXC5 reaction constants determined via HED assay

Protein	**K_m ^{app}** [mM]	**k_{cat} ^{app}** [s^{-1}]	**k_{cat} ^{app} /K_m ^{app}** [$M^{-1}s^{-1}$]
*Pp*GRXC5 (β-ME-SSG)	0.39 ± 0.11	39.45 ± 4.16	$1.00*10^5$
*Pp*GRXC5 (GSH)	3.09 ± 0.61	86.9 ± 8.73	$2.81*10^4$

4.1.4 Generation and characterization of the GRXC5 knock-out in *P. patens*

*Pp*GRXC5 knock-out plants were generated with the help of Alexa Brox (Prof. Frank Hochholdinger, Crop Functional Genomics, University of Bonn), who executed moss transformation and PCR screening experiments.

*Pp*GRXC5, with its oxidoreductase activity (Figure 22, Table 17), is an intriguing candidate for studying the GRX function on protein S-glutathionylation *in vivo*. Because only one member of class I GRX was identified in *P. patens* (*Pp*GRXC5), the moss is an ideal model organism for studying *in vivo* function by a gene knock-out. Knock-outs in *P. patens* can be achieved by homologous recombination, transforming protoplasts of the haploid gametophyte (Schaefer & Zryd 1997). In this work we generated a knock-out construct replacing the complete coding region between the first and last exon of Pp1s321_10V6.1 with a neomycin (nptI, G418) resistance cassette (Figure 24). As homologous regions, 602 bp upstream of the 5' genomic DNA sequence and 621 bp of downstream of the 3' sequence were chosen. Regenerated moss colonies surviving G418 (neomycin) selection were tested via PCR for correct construct integration (Figure 24 B) and absence of transcript (Figure 24 C). Three independent lines (Δ*grxc5* #54, #64 and #249) were used for further experiments. For line #249 no band was obtained in the PCR for 3' integration of the construct but showed an absence of transcript on cDNA level. For line #64 a weak band was detected (#64 '+'), therefore following experiments focused on #54 and #249 with a clear absence of *GRXC5* transcript.

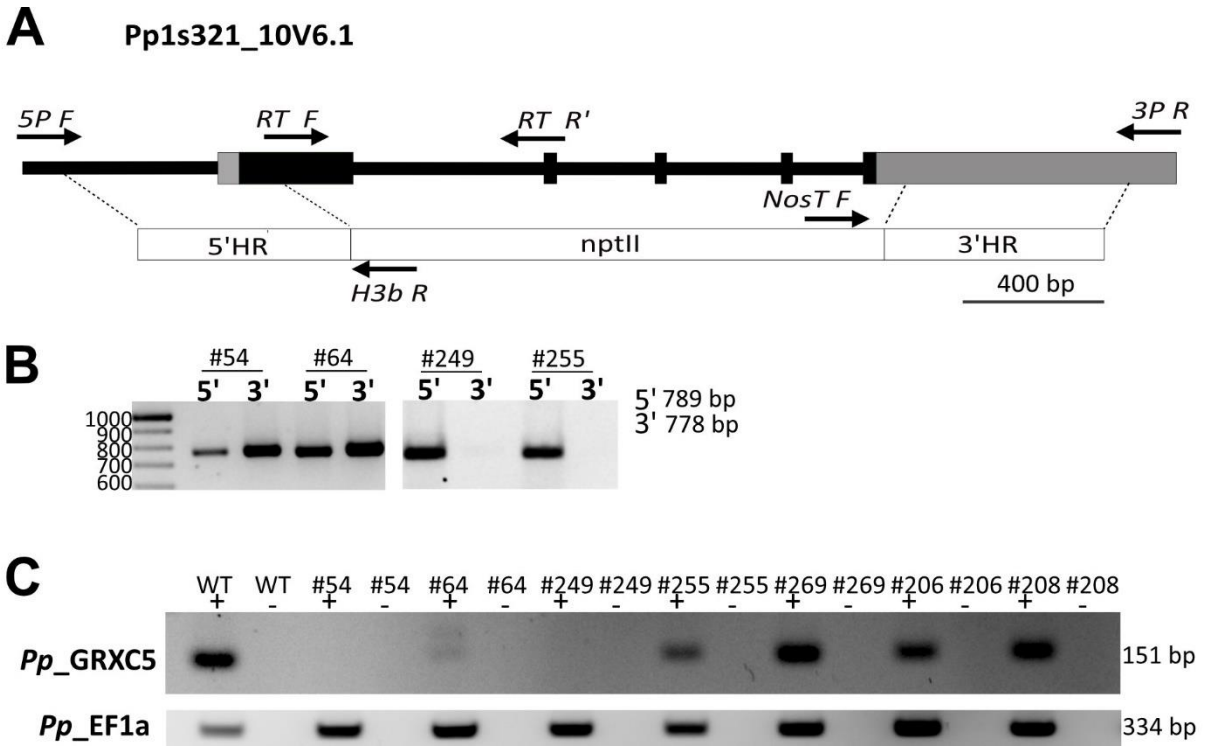

Figure 24: Generation and verification of Δ*grxc5* in *Physcomitrium patens*

A Schematic overview of the construct including an antibiotic resistance cassette (nptII) transformed via homologous recombination into the Pp1s321_10V6.1 locus of *P. patens*. Exons are depicted as black box. Grey boxes display 5'and 3' UTR. Arrows indicate primers used for screening as seen in Table 14. **B** 5' and 3' integration of construct verified by PCR using 5P F

and H3b R (5') or NosT F and 3P R (3') primer sets. **C** Verification of the absence of transcript on cDNA-level using gene specific primers for the *GRXC5* locus (*Pp*GrxC5ko_RT F and *Pp*GrxC5ko_RT R see Table 14). *EF1a* locus was used as cDNA positive control (PpEF1a_RT F and PpEF1a_RT R see Table 14).'-' indicates RNA samples to which no reverse transcriptase was added to the preparation of cDNA as control for absence of genomic DNA.

4.1.4.1 Phenotypic appearance of Δ*grxc5* under control and stress conditions

The function of plastidial class I GRX may be severely impacted by the loss of GR activity, because their kinetic activity is influenced by the GSH:GSSG ratio (Figure 7, see 4.1.1.1), which is maintained at a constantly high level by the organellar GR. Previously characterized plastidial and mitochondrial knock-outs of *Pp*GR1 with impairments in plastidial E_{GSH} showed a phenotype under high light (450 µE/m^{2}s) treatment also in combination with elevated temperature (35°C) (Müller-Schüssele *et al.* 2020). To test whether GRXC5 loss would result in the same phenotype as observed for Δ*gr1* (dwarfed, stress sensitive) and further confirming a function downstream of GR1, experiments were carried out as described in Müller-Schüssele *et al.* 2020.

All three lines (#54, #64, #249) lacking *GRXC5* transcript revealed a WT-like phenotype when grown under control conditions (Figure 25). Furthermore, Δ*grxc5* #54, #64 and #249 were exposed to elevated temperature (37°C) for 7 days in the dark (Figure 25 B). The knock-out lines showed no difference in growth, leaf shape or color compared to WT grown in the same conditions. Δ*grxc5* #54, #64 and #249 treated with two days of high light (450 µE/m^{2}s) combined with elevated temperature (35°C) lead to complete bleaching of the colonies of WT and mutants and death of the colonies, concluded from the absence of green tissue five days after treatment (Figure 25 C).

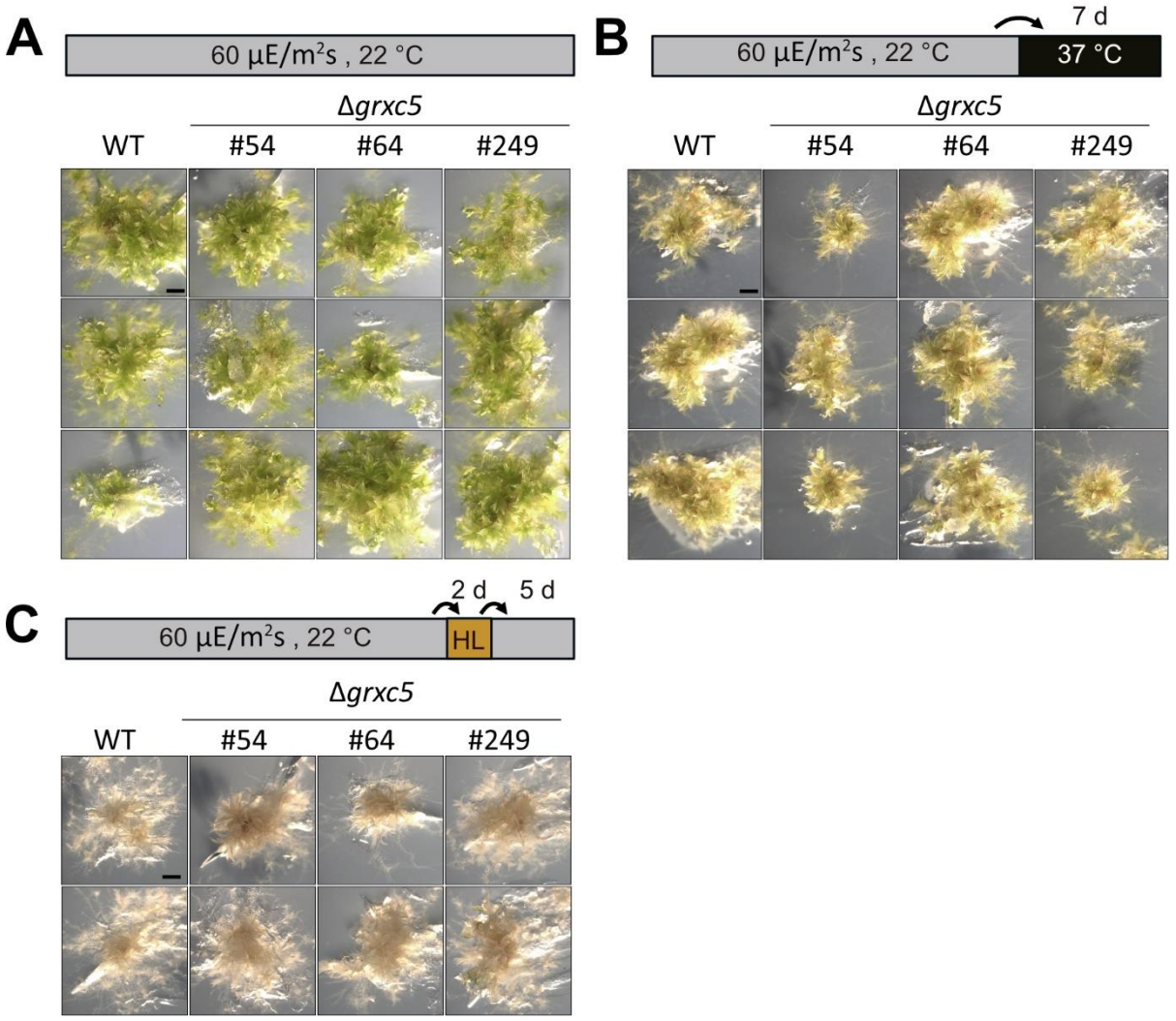

Figure 25: Four-week-old gametophores of *P. patens* under different light and temperature regimes

Four-week-old *P. patens* colonies grown on KNOP-ME pH 5.8 agar plates in 60 µE/m²s (16h light, 8h dark) for four weeks (A, control). After three weeks of growth, plates with moss colonies were transferred to 37°C and incubated in the dark for one week (B) or treated for two days with high light (450 µE/m²s) and elevated temperature (35°C) before transferring back to control conditions for 5 days (C). Size bar = 0.4 cm

Already identified plastidial targets of protein *S*-glutathionylation are important key enzymes in or associated to the Carbon Benson Cycle (CBC), such as fructose-1,6-bisphosphatase, glyceraldehyde-3-phosphate dehydrogenase (GAPDH), ribulose bisphosphate carboxylase or redox-regulating enzymes like the 2-Cys peroxiredoxin (Zaffagnini, Bedhomme, Groni, *et al.* 2012; Müller-Schüssele, Bohle, *et al.* 2021). Based on these results, we investigated mutant growth under fluctuating light conditions similar to 80 s 20 µE/m²s and 10 s 800 µE/m²s as seen for the identification of the plastidial 2-Cys peroxiredoxin mutant (2-*cysprxAB,* Vaseghi *et al.* 2018) Rapidly changing light intensities could reveal possible problems in regulating CBC enzyme activities. Gametophores were transferred to a petri dish containing solid KNOP-ME

medium and either grown for 14 days under control conditions or subjected to a fluctuating light regime with 15 min of 30 µE/m²s followed by 15 min with 800 µE/m²s (Figure 26 A,B) or 10 s at 800 µE/m²s and 80 s at 30 µE/m²s (Figure 26 C,D). Although moss colonies appeared slightly smaller, no difference was observed between the genotypes.

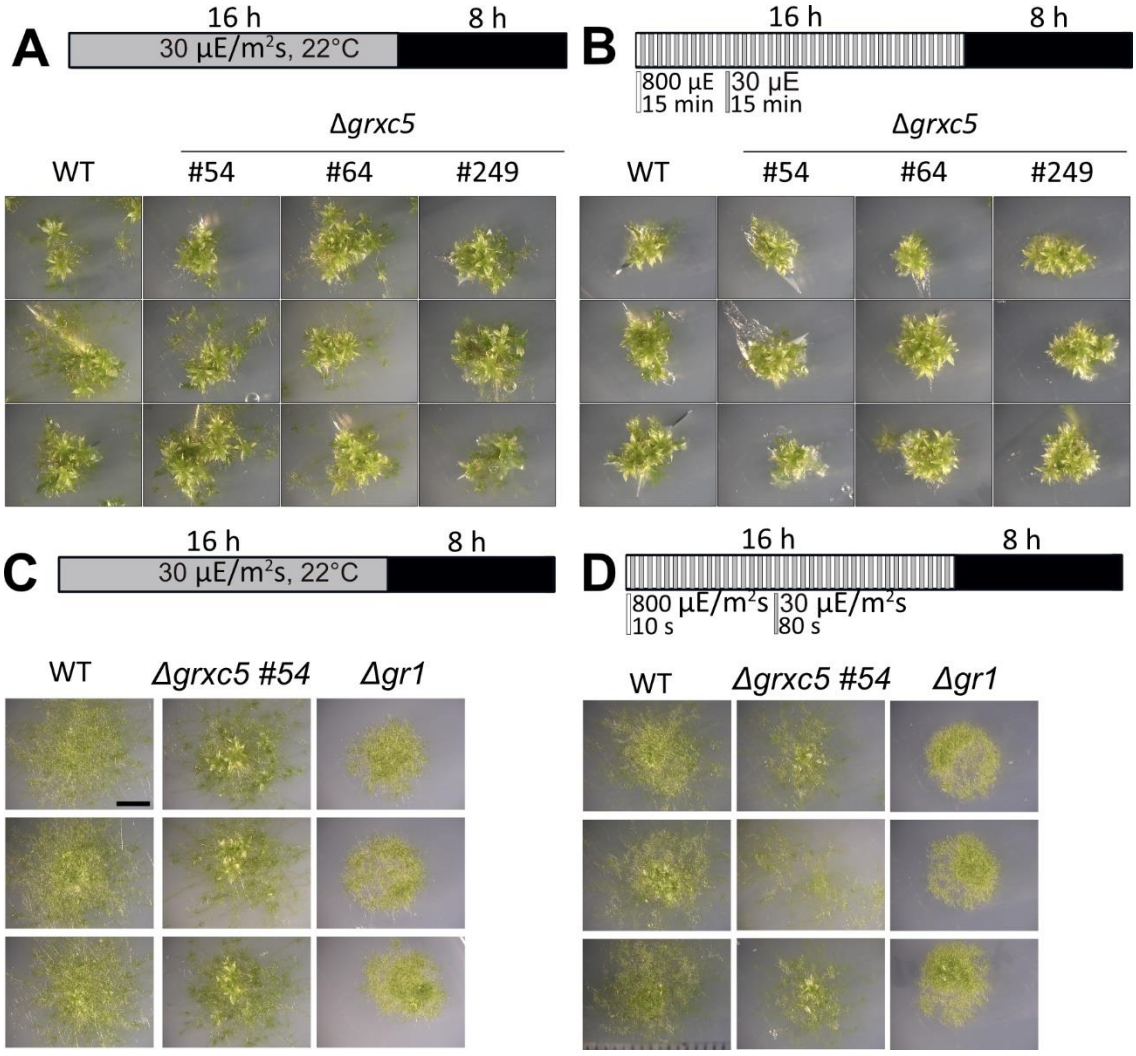

Figure 26: Δ*grxc5* shows WT-like growth in fluctuating light conditions

14-day old *P. patens* colonies of WT and Δ*grxc5* (#54, #64, #249) gametophores (**A**,**B**) or drops of protonema culture of WT, Δ*grxc5 #54* and Δ*gr1* (**C**,**D**) tissue, cultured in 30 µE/m²s for 14 days (**A**,**C**) or in a fluctuating light regime with 15 min of 800 µE and 15 min of 30 µE (**B**) or 10 s of 800 µE/m²s followed by 80 s of 30 µE/m²s (**D**) under long day conditions (16h/8h). Scale bar = 0.4 cm

Because GRXC5 is involved in target protein deglutathionylation, I suspect a phenotype downstream of target protein activity in the GRXC5 mutant. With the absence of GRXC5, these target proteins can no longer be deglutathionylated by GRXC5, potentially leading to changes in enzyme activity. *S*-glutathionylation has been shown to increase under oxidative stress conditions, for example, *S*-glutathionylation of the plastidial thioredoxin f (TRXf) (Michelet *et*

al. 2005; Zaffagnini, Bedhomme, Groni, *et al.* 2012). To induce oxidative stress in Δ*grxc5*, protonema culture Δ*grxc5* #54 was supplemented with 10 mM H_2O_2 for 15 min and placed on a KNOP-ME containing petri dish (Figure 27).

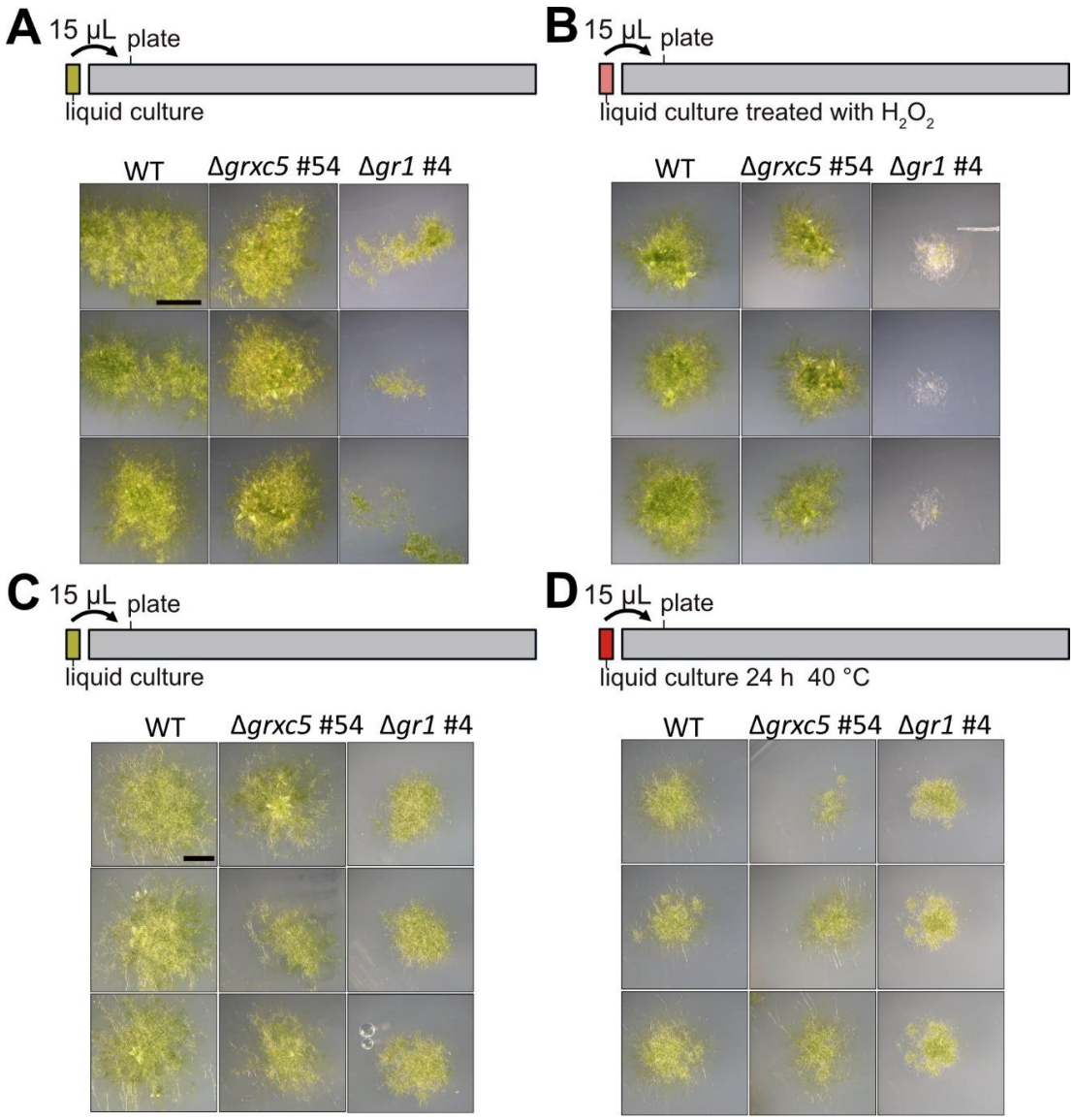

Figure 27: *P. patens* protonema culture after oxidative challenge or heat stress and subsequent recovery

Protonema (liquid) culture dropped onto KNOP-ME plates without treatment (A,C). Prior to transferring protonema culture to the plates, the culture was treated with 10 mM H_2O_2 for 15 min (**B**) or treated for 24 h with 40°C in the dark (**D**). 15-20 µL of protonema culture was placed on a KNOP-ME agar plate and grown under standard conditions (60 µE/m^2s, 22°C, 16 h/8 h). After 14 days (**A**,**B**) and 20 days (**C**,**D**) of growth images were taken. Scale bar for A and B = 5 mm, C and D = 4 mm

The regeneration of colonies was recorded after 14 days and showed a reduced growth for WT and Δ*grxc5* #54. To compare Δ*grxc5* growth, Δ*gr1* was simultaneously treated with H_2O_2 leading to death of the protonema. The dwarfed and slow growth of Δ*gr1* could be replicated

under control conditions (Figure 27 A; Müller-Schüssele *et al.* 2020).To investigate the photosynthetic performance of Δ*grxc5* and to relate it to the already available data of Δ*gr1* (Δ*gr1* #4,Müller-Schüssele *et al.* 2020), pulse amplitude modulated fluorometry (PAM) was performed with moss grown in light intensities of 60 µE/m^{2}s and 450 µE/m^{2}s (for 1 h and 4 h) prior to measurements. Moss colonies were dark incubated for 45 min. PAM measurements were performed by Stefanie Bethmann in the laboratory of Prof. Jahns (University of Düsseldorf). While Δ*gr1* showed a significant increase in non-photochemical quenching (NPQ) under control light (60 µE/m^{2}s), as well as after high-light (450 µE/m^{2}s) treatment, Δ*grxc5* #54 and #249 clustered with WT-levels of NPQ. As published in Müller-Schüssele *et al.* 2020, Δ*gr1* showed a slower NPQ dark relaxation which was not observed for Δ*grxc5* #54 and #249. After 4 h of 450 µE/m^{2}s the amount of NPQ of WT and Δ*grxc5* also increased, but differed significantly from Δ*gr1.*

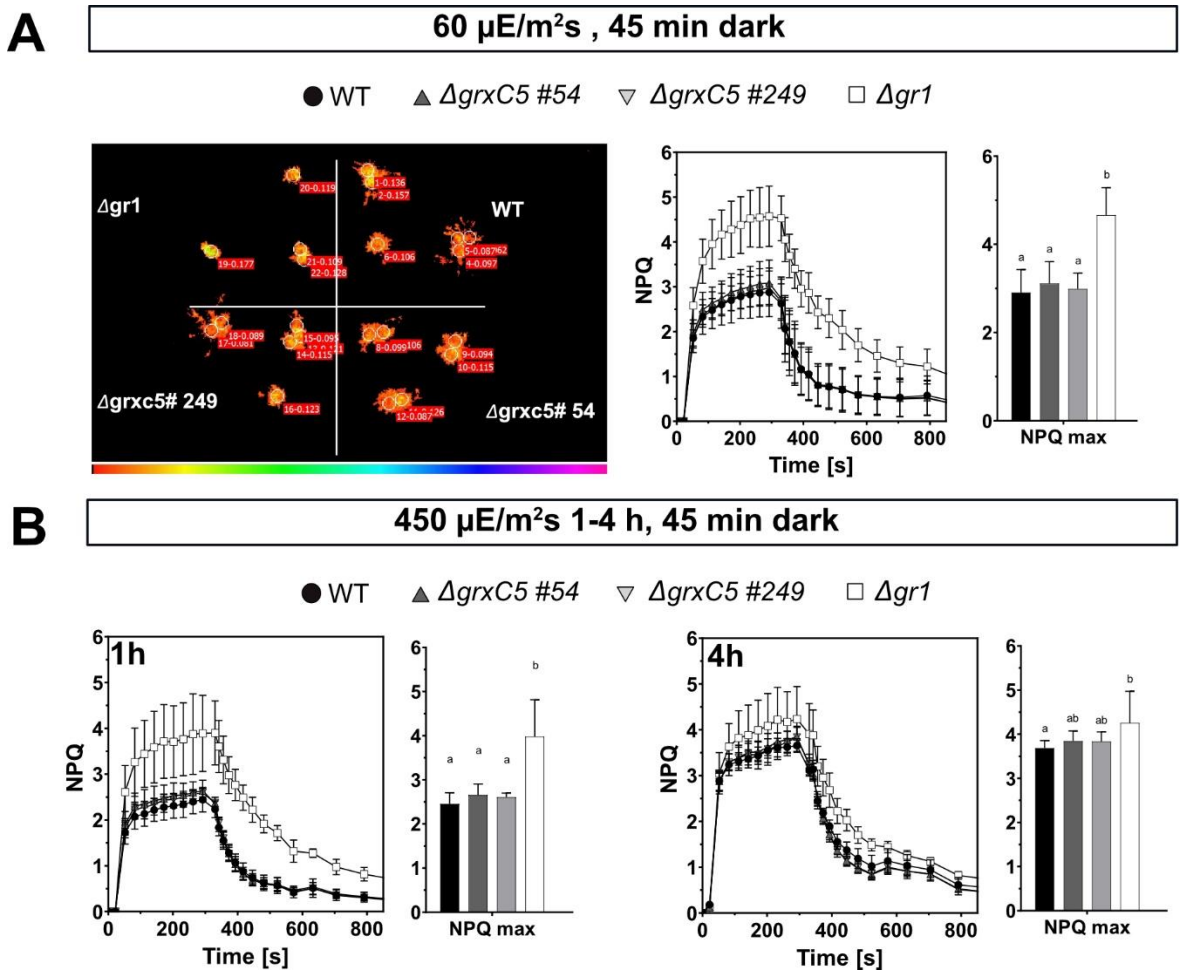

Figure 28: NPQ measurements of 4-week-old gametophores under low and high light regimes

4-week-old gametophore colonies measured with an imaging PAM either grown in control light at 60 µE/m²s (**A**) or treated for 1 h or 4 h with light intensities of 450 µE/m²s prior to experiment start (**B**). Dark adaption of 45 min took place before each NPQ measurement. Photosynthetically active radiance (PAR) was kept at 531 nm. Three agar plates with each three moss colonies were measured for control conditions, two agar plates for 1 h of 450 µE/m²s treatment and one plate for 4 h 450 µE/m²s treatment (each shown as mean + SD). Overview of the fluorescence emitted by the moss colonies shown in **A** (left). A two-way ANOVA with Tukey's multiple comparison test was conducted on NPQ_{max} to test for significant differences between the genotypes ($p<0.0055$). Small letter code: samples with different letters differ significantly.

4.1.5 (De)-glutathionylation activity in plastids of Δ*grxc5* – introducing roGFP2 as artificial *S*-glutathionylation target

roGFP2 oxidation occurs via a *S*-glutathionylation intermediate state and is catalyzed by class I GRX (Meyer *et al.* 2007; Meyer & Dick 2010), therefore roGFP2 can be used as artificial glutathionylation-target protein. Hence, we introduced roGFP2 into Δ*grxc5* #54 to investigate if (de)glutathionylation of roGFP2 will still be detectable in plastids of class I GRX knock-outs, verifying no remaining activity of class I GRX.

4.1.5.1 Cloning a TKTP-roGFP2 construct targeted to chloroplasts

To target roGFP2 into plastids, a transketolase targeting peptide of tobacco (TKTP; Wirtz & Hell 2003) was cloned by overlap PCR to the N-terminus of roGFP2 and was introduced into the PTA2_GW vector via Gateway™ cloning (see Table 7 for primer sequences; Figure 29 A). The construct PTA2_GW_TKTP-roGFP2 was used to transform *P. patens* WT (XI) and Δ*grxc5* #54 protoplast transiently and stably. Transiently transformed protoplasts were analyzed regarding the TKTP-roGFP2 localization and fluorescence signal (Figure 29 B,C). The signal was located to the plastids, verified by colocalization with chlorophyll autofluorescence. TKTP-roGFP2 in WT and Δ*grxc5* #54 revealed a dynamic range of δ = 5.13 (WT) and 4.46 (Δ*grxc5*). A two-way ANOVA (with Tukey's multiple comparison) showed significance between the oxidizing and reducing treatments but no difference between the genotypes within the respective treatments. Transformed protoplasts were regenerated and screened for roGFP2 fluorescence. The expression of plastidial roGFP2 in WT and Δ*grxc5* background did not reveal a different growth phenotype (Figure 30 A). However, fluorescent signal was not evenly distributed in the moss gametophore tissue of WT and Δ*grxc5*. Leaflets partially showed no fluorescence or high patches of fluorescence close to the midrib. For analysis only leaflets revealing a fluorescence pattern shown in Figure 30 B were used. Based on the fluorescent

signal, lines #20 and #46 were further used for WT imaging, while #17 and #21 were chosen for Δ*grxc5*.

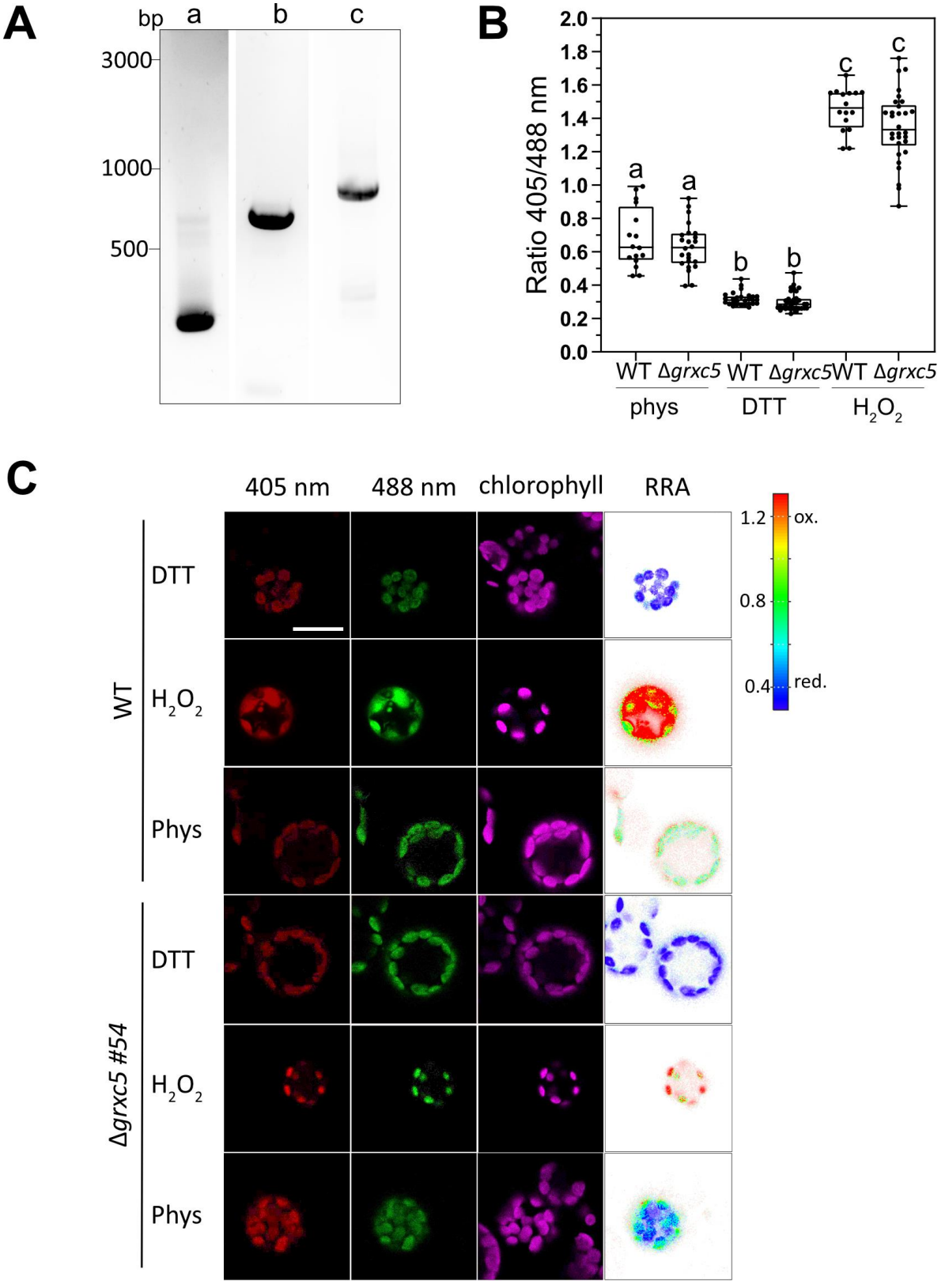

Figure 29: Cloning and transient calibration of TKTP-roGFP2 in protoplasts of WT and *Δgrxc5*

A Cloning of the gateway cloning construct *attB1*_TKTP-roGFP2_*attB2* was conducted in three steps. (a) the cloning of *attB1*-TKTP-roGFP2 (263 bp), (b) roGFP2_*attB2* (763 bp) and the final construct *attB1*-TKTP-roGFP2-*attB2*(c) with an expected size of 1026 bp. Primers are shown in Table 7. **B** Protoplasts transiently expressing TKTP-roGFP2 calibrated with 10 mM DTT and 10 mM H_2O_2 for 30 min prior to imaging (CLSM). Shown are all data points with whiskers showing min and max values. Median is displayed as horizontal line. Two-way ANOVA with Tukey's multiple comparison analysis ($p<0.0001$) was conducted to test for significance. Different lowercase letters display significant differences. Each data point shows the roGFP2 ratio for a protoplast (n>20) **C** Confocal images of TKTP-roGFP2 protoplast of WT and Δ*grxc5* treated with 10 mM DTT, 10 mM H_2O_2 or imaged in regeneration medium (Phys).Ratio image analysis was done on raw images using the RRA imaging software (Fricker 2016). Scale bar = 20 µm

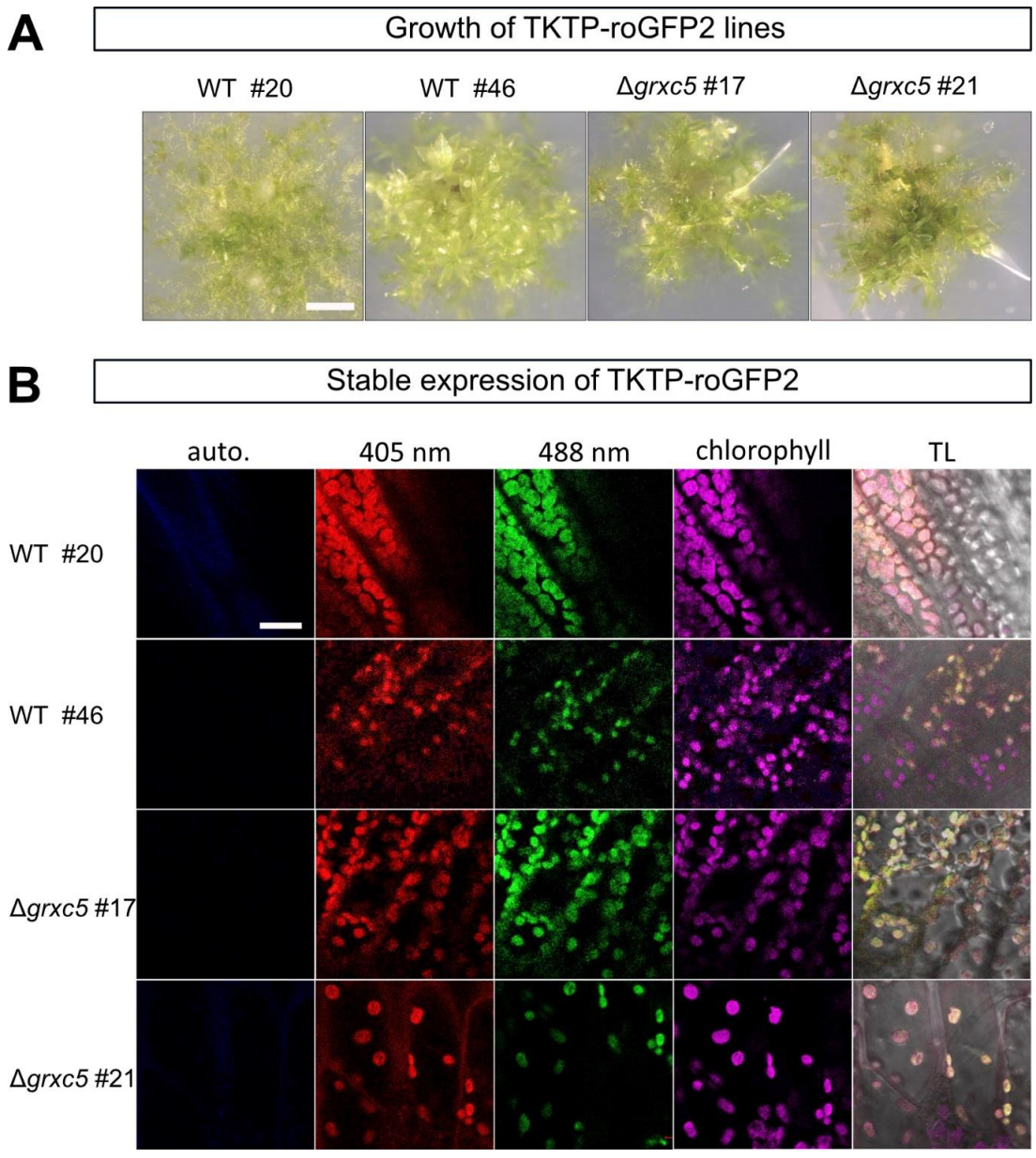

Figure 30: Phenotype of *P. patens* gametophores stably expressing TKTP-roGFP2

A Growth of 4-week-old *P. patens* gametophores on KNOP-ME under standard growth conditions. Scale bar = 0.2 mm. **B** Fluorescent images of *P. patens* gametophores stably expressing TKTP-roGFP2 obtained with the CLSM. Autofluorescence (auto.) TL (transmitted light). Scale bar = 20 µm.

4.1.5.2 TKTP-roGFP2 *in vivo* calibration and E_{GSH} determination

To test for specific roGFP2 signal in *P. patens* WT and Δ*grxc5* an excitation scan was performed. Reduction of TKTP-roGFP2 with DTT led to an increase in peak intensity at 480 nm while oxidation via DPS (2,2'-Dipyridyldisulfide) resulted in a decrease of the peak intensity at 480 nm in WT and mutant background (Figure 31). roGFP2 in the stroma of WT was more reduced than the mutant under physiological (Phys) conditions, indicated by a higher peak at 480 nm than in both Δ*grxc5* (#17 and #21) lines. Intensities below the isosbestic point of roGFP2 at 425 nm did only show minor changes in fluorescence upon treatments with either DTT or DPS. The *in vivo* dynamic range (405 nm/488 nm) was determined to be 2.15-fold for WT and 2.2-fold for Δ*grxc5* (#17 δ= 2.2, #21 δ= 2.0).

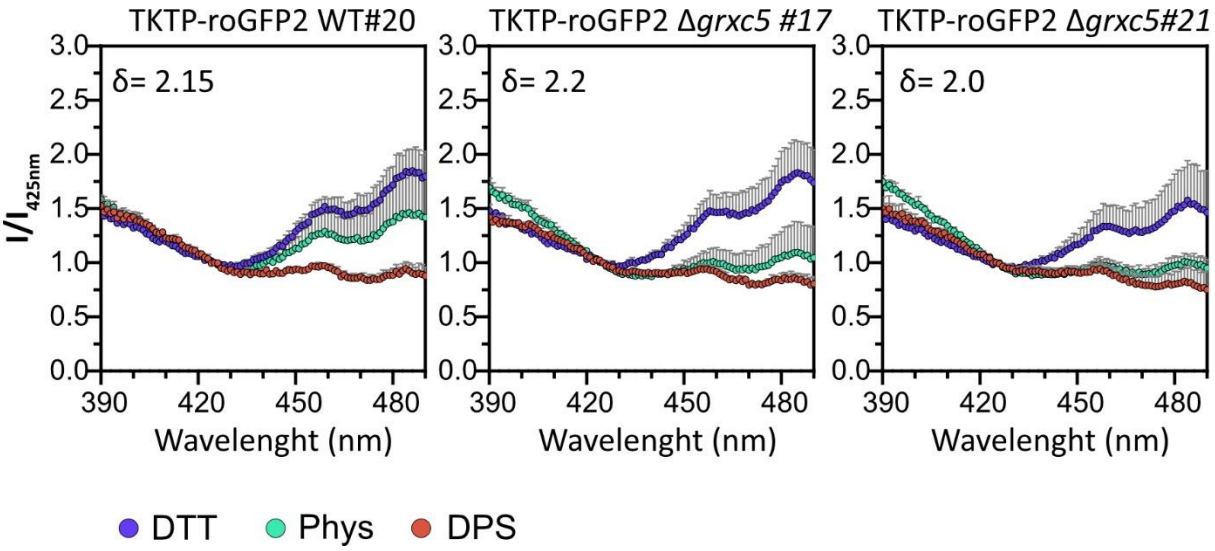

Figure 31: Excitation scan of *P. patens* protonema culture stably expressing plastidial roGFP2

Protonema culture of *P. patens* was treated for 30 min with 10 mM DTT or 5 mM DPS and transferred into a 96-well plate. Wells were excited at 390-490 nm while emission was collected at 535-16 nm via the plate reader. Intensities were normalized to the intensity of the isosbestic point or roGFP2 (425 nm). Shown is the mean and SD (n=3).

Protonema cultures of WT and Δ*grxc5* stably expressing TKTP-roGFP2 were additionally calibrated with 10 mM DTT, 10 mM H_2O_2 and 5 mM DPS and imaged with the CLSM. Complete oxidation (DPS) and reduction (DTT) of TKTP-roGFP2 revealed a dynamic range of δ =2.9 (WT; TKTP-roGFP2 #20) to 3.83 (WT; TKTP-roGFP2 WT #46) and 2.79-fold (Δ*grxc5;* TKTP-roGFP2 #17) to 3.47-fold (Δ*grxc5;* TKTP-roGFP2 #21) for Δ*grxc5* (Figure 32). A two-way ANOVA displayed significant differences between treatments, but no significant difference between genotypes and the respective lines.

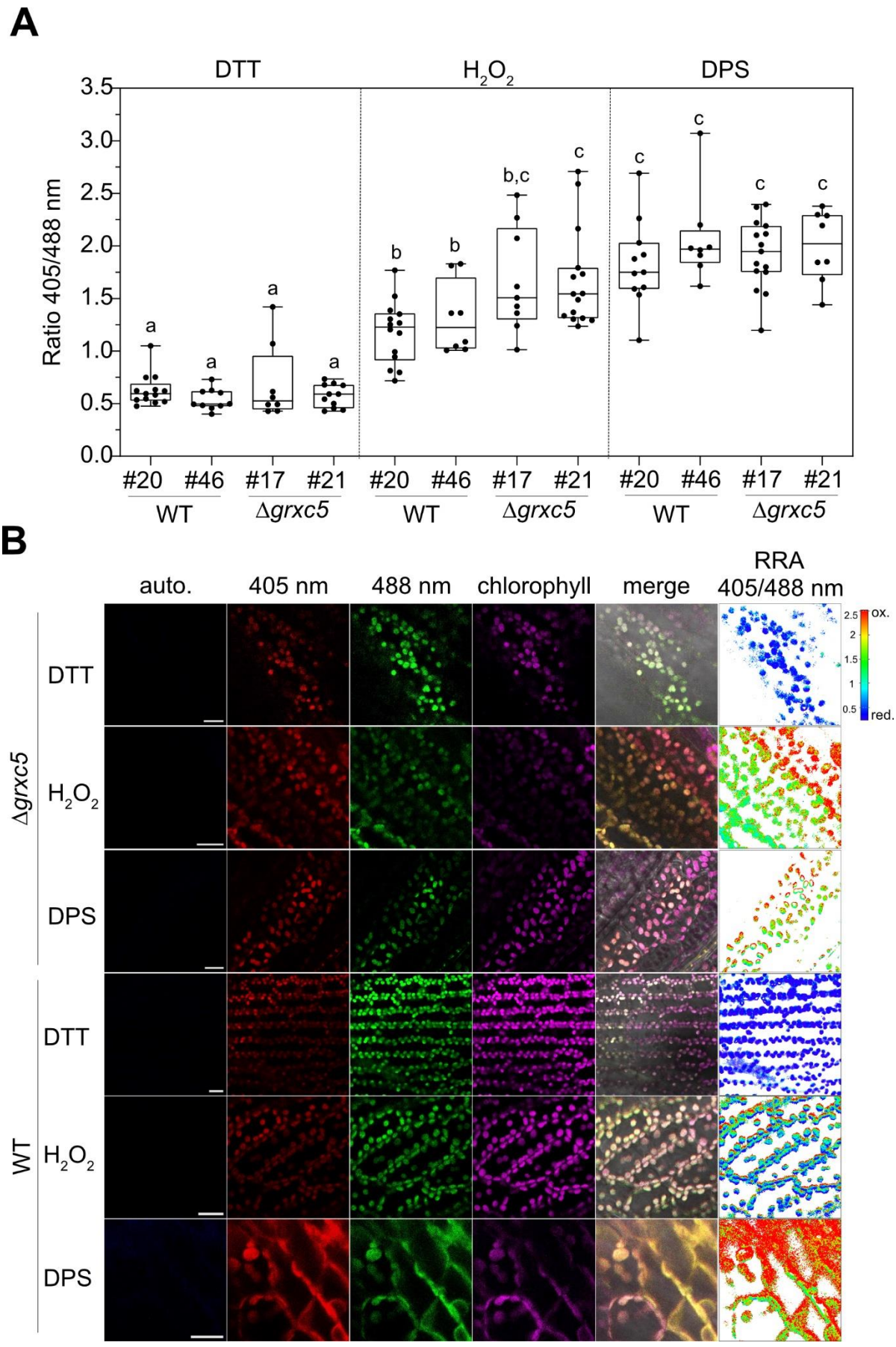

Figure 32: *In vivo* sensor calibration of TKTP-roGFP2 and ratiometric image analysis

A Sensor calibration of TKTP-roGFP2 in *P. patens* grown in protonema and gametophore mix culture with 10 mM DTT, 5 mM DPS or 10 mM H_2O_2 incubated for at least 20 min. Shown are whiskers as min and max values with the horizontal line indicating the median. Two-way ANOVA (+ Tukey's multiple comparison) was conducted to test for significance ($p<0.0001$). Different lowercase letters indicate significant difference. ($n>7$) **B** Ratiometric images of confocal images used for sensor calibration (see A) via RRA analysis software. roGFP2 was excited at 405 nm and 488 nm with emission set to 508-535 nm. Scale bar = 20 µm.

Next, *P. patens* WT and Δ*grxc5* were imaged in liquid culture to determine the extent to which roGFP2 is oxidized under physiological, unstressed conditions. Because there is more moss material per area on the slide when using densely grown liquid culture, it is easier to set a focus to fluorescent material in the CLSM without prescreening. Therefore, liquid culture was imaged in the CLSM with pre-incubation in the dark before imaging and minimizing potentially oxidizing effects by laser scanning and epifluorescence screening, to investigate potentially differences between WT and Δ*grxc5* in the ratio of roGFP2 under physiological conditions. The stromal targeted roGFP2 in WT showed a significant lower 405/488 nm ratio of 0.62 ± 0.29, while Δ*grxc5* #17 and #21 showed a ratio of 1.3 ± 0.37 and 1.0 ± 0.27 indicating that roGFP2 was more oxidized in the mutants lacking plastidial GRXC5 (Figure 33). Interpretation of roGFP2 oxidation degree in Δ*grxc5* must be done with caution, due to the lack of GRX as catalyst and therefore only the thermodynamic equilibration of the E_{GSH} with roGFP2.

To further elucidate if higher roGFP2 ratios in the mutants were due to the lack of GRXC5 resulting in a slower deglutathionylation of roGFP2, we monitored roGFP2 ratios after oxidative stress treatment and analyzed the recovery rate for the reduction of roGFP2.

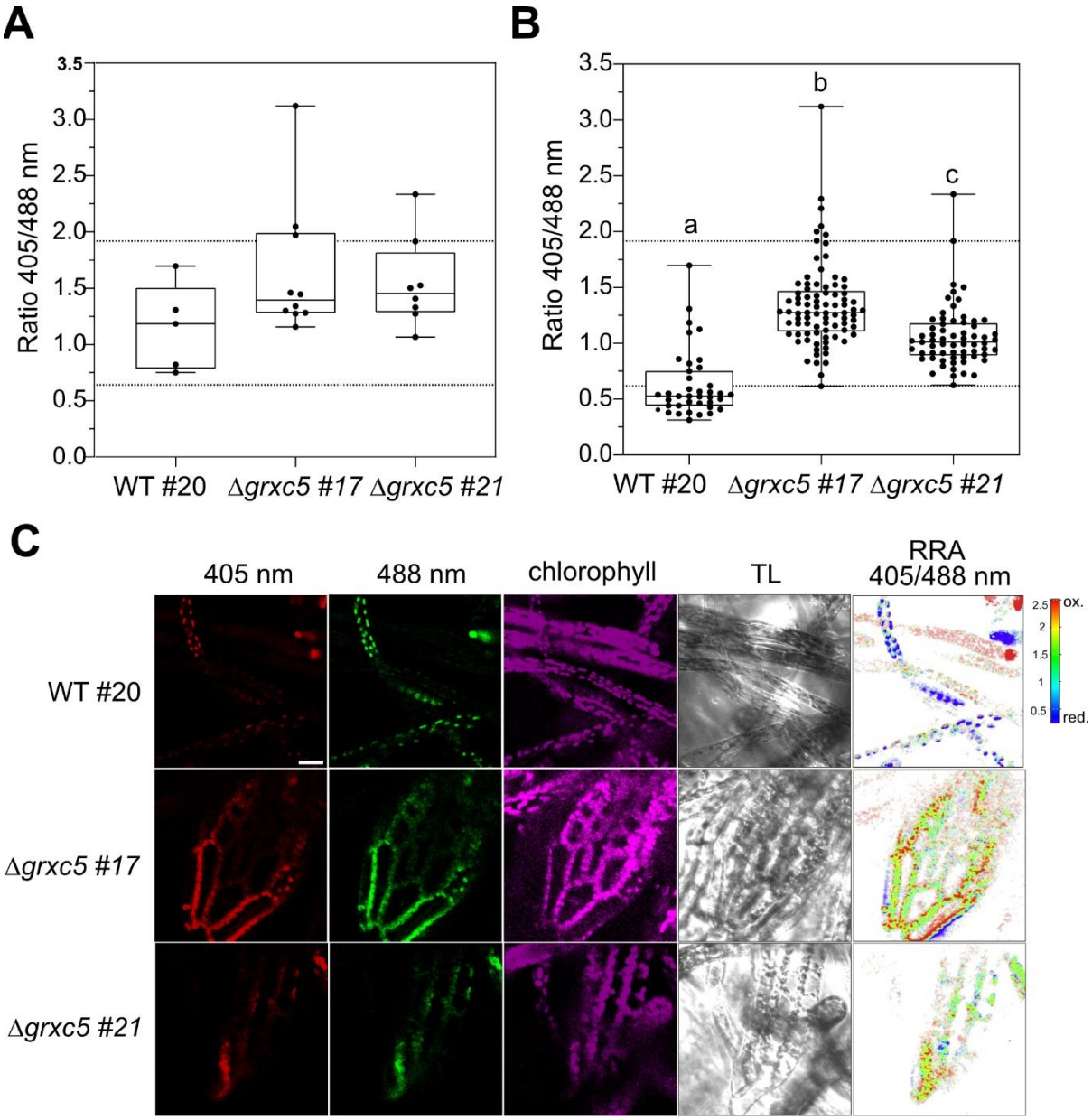

Figure 33: Ratio of TKTP-roGFP2 in dark adapted protonema culture

P. patens protonema culture was pre-incubated in the dark for 30 min before imaging with the CLSM (Ex. 405, 488 nm; Em. 508-535 nm). Samples were not screened prior to imaging to limit laser exposure of the chloroplasts. Fluorescence was extracted from the total image (n=5-10) (**A**) or regions of interest were set into chloroplasts with the images of A (**B**). Intensities were extracted using the RRA ratio analysis software. Dotted lines depict the dynamic range of the sensor *in vivo (*R_{min} 0.6 R_{max} 1.9; Figure 32*)*. Whiskers are min and max values with the median shown as horizontal line. One-way ANOVA (with Tukey's multiple comparison test) was conducted to test for significance ($p<0.0001$). No significant difference was detected in A. B shows significant differences indicated with different letters. Exemplary image cutouts are displayed in **C**. Scale bar = 20 µM

To study the roGFP2 oxidation and reduction rates in plastids of WT and Δ*grxc5,* moss gametophores were imaged with the CLSM. The change in fluorescence of roGFP2 was studied within a few cells and their chloroplasts after oxidizing or reducing *P. patens* leaflets (Figure 34). roGFP2 targeted to plastids in WT showed an increase in 405/488 nm ratio after H_2O_2 addition and a ratio reduction after DTT addition. While the increase in roGFP2 ratio after H_2O_2 application was also detected in Δ*grxc5*, the decrease of roGFP2 ratio after DTT addition was not detected within 15 min of imaging, seen either in the unchanged ratio as well as in the unchanged false-color fluorescence images of the roGFP2 time series (Figure 34). However, the CLSM data verifies that the measured roGFP2 changes are due to specific changes in plastidial roGFP2 signal.

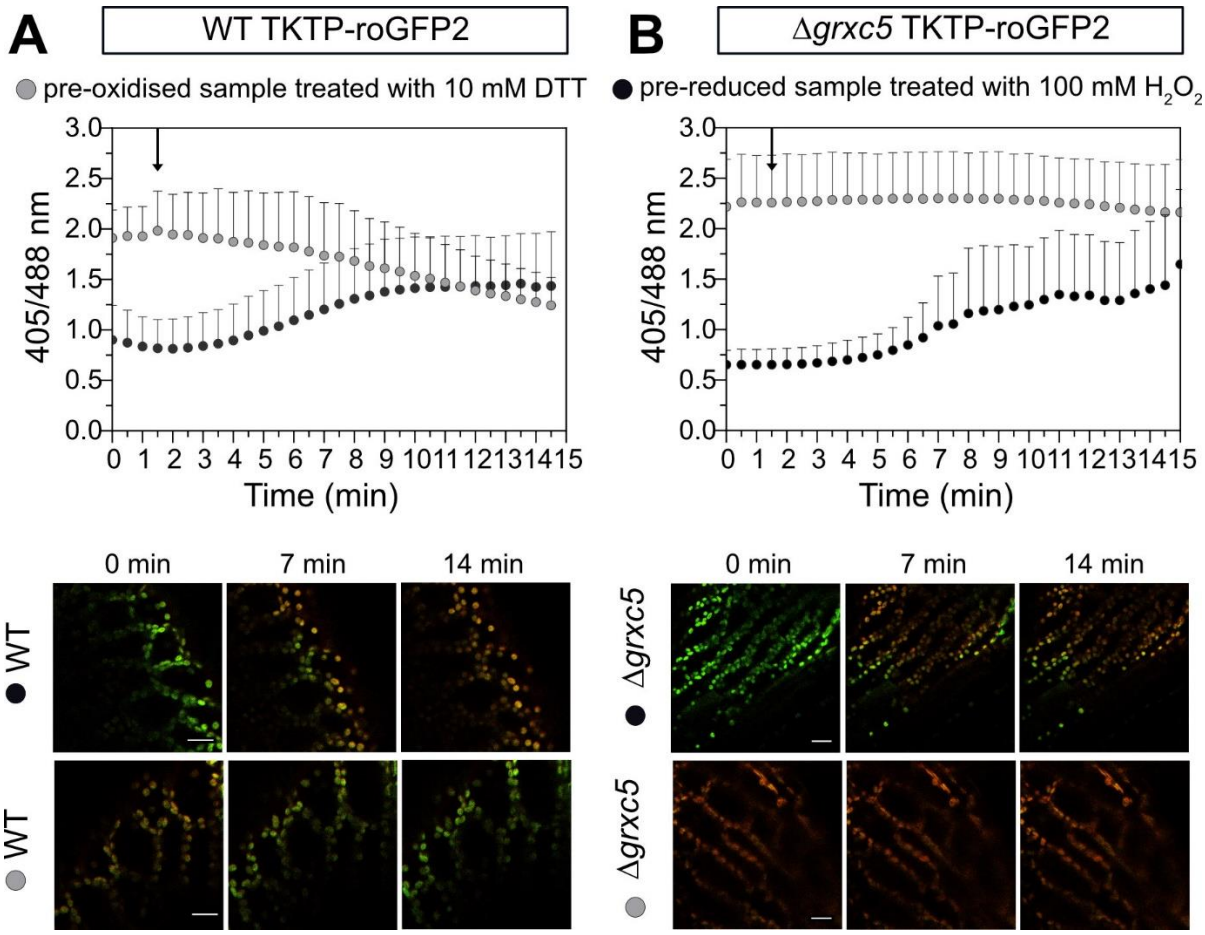

Figure 34: Sensor reduction and oxidation of WT and *Δgrxc5* in leaflets of *P. patens*

Leaflets of WT (**A**) and Δ*grxc5* (**B**) *P. patens* gametophores grown on agar plates were either treated with 100 mM H_2O_2 or with 10 mM DTT for 15 min via a perfusion chamber set-up and imaged with the CLSM (Ex. 405 nm, 488 nm; Em. 508-535 nm). Images display the 405/488 nm ratio. After 1.5 min of imaging, DTT (10 mM) was added to the pre-oxidized samples, while H_2O_2 (100 mM) was added to the pre-reduced samples. Changes in intensities were imaged every 30s for up to 15 min. Shown is the mean with SD (n=4-7). Example images taken after 0, 7 and 14 min and are depicted below the graphs. Intensities were extracted using RRA image analysis.

4.1.5.3 Decreased velocity of roGFP2 reduction in Δ*grxc5* compared to WT

The differences in roGFP2 reduction rate between WT and Δ*grxc5* (Figure 34) prompted us to further investigate roGFP2 recovery after oxidative stress. Δ*grxc5* and WT expressing TKTP-roGFP2 were challenged by the addition of either 1, 2, 5 or 10 mM H_2O_2 to protonema culture (Figure 35). The initial roGFP2 ratio was measured before H_2O_2 addition. roGFP2 expressed in Δ*grxc5* had an initial sensor oxidation of 60%, whereas roGFP2 in WT showed 30% sensor oxidation. Partial sensor oxidation may be light-induced, due to previous results showing complete reduction of roGFP2 in dark-incubated WT (see Figure 33).

Within 20 min after 1 mM H_2O_2 addition, roGFP2 in WT was rapidly oxidized (Figure 35 A). A rapid re-reduction of roGFP2 was observed after 40 min leaving only 53.1 ± 32.3% of roGFP2 oxidized. After the removal of H_2O_2 from the sample, roGFP2 was further reduced to 2.9 ± 48.8%. This behavior of roGFP2 expressed in WT was detectable for H_2O_2 concentrations up to 2 mM (Figure 35 B). Concentrations equal or higher than 5 mM prevented the reduction of roGFP2 before removal of H_2O_2 (Figure 35 C, D, E). While these roGFP2 reduction kinetics were measurable within the WT, they were completely abolished in Δ*grxc5* lines (#17, #21). The addition of 1 to 10 mM H_2O_2 increased sensor oxidation to 100%, but did not result in a detectable sensor reduction before H_2O_2 removal. roGFP2 in Δ*grxc5* remained up to 78% oxidized 20 min after H_2O_2 removal (1 mM H_2O_2, #17 = 76 ± 17.5%, #21 = 80.9 ± 14.8%).

To compare the kinetics of roGFP2 reduction after H_2O_2 removal, intensities were normalized to initial ratio values over fluorescence intensities measured for 100% oxidized roGFP2 (Figure 35 E). roGFP2 in WT was reduced within the first 40 min after H_2O_2 removal to a plateau value of 0.7 (405/488 normalized to t_0), while roGFP2 in Δ*grxc5* #17 and #21 showed a ratio of ~ 0.90 after 70 min. A two-way ANOVA (with Tukey's multiple comparison test; comparing normalized ratios at each time point between lines) revealed significant differences in the kinetics of roGFP2 reduction starting from 11 min after H_2O_2 removal.

As additional control, roGFP2 oxidation was monitored in WT and Δ*grxc5* not exposed to H_2O_2 (Figure 35 F). While roGFP2 in Δ*grxc5* #17 and 21 showed a rather constant level of oxidation (~80% oxidized), roGFP2 in WT background showed a fast decrease in the first 10 min (from 30% - 5% of oxidation) of measuring and a fast increase with a concomitant decrease of roGFP2 oxidation after taking out the 96-well plate.

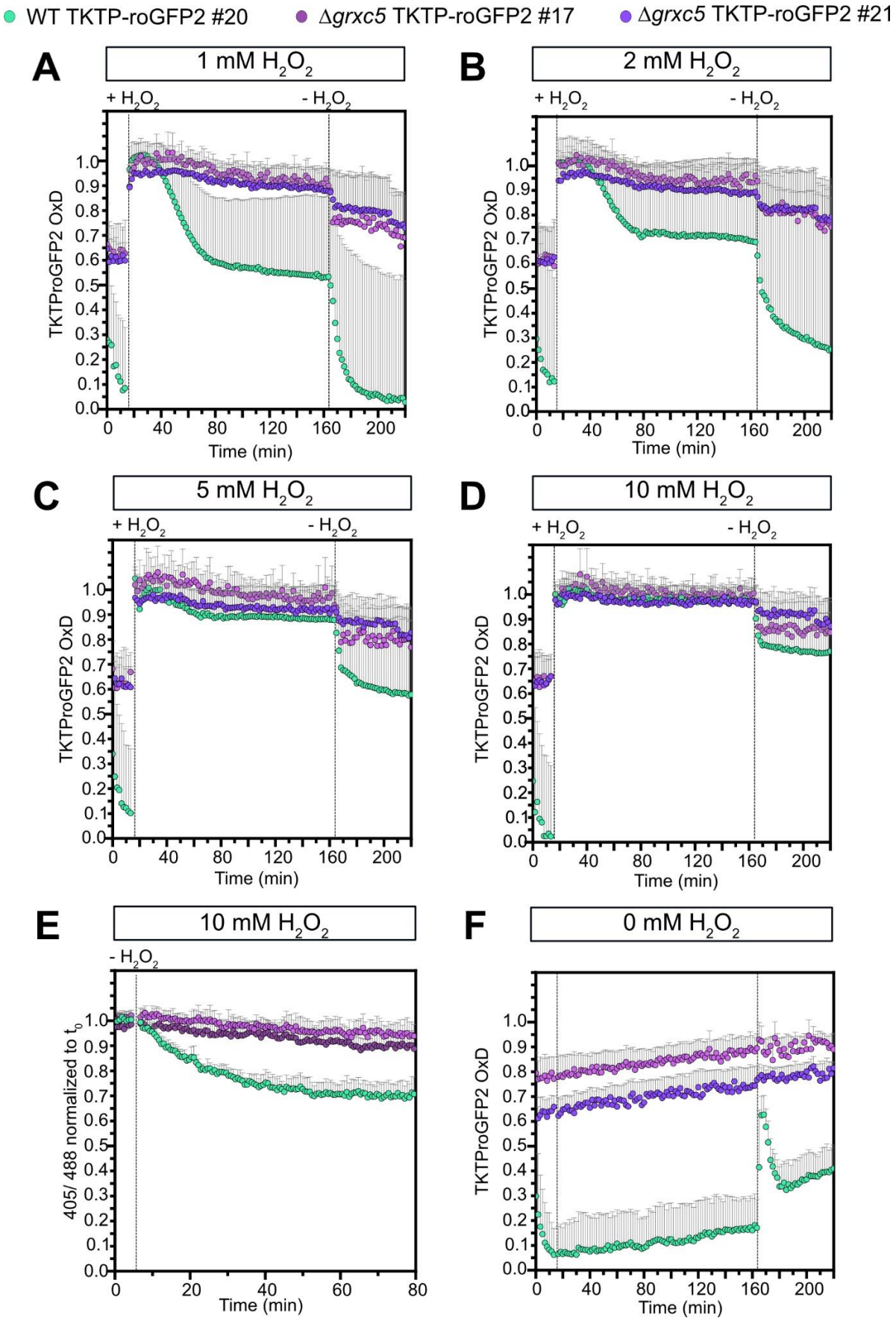

Figure 35: Recovery of TKTP-roGFP2 after oxidative challenge in protonema culture of *P. patens*

Protonema culture of *P. patens* expressing TKTP-roGFP2 was imaged for 16 min before addition of 1 mM (**A**), 2 mM (**B**), 5 mM (**C**) 10 mM (**D**) H_2O_2 ('+H_2O_2') or 0 mM H_2O_2 (**F**) Removal of H_2O_2 is indicated as '- H_2O_2'. Addition or removal of H_2O_2 are indicated by dotted lines. For fully oxidized and fully reduced controls 10 mM H_2O_2 or 10 mM DTT were preincubated for 30 min with the protonema culture and used for calculation of the degree of oxidation of roGFP2. After 165 min the buffer containing peroxide was exchanged to imaging buffer for measuring the recovery rate ('reduction') of roGFP2. Three biological replicates with three technical replicates each were done for each line and treatment (n=9). Shown are the mean + SD values. **E** Protonema culture expressing roGFP2 treated with 10 mM H_2O_2 for 30 min prior to measurement start. H_2O_2 was exchanged with imaging buffer ~5 min after measuring start and 405/488 nm ratio was normalized to t_0. Shown is the mean + SD of two independent experiments with 3 technical replicates (n=6). A two-way ANOVA (with Tukey's multiple comparison test) was conducted on data of E for each time point revealing significant differences in roGFP2 kinetics between WT and both Δ*grxc5* #17 and #21 starting from 11 min after peroxide removal ($p < 0.001$).

4.1.5.4 Quantification of protein-bound GSH in mutants with impairments in the organellar glutathione system

There were significant differences in the reduction of stroma-localized roGFP2 after oxidative stress between WT and Δ*grxc5* (Figure 35, Figure 34). The time point 30-40 minutes after 10 mM H_2O_2 treatment had the greatest difference between the lines (Figure 35 E). The rates of roGFP2 reduction after oxidative stress indicated that target proteins of *S*-glutathionylation are deglutathionylated more slowly in Δ*grxc5*. Thus, 30 minutes after oxidative stress, a difference in *S*-glutathionylated proteins between WT and Δ*grxc5* would be expected. To test this hypothesis, total protein was isolated and immunodetection analysis was performed to determine whether the *in vivo* target proteins of *S*-glutathionylation differ in the amount of glutathionylation in mutants lacking class I GRX in plastids.

First immunoblots were performed with protein extracts of gametophores tissue of WT and Δ*grxc5* #54 treated with 10 mM H_2O_2 for 30 min and compared to untreated gametophore tissue. Gametophore tissue was treated by submergence of the in-agar-grown moss colonies with 15 mL of 10 mM H_2O_2 diluted in KNOP-ME medium. H_2O_2 was discarded after treatment and the gametophores were dried with a paper tissue before freezing in liquid nitrogen. Frozen moss samples were used for protein extraction in the presence of NEM to block free thiol groups. A non-reducing SDS-PAGE as protein loading control and a Western Blot was done against glutathione (see Figure 36 A).

No difference in the total amount of protein glutathionylation between WT and Δ*grxc5* before oxidative challenge ('C', before 10 mM H_2O_2) were observed (Figure 36 B, C). An increase of *S*-glutathionylation was observed for WT and Δ*grxc5* after oxidative challenge ('H_2O_2').

However, no apparent difference in the intensities of protein-bound GSH was observed within control or treatment between WT and Δ*grxc5*.

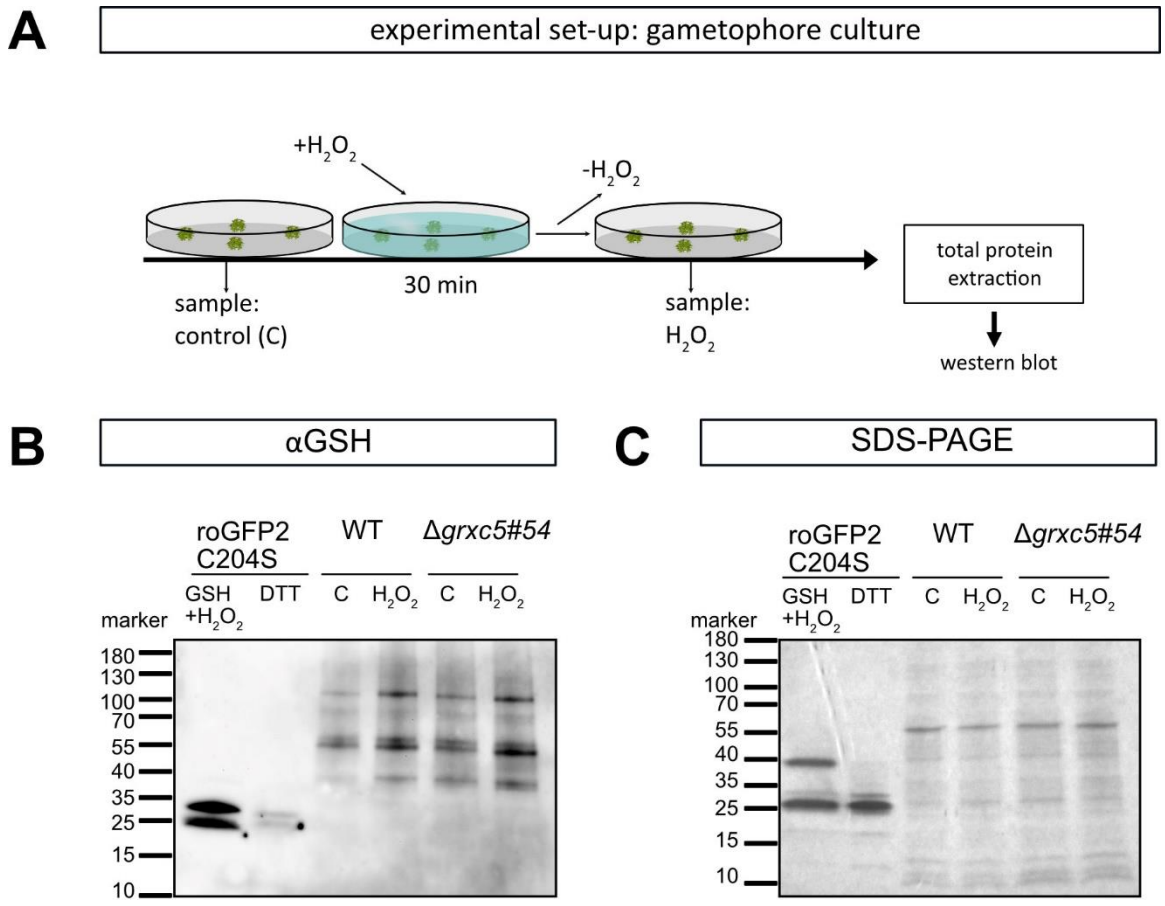

Figure 36: Protein *S*-glutathionylation state of *Δgrxc5* gametophores treated with 10 mM H_2O_2

A Schematic overview of the experimental set-up and sampling. **B** Immunoblot with αGSH (ThermoFisher) of glutathionylated proteins extracted from *P. patens* WT and Δ*grxc5* #54 gametophore tissue treated with 10 mM H_2O_2 and harvested at different time points ('C', 'H_2O_2'). Proteins were extracted and blocked with 20 mM NEM in the protein lysis buffer. As additional controls to test antibody specificity, 10 µg roGFP2-C204S was treated with 10 mM H_2O_2 and 2 mM of GSH for 30 min (positive control) or treated with 10 mM DTT (negative control). Proteins were extracted in the presence of 20 mM NEM. Simultaneously, 10 µg total protein was loaded onto a 4-20% gradient non-reducing SDS-PAGE as loading control (**C**).

Additional Western blots were performed to compare protein *S*-glutathionylation before and 30 min after H_2O_2 treatment (H_2O_2 recovery). To test for the recovery rate (deglutathionylation after H_2O_2 treatment) the experimental set-up in Figure 36 A was extended with an additional step. After removing the H_2O_2, moss colonies were washed with H_2O_2, dried with a paper tissue, and incubated for 30 min (Figure 37 A). In addition to the GRXC5 mutant, the organellar GR mutant (Δ*gr1* #4, Müller-Schüssele *et al.* 2020) will be tested for differences in glutathionylation levels after oxidative stress. This is motivated by the fact

that the cause of the GR1 mutant's phenotype has yet to be identified (Müller-Schüssele *et al.* 2020). One possible cause may be the malfunction of plastidial class I GRX through changes in E_{GSH} and GSH:GSSG ratio (see 4.1.1.1).

WT, Δ*gr1* #4, Δ*grxc5* #54 and #249 showed higher intensities in glutathionylated proteins after 30 min of oxidative stress ('H_2O_2 recovery'). The highest level of protein-bound GSH was detected in Δ*gr1* (Figure 37 B).

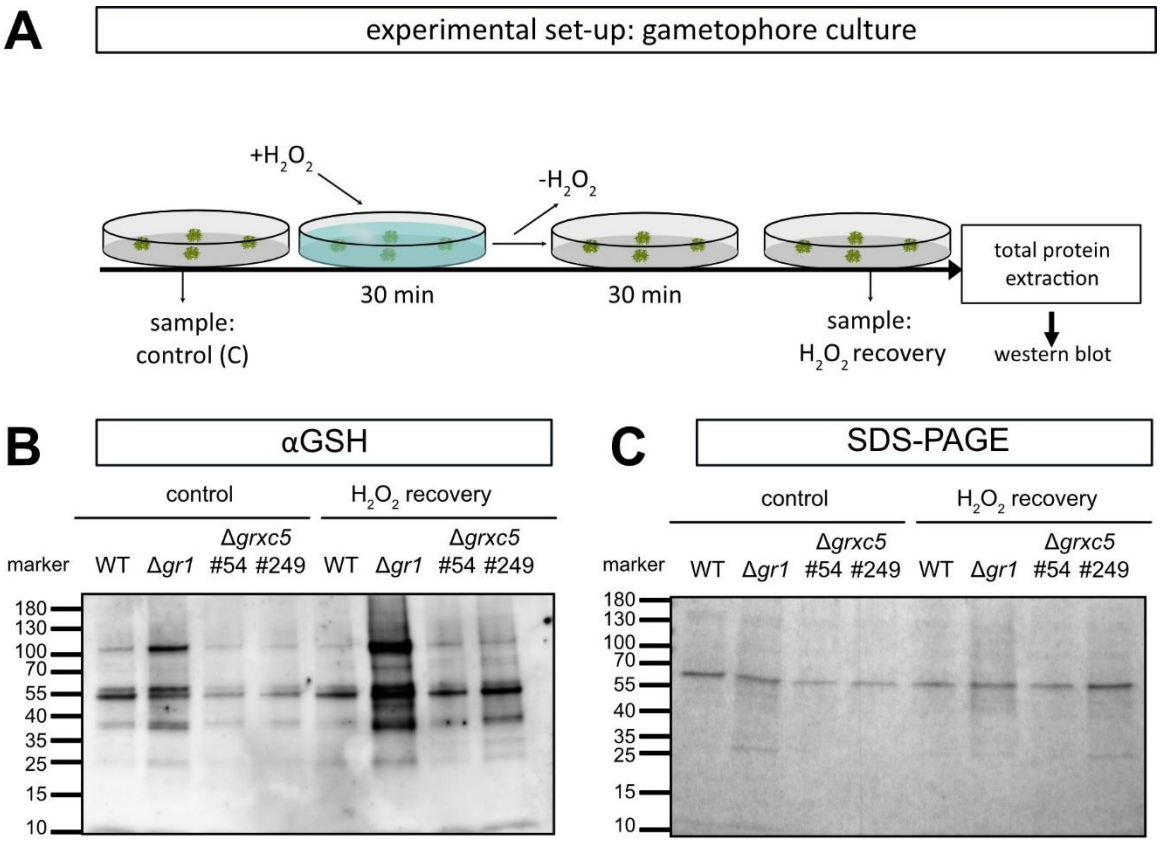

Figure 37: Detection of protein-bound glutathione in protein extracts of Δ*grxc5* and WT gametophores after 30 min recovery from treatment with 10 mM H_2O_2

A Schematic overview of the experimental set-up and sampling. **B** Immunoblot with αGSH (ThermoFisher) of glutathionylated proteins extracted from *P. patens* WT and Δ*grxc5* #54 gametophore tissue treated with 10 mM H_2O_2 and harvested at different time points (C, H_2O_2 recovery). Proteins were extracted in the presence of 20 mM NEM and 5 µg total protein was loaded onto a 4-20% gradient SDS-PAGE as loading control (**C**).

Although already higher amounts of protein *S*-glutathionylation for WT and Δ*gr1* were detected in non-treated samples ('control'), Δ*gr1* showed even higher amounts after peroxide recovery. To account for potential differences in protein loading between samples, an SDS-PAGE with the same amount of protein was performed as a loading control. Variances in the amount of proteins loaded onto the SDS-PAGE (Figure 37 C) may contribute to increased

differences in detection levels of glutathionylated proteins. Despite the unequal loading of the SDS-PAGE, the previous experiments (Figure 36, Figure 37) demonstrate the quantifiability of *S*-glutathionylated proteins with the αGSH antibody.

Further protocol adjustments had been made to optimize the experimental set-up. When cultivating *P. patens* on agar plates, parts of the colonies grow in the agar and are therefore not directly accessible for H_2O_2 treatment. To circumvent errors due to parts of colonies not being in contact with H_2O_2, we switched systems and treated gametophores in falcon tubes, allowing total submersion of plant material in H_2O_2 solution. At the start of the experiment, gametophores were transferred from the plate into 15 mL falcons filled up with KNOP-ME media (control) or KNOP-ME media supplemented with 10 mM H_2O_2. The moss-containing falcons were incubated for 30 min in the light (growth conditions see 2.6.2). After that, half of the moss submerged in the H_2O_2 solution was dried with a paper tissue and frozen in liquid nitrogen ('T_1'). The other half was transferred to a new falcon with KNOP-ME and was given 30 min to recover ('T_{30}') from the oxidative treatment. Control ('T_0') and recovery samples ('T_{30}') were harvested and protein extracts were prepared as described before (Figure 38 A).

The amount of protein *S*-glutathionylation was detected via immunoblot analysis at three different timepoints: initial status (T_0), immediately after 30 min of H_2O_2 treatment (T_1) and after 30 min of recovery from the H_2O_2 treatment (T_{30}). A band at ~55 kDa was detected in all samples independent of genotype and treatment but increasing in intensity in oxidative stress and recover conditions. Additionally, a band at >100 - <130 kDa was observed appearing more intense in samples of oxidative stress treatment (T_1, $T_{30,}$ Figure 38, Supplemental Figure 3). In WT, less protein-bound glutathione was detected in samples before treatment (T_o) followed by an increase of signal after 30 min of H_2O_2 treatment and the appearance of the >100 - <130 kDa band. The intensity of the >100 - <130 kDa band faded 30 min after H_2O_2 treatment, while the 55 kDa signal was comparable to that detected in T_1. For Δ*grxc5* #54 and #249, the ~55 kDa band showed a higher intensity than the WT T_0 sample implying more glutathionylated proteins under physiological conditions. Even though the >100 - <130 kDa band faded as well in the Δ*grxc5* mutant at T_{30}, the signal detected at ~55 kDa showed similar intensities to the samples of T_1. In Δ*gr1* only T_1 and T_{30} were evaluable due to less protein amounts of T_0 as seen in the SDS-PAGE loading control. The experiment was repeated three times (see Supplemental Figure 3)

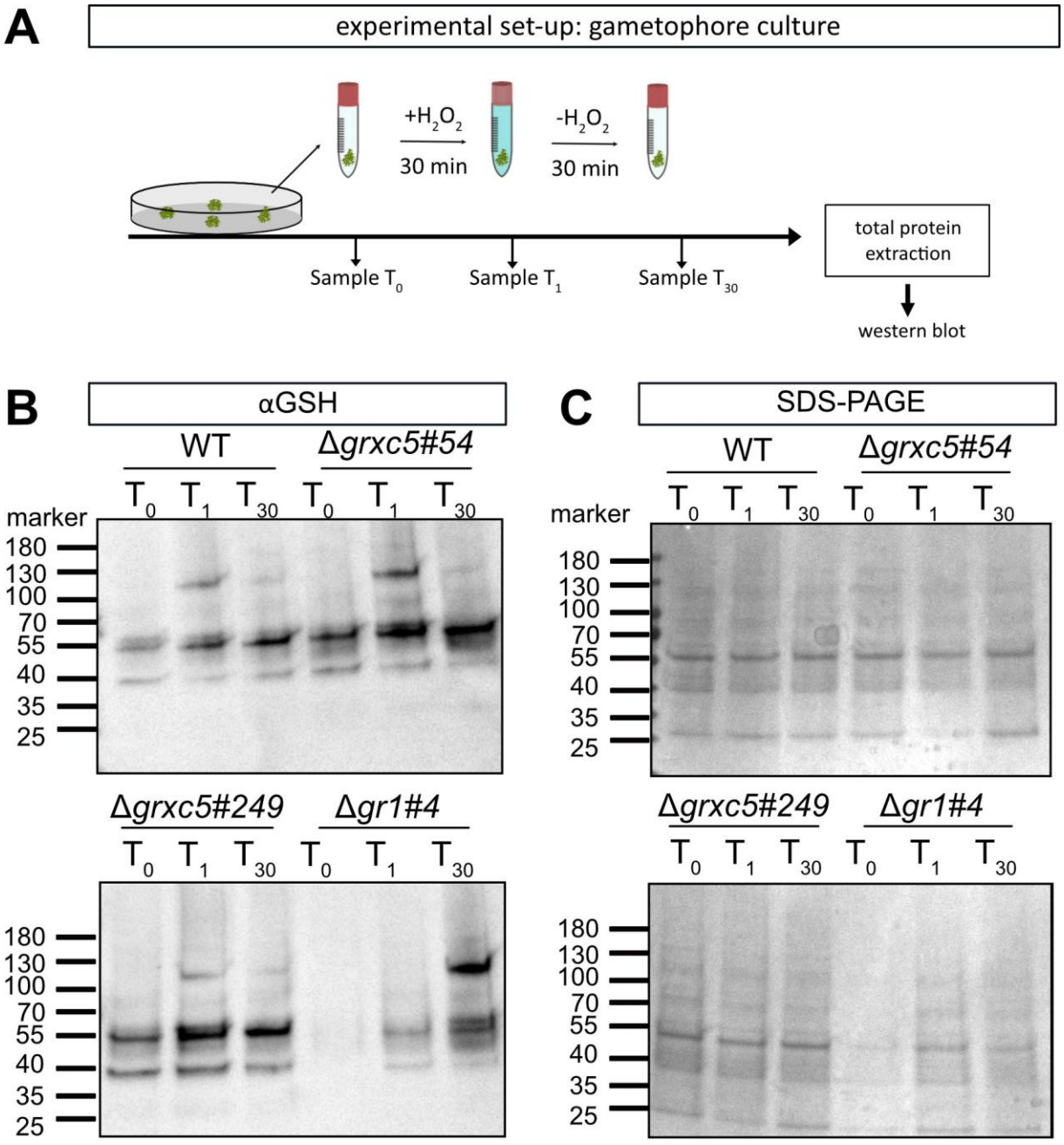

Figure 38: Detection of protein-bound glutathione in protein extracts of Δ*grxc5* and WT gametophores treated with H_2O_2 in falcon tubes

A Schematic overview of the experimental set-up and sampling. **B** Western blot (αGSH, ThermoFisher) of glutathionylated proteins extracted in the presence of 20 mM NEM from *P. patens* gametophore tissue treated with 10 mM H_2O_2 and harvested at different time points (T_0, T_1, T_{30}). Proteins were extracted in the presence of 20 mM NEM and 5 µg total protein was loaded onto a 4-20% gradient non-reducing SDS-PAGE as loading control (**C**).

Immunoblot analysis was additionally performed on protonema tissue, using the experimental set-up as seen in Figure 38 A with time points of protein harvest labeled T_0, T_1 and T_{30} (Figure 39 A). Comparison of *S*-glutathionylation of proteins in protonema at different timepoints displayed low amounts of glutathionylated proteins in the WT T_0 sample, increased

glutathionylation at T_1 (WT) and a decrease in glutathionylation from T_1 to T_{30} (WT) (Figure 39) revealing thereby the same band pattern at ~55 kDa and >100 - <130 kDa as seen for the gametophore tissue (Figure 38). In the other two repetitions of the experiment (see Supplemental Figure 2), the mutants showed low initial glutathionylation levels as seen for WT with a tendency to higher intensities of the ~55 kDa band. In Δ*grxc5* (#54, #249) directly after H_2O_2 treatment and 30 min after recovery from oxidative treatment (T_{30}) signal intensities indicated higher amounts of glutathionylated proteins shown by an increase in signal at ~ 100 kDa. The WT sample showed an increase in intensity at ~ 100 kDa directly after (T_1) and 30 min after (T_{30}) peroxide treatment similar to the one seen for the mutant lines.

If the absence of *Pp*GRXC5 causes plastidial proteins to be inefficiently deglutathionylated, I expect that the activity of the respective glutathionylation targets will be impacted. Potential protein *S*-glutathionylation targets have already been identified and some are related to photosynthetic activity (see Chapter 3).

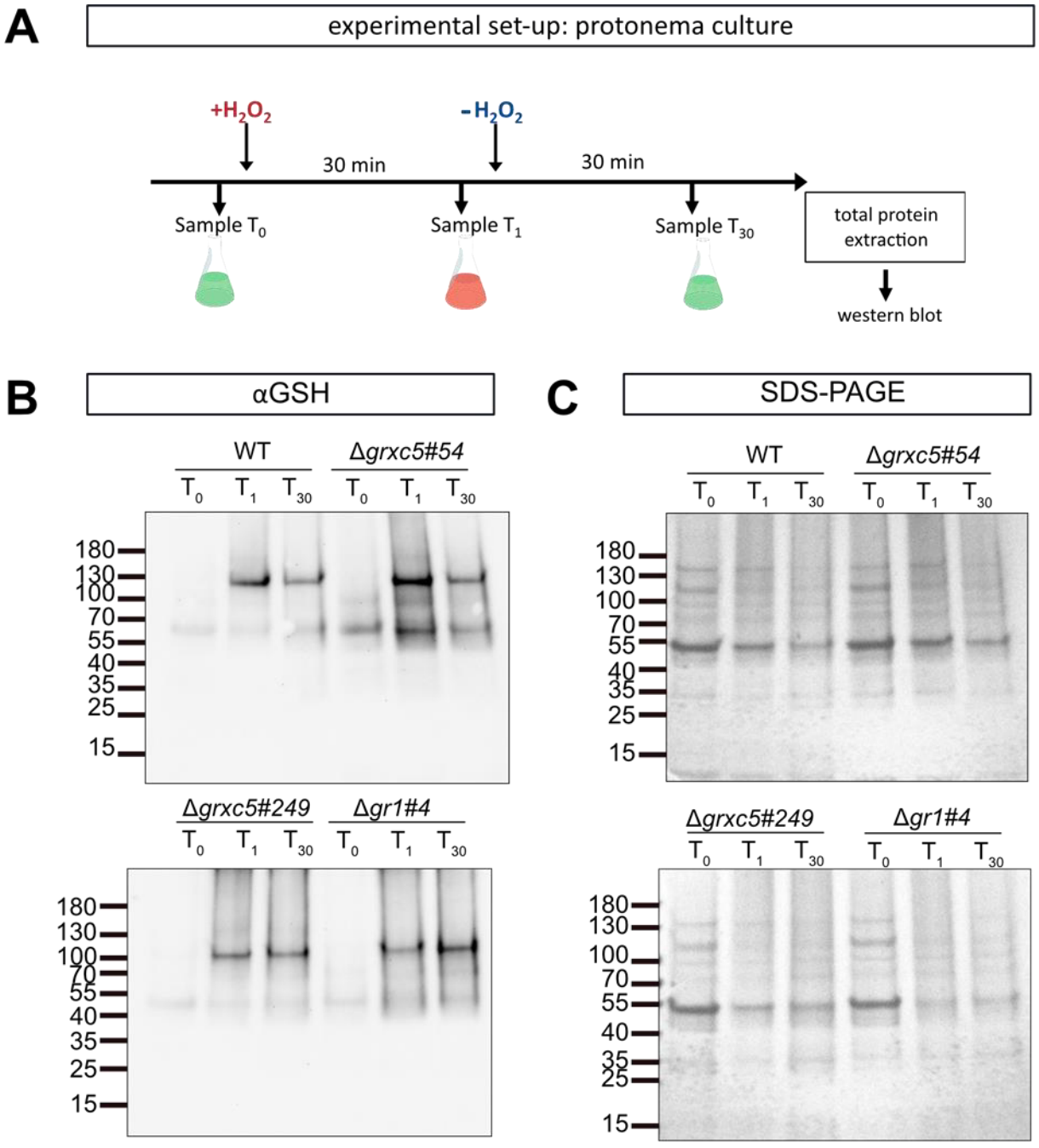

Figure 39: Detection of protein-bound glutathione in protein extracts of protonema culture treated with H_2O_2

A Schematic overview of the experimental set-up and sampling. **B** Immunoblot of proteins extracted (in the presence of 20 mM NEM) from *P. patens* protonema tissue treated with 10 mM H_2O_2 and harvested at different time points (T_0, T_1, T_{30}) with the αGSH antibody (ThermoFisher). Proteins were extracted in the presence of 20 mM NEM and 10 µg protein was loaded onto a 4-20% gradient non-reducing SDS-PAGE as loading control (**C**).

4.1.5.5 The lack of plastidial class I GRX shows no impact on photosynthetic performance and CO_2 assimilation rates in *P. patens*

Plastidial proteins involved in the light-dependent photosynthesis reaction such as plastocyanin (PC, transfer of electrons from cytochrome *b6f* to P700; Taiz *et al.* 2015), photosystem II core phosphatase (PBCP, dephosphorylation of PSII; Puthiyaveetil *et al.* 2014) and ferredoxin 1 (FDX 1, electron transport at PSI; Taiz *et al.* 2015) have been identified as *S*-glutathionylation targets (Zaffagnini *et al.* 2012; Liu *et al.* 2019; see chapter 3). The impact of the absence of a class I GRX capable of catalyzing the deglutathionylation of those enzymes was investigated by comparing the photosynthetic performance of Δ*grxc5* to that of WT. Prior to measurements, an oxidative stress treatment with 10 mM H_2O_2 was performed to enhance possible differences by inducing glutathionylation of those enzymes. The photosynthetic efficiency was determined with increasing light intensity (PAR: photosynthetic active radiation µmol/m^2s) to measure possible changes in photosynthetic performance between WT and Δ*grxc5* after 15 minutes of oxidative stress treatment. Photosynthetic efficiency was determined with an Imaging-PAM M-Series system (Heinz Walz) in collaboration with Frank Reinhardt (Prof. Ekkehard Neuhaus, University of Kaiserslautern). We additionally performed experiments on Δ*gr1* with a previously reported increase in non-photochemical quenching (NPQ; Müller-Schüssele *et al.* 2020) (Figure 40).

We determined the photosynthetic yield of photosystem II (YII) and the resulting electron transport rate (ETR) to elucidate photosynthetic efficiency. To assess the ability to dissipate excess excitation energy, non-photochemical quenching (NPQ) was determined within light intensities in ranges of 0-726 PAR (Figure 40).

No differences in the percentage of energy channeled into NPQ was observed for WT, Δ*gr1* and Δ*grxc5* before and 15 min after oxidative stress treatment (10 mM H_2O_2, 15 min) (Figure 40). However, NPQ decreased in all genotypes after oxidative stress treatment at 726 PAR (Figure 40 B). A two-way ANOVA did not reveal significant differences between WT and Δ*grxc5* within the respective treatment (control, H_2O_2). Differences were observed for Δ*gr1* which significantly differed between WT and Δ*grxc5* #54 and partially differed from *Δgrxc5* #249.

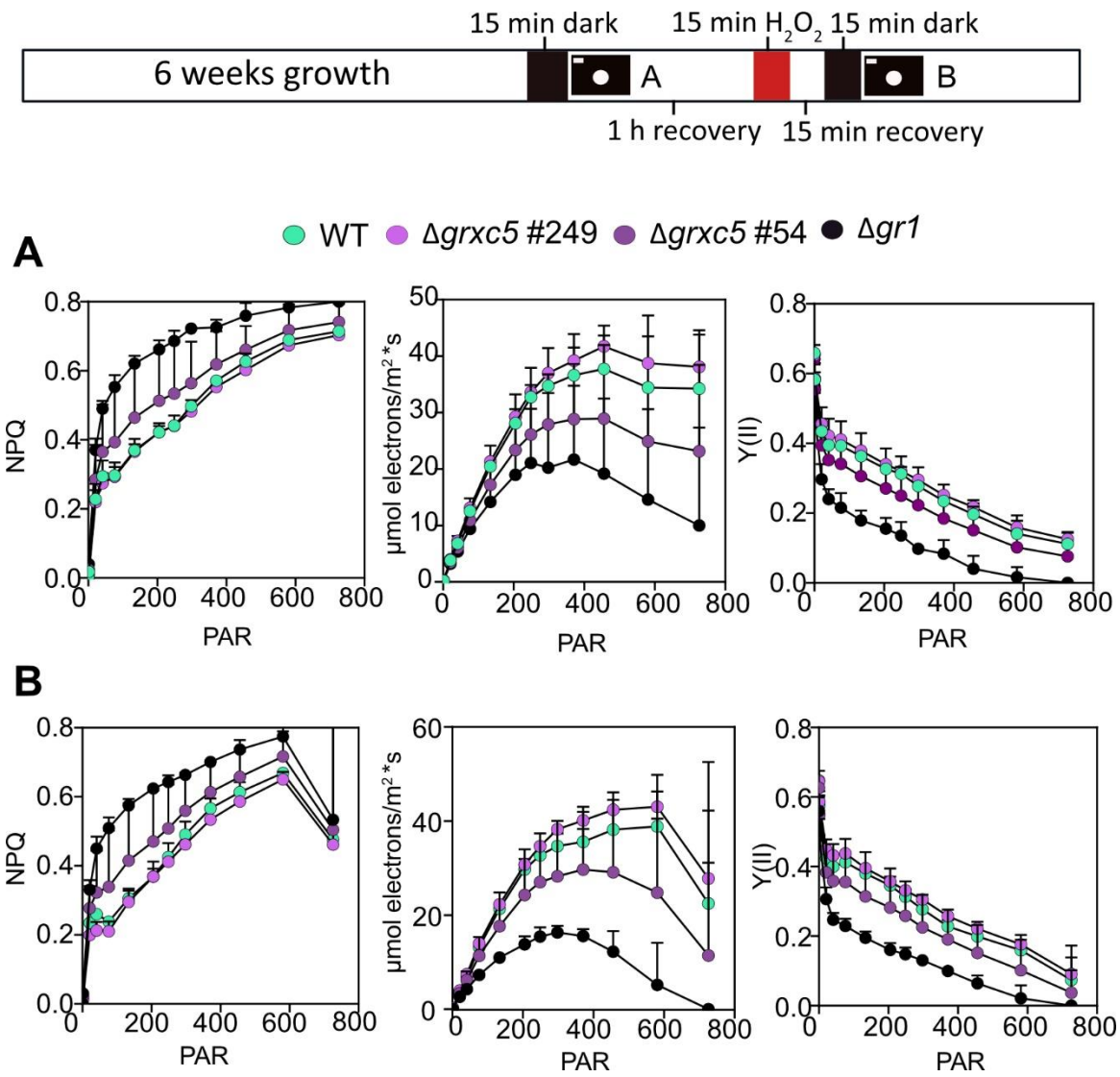

Figure 40: Photosynthetic parameters (NPQ, ETR, Y(II)) 30 min after treatment with H_2O_2 (15 min, 10 mM)-

NPQ, ETR (µmol electrons/m^2s) and photosynthetic yield of PSII (Y(II)) of 6-week-old *P. patens* colonies measured under standard conditions (60 µE/m^2s, 16h/8h KNOP-ME pH 5.8) Before each measurement, moss was dark-incubated for 15 min. Photosynthetic parameters before (**A**) and after oxidative stress treatment with 10 mM H_2O_2 for 15 min (**B**) were measured on the same colonies. Shown is the mean + SD of three biological replicates. A Two-way ANOVA (Tukey's multiple comparison; $p<0.0001$) was done at each light intensity between genotypes and treatment.

Since no difference in light-dependent photosynthetic activity could be detected with the current findings (Figure 28, Figure 40), we investigated the photosynthetic dark reaction in closer detail by measuring CO_2 assimilation of WT, Δ*gr1* and Δ*grxc5* #54, in dark-light transitions. In the light-independent photosynthetic reaction, CO_2 is reduced and fixated via the Calvin-Benson-Cycle (CBC) requiring NADPH and ATP formed during the light-dependent reaction (Taiz *et al.* 2015). During dark-light transition the CBC enzyme activity is increasing in the first minutes after illumination. This activation of CBC enzymes is regulated by the

ferredoxin/thioredoxin system (Buchanan 1991). The plastidial thioredoxin TRXf plays a crucial role in CBC enzyme regulation and was identified among other CBC involved enzymes as target site of glutathionylation (Michelet *et al.* 2005; Müller-Schüssele, Bohle, *et al.* 2021). TRXf dysfunction due to ineffective deglutathionylation may influence the initial activation of CBC enzymes after illumination, leading to a change in the assimilation rate measured within the first few minutes after the dark-light transition.

To test if CO_2 assimilation is affected in Δ*grxc5*, we measured the CO_2 assimilation rate in moss protonema culture via the GFS-3000 (Walz) in collaboration with Frank Reinhardt (Prof. Ekkehard Neuhaus, University of Kaiserslautern). Protonema culture was placed on a Whatman filter paper with excess culture medium being removed. The filter paper, coated with protonema tissue, was transferred to a petri dish and measured. To prevent the sample from dehydrating, the humidity was set to 90% during the GFS measurement.

Absolute changes in CO_2 levels of Δ*grxc5* showed a non-significant tendency of lower CO_2 uptake in the light compared to WT. Assimilation (light) and respiration (dark) rates showed the same non-significant trend of lower CO_2 assimilation of Δ*grxc5* #54 and #249 compared to WT (Figure 41 A, C). Comparison of the slopes of ΔCO_2 change and CO_2 assimilation rate upon dark to light (t_{300}-t_{450}s and t_{300}-t_{303}s) and light to dark (t_{750}-t_{945}s and t_{750}-t_{753}s) transition revealed no significant difference in the velocity of turning on (dark to light) or turning off (light to dark) the CBC (Figure 41 B, D).

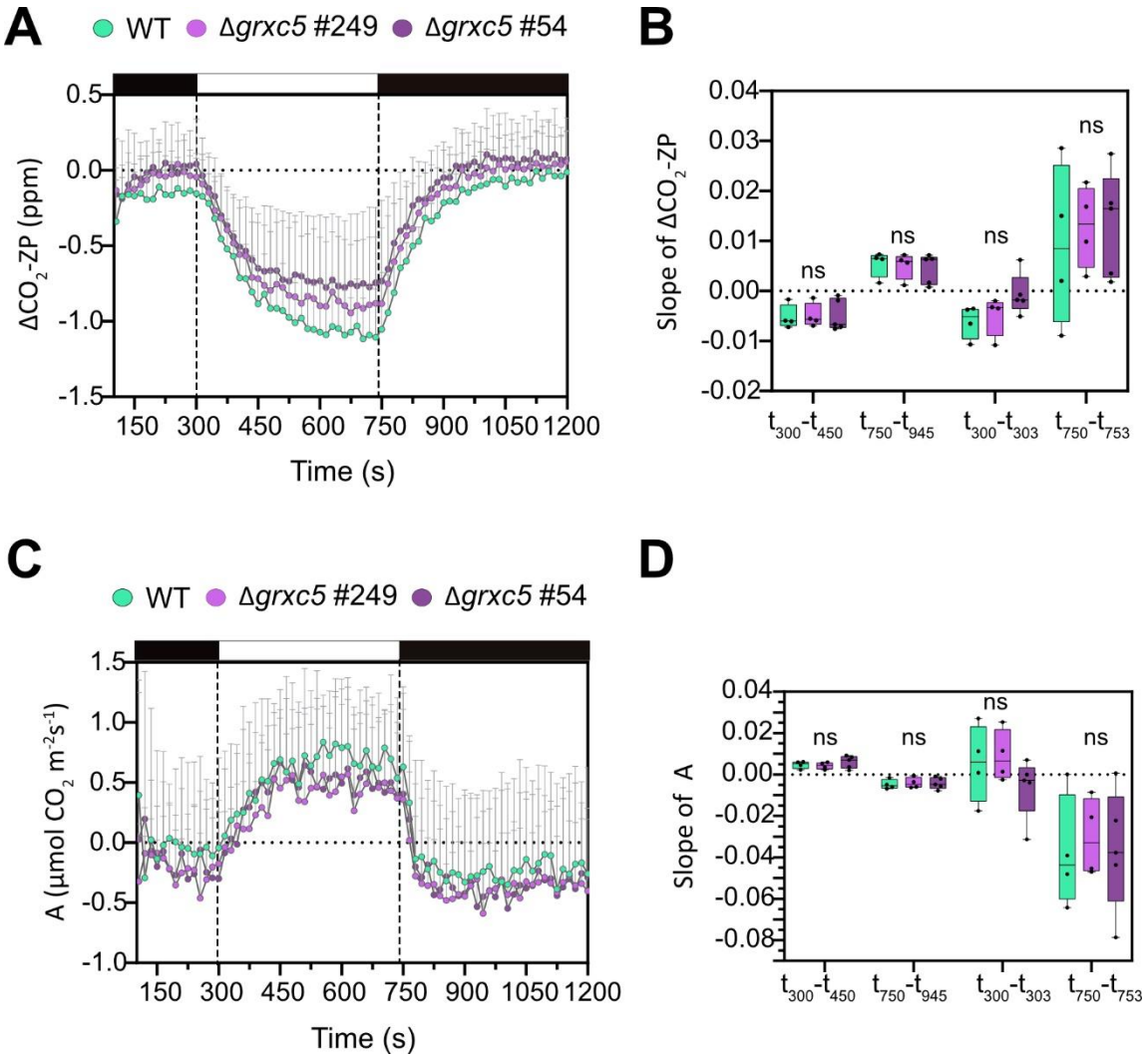

Figure 41: CO_2 assimilation and respiration of WT and *Δgrxc5* protonema culture in light-dark transition

Changes in CO_2 assimilation upon dark-light-dark transitions in protonema culture of Δ*grxc5* and WT measured with the GFS-3000 with 7.5 min of light and 7.5 min of darkness (90% humidity, 500 ppm CO_2, 22°C, 125 µE light intensity). Experiments were conducted in cooperation with Frank Reinhardt (Prof. Ekkehard Neuhaus, University of Kaiserslautern) **A** Absolute changes in CO_2 levels after zero point (Whatman filter paper, wetted with KNOP-ME; ZP) subtraction. **B** Slope between dark and light plateaus of ΔCO2-ZP upon dark-light and light-dark transitions between 300-450 s, 750-945s and 300-303 s and 750-753 s. **C** Assimilation rate calculated by GFS-Win software upon dark-light and light-dark transition. **D** Assimilation rate/time upon dark-light to light-dark transition between 300-450 s, 750-945 s and 300-303 s and 750-753 s. Two-way ANOVA was conducted to test for significant differences (p=0.51 (B) and p=0.95(D)) **B, D** Boxes display 25-75 percentiles with min and max values indicated by the whiskers. The median is indicated by the horizontal line. (n=4-5). One way ANOVA (Tukey's multiple comparison) was done to test for significant differences of dark and light plateaus but reveled non-significance.

4.1.5.6 Light-dependent E_{GSH} dynamics measured are absent in Δ*grxc5*

In Müller-Schüssele *et al.* 2020 a dynamic, light-dependent change in E_{GSH} was observed in WT with the plastid targeted GRX1-roGFP2 sensor, while the dynamic was not measurable in

mutants of the plastidial GR (Δ*gr1*) with GRX1-roGFP1 showing a 92% sensor oxidation in Δ*gr1*. Therefore, Δ*grxc5* and WT expressing TKTP-roGFP2 were exposed to light to test for differences in the roGFP2 oxidation and reduction kinetics in dark and light transitions. In the WT background, a fast oxidation was measured upon light to dark transition followed by a fast reduction of the sensor in the dark (Figure 42 A). In the Δ*grxc5* lines the stromal roGFP2 showed no change in oxidation upon light-dark transition. The oxidation of roGFP2 after light to dark transition in WT was on the lower detection limit of the assay set-up with a cycle time of 60 s. To be able to measure during light exposure, protonema tissue was imaged with the CLSM (Figure 42 B) also allowing a faster image acquisition. roGFP2 in WT showed a slight decrease in the ratio during light exposure and a fast increase of 405/488 nm after transition from light to dark. Neither the oxidation and fast reduction of roGFP2 measured for WT in the plate reader nor the reduction of roGFP2 in the light were detectable with roGFP2 expressed in the Δ*grxc5* background. To verify the dynamics of roGFP2 each well was treated with DTT (red) or H_2O_2 (ox) to obtain min and max roGFP2 ratio values (Figure 42).

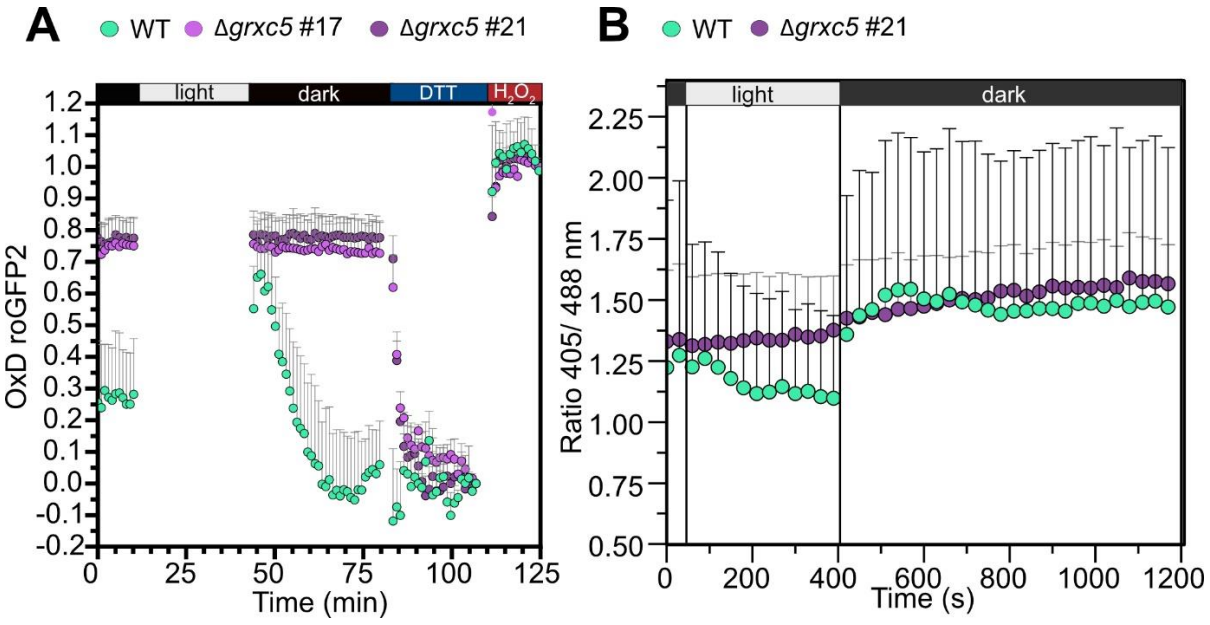

Figure 42: roGFP2 oxidation state in WT and Δ*grxc5* plastids in dark:light transition

A 200 µL protonema culture of *P. patens* was transferred into a 96 well plate and initial fluorescence was measured after 30 min dark incubation using the plate reader. After the formation of a steady-state of roGFP2 oxidation (10 min) the plate was illuminated for 30 min (~ 200 µE/m^2s, external illumination with LED). As internal calibration control, the buffer in the wells was exchanged with 10 mM DTT. After obtaining a stabilized roGFP2 signal, the DTT solution was exchanged with 10 mM of H_2O_2 and the fluorescence was followed again for serval minutes. The degree of oxidation was calculated over the ratio of 405/488 nm and calibrated with DTT and H_2O_2. Shown is the mean and SD of n=3. **B** *P. patens* gametophores and protonema tissue grown in liquid culture were dark incubated for 45 min. To avoid laser-scanning stress samples were imaged without pre-screening for signal. Time series were imaged with the CLSM

for 1 min in the dark. After that an external light source was illuminating the sample for 5 min with 100 µE/m²s, while imaging. roGFP2 was excited at 405 and 488 nm and emission was collected at 508-535 nm. Images were taken every 30s for 20 min. Shown is the mean + SD of n=7-8.

4.2. Discussion

4.2.1 Glutathione ratios and their influence on protein *S*-glutathionylation

The cytosolic GSH concentration in Arabidopsis root tissue was determined using MCB labeling to be between 2-3 mM (Fricker *et al.* 2000; Meyer *et al.* 2007). Similarly, Noctor & Foyer 1998 report plastid GSH concentrations to be in a range between 1-4.5 mM. Further studies based on the redox-sensitive GFP revealed highly negative cytosolic redox potentials of ~-320 mV at pH 7.2 with 0.002% of the cytosolic glutathione pool being oxidized (Meyer *et al.* 2007; Schwarzländer *et al.* 2008, 2016). Based on 10 mM glutathione, the ratio between GSH and GSSG *in vivo* was calculated to be 50000:1, resulting in only nanomolar concentrations of GSSG. (Meyer *et al.* 2007; Schwarzländer *et al.* 2016). The highly negative redox potential and low oxidation degree of the glutathione pool is maintained by the glutathione reductase (GR), reducing GSSG back to two molecules of GSH (Halliwell & Foyer 1978; Marty *et al.* 2009; Kataya & Reumann 2010). Cytosolic redox potentials of mutants with impairments in GSSG reduction like *gr1-1* (Marty *et al.* 2009) or deficits in glutathione synthesis, like *rml1* (Aller *et al.* 2013), are shifted to less negative values, showing redox potentials of −315 ± 9 mV in *gr1-1* Arabidopsis leaves (Marty *et al.* 2009), including GSH:GSSG ratio changes.

Based on a fruitful collaboration with Paolo Trost, Mirko Zaffagnini and Jacopo Rossi (University of Bologna, Italy), we hypothesized that glutathione ratio influences protein glutathionylation on monothiol (or non-disulfide forming) proteins while the glutathione redox potential influences glutathionylation in disulfide forming proteins that are able to release glutathione via the intramolecular disulfide bridge. Based on this argument, intramolecular disulfide forming proteins like roGFP2 might therefore depend on the E_{GSH} ($f(GSH^2:GSSG)$) rather than the ratio of GSH:GSSG for protein *S*-glutathionylation, while the monothiol roGFP2 variant might rather be dependent on the glutathione ratio (see Figure 6, Figure 43).

4.2.1.1 Higher GSH concentrations increase GRX deglutathionylation leading to slowed down roGFP2 oxidation

We investigated the kinetics of roGFP2 oxidation in varying GSH:GSSG buffers at constant E_{GSH}. The *in vivo* ratio of 50000:1 (Meyer *et al.* 2007; Schwarzländer *et al.* 2016) of GSH to GSSG could not be applied *in vitro.* Limited by the low amounts of GSSG and the solubility of the stock solutions, glutathione redox potentials were calculated regarding the largest possible ratio difference (Table 16). At -232 mV (pH 7.4) 98% of roGFP2 is in its oxidized state. We observed >90% of sensor oxidation in the presence of *At*GRXC1 independent of the tested GSH:GSSG ratio (Figure 7). The end level of roGFP2 oxidation is independent of the GSH:GSSG ratio but dependent on the glutathione redox potential. The oxidation kinetics of roGFP2 are dependent on the GSH:GSSG and are discussed in the following paragraph (Figure 43 A).

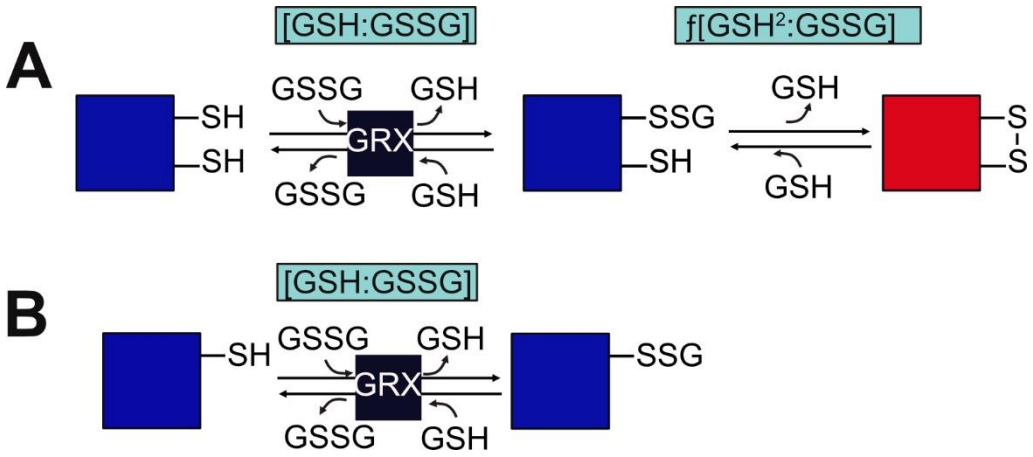

Figure 43: Monothiol vs. dithiol roGFP2 dependency on GSH:GSSG ratio and E_{GSH}

Schematic overview of roGFP2 (**A**) and roGFP2-C204S (**B**) dependency on GSH:GSSG ratio and E_{GSH}. The glutathionylation of roGFP2 and roGFP2-C204S would be dependent on the molar ratio of GSH to GSSG, since one molecule of GSSG is consumed and one GSH molecule will be released. The formation of the disulfide bond in roGFP2 in which another GSH molecule is released therefore dependents on the concentration of GSH^2:GSSG corresponding to the E_{GSH}.

The velocity of roGFP2 oxidation increased in the ratio of 72.5 showing lower total amount of glutathione compared to the 10.5 and 5.25 ratio. In the absence of *At*GRXC1, the velocity of roGFP2 oxidation increased as the total amount of GSSG in the GSH:GSSG ratios increased, resulting in higher total amounts of glutathione in the solution and favoring the enzyme-independent reaction of GSSG with roGFP2-SH to roGFP2-SSG and GSH. The reduction of GRX-SSG to GRX-SH is accomplished by a nucleophilic attack of a GS^- on the thiol of the glutathionylated GRX (Vlamis-Gardikas & Holmgren 2002; Michelet *et al.* 2009). Hence, the total concentrations of GSH and GSSG influences the glutathionylation state of the

glutaredoxin (Figure 5, k_4, k_{-4}). At least three different reactions have to be noted: (I) the reaction of the *At*GRXC1 with GSH and GSSG, (II) the reaction of roGFP2 with *At*GRXC1 and (III) the direct but slow reaction of GSH and GSSG with roGFP2. Reaction velocities are dependent on substrate concentration and can be described as followed with v = velocity, k=thermodynamic equilibrium constant c(A) and c(B) as substrate concentrations (Mortimer & Müller 2015).

$$v = k * c(A) * c(B)$$

The modification of this equation into the roGFP2 oxidation and reduction reaction in the presence and absence of GRX is depicted below. With -SH corresponding to the reduced thiol, -SS to the intramolecular disulfide bridge formed in roGFP2 and -SSG to the glutathionylated thiol.

In the absence of GRX:

$$v_{forward} = k_{forward} * c(roGFP2 - SH) * c(GSSG) \quad [1\}$$

$$v_{back} = k_{back} * c(roGFP2 - SS) * c(GSH) \quad [2]$$

$$v_{back} = k_{back} * c(roGFP2 - SSG) * c(GSH) \quad [3]$$

In the presence of GRX:

$$v_{forward} = k_{forward} * c(GRX - SH) * c(GSSG) \quad [4]$$

$$v_{forward} = k_{forward} * c(roGFP2 - SH) * c(GRX - SSG) \quad [5]$$

$$v_{back} = k_{back} * c(roGFP2 - SS) * c(GSH) \quad [6]$$

$$v_{back} = k_{back} * c(roGFP2 - SSG) * c(GRX - SH) \quad [7]$$

$$v_{back} = k_{back} * c(GRX - SSG) * c(GSH) \quad [8]$$

Due to the glutathione redox potential of -232 mV the thermodynamic equilibrium, the point at which the roGFP2 oxidation rate equals the roGFP2 reduction rate, is calculated to be at the site of 98% oxidized roGFP2. Thermodynamic equilibrium is reached in all the tested GSH:GSSG ratios in presence and absence of *At*GRXC1 (Figure 7). However, the velocity of the non-catalyzed oxidation [1] of roGFP2 was higher in lower ratios than the backreaction [2, 3]. We observed that a higher ratio (GSH:GSSG ratio of 72.5) resulted in a faster oxidation of roGFP2, detectable by a 405/488 nm ratio increase (Figure 7). We observed that in the

presence of *At*GRXC1 higher ratios led to faster roGFP2 oxidation velocities, while in high ratios without *At*GRXC1, thermodynamic equilibration of GSH:GSSG with roGFP2 led to slower roGFP2 oxidation. The results are in line with determined reaction rates of 0.1-200 $M^{-1}s^{-1}$ for the non-enzymatic reaction of protein thiols with glutathione, while the GRX catalyzed reaction showed reaction rates of 10^5-10^6 M^{-1} s^{-1} (Deponte 2017). This may be due to a higher GSSG concentration in lower ratios, thus reaching the reaction equilibrium faster than GSH:GSSG ratios with lower GSSG concentration. Without GRX, an increase in GSSG concentration will drive the forward reaction [1], seen by faster roGFP2 oxidation in lower ratios such as a GSH:GSSG ratio of 5.25 with 8 mM GSSG and 42 mM GSH. Simultaneously, higher GSH concentrations increase the backreaction of roGFP2 reduction [2,3], however not to the extent that slowed down roGFP2 oxidations were observed in the 5.25 GSH:GSSG ratio.

In the presence of GRX, the reaction rate of roGFP2 glutathionylation in the presence of GSSG [4, 5] is 10^5-fold higher compared to the non-enzymatic reaction [1] (Deponte 2017). Consequently, the non-catalyzed reaction of roGFP2 with GSH or GSSG is too slow to compete with the GRX catalyzed reaction and may be neglectable in the presence of a class I GRX (Meyer *et al.* 2007; Deponte 2017). In the presence of *At*GRXC1, higher ratios such as 72.5 with a lower total amount of GSH (2.4 mM) compared to the other tested ratios (with 20 mM and 42 mM GSH), showed the fastest roGFP2 oxidation rate (Figure 7). The decreased GSH concentration may have lowered the velocity of oxidized roGFP2 with GSH [2, 6]. Therefore, higher ratios such as 72.5 with only 2.9 mM total GSH and 0.04 mM GSSG showed faster reaction kinetics than lower ratios with GSH concentrations of 20 - 42 mM in the presence of *At*GRXC1.

Minimizing the enzymatically catalyzed reduction of roGFP2 [6, 7, 8] by using *At*GRXS15 resulted in similar ratio dependent roGFP2 oxidation kinetics as seen for *At*GRXC1. Since *At*GRXS15 showed a 30-fold slower oxidation of roGFP2 than *At*GRXC1 (Moseler *et al.* 2015), concentration of *At*GRXS15 was increased to 6 instead of 1 µM in the assay (Figure 7). Similar roGFP2 oxidation kinetics at different GSH:GSSG ratios, independent of the use of *At*GRXC1 or *At*GRXS15 further support the hypothesis that high GSH concentrations drive the reaction to reduction of roGFP2 [3,7] (Figure 6, k_4 and k_3). It should be noted, however, that the experiments without GRX are less relevant regarding redox dynamics in physiological conditions. *In vivo*, many factors such as concentrations of substrates and enzymes, presence

or absence of catalysts and competing reactions, influence the reaction of a protein with glutathione (Deponte 2017) which are to are large extend neglected in an *in vitro* approach.

In vivo, high accumulation of GSSG would be prevented by GR activity with reaction rates in the range of ~10^6 $M^{-1}s^{-1}$ (Marty *et al.* 2009, 2019; Deponte 2017; Müller-Schüssele *et al.* 2020). The accumulation of high GSSG concentrations, tested in *in vitro* experiments (up to 8 mM) are unlikely to occur *in vivo* but might occur under oxidative stress conditions in compartments with impaired GR function.

4.2.1.2 Varying GSH:GSSG ratios at constant E_{GSH} did not result in detectable changes in the *S*-glutathionylation state of roGFP2-C204S

Monothiol target proteins of glutathionylation like roGFP2-C204S might rather depend on the GSH:GSSG ratio than on the redox potential (Figure 43 B). It was shown that glutathionylation of the monothiol roGFP2-C204S at Cys 147 takes places in the presence of *At*GRXC1 and GSSG by Trnka *et al.* 2020 via ESI-Q-TOF analysis.

Experiments conducted in an E_{GSH} of -232 mV (GSH:GSSG ratio of 10.5- 72.5), -280 mV (GSH: GSSG ratio of 1500-2000) and -220 mV (GSH:GSSG ratio of 134-20) displayed a maximum of ~6.9-fold change differences in GSH:GSSG ratios. roGFP2-C204S MPEG-Mal labelling revealed no detectable difference of free thiols of roGFP2-C204S. However, these experiments were limited by the efficiency of MPEG-Mal labeling in the roGFP2-C204S samples. Whereas roGFP2 showed a total band shift after reduction with DTT or TCEP and a subsequent labeling with MPEG-Mal, roGFP2-C204S did only show a partial shift (Figure 11, Figure 12). Despite the fact that NEM-labeled roGFP2-C204S was detected in DTT-reduced samples via MS/MS (Figure 10) only weak bands appeared at the expected height for MPEG-Mal labeled roGFP2-C204S (at ~40 kDa) (e.g. Figure 11). Different ratios of GSH:GSSG did not influence the intensity of the ~40 kDa bands (Figure 11, Figure 12, Figure 13, Figure 14). Hence, roGFP2-C204S read-out via MPEG-Mal labeling was insufficient to support the hypothesis of the GSH:GSSG ratio influencing the amount of protein glutathionylation at constant E_{GSH}.

Glutathionylation of roGFP2-C204S was shown in an MS/MS approach, which revealed that roGFP2-C204S is partially glutathionylated when treated with 40 µM GSSG in the presence of *At*GRXC1 (Figure 10). However, higher levels of NEM modified and thus previously reduced roGFP2-C204S were detected in the same sample run, concluding an inefficient

glutathionylation of roGFP2-C204S, even in conditions (40 µM GSSG + *At*GRXC1) known to completely oxidize roGFP2 (Figure 10).

Immunodetection of glutathionylated roGFP2-C204S might be a more suitable approach to visualize and detect small difference in glutathionylation. The preliminary data in Figure 15 showed two bands for glutathionylated roGFP2-C204S at ~ 25 kDa and >35 kDa. A tendency to higher glutathionylation in lower GSH:GSSG ratios (GSH:GSSG ratio 20) can be seen by a slight increase in the ~25 kDa band intensity. The >35 kDa band is as well visible on the Coomassie-stained SDS-PAGE but not under UV-light, concluding that the band corresponds to a potentially degraded roGFP2-C204 bound to GSH.

Interestingly, roGFP2-C204S as well as roGFP2 under reducing conditions with no external addition of glutathione in the buffer showed GFP-bound glutathione. Within the protein sequence of roGFP2, a third cysteine at position 70 is present but, due to structural constrains, a glutathionylation of Cys 70 is not likely, even though it cannot be ruled out (Hanson *et al.* 2004). However, since roGFP2 bound glutathione was not detected in oxidizing control runs and assay conditions due to the formed intramolecular disulfide bridge of Cys 147 and 204, glutathionylation of Cys 70 seems improbable.

4.2.2 Changes in E_{GSH} influence the expression level of GAPC in roots of *A. thaliana*

GAPC1 is a cytosolic isoform of GAPDH in Arabidopsis, fulfilling important functions in glycolysis by conversion of glyceraldehyde-3-phosphate to 1,3-bisphosphoglyceric acid (Zaffagnini *et al.* 2013; Vescovi *et al.* 2013). However, additional functions of GAPDH, often referred to as moonlighting functions, were deeply explored in animals (Sirover 2012), while less is known for the plant kingdom. Plant GAPDH, prone to redox modifications, might function as redox sensor and as well show moonlighting functions (Zaffagnini *et al.* 2013). *In vitro* experiments linked glutathionylation of *At*GAPC1 after treatment with H_2O_2 and GSSG in a 25:1 ratio with the formation of inactive aggregates within 10 min after treatment. They further identified Cys 149 as important for glutathionylation and aggregate formation, while Cys 153 initiates a nucleophilic attack on glutathionylated Cys 149 and resolves the glutathionylation by disulfide formation (Cys 149-Cys 153) (Zaffagnini, Marchand, *et al.* 2019).

To test if an *in vivo* change in E_{GSH} results in an alternation in protein glutathionylation, GAPC1 expression and aggregate formation was investigated in root cells of Arabidopsis *gr1-1*

compared to WT. To monitor GAPC1 *in vivo* the GAPC1-YFP sensor (Vescovi *et al.* 2013) was introduced into *gr1-1* and WT. Glutathionylation of GAPC1-YFP may induce sensor accumulation and YFP-signal aggregation (Bedhomme *et al.* 2012; Vescovi *et al.* 2013).

An overall increase in GAPC1-YFP expression was detectable in *gr1-1* compared to WT, but no aggregating YFP-sensor signal was observed (Figure 19). An additional stressor in the form of 0.1 mM cadmium was applied to induce accumulation of GAPC1 in WT. Cadmium induces the accumulation of NO and ROS (Sharma & Dietz 2009; Vescovi *et al.* 2013) and activates the GAPC1 promotor (Vescovi *et al.* 2013). A concentration of 10 µM cadmium (for 24 h) led to a higher ratio of GSSG:GSH from 0.03 in Arabidopsis roots (control) to 0.19 after treatment and an increase of total glutathione compared to control conditions (HPLC data of Cuypers *et al.* 2011). A ~5 x 405/488 nm ratio change in Arabidopsis roots expressing roGFP2 upon 72 h of 0.1 mM cadmium treatment further pin-points the E_{GSH} as potential factor for GAPC1-YFP accumulation (Vescovi *et al.* 2013). Cadmium-treated WT (0.1 mM) expressing GAPC1-YFP showed an increase in YFP intensity. This supports the observation of increased GAPC1 expression upon cadmium exposure published in Vescovi et al (2013).

In rats it was shown that upon *S*-nitrosylation of the catalytic cysteine (Cys 150), GAPDH relocalizes to the nucleus by binding to a ubiquitin ligase protein (SIAH1; Hara *et al.* 2005). In Arabidopsis protoplasts and pea leaf cells, nuclear localization of GAPC1 was also detected (Anderson *et al.* 2004; Holtgrefe *et al.* 2008). *At*GAPC1 translocation to the nucleus was increased upon oxidative stress via cadmium treatment (Vescovi *et al.* 2013). An Arabidopsis mutant of the catalytic Cys 155 of GAPC1, with Cys 149 shown to be a target of *S*-glutathionylation and *S*-nitrosylation, showed an increased nuclear YFP signal after cadmium treatment (Vescovi *et al.* 2013) concluding, that another factor in plants than in mammalians plays a crucial role for GAPDH-translocation upon cadmium treatment.

In Arabidopsis *gr1-1*, GAPC-YFP expression under the endogenous promotor was increased already under control conditions and did not further increase in fluorescence intensity after cadmium treatment (Figure 19). With increasing signal, nuclei were easier to detect in the YFP-channel but did not show an apparent increase in nuclear localized YFP. Concluding from the first experimental data on GAPC-YFP under less reducing E_{GSH}, GAPC1 expression increased under conditions with less reducing E_{GSH} (Figure 19). However, aggregation of GAPC1 as seen

in the *in vitro* experiments of Zaffagnini et al. (2019) was not detected in *gr1-1* and WT expressing GAPC1-YFP.

GAPC1-YFP overexpression (2xCaMV35S promotor) in WT and *gr1-1* showed a high aggregation of the YFP sensor in Arabidopsis root tips (Figure 18). However, due to strong overexpression of the GAPC1-YFP construct, nuclear localization might be additionally induced by higher expression-levels. An increase ratio between nucleus-localized GAPC1-YFP to cytosol-localized GAPC1-YFP ratio was observed in *gr1-1* compared to WT.

4.2.3 *Pp*GRXC5 shows a strong oxidoreductase activity

Class I glutaredoxins are known to play a crucial role in regulating a proteins redox state via the mechanism of protein glutathionylation and deglutathionylation and providing an electron source for antioxidant enzymes such as MSRB1 (Zaffagnini, Bedhomme, Marchand, Morisse, *et al.* 2012; Couturier, Jacquot, *et al.* 2013; Müller-Schüssele, Bohle, *et al.* 2021). Oxidoreductase activity of *Pp*GRXC5 was confirmed *in vitro* showing even faster roGFP2 oxidation and reduction kinetics than *At*GRXC1 when tested simultaneously (Figure 22*,* Table 18). The reason behind this is unknown so far. One might speculate that the proline in the active site of *Pp*GRXC5 (YCPYC) has an influence on the activity compared to *At*GRXC1 (YCGYC). Nevertheless, *At*GRXC2, which has a similar active site than *Pp*GRXC5, shows similar deglutathionylation activities measured in HED compared to *At*GRXC1 (Table 18). Hence, other differences in the amino acids might result in slight structural changes that enhance the activity of *Pp*GRXC5. This, however, exceeds the scope of this work and will be the goal of future research. Deglutathionylation activity tested with GSH or β-ME-SSG as substrates in the HED-assay revealed similar activities between Poplar *Pt*GRXS12 and Physcomitrium *Pp*GRXC5 with GSH as variable substrate (Table 18). *Pt*GRXS12 is a monothiol class I GRX with a 'WCSYS' motif able to deglutathionylate e.g. glyceraldehyde-3-phospate dehydrogenase (Couturier, Koh, *et al.* 2009). Even though *At*GRXC5 ('WCSYC') has two cysteines in its active site motif, as seen for *Pp*GRXC5 ('YCPYC'), the resolving function of *At*GRXC5 glutathionylation occurs via a monothiol reaction mechanism (Couturier *et al.* 2011; Zaffagnini, Bedhomme, Marchand, Couturier, *et al.* 2012; Zimmermann *et al.* 2020).

Table 18: GRX class I deglutathionylation activities determined via HED assay

Protein	**K_m app** [mM]	**k_{cat} app** [s^{-1}]	**k_{cat} app /K_m app** [$M^{-1}s^{-1}$]	**source**
*Pp*GRXC5 (β-ME-SSG)	0.39 ± 0.11	39.45 ± 4.16	$1.00*10^5$	Finja Bohle, this work
*Pp*GRXC5 (GSH)	3.09 ± 0.61	86.9 ± 8.73	$2.81*10^4$	Finja Bohle, this work
*At*GRXC5 (β-ME-SSG)	0.20 ±0.02	1.21 ± 0.03	$6.05*10^3$	Couturier *et al.* 2011
*At*GRXC5 (GSH)	3.6 ± 0.8	0.69 ±0.11	192	Couturier *et al.* 2011
*Pt*GRXS12 (GSH)	3.99 ± 0.48	92.78 ± 5.32	$2.33*10^4$	Couturier *et al.* 2009
*At*GRXC1 (β-ME-SSG)	0.74 ± 0.01	38.91 ± 0.43	$5.25*10^4$	Riondet *et al.* 2012
*At*GRXC1 (β-ME-SSG)	0.173 ±0.02	14.3±0.5	$8.3*10^4$	Michelle Schlösser, unpublished
*At*GRXC2 (β-ME-SSG)	0.154 ±0.02	14.7±0.4	$9.5*10^4$	Michelle Schlösser, unpublished

4.2.4 The Δ*gr1* dwarfed phenotype is not dependent on GRXC5 activity

Plastid glutathione redox potential was determined with the use of GRX1-roGFP2 to be around - 311 mV in *P. patens* (Müller-Schüssele *et al.* 2020) and - 361 mV in epidermal plastids of Arabidopsis (Schwarzländer *et al.* 2008). The reduced redox potential is obtained by the glutathione reductase, reducing GSSG to two molecules of GSH. Loss of the organellar glutathione reductase GR2 in Arabidopsis (At3g54660) led to embryo lethality in the globular stage (Marty *et al.* 2019). Complementation studies with mitochondrial or plastidial targeted GR2 pin-pointed the essential factor for Arabidopsis survival to the plastidial activity (Tzafrir *et al.* 2004; Marty *et al.* 2019). The loss of mitochondrial GR activity was compensated by the NADPH-dependent thioredoxin reductase A/B (NTRA/NTRB), however plastidial GR activity could not be compensated by the FTR/TRX system (Marty *et al.* 2019).

The dwarfed but viable knock-out of organellar glutathione reductase in *P. patens* (Δ*gr1*) revealed a less reducing glutathione redox potential in plastids (-278 mV) and a light-sensitive

phenotype diminished in growth and photosynthetic activity (Müller-Schüssele *et al.* 2020). To investigate the lethality of *gr2* in Arabidopsis and the phenotype of Δ*gr1* in *P. patens*, a promising approach might be to look further into enzymes depending on GSH as electron donor. We were able to exclude plastidial GRX activity as the cause for the Δ*gr1* phenotype by acquiring a null mutant of the only plastidial class I glutaredoxin C5 in *P. patens.*

Here we performed phenotypic comparison under control conditions, light stress and elevated temperatures (Figure 25, Figure 26). A dwarfed, Δ*gr1*-like phenotype would be expected if GRXC5 malfunction would be the source for the stress-sensitive phenotype. The WT-like phenotype of Δ*grxc5* therefore suggests that GRXC5 malfunction is not the cause of the Δ*gr1* phenotype, is not essential in its function, or GRXC5 has a negatively regulating effect on GR1. In the latter case, the absence of GRXC5 in Δ*gr1* would suppress the Δ*gr1* phenotype and lead to a WT-like growth of a Δ*gr1*Δ*grxc5* double mutant. So far, Δ*grxc5*Δ*gr1* double mutants are generated to further test the relation between *Pp*GR1 and *Pp*GRXC5 (preliminary data, Sadia Sayed Tamanna). WT-like growth (Figure 25) and photosynthetic performance (Figure 28) of Δ*grxc5* indicated that another GSH-dependent pathway might be responsible for the dwarfed phenotype of Δ*gr1.*

Some GSH-dependent enzymes in plastids involved in ROS scavenging such as dehydroascorbate reductase (DHAR), peroxide detoxification like PRXIIE or lipid and protein damage repair like glutathione-*S*-transferases (lambda or iota type) and methionine sulfoxide reductases B1 (MSRB1) are important enzymes for redox homeostasis (Liu *et al.* 2013; Noshi *et al.* 2016; Rey & Tarrago 2018; Müller-Schüssele, Bohle, *et al.* 2021; see chapter 3.2). A *S*-glutathionylation target in the plastids is the 2-cys-peroxiredoxin (pea 2-Cys-PRX) (Calderón *et al.* 2017; Dreyer *et al.* 2021). Plastidial 2-cys peroxiredoxin A and B knock-outs in Arabidopsis revealed a role in the oxidative inactivation of CBC enzymes like FBPase in light:dark transition (Vaseghi *et al.* 2018; Dreyer *et al.* 2021). An increased growth of the *2-cys-peroxiredoxinAB* knock-out was detected under 10 s high light, 80 s low light, fluctuating light conditions due to the ability of *2-cys-peroxiredoxinAB* to utilize the short high light pulses for photosynthesis (Vaseghi *et al.* 2018). However, the reduction of 2-Cys-PRX occurs via the NADPH-dependent thioredoxin system (NTS) (Vaseghi *et al.* 2018). In contrast to that, the plastidial PRX (PRXIIE) is regenerated by the GRX-glutathione system (Gama *et al.* 2008; Dreyer *et al.* 2021). Poplar plastidial GRXS12 was identified to efficiently deglutathionylate PRXIIE at Cys 121, interestingly, GSH alone was also able to deglutathionylate PRXIIE-SSG (Gama *et al.*

2008; Dreyer *et al.* 2021). PRXIIE shows a thiol peroxidase activity with H_2O_2 of 2.6×10^4 M^{-1} s^{-1} (Gama *et al.* 2008) and a potential function in peroxynitrite detoxification (Romero-Puertas *et al.* 2008). In an affinity chromatography approach with His-tagged PRXIIE 14 plastidial proteins were identified as potential interaction partners of PRXIIE, with 5 proteins being involved in photosynthetic processes (Dreyer *et al.* 2021).

The growth and photosynthetic activity in the Δ*grxc5* mutant was examined to see if the loss of plastidial class I activity affects PRXIIE activity and its putative regulation of proteins involved in photosynthetic processes. First, fluctuating light conditions comparable to Vaseghi *et al.* (2018) were chosen. However, no deviation from the WT phenotype was observed for Δ*grxc5* under 10 s low light, 80 s high light or 15 min low light and 15 min high light regimes (Figure 26). Further experiments monitoring photosynthetic performance via PAM and GFS measurements (Figure 40, Figure 41) showed no differences in WT and Δ*grxc5* but showed an altered photosynthetic performance for Δ*gr1* as seen in Müller-Schüssele *et al.* (2020). The impact of the loss of GRXC5 needs to be further analyzed e.g. via PRXIIE activity assays in Δ*grxc5*. However, Western blot analysis showed that 0.5 mM GSH alone is enough to completely reduce PRXIIE-SSG within 10 min *in vitro* without the presence of a GRX (Dreyer *et al.* 2021). In Δ*gr1* with a less reducing E_{GSH} (Müller-Schüssele *et al.* 2020), analyzing the PRXIIE activity might be of great interest, since the deglutathionylation of GSH alone due to higher GSSG concentrations might be less likely to occur.

Furthermore, plastidial methionine sulfoxide reductase knock-outs in Arabidopsis did not reveal an embryo lethal *gr2* like phenotype (Laugier *et al.* 2009). Other plastidial proteins relying on the availability of GSH as electron donor are GST-L/I and DHAR (see 3.2, Fig.2). Higher ascorbate levels in Δ*gr1* and high-light sensitivity of the plastidial knock-out of DHAR (*At*DHAR3) link part of the phenotype to impairments in the ascorbate-glutathione cycle (Noshi *et al.* 2016; Müller-Schüssele *et al.* 2020). However, even the loss of total DHAR activity in DHAR triple knock-outs did not result in embryo lethality of Arabidopsis as seen for *gr2* (Rahantaniaina *et al.* 2017).

Light-dependent dynamic changes in the stromal E_{GSH} were observed in WT plastids of *P. patens* expressing GRX1-roGFP2 with a decrease in stromal E_{GSH} upon illumination and a fast increase in stromal E_{GSH} upon darkness with an immediate subsequent decrease. Due to the high oxidation level of GRX1-roGFP2 in Δ*gr1,* these dynamics could not be measured in the

respective mutant (Müller-Schüssele *et al.* 2020). However, these E_{GSH} dynamics were not detectable in Δ*grxc5* expressing plastidial targeted roGFP2 (Figure 42). The dynamics might therefore either be absent in mutants lacking class I GRX in plastids or undetectable in roGFP2 assays. This might be due to uncatalyzed and therefore slower equilibration of the GSH:GSSG buffer with roGFP2 compared to WT in which the plastidial class I GRX is present (*in vitro* +/- GRX see Figure 22, Figure 42).

Fast oxidation of the stromal E_{GSH} upon darkness may play a role in the oxidation of plastidial TRX, which is important for enzyme regulation of the CBC (Wolosiuk & Buchanan 1977; Yoshida *et al.* 2018; Sugiura *et al.* 2019; Müller-Schüssele *et al.* 2020). CBC enzymes reduced under light conditions by the FDX-FTR-TRX system, such as FBPase or GAPDH (Ojeda *et al.* 2018), connect the fixation of CO_2 to the light-dependent photosynthetic reaction (Michelet *et al.* 2013). Interestingly, chloroplastic GAPDH can occur as homo tetramers A_4 or hetero tetramers of A and B subunits (A_2B_2) and even form higher oligomers $(A_2B_2)_n$, whereas so far only for the homo tetramer A_4 an inactivation upon glutathionylation was detected (Zaffagnini *et al.* 2007; Marotta *et al.* 2022).

The link of the thiol-switching TRX and GRX systems was studied in cytosol and mitochondria and showed that the cytosolic TRX system can function as back-up system for the GRX system (Reichheld *et al.* 2009; Marty *et al.* 2009). However, the plastidial TRX system is not able to serve as functional back-up system for the loss of glutathione reductase activity in plastids (Marty *et al.* 2019; Müller-Schüssele *et al.* 2020). In plastids, thioredoxins such as TRXf have been identified as *S*-glutathionylation target (Michelet *et al.* 2005), as well as thioredoxin-regulated CBC-enzymes such as FBPase (Zaffagnini, Bedhomme, Groni, *et al.* 2012; Ojeda *et al.* 2018).

We measured CO_2 uptake and assimilation in Δ*grxc5* in light to dark transitions to see if plastids lacking class I GRX have differences in the rate at which enzymes involved in CO_2 fixation turn on and off. Since proteins like GAPDH, FBPase, TRXf and RuBisCO were identified as plastidial glutathionylation targets (Michelet *et al.* 2005; Zaffagnini *et al.* 2007; Zaffagnini, Bedhomme, Groni, *et al.* 2012), lack of respective plastidial GRX might then lead to the inefficient deglutathionylation of these enzymes, which might influence their activity. We did not detect a significant difference in CO_2 uptake and assimilation between WT and Δ*grxc5* nor a difference in the rate of ΔCO_2 and ΔA upon light to dark and dark to light transition (Figure

41) questioning the role of GRXC5 on CBC enzyme regulation. The biological relevance and function of the stromal E_{GSH} dynamics remains unsolved. Further experiments, like using the plastidial thioredoxin sensor CROST2 (see Chapter 5), are needed to elucidate if the E_{GSH} dynamic can influence the thioredoxin redox state.

4.2.5 Without GRXC5, reduction kinetics after oxidation are severely impacted

To test for the absence of class I GRX activity roGFP2 alone (without linked hGRX1) was targeted to the plastid stroma of the Δ*grxc5* #54 mutant generating two independent lines #17 and #21, which were further characterized. The dynamic range of TKTP-roGFP2 with δ = 5.13 (WT) and 4.46 (Δ*grxc5*) is in line with an *in vivo* dynamic range of ~5 for GRX1-roGFP2 via CLSM measurements in Arabidopsis cytosol (Meyer *et al.* 2007; Ugalde, Fuchs, *et al.* 2021; Ugalde *et al.* 2022) and ~5-6 of roGFP2 in chloroplasts (Schwarzländer *et al.* 2008). Dynamic ranges determined in a plate reader-based system resulted in δ ~3.5 for GRX1-roGFP2 (Ugalde, Fuchs, *et al.* 2021), while in this study the plate reader-based dynamic range of roGFP2 was lower with 2.15 for WT and 2.0 - 2.2 for Δ*grxc5* (#21, #17) (Figure 31). The oxidation of roGFP2 in physiological conditions revealed an oxidation degree of 45% for WT and 65% (#21) to 68% (#17) for the two respective Δ*grxc5* lines. Calculation of E_{GSH} according to Nernst Equation in Schwarzländer *et al.* 2008 with a pH of 8 and a resulting E'_0(roGFP2) of -309.58 mV (-280 mV roGFP2 midpoint potential, Aller *et al.* 2013) revealed a redox potential of -311.78 mV of WT and a shift of ~10 mV to -299.3 (#17) and -301.1 mV (#21) for the Δ*grxc5* lines (Figure 32, Figure 33). The same stromal E_{GSH} redox potential of -311 mV for the WT was measured in Müller-Schüssele *et al.* (2020) with GRX1-roGFP2, while a less negative redox potential of -278 mV was measured in Δ*gr1.*

The resulting redox potential in Δ*grxc5* must be interpreted with caution, due to the lack of class I GRXs in the measured compartment. Because of the absence of class I GRX activity, the rapid equilibration of roGFP2 with the E_{GSH} is not catalyzed anymore, thus only allowing a thermodynamic equilibration. Potential changes in the glutathione ratio or glutathione redox potential might be too slow to be monitored without a catalyst present (Meyer *et al.* 2007). Reaction rates in the presence or absence of a catalyst support this hypothesis: the reaction of a low molecular weight thiol such as GSH with a glutathionylated protein (RSSG) shows a rate constant between 0.01-200 $M^{-1}s^{-1}$, while the reaction coupled to a GRX increases to 10^5-10^6 $M^{-1}s^{-1}$ (Deponte 2017). By calibrating the sensor *in vivo*, it was possible to conclude that

roGFP2 was not fully oxidized in the mutants, so that an increase in sensor oxidation would still be within the dynamic measurement range of roGFP2. The increase in roGFP2 oxidation observed in the mutants may thus be uncoupled from E_{GSH} and only displaying the oxidation status of roGFP2.

We confirmed the absence of enzymes able to deglutathionylate roGFP2 by monitoring the *in vivo* response of roGFP2 after 1-10 mM H_2O_2 treatment (Figure 35). We observed a short-term difference between WT and Δ*grxc5* in the degree of roGFP2 oxidation 30 min after H_2O_2 removal. Interestingly, we observed already a reduction of roGFP2 in WT treated with 1-2 mM H_2O_2 prior to H_2O_2 removal. This response might be linked to catalase activity (Mhamdi *et al.* 2010) dismutating two H_2O_2 molecules to two molecules of H_2O and O_2. A similar response was not detected in Δ*grxc5*. The absence of roGFP2 reduction within 80 min after H_2O_2 application (1-2 mM) in Δ*grxc5* further supports the hypothesis that the E_{GSH} is kinetically uncoupled from cysteine redox state by the lack of a suitable catalyst such as GRXC5. The plastid-targeted roGFP2 might therefore not be suitable to estimate a potential shift in E_{GSH} or GSH:GSSG ratio in the Δ*grxc5* background, emphasizing the need to further determine total GSH and GSSG concentrations via e.g. HPLC analysis as seen for Δ*gr1* in Müller-Schüssele *et al.* 2020.

4.2.5.1 *P. patens* shows increased glutathionylation levels after oxidative stress treatment

Immunodetection with a monoclonal glutathione antibody was performed to determine the glutathionylation state of *in vivo* target proteins 30 minutes after H_2O_2 treatment (Figure 36, Figure 37, Supplemental Figure 2, Supplemental Figure 3). It should be noted that the experiments were based on total protein extracts and thus reflect not only plastid but total cell status of protein-bound glutathione. Experiments in protonema and gametophore tissue revealed prominent bands of glutathionylated proteins at ~55 kDa and ~100 kDa. The ~55 kDa might be identified as the large subunit of RuBisCO (RBCL) with a molecular weight of ~52.7 kDa in *P. patens* (UniProt: UniRef100_P34915) and a high protein abundancy throughout photosynthetic organisms (Ellis 1979; Raven 2013). Post-translational modifications of RBCL at Cys 172, 247 and 427 including *S*-glutathionylation and *S*-nitrosylation were identified in Chlamydomonas and Arabidopsis (Zaffagnini, Bedhomme, Groni, *et al.* 2012; Michelet *et al.* 2013).

Additional studies suggested the thiol modifications to be responsible for downregulation of RuBisCO activity and increased proteolysis upon oxidative stress (Tenaud & Jacquot 1987; Peñarrubia & Moreno 1990; Moreno *et al.* 2008; Michelet *et al.* 2013; Roni *et al.* 2022). Weaker band intensities at ~55 kDa (e.g. Figure 31) in PageBlue™ stained protein samples of *P. patens* protonema and gametophore tissue suggest that after 30 min of peroxide treatment (T_1) RBCL was partially degraded. (e.g. Figure 39). We observed an increase of the apparent band at ~55 kDa after 10 mM H_2O_2 treatment compared to unstressed conditions in protonema and gametophore tissue (Figure 38, Figure 39). Reductants like NADPH generated during the light-dependent photosynthesis reaction provide electrons to the Calvin Benson cycle but also to NADPH-dependent enzymes such as the organellar GR. Increased levels of H_2O_2 inhibit photosynthesis by oxidizing enzymes of the CBC (Foyer & Shigeoka 2011). Glutathionylation of RBCL induced by oxidative stress might contribute to the reduced efficiency of the CBC- reaction leaving more NADPH for enzymatic pathways involved in ROS scavenging.

An increase in glutathione-labelled protein was detected in all genotypes directly after H_2O_2 treatment (T_1) compared to unstressed conditions (T_0) (Figure 36, Figure 37, Figure 39, Supplemental Figure 2, Supplemental Figure 3). Thus, the absence of GRXC5 or GR1 in the respective mutants did not lead to an increased glutathionylation level, concluding that the glutathionylation of proteins *in vivo* seems to be independent of organellar GR or plastidial class I GRX activity.

If GRXC5 is essential for deglutathionylation of proteins in plastids I expected a higher level of glutathionylated proteins in protein extracts of Δ*grxc5* 30 min after H_2O_2 treatment (T_{30}). However, glutathionylation levels 30 min after treatment decreased slightly in all genotypes of protonema and gametophore tissue, supposing a non-essential function of GRXC5 on protein deglutathionylation *in vivo*. T_{30} signal did not show severe differences between the genotypes, indicating that Δ*grxc5* is still able to deglutathionylate proteins in the same amount as WT.

If a shift in E_{GSH} is observed already under physiological conditions like seen in Δ*gr1*, I would expect higher glutathionylation levels already under control conditions (T_0). Interestingly, higher glutathionylation levels were not detected for Δ*gr1* in the Western blot experiments compared to WT and Δ*grxc5*.

The Western blots showed variances between the biological replicates. A possible factor was

the protein loading in the respective SDS-PAGE. Untreated samples often displayed more intense bands in the PageBlue™ staining, then H_2O_2 treated samples, suggesting a potential degradation of proteins after H_2O_2 treatment. Differences between the biological replicates in the intensities of the Western blot may as well occur through mechanical stress (by tweezers or pipettes) during the treatment and harvesting procedure. NEM-labelling was done to block free thiols before the protein extraction process to prevent oxidation events during the cell lysis to influence the detected redox status in the blots. However, I did not include a control for complete NEM-labelling and can not rule out that inefficient NEM-labelling might contribute to variances in the Western blots.

4.2.5.2 Possible pathways of protein *S*-glutathionylation *in vivo*

Possible pathways of protein (de)glutathionylation are displayed in Figure 44 with their approximate reaction rates (unit: $M^{-1}s^{-1}$, k_{cat}^{app}/K_m^{app}) retrieved from literature (Hiner *et al.* 2000; Can *et al.* 2010; Deponte 2017; Zaffagnini, Fermani, *et al.* 2019). Under physiological conditions, the reaction of peroxide with a protein's thiol is described as a slow pathway for protein glutathionylation, since reactions of H_2O_2 with enzymes such as ascorbate peroxidase (APX) are being favored due to higher reaction rates (Mittler & Zilinskas 1991; Deponte 2017). This assumption is further supported by the slower reaction rates of GAPDH oxidation via H_2O_2 of ~10^2 $M^{-1}s^{-1}$ (k_{cat}^{app}/K_m^{app}), compared to the interaction of a human PRX (PRX2) with H_2O_2 at a rate constant of 10^8 $M^{-1}s^{-1}$ (Little & O'brien 1969; Manta *et al.* 2009; Deponte 2017). A direct oxidation of the glutathione pool shows a slow reaction rate for H_2O_2 and GSH of 0.87 M^{-1} s^{-1}, competing with the reactions of PRX and other H_2O_2 scavenging enzymes (Winterbourn & Metodiewa 1999; Deponte 2017). An increase in GSSG concentration *in vivo* thus is mainly a result from an increase in the activity of GSH-dependent enzymes such as: DHAR, MSRB1, GSTI/L, PRXIIE (Foyer & Noctor 2011; Dietz 2011; Liu *et al.* 2013; Rey & Tarrago 2018b; Müller-Schüssele, Bohle, *et al.* 2021).

Direct interaction of GSSG with a cysteine thiol showed a reaction rate of 0.8 M^{-1} s^{-1} (Nagy 2013), while GSSG with GRX showed a reaction rate in the order of 10^5 M^{-1} s^{-1} (Nagy 2013; Deponte 2017). This was also observed in the interaction of roGFP2 and GSH:GSSG ratios in the presence or absence of GRXC5 (Figure 7, see chapter 4.1.1.1). A direct glutathionylation of a protein thiol with GSSG may has to compete with other GSSG-dependent reactions (Deponte 2017). An exemplary competing reaction for GSSG would be the reduction of GSSG

by GR with reaction rates determined of rat liver GR to be around $4.9*10^6$ M^{-1} s^{-1} (Can *et al.* 2010). The likelihood of a reaction occurring *in vivo* is determined not only by the reaction kinetics, but also by the concentrations of the substrates, reaction products, and enzymes (Mortimer & Müller 2015; Deponte 2017).

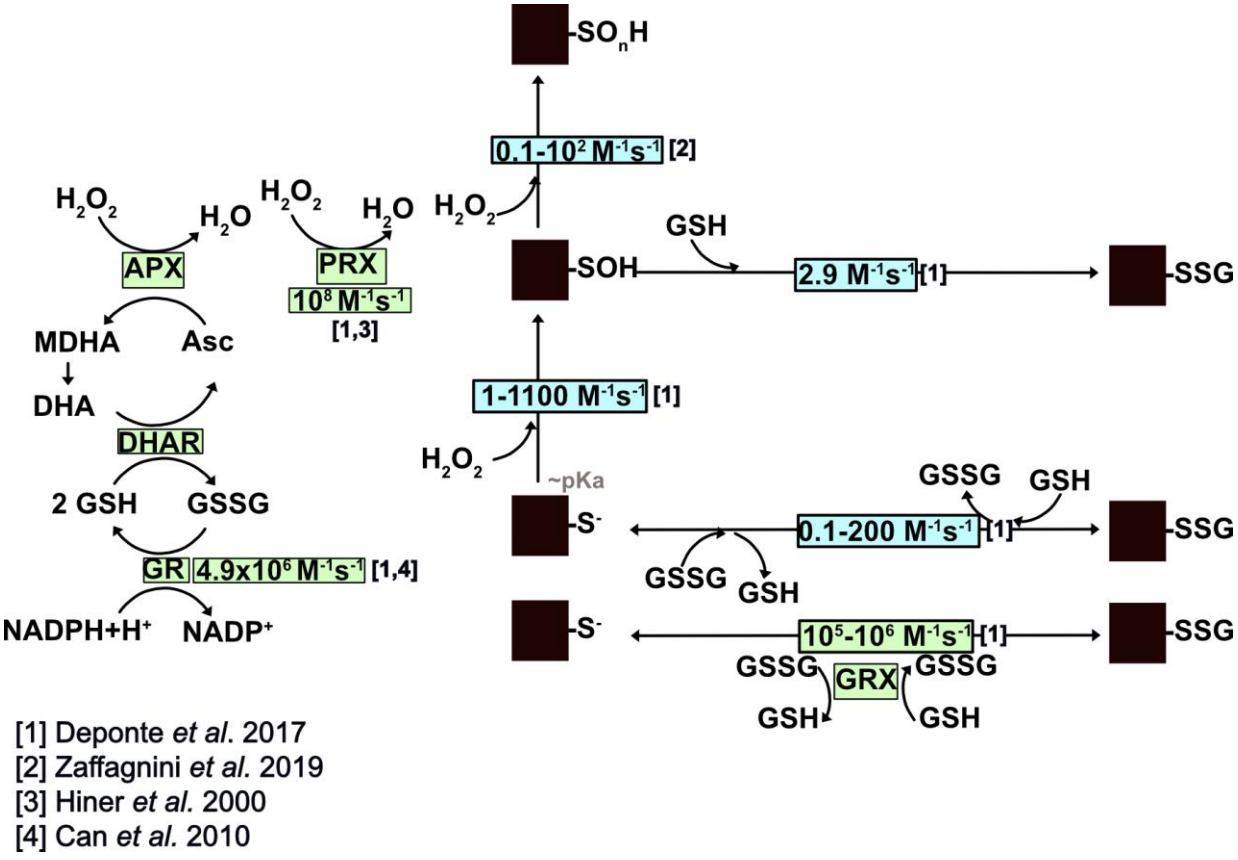

Figure 44: Reaction rates of enzymatic and non-enzymatic pathways leading to protein glutathionylation

Schematic overview of protein glutathionylation pathways and their exemplary and approximated reaction rates or rate constants [$M^{-1}s^{-1}$, $k_{cat}{}^{app}/K_m{}^{app}$] from literature. Enzymes with their respective rate constants are depicted in green, non-enzymatic reaction in blue. Reaction rates are based on Hiner *et al.* 2000; Can *et al.* 2010; Deponte 2017 and Zaffagnini *et al.* 2019. Exemplary target proteins are depicted as black box.

Based on the results of the H_2O_2 experiments with the subsequent detection of glutathione-associated proteins (Figure 37, Figure 38, Figure 39, Supplemental Figure 2, Supplemental Figure 3), several pathways of *S*-glutathionylation may be more likely to occur *in vivo* (Figure 45). The addition of H_2O_2 leads to an increased activity of the scavenging enzymes, which detoxify a large part of the H_2O_2 (Mittler 2002). In the experimental series, it remains undetermined how much H_2O_2 reached the plastids of *P. patens* after treatment with 10 mM H_2O_2. However, the H_2O_2 reaching the plastid stroma, increases enzyme activities of the scavenging enzymes resulting in an increase in the GSSG concentration (Figure 45 B). GSSG is

rapidly reduced by the organellar GR. In the organellar GR mutant (Δ*gr1*), GSSG is not reduced back to GSH and may be exported to the cytosol to lower plastidial GSSG concentration (Müller-Schüssele *et al.* 2020). However, since no consistent difference in glutathionylated proteins was observed under control conditions in Δ*gr1* compared to WT, increased GSSG levels alone might not drive protein *S*-glutathionylation. Higher concentrations of H_2O_2 could thus lead to the oxidation of individual, oxidation-sensitive proteins such as GAPDH (Zaffagnini *et al.* 2013) and contribute to *S*-glutathionylation through interaction with GSH. Glutathionylation could then function as a thiol protection against overoxidation after sulfenic acid formation. Dithiol target proteins might form intramolecular disulfide bridges upon glutathionylation, making it more difficult to identify those *in vivo* disulfide target proteins of *S*-glutathionylation.

Concluding, we observed that Δ*grxc5* showed similar amounts of glutathionylated proteins after 10 mM H_2O_2 treatment compared to WT, which rather suggests a non-essential role of GRXC5 in protein glutathionylation. In steady state conditions, GRX with a midpoint potential of -263 mV (poplar GRXC1, Couturier *et al.* 2013) might rather function in the deglutathionylation and reduction of disulfides. The impaired reduction after oxidative stress of plastid-targeted roGFP2 showed that roGFP2 was not efficiently reduced in the absence of *Pp*GRXC5 and that *Pp*GRXC5 fulfills an important function in protein deglutathionylation. *In vivo* target proteins of disulfide reduction by the GRX system have not been identified yet. However, results showed that enzyme catalyzed stromal deglutathionylation of proteins is not essential for survival of *P. patens* within the here tested conditions.

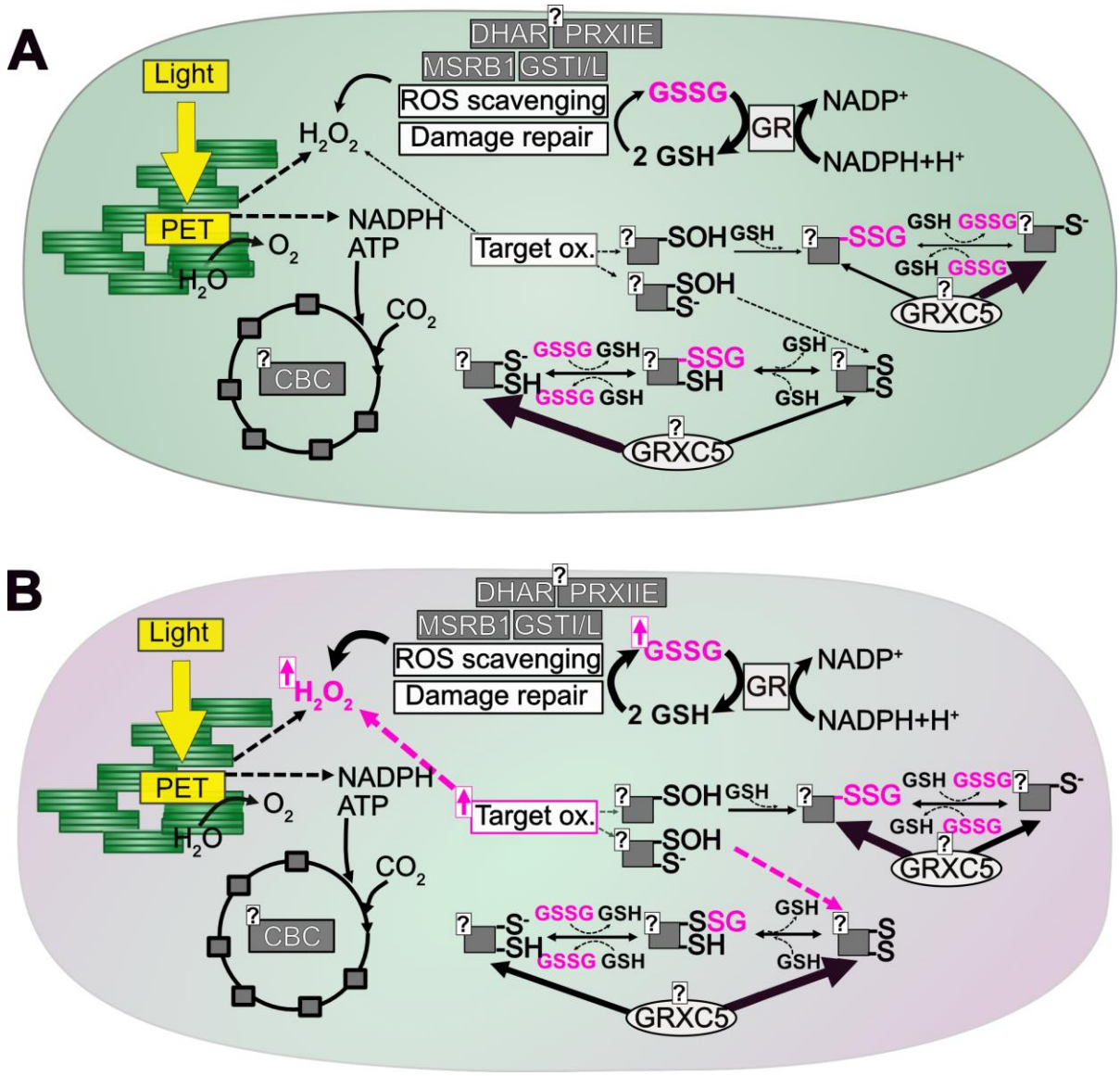

Figure 45 Protein *S*-glutathionylation and deglutathionylation in steady state (A) or oxidative stress (B) conditions in the plastid stroma

A In unstressed, steady-state conditions, a redox potential of -311 mV in plastids (Müller-Schüssele *et al*.2020 suggests that GRXs (with a midpoint potential of -263 mV, poplar GRXC1, Couturier *et al*. 2013) push towards deglutathionylation and disulfide reduction. **B** Addition of external H_2O_2 will trigger ROS scavenging and damage repair pathways producing GSSG which will be reduced by GR. Oxidation-sensitive thiol groups (with low pKa) will be directly oxidized by H_2O_2 (purple arrow) leading to the formation of sulfenic acid which can be further modified by GSH to form a *S*-glutathionylation. In proteins with two cysteines in proximity (such as roGFP2), further intramolecular disulfide formation might occur as a consequence of *S*-glutathionylation. In conditions with less reducing E_{GSH} and lower GSH:GSSG ratios, GRXs might rather push towards *S*-glutathionylation. **A, B** Oxidation-sensitive proteins undergoing *S*-glutathionylation in plastids or *in vivo* targets for GRX-mediated disulfide reduction (such as the artificial target protein roGFP2) still have to be identified.

5. The thioredoxin redox state in mutants with impaired E_{GSH} – a potential link between the plastidial thioredoxin and glutathione system?

Many enzymes identified as thioredoxin targets were also identified as potentially *S*-glutathionylated for example the plastidial TRXf (Michelet *et al.* 2005), fructose 1.6-bisphosphatase (Schurmann *et al.* 1981; Zaffagnini, Bedhomme, Groni, *et al.* 2012) and phosphoribulokinase (Brandes *et al.* 1996; Zaffagnini, Bedhomme, Groni, *et al.* 2012). While in the cytosol, the NADPH-dependent thioredoxin system was able to compensate for the loss of the cytosolic GR, this was not the case in plastids (Marty *et al.* 2009, 2019; Müller-Schüssele *et al.* 2020). To better understand what happens in the organellar GR mutants of *P. patens* (Δ*gr1*) and Arabidopsis (*miao*) and why the plastidial TRX system is unable to compensate, I introduced the TRX-redox status sensing CROST2 sensor (Sugiura *et al.* 2019) into these lines. The FRET-based sensor consists of a thioredoxin target protein CP12 of *Anabaena sp* connecting mTurquoiseΔ11 (CFP) and a circular permuted-mVenus (cp173 mVenus (YFP)) (Sugiura *et al.* 2019). *In vitro* characterisation of CROST2 confirmed the interaction with plastidial f and -m type thioredoxins from various plant species but also showed high pH dependency in lower pH ranges (Sugiura *et al.* 2019).

5.1. Results

The CROST2 pRI201_AN was obtained from Prof. Toru Hisabori (Institute of Technology, Tokyo, Japan) and used for transformation of *A. tumefaciens* and for floral dip of *Arabidopsis thaliana* transformation (WT and *miao*). Agrobacteria containing CROST2 were verified via PCR and sent for sequencing for further validation of the correct plasmid (Figure 46 A). Arabidopsis was transformed with clone #1 and the respective T_1 generation was screened for fluorescence and kanamycin resistance. T_2 was screened for a 3:1 fluorescence and kanamycin resistance segregation. Plants showing this segregation were propagated and T_3 plants further screened for homozygosity via fluorescence. For WT lines 2 #10 and 4 #4 were verified as homozygous. 3 #9 and 5 #7 were homozygous for CROST2 expression in the *miao* background. Homozygous T_3 of all lines showed less to no fluorescence signal after ~4 weeks of growth. Progeny of these plants showed a regain in fluorescence in the following

generation. This loss of fluorescence at the older stage might be consistent with CROST2 degradation observed in *A. thaliana* described in Sugiura *et al.* 2019.

For transformation of CROST2 into *P. patens*, CROST2 was amplified via PCR (for primers refer to Table 7) and cloned into pDONR207 as Gateway entry vector. Via LR reaction, CROST2 was cloned into PTA2_Act5_GW, sequenced and used for transformation of WT and Δ*gr1* #4 protoplasts (Figure 46 B). *P. patens* protoplast transformation with PTA2_Act5_GW_CROST2 and regeneration of vegetative tissue on neomycin selection media (G418) followed by fluorescence screening was done by Alexa Brox (Prof. Frank Hochholdinger, INRES, University of Bonn, Germany). Fluorescent moss colonies were transferred to fresh KNOP-ME plates and numbered (CROST2 in Δ*gr1* #4*:* #11, #13, #12, #19, #22, #29, #34, #37, #42; CROST2 in WT: #204, #250, #263).

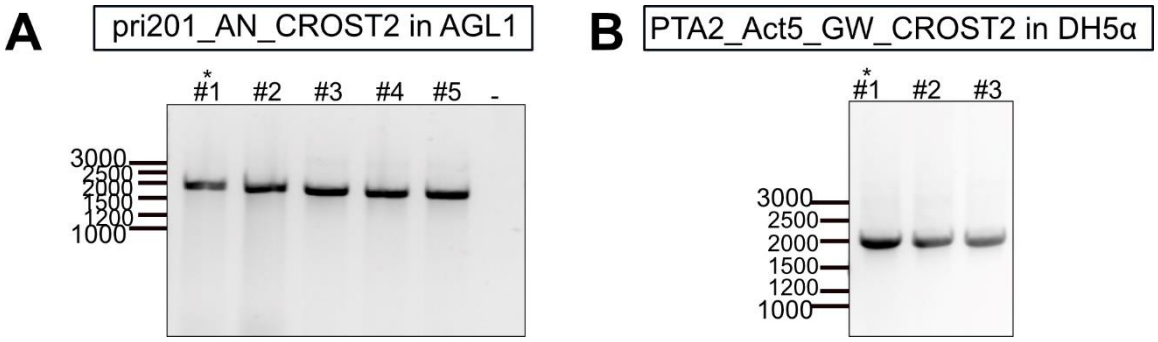

Figure 46: Verification of CROST2 containing expression vectors in AGL1 and DH5α via colony PCR

A CROST2 in the vector of pRI201AN (obtained from Prof. Tori Hisabori) expressed by *Agrobacterium tumefaciens* (AGL1). Verification PCR was done using primers binding in the in the 35S-promotor region (35S_F) and within the CROST2 (CROST2_R), expecting a size of 2200 bp (see Table 4). The clone marked with an asterisk was used for floral dip transformation of A. thaliana. **B** Expression of CROST2 in the gateway vector PTA2_Act5_GW in DH5α. Verification PCR was done using primers binding in the NOS-T terminator of the vector and in the Act5 promotor region (see Table 4), expecting a size of 2200 bp. The clone marked with an asterisk was used for further transformation of *P. patens* protoplasts.

5.1.1 Localization of the FRET-based thioredoxin sensor CROST2 in Arabidopsis

Homozygous Arabidopsis lines for CROST2 were analyzed with the CLSM regarding sensor localization and fluorescence signal (Figure 47). CROST2 localized to plastids in WT and *miao* verified by co-localization with chlorophyll autofluorescence. Chloroplasts with higher fluorescence signal were detected similar to observations shown in Sugiura *et al.* 2019. To verify for specific CROST2 signal an excitation and emission scan was carried out in a plate reader-based set-up (Figure 48). CROST2 emission at 494-16 nm after excitation with

wavelengths from 390-460 nm showed higher intensities in WT than in the *miao* background, both displaying high standard deviations. The CROST2 sensor displayed two emission peaks at 530 nm (YFP) and 475 nm (CFP) after excitation with 430 nm.

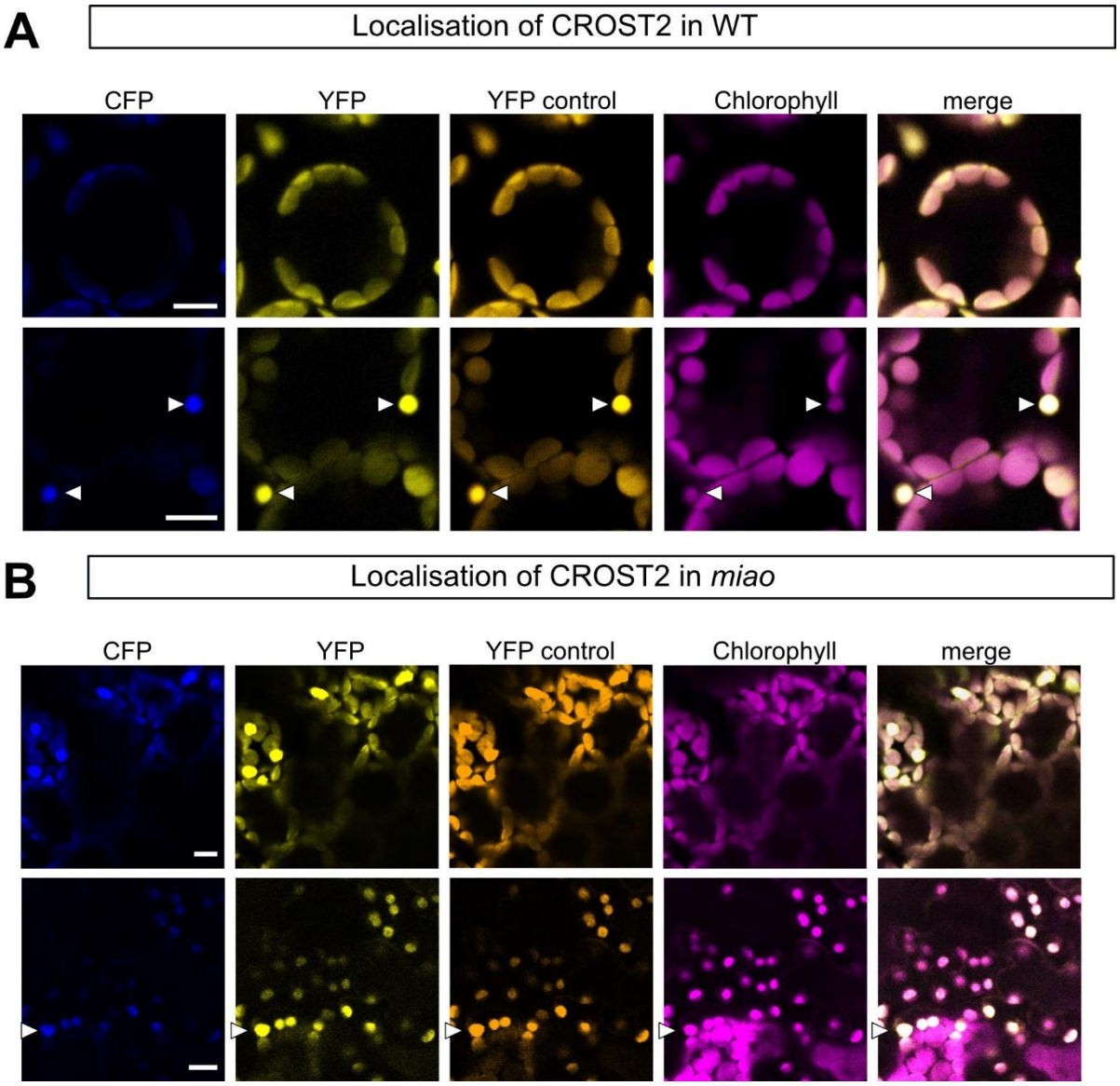

Figure 47: Fluorescence signal of CROST2 in chloroplasts of *A. thaliana* WT and *miao*

7-day old *A. thaliana* seedlings with plastid-targeted CROST2. Cotyledons of stably transformed CROST2 WT (Col-0) (**A**) and *miao* (**B**) plants were imaged using the CLSM. CFP fluorescence was detected with excitation at 405 nm and emission at 464-490 nm. FRET was detected after excitation with 405 nm and emission at 517-544 nm. YFP fluorescence was additionally collected at 488 nm with emission at 517-544 nm ('YFP control'). Chlorophyll was excited with 488 nm and an emission wavelength 624-673 nm. Arrows point to bright fluorescence signal spots, which may belong to plastids in pavement cells. Scale bars = 10 µm.

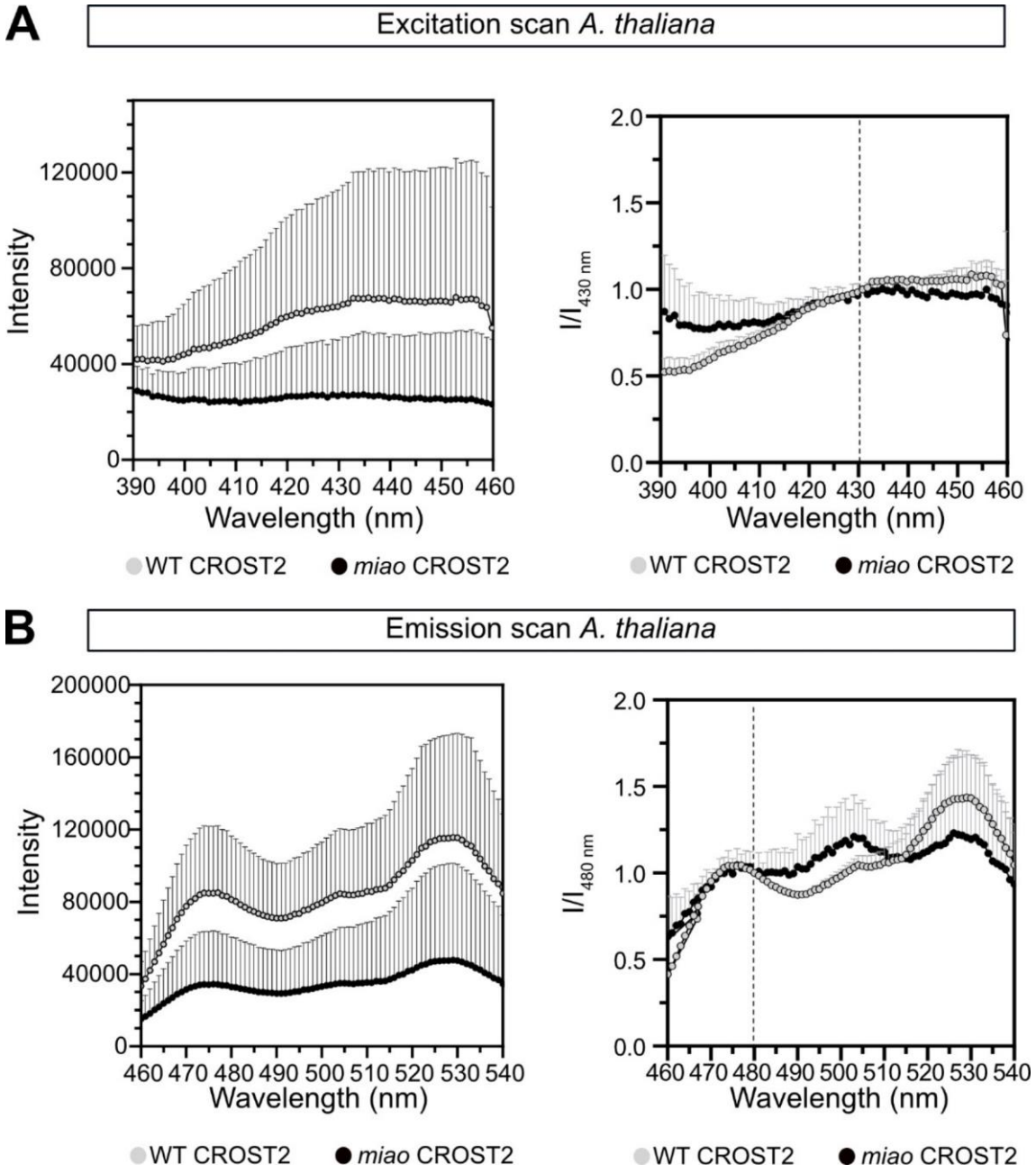

Figure 48: Excitation and emission scan of CROST2 expressed in *A. thaliana* leaf discs

A Excitation scan (Ex. 390-460-10 nm; Em.494-16) of 4-6 week old *A. thaliana* leaf discs expressing plastid-targeted CROST2. On the left side, raw intensities are plotted against excitation wavelengths. On the right site, intensities are normalized over intensities measured at 430 nm ($I/I_{430\ nm}$) **B** Emission scan (Em. 460-540 nm; Ex. 430-10 nm) of leaf discs of *A. thaliana* expressing plastid-targeted CROST2. On the left side, raw intensities are plotted against emission wavelengths. On the right site, intensities are normalized over intensities measured at 480 nm ($I/I_{480\ nm}$). Shown are the mean + SD of n= 10.

5.1.2 Thioredoxin redox state in mutant lines with impairments in the plastidial glutathione-dependent redox network

Arabidopsis leaf discs and 7-day-old seedlings were exposed to a light:dark regime, while CROST2 fluorescence was imaged in the plate reader during the dark phase to compare

thioredoxin redox status in *miao* with a less reducing E_{GSH} in the plastids with WT thioredoxin redox status (Figure 49). The CROST2 sensor showed a high YFP/CFP ratio in the dark. Subsequently after light treatment the ratio of the sensor is decreased about 0.2 and showed an increase in sensor ratio to initial values within 3 to 5 min in darkness. This behavior was observed independent of genotype (WT/*miao*) and tissue type (leaf, seedlings). *miao* showed a tendency to a steeper increase directly after light compared to WT but revealed no significant difference.

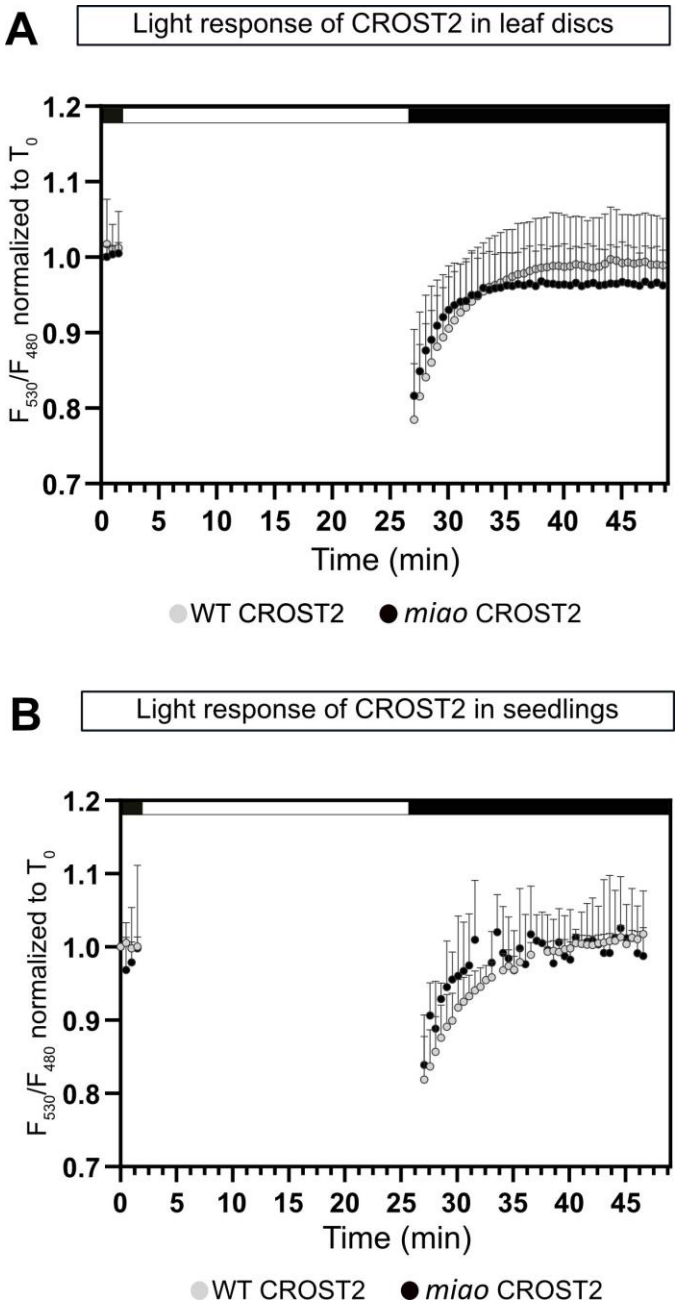

Figure 49: Light-dependent response of CROST2 expressed in *A. thaliana* in WT (Col-0) and *miao*

A *A. thaliana* leaf discs of WT 2 #10 and *miao* 3 #9 were pre-incubated in the dark for 20 min. Fluorescence was followed for 1.5 min (black bar) with excitation at 430-10 nm and emission at 530-20 and 480-10 nm before treatment of the leaf discs with 200 µE/m^2 s for 20 min (white bar). Fluorescence intensity was followed for a total of 50 min. (n=12-24 leaf disc samples of two independent measurements, measured on different days) **B** 7-day old seedlings of *A. thaliana* were imaged after pre-incubation in the dark for 20 min. Fluorescence was followed for 1.5 min (black bar) with excitation at 430-10 nm and emission at 530-20 and 480-10 nm before treatment with 200 µE/m^2 s for 20 min (white bar). Fluorescence intensity was followed for a total of 48 min. (n= 6 wells with a pool of 10 seedlings of two independent measurements, performed on different days)

5.1.3 Localization and calibration of the FRET-based thioredoxin sensor CROST2 in *Physcomitrium patens*

CROST2 (with a recA targeting peptide) in *P. patens* gametophores showed a clear plastidial localization, verified by co-localization with chlorophyll autofluorescence (Figure 50 A, B). A first calibration experiment was conducted using WT #204 and *Δgr1* #11 incubated with 10 mM DTT and 5 mM DPS. Additional reduction of the sensor via the light-dependent pathway involving the ferredoxin-dependent thioredoxin reductase (FTR) was further tested by incubation of the gametophores for 30 min in the dark before imaging (Figure 50 C). DTT and DPS treatment of the moss gametophores revealed dynamic ranges of δ = 1.16 (WT #204) and δ = 1.24 (*Δgr1* #11). Prior dark incubation of gametophores did not lead to a significant YFP/CFP ratio change in WT #204 or *Δgr1* #11. Excitation and emission scans were performed on WT #204 and *Δgr1* #11 gametophores leading to a small peak of excitation at ~430 nm and emission peak at 475 nm (CFP) and a weak peak at 530 nm (YFP) (Figure 51).

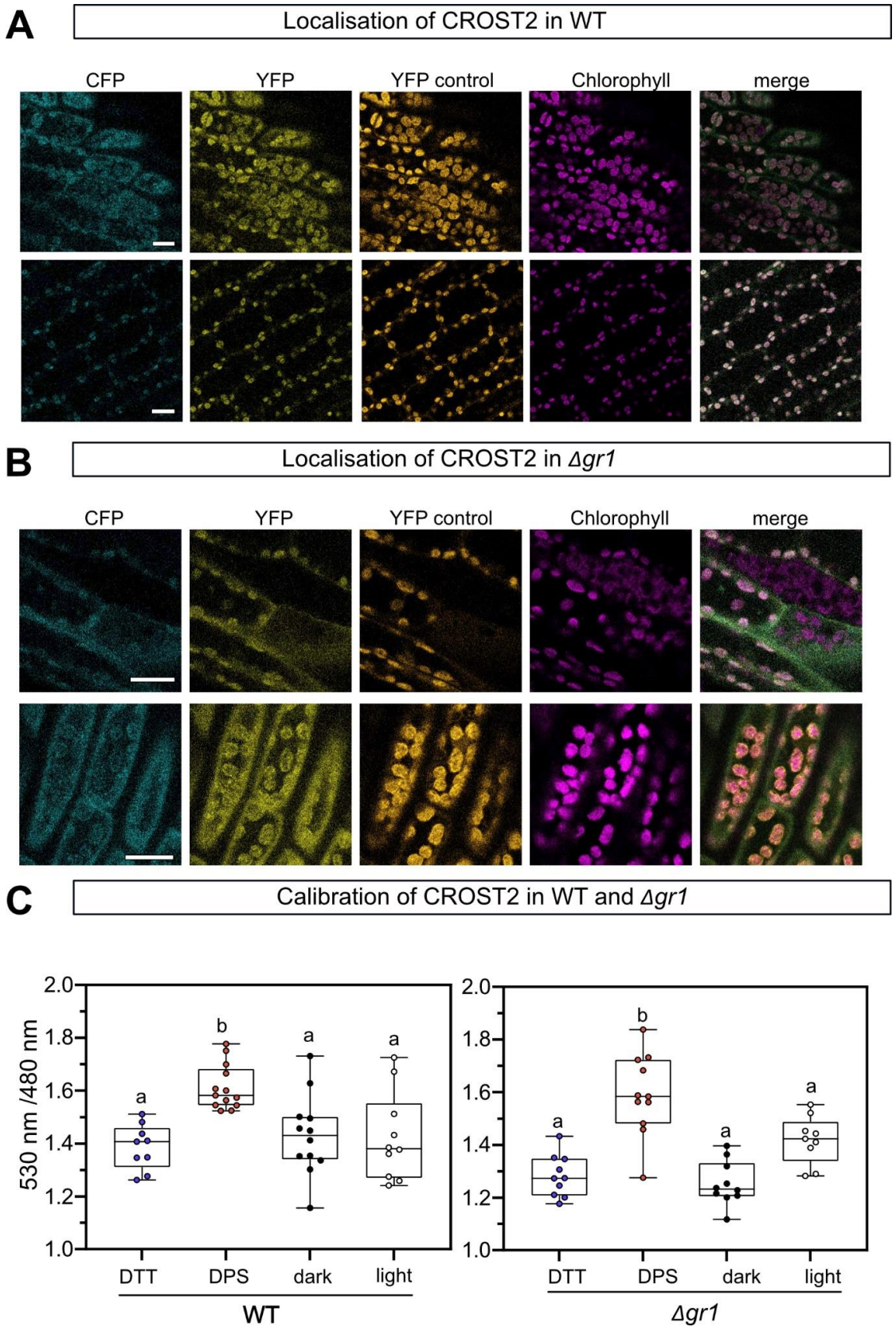

Figure 50: Plastid-targeted CROST2 in *P. patens* WT and *Δgr1* #4

P. patens WT #204 (**A**) and Δ*gr1* #11 (**B**) stably expressing CROST2. Gametophores were imaged using the CLSM. FRET was detected with CFP (Ex. 405 nm; Em. 464-490 nm) and YFP (Ex. 405 nm; Em. 517-544 nm), YFP was additionally excited at 488 nm in a separate track (Em. 517-544 nm) ('YFP control'). Chlorophyll was excited with 488 nm and emission wavelength of 624-673

nm. Scale bars = 20 µm. **C** Calibration of plastids of WT #204 and *Δgr1* #11 using 10 mM DTT or 5 mM DPS or dark incubation (30 min) or imaging without pre-dark incubation (labeled as 'light'). A minimum of 9 images were acquired of each treatment from at least three different gametophores. Boxes show 25-75 percentile with whiskers as min and max values. The horizontal line displays the median value. Intensities of the full image were extracted with the RRA ratio software. Different lowercase letters depict significant differences of a one-way ANOVA with Tukey's multiple comparison analysis ($p<0.012$).

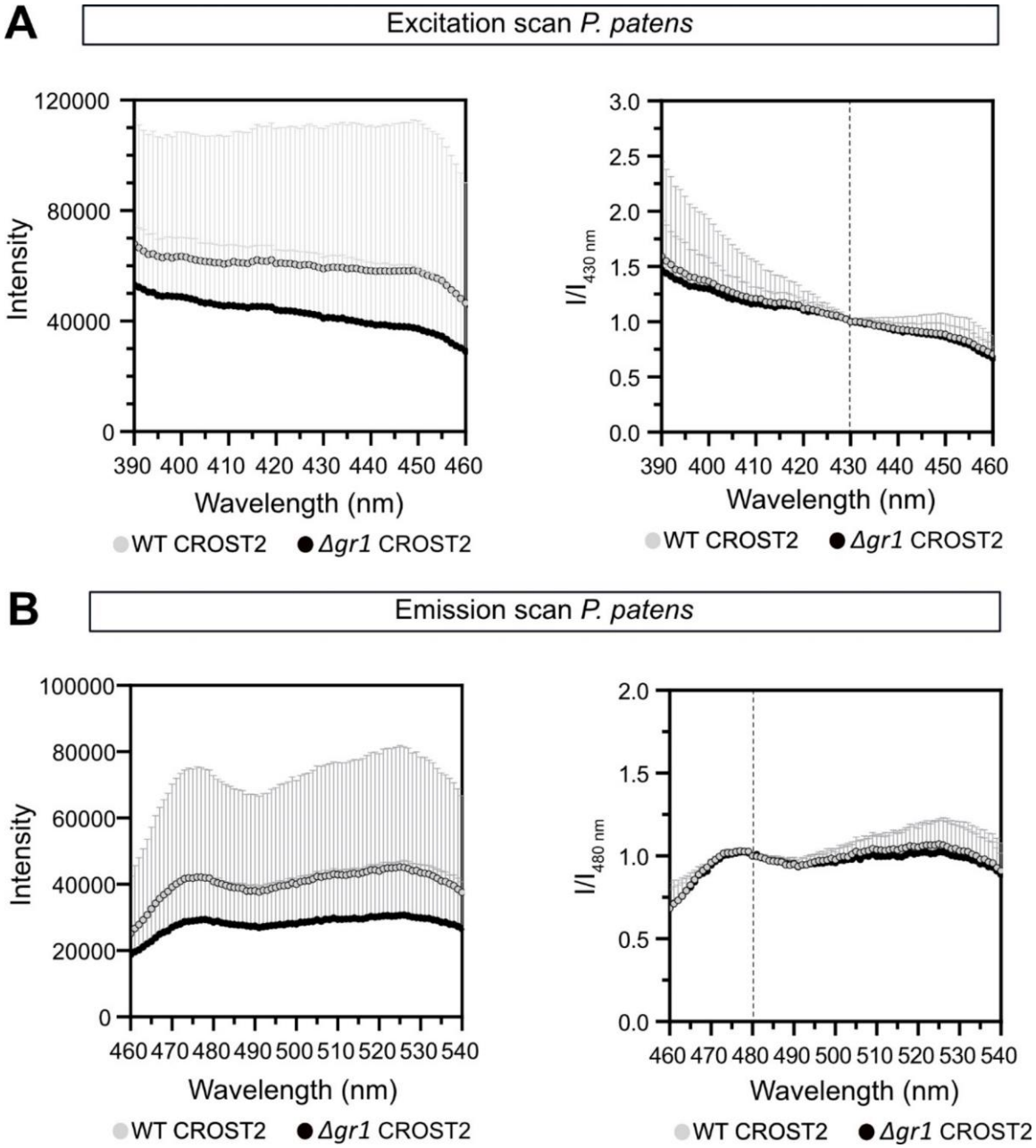

Figure 51: Excitation and emission scan of plastid-targeted CROST2 in *P. patens* gametophores

A Excitation scan (Ex. 390-460 nm; Em.494-16nm) of *P. patens* gametophores expressing CROST2. WT lines #204 and #263 and Δ*gr1* lines #11, #12, #13 and #19 were used. On the left side, raw intensities are plotted against excitation wavelengths. On the right site, intensities are normalized over intensities measured at 430 nm ($I/I_{430\ nm}$). **B** Emission scan (Em. 460-540 nm; Ex. 430-10 nm) of *P. patens* gametophores expressing CROST2. WT lines #204 and #263 and Δ*gr1* lines #11, #12, #13 and #19 were used. On the left side, raw intensities are plotted against

emission wavelengths. On the right site, intensities are normalized over intensities measured at 480 nm ($I/I_{480\ nm}$). The mean + SD of n= 11-16 wells is shown with at least 3 wells /line.

5.2. Discussion

Application of dynamic redox sensors will further increase knowledge in the mechanism of photosynthetic regulated redox processes in the plastids (Müller-Schüssele, Schwarzländer, *et al.* 2021). CROST2 itself is a powerful tool for measuring thioredoxin redox state in plants, however displaying a sensitivity in the lower pH range observed by a decrease in YFP-signal (Sugiura *et al.* 2019). Arabidopsis leaves expressing CROST2 in light:dark transitions showed dynamic changes in the 530/480 nm ratio. This dynamic was absent within the application of DCMU (3-(3,4-dichlorophenyl)-1,1-dimethylurea) as photosynthesis inhibitor. Thus, CROST2 sensor response is specific to the photosynthetic electron flux (Sugiura *et al.* 2019).

In this study, CROST2 was successfully expressed in Arabidopsis (WT, *miao*) and Physcomitrium (WT, Δ*gr1*) showing complete plastidial targeting (Figure 47, Figure 50 A,B) as seen in Sugiura *et al.* 2019. Seedlings and young rosettes of Arabidopsis plants showed high fluorescence while up to 4–6-week-old Arabidopsis leaves showed less to no remaining fluorescence signal. Progeny of these Arabidopsis lines in young age showed high fluorescence signal again. This unexpected loss of fluorescence can be explained by CROST2 sensor degradation, detected with a western blot against GFP in Arabidopsis leaves (Sugiura *et al.* 2019). However, possible reasons may be the inhibition of *de novo* synthesis paired with CROST2 proteolysis or silencing, resulting in a complete loss of fluorescence. Interestingly, silencing was observed in multiple T-DNA transformed reporter lines in *A. thaliana* and linked to multiple copy-numbers and higher expression levels (Schubert *et al.* 2004). CROST2 in pRI201_AN is expressed under the 35S promotor, which is known to potentially induce gene silencing in plants (review in Rajeevkumar *et al.* 2015). The likelihood for a higher copy number of CROST2 was minimized by following a 3:1 segregation but cannot be excluded when selecting for homozygous plants (see 5.1).

In response to a light to dark transition, CROST2 in Arabidopsis seedlings and leaf discs showed a rapid increase in YFP/CFP ratio, indicating sensor oxidation by lack of illumination (Figure 49). No significant difference was detected between WT and the plastidial glutathione knock-down mutant *miao*. From these results, a potential influence of plastidial GR-activity on TRXf and TRXm activities measured by CROST2 might be rather unlikely or not detectable within

this experimental set-up. However, we observed a non-significant trend of a more rapid CROST2 oxidation after light to dark transition in the *miao* background. Light to dark transitions and the effect on CROST2 oxidation might therefore be interesting to monitor in Δ*gr1*. To further conclude if the activity of the thioredoxin system is influenced by the absence or down-regulation of plastidial glutathione reductase, experiments also measuring during the light phase might be of great interest. Testing the potential interaction of the glutathione system with the thioredoxin system in plastids might be possible by introducing CROST2 in the available *P. patens* knock-out of plastidial class I GRX (Δ*grxc5*). Changes in kinetics in response to light to dark transitions are expected, if the absence of GRXC5 influences thioredoxin redox state.

6. Measuring glutathione redox potential in the crop plant *Hordeum vulgare*

Chapter six of this thesis is published on BioRxiv (open access)

Bohle F., Klaus A., Tegethof H., Schwarzländer M., Hochholdinger F., Meyer A.J., Acosta I.F., Müller-Schüssele S.J. (2022) High robustness of cytosolic glutathione redox potential under combined salt and osmotic stress in barley as revealed by the biosensor Grx1-roGFP2. https://doi.org/10.1101/2022.12.22.521445

6.1. Summary and personal contribution

Genetically encoded biosensors have been in use for over a decade and enabled the study of redox-related physiological parameters *in planta (*reviewed in Meyer *et al.* 2021; Müller-Schüssele, Schwarzländer, *et al.* 2021). The application of redox sensors has been primarily focused on easily transformable model plants such as *Arabidopsis thaliana* or *Physcomitrium patens* (Meyer *et al.* 2007; Schwarzländer *et al.* 2008; Müller-Schüssele *et al.* 2020; Ugalde, Fuchs, *et al.* 2021), but interest is increasing in establishing genetically encoded biosensors in crop plants like potato (Hipsch *et al.* 2021), tobacco (Moreno-García *et al.* 2022) and barley (Kirschner *et al.* 2018; Giridhar *et al.* 2022). Grx1-roGFP2 is a frequently used sensor to monitor glutathione redox potential and is well characterized *in vitro* and *in vivo* (Meyer *et al.* 2007; Gutscher *et al.* 2008; Schwarzländer *et al.* 2008). The glutathione buffer functions as electron source for enzymes involved in ROS scavenging and oxidative damage repair (Foyer & Noctor 2011; Müller-Schüssele, Bohle, *et al.* 2021) and is kept at a highly negative redox potential in animals, fungi and plants (Schwarzländer *et al.* 2016). For example the Arabidopsis cytosol displayed a redox potential of -320 mV (Meyer *et al.* 2007). Shifts in cytosolic E_{GSH} of Arabidopsis were observed upon exposure to heat or heavy metal stresses (Schwarzländer *et al.* 2009), oxygen deficiency (Wagner *et al.* 2019), pathogens and their elicitors (Arnaud *et al.* 2022) or in mutants with impairments in the glutathione homeostasis like the cytosolic and peroxisomal glutathione reductase mutant *gr1-1* (Marty *et al.* 2009). Within this study, we introduced Grx1-roGFP2 in the crop model plant barley (*Hordeum vulgare*; var. Golden Promise fast) to study cytosolic E_{GSH} shifts. We obtained homozygous reporter lines and characterized two independent lines named 2#1 and 5#39 with specific, cytosolic, and nuclear

GFP signal. We observed a high autofluorescence after excitation at 405 nm in vacuoles and cell walls. However, by focusing on fluorescence intensities of the nucleus, we were able to determine the dynamic range of Grx1-roGFP2 to vary between ca. 1.3 in leaf to ca. 2.3 fold change in root tissues with a cytosolic E_{GSH} estimated between -308 and -320 mV. Variations between tissue types might be most likely due to differences in permeability of solutes through the cell wall or different composition of autofluorescence emitting substances. A previously performed transcriptomic analysis of differently expressed genes under osmotic and salt stress revealed a change in GR expression after 24 h in root cells of barley (Osthoff *et al.* 2019). Upon replication of these osmotic and salt conditions, the here tested barley cultivar showed phenotypic impairments in root growth similar to Osthoff *et al.* 2019. Nevertheless, we observed a robust E_{GSH} with only minor changes in the roGFP2 oxidation after 96 h. To determine the cause of the robust E_{GSH}, we investigated whether E_{GSH} is counterbalanced by increased activity of GR or an overall increase in GSH concentrations under stress conditions. A significant upregulation of total GR activity in roots was not supported by DNTB (5,5'-dithiobis(2-nitrobenzoic acid))-based GR activity assays, which revealed GR activities to be around 92-105 nmol TNB/min/mg protein. An increase in glutathione amounts as source for the robust E_{GSH} was analyzed by labeling the total glutathione pool of barley roots with monochlorobimane (MCB). Here, similar staining intensities were observed for stressed and non-stressed plants. Within Golden Promise (fast), a very drought resilient barley variety (Gol *et al.* 2021), we did not observe a condition where the E_{GSH} shifted to less reducing conditions after stress. Our study emphasizes the need for further experiments analyzing the mechanism behind the high robustness of E_{GSH} in barley.

Within this study I performed all experiments involving the Grx1-roGFP2 transformed barley (seeds provided by Ivan Acosta, Max Planck Institute for Plant Breeding Research, Cologne). I further screened barley seeds for generating homozygous candidates. I conducted the seed propagation in the green house and characterized the candidates based on their fluorescence signal (Supplemental Fig 1). I conducted the roGFP2 calibration *in vivo* (Fig. 1, 2) and performed the osmotic and salt stress related experiments and the following analyses (Fig. 3, 4, 5, 6). I designed all figures and largely contributed to the writing of the manuscript.

6.2. Manuscript 2

bioRxiv preprint doi: https://doi.org/10.1101/2022.12.22.521445; this version posted December 22, 2022. The copyright holder for this preprint (which was not certified by peer review) is the author/funder, who has granted bioRxiv a license to display the preprint in perpetuity. It is made available under aCC-BY-NC-ND 4.0 International license.

High robustness of cytosolic glutathione redox potential under combined salt and osmotic stress in barley as revealed by the biosensor Grx1-roGFP2

Finja Bohle[1,3] Alina Klaus[2], Hendrik Tegethof[3,§], Markus Schwarzländer[4], Frank Hochholdinger[2], Andreas J. Meyer[3], Ivan F. Acosta[5], Stefanie J. Müller-Schüssele[1]

[1] Molecular Botany, Department of Biology, Technical University of Kaiserslautern, D-67633 Kaiserslautern, Germany

[2] Crop Functional Genomics, Institute of Crop Science and Resource Conservation (INRES), University of Bonn, D-53113 Bonn, Germany

[3] Chemical Signalling, Institute of Crop Science and Resource Conservation (INRES), University of Bonn, D-53113 Bonn, Germany

[4] Institute of Plant Biology and Biotechnology, University of Münster, D-48143 Münster, Germany

[5] Max Planck Institute for Plant Breeding Research, D-50829 Cologne, Germany

[§] current address: Miltenyi Biotec B.V. & Co. KG, 51429 Bergisch Gladbach

Short title: Grx1-roGFP2 reporter lines in barley

Correspondence:
Stefanie Müller-Schüssele
TU Kaiserslautern
Erwin-Schrödinger-Str. 70
67663 Kaiserslautern
mueschue@rhrk.uni-kl.de
Tel.: +49 (0)631-205-4391
Fax: +49 (0)631-205-2998

Keywords: *Hordeum vulgare*, redox-sensitive GFP, E_{GSH}, genetically encoded biosensor, water deficit, crop

One sentence summary: Generation and characterization of barley plants stably expressing Grx1-roGFP2 reveal high robustness of cytosolic glutathione redox potential (E_{GSH}) under combined salt and osmotic stress.

bioRxiv preprint doi: https://doi.org/10.1101/2022.12.22.521445; this version posted December 22, 2022. The copyright holder for this preprint (which was not certified by peer review) is the author/funder, who has granted bioRxiv a license to display the preprint in perpetuity. It is made available under aCC-BY-NC-ND 4.0 International license.

Abstract

- Barley is a staple crop of major global importance and relatively resilient to a wide range of stress factors in the field. Transgenic reporter lines to investigate physiological parameters during stress treatments remain scarce.
- We generated and characterized stable homozygous barley lines (cv. Golden Promise Fast) expressing the genetically-encoded biosensor Grx1-roGFP2, which indicates the redox potential of the major antioxidant glutathione in the cytosol.
- Our results demonstrate functionality of the sensor in living barley plants. We determined the glutathione redox potential (E_{GSH}) of the cytosol to be in the range of -308 to -320 mV. E_{GSH} was robust against a combined NaCl (150 mM) and water deficit treatment (-0.8 MPa) that caused growth retardation and showed only a minor oxidation after 96 h of treatment.
- We conclude that the generated reporter lines are a novel resource to study stress resilience in barley.

INTRODUCTION

Barley is among the most important crop species worldwide (Newton *et al.* 2011) and exhibits a high abiotic stress tolerance as compared to other cereal crops (FAO, https://www.fao.org/3/Y4263E/y4263e0e.htm; Munns *et al.* 2006). Varieties, landraces and wild barley accessions form a valuable genetic reservoir to screen for factors influencing resilience to the extreme conditions associated to climate change (Dawson *et al.* 2015; Muzammil *et al.* 2018). Several markers affecting winter survival, flowering time and abiotic stress tolerance have already been identified and are used in breeding (Newton *et al.* 2011; Dawson *et al.* 2015; Muzammil *et al.* 2018). Transcriptomic datasets investigating the response of barley to salt and/or water deficit identified oxidation-reduction processes as part of the stress response, especially after several days of stress exposure (Kreszies *et al.* 2019; Osthoff *et al.* 2019).

With its diploid, sequenced genome (Mascher *et al.* 2017), barley is a prime genetic model for the cereal grasses of the Triticeae tribe. Moreover, the variety Golden Promise is genetically accessible via embryo transformation (Imani *et al.* 2011; Amanda *et al.* 2022). Drought stress affects plant height, developmental timing and spikelet development with a role of PHOTOPERIOD-H1 (Ppd-H1), as demonstrated via introgression lines (Gol *et al.* 2021). However, while transgenic reporter lines are a standard research tool in other model plants,

bioRxiv preprint doi: https://doi.org/10.1101/2022.12.22.521445; this version posted December 22, 2022. The copyright holder for this preprint (which was not certified by peer review) is the author/funder, who has granted bioRxiv a license to display the preprint in perpetuity. It is made available under aCC-BY-NC-ND 4.0 International license.

only few fluorescent reporter lines have been generated to gain insight into barley growth and physiology, as e.g. for auxin and cytokinin signalling (Kirschner *et al.* 2018; Amanda *et al.* 2022) or calcium signatures (Giridhar *et al.* 2022).

Genetically encoded biosensors are fluorescent proteins (or protein pairs) that change their properties specifically in response to a physiological parameter. As any other protein, they can be targeted to specific subcellular localizations with targeting signals. The development and characterization of biosensors for a wide array of physiological parameters has paved the way for the specific assessment of physiological states of subcellular compartments, ultimately challenging and shifting many paradigms of cell biology (reviewed in Meyer *et al.* 2021; Müller-Schüssele, Schwarzländer, *et al.* 2021). For example, the redox potential of the redox pair of glutathione (GSH) and its oxidized form glutathione disulfide (GSSG) has been revealed to be far from its midpoint potential in subcellular compartments harboring a glutathione reductase (GR), with only nanomolar amounts of GSSG present. This results in glutathione redox potentials (E_{GSH}) as low as c. -320 mV in the cytosol of plant cells, making the largely reduced pool of glutathione a versatile electron donor reservoir for enzymes that draw electrons from GSH to perform reduction reactions. This includes enzymes involved in the scavenging of reactive oxygen species (ROS) or oxidative damage repair, e.g. dehydroascorbate reductase (DHAR) or atypical methionine sulfoxide reductases B (MSRB1) (Foyer & Noctor 2011; Rey & Tarrago 2018; Müller-Schüssele, Bohle, *et al.* 2021). The compartment-specific study of E_{GSH} has been largely driven by the characterization of redox-sensitive GFP2 (Meyer *et al.* 2007; Schwarzländer *et al.* 2008) that contains a GSH-dependent thiol switch on the outer face of the GFP beta-barrel structure. The redox status of this cysteine pair is dependent on E_{GSH} while reaction kinetics are accelerated by class I glutaredoxin (GRX) catalysis, resulting in roGFP2 linked to human glutaredoxin 1 (Grx1-roGFP2) as the most widely used E_{GSH} biosensor (Gutscher *et al.* 2008; Schwarzländer *et al.* 2016; Müller-Schüssele, Schwarzländer, *et al.* 2021).

The study of redox networks in *Arabidopsis thaliana* has already revealed that glutathione-dependent and thioredoxin-dependent systems can at least partially compensate for each other in mitochondria and the cytosol (Marty *et al.* 2009, 2019). This partially redundant input of electrons via glutathione reductase or the NADPH-dependent thioredoxin reductase A and B (NTRA, NTRB) largely prohibits oxidation of the glutathione pool. Nevertheless, null mutants of the cytosolic/peroxisomal glutathione reductase 1 (*gr1-1, gr1-2*) show a less negative cytosolic E_{GSH} than the wild type (WT) (Marty *et al.* 2009) with enhanced oxidation after osmotic stress (300 mM mannitol) (Bangash *et al.* 2019). In wildtype *A. thaliana*, oxidative shifts in cytosolic E_{GSH} have been observed under oxygen deprivation (Wagner *et al.* 2019), heat or

bioRxiv preprint doi: https://doi.org/10.1101/2022.12.22.521445; this version posted December 22, 2022. The copyright holder for this preprint (which was not certified by peer review) is the author/funder, who has granted bioRxiv a license to display the preprint in perpetuity. It is made available under aCC-BY-NC-ND 4.0 International license.

heavy metal stress (Schwarzländer *et al.* 2009) and after herbicide treatment of chloroplasts (Ugalde *et al.* 2021).

While transgenic sensor lines in the model dicotyledon *A. thaliana* are in use since more than a decade, the progress in other genetically accessible model plants has only recently started to gain momentum (Kirschner et al. 2018; Müller-Schüssele et al. 2020; Hipsch et al. 2021; Giridhar et al. 2022). To start filling this gap in temperate cereal crops, we created transgenic barley lines expressing the genetically-encoded redox biosensor cytosolic Grx1-roGFP2 for E_{GSH}. We aimed to investigate stress resilience in barley and to monitor E_{GSH} changes in different tissues *in vivo*. In this article, we characterise the obtained sensor lines and expose them to different stress treatments, revealing remarkable robustness of the cytosolic E_{GSH} in barley (cv. Golden Promise Fast).

MATERIAL AND METHODS

Plant materials and growth conditions

Experiments were conducted in ‘‘Golden Promise Fast’’, the *Ppd-H1* introgression line of the transformable barley (*Hordeum vulgare* L.) cultivar Golden Promise (Gol *et al.* 2021; Amanda *et al.* 2022). After 3 days of stratification at 4°C on wet filter paper, seeds were transferred to germination paper (Anchor Paper Co, Saint Louis, USA). Barley was grown for up to 7 days in germination paper rolls with ½ strength Hoagland solution (Hoagland and Arnon, 1938). Stress treatments were carried out as described in Osthoff *et al.* (2019) with three days of growth in ½ strength Hoagland solution before transfer to nutrient solution with 150 mM NaCl and -0.8 MPa water potential (adjusted with PEG8000). Paper rolls were grown upright in a beaker in a climate cabinet under 16 h light (120 µmol photons m^{-2} s^{-1}) at 22°C and 8 h dark at 18°C.

For propagation and seed production, 7-10-day-old barley seedlings were transferred to the green house and soil-grown with 15 h of light (1000-6000 lux) at 22°C and 9 h of dark at 18°C.

Generation of barley Grx1-roGFP2 lines

A barley-compatible expression vector for Grx1-roGFP2 was constructed by restriction enzyme-based cloning in the binary vector p6i-2x35s-TE9, kindly provided by Jochen Kumlehn (Himmelbach *et al.* 2007), along with the pUBI-ABM (Watanabe *et al.* 2016), as source of the maize (*Zea mays*) ubiquitin promoter *ZmUbi1* and the *nos* terminator. A Grx1-roGFP2 fragment with BamHI and SalI restriction sites was ligated into the linearized UBIp-ABM (BamHI, SalI) with the ClonJet kit (ThermoFisher), to produce pZmUBI1pro-Grx1roGFP2-nosT.

bioRxiv preprint doi: https://doi.org/10.1101/2022.12.22.521445; this version posted December 22, 2022. The copyright holder for this preprint (which was not certified by peer review) is the author/funder, who has granted bioRxiv a license to display the preprint in perpetuity. It is made available under aCC-BY-NC-ND 4.0 International license.

The ZmUBI1pro-Grx1roGFP2-nosT cassette was released by digestion with SfiI and ligated into binary vector p6i-d35STE9 previously cut with the same enzyme. The resulting expression plasmid was transformed in Golden Promise Fast as described in Amanda *et al.* (2022) and T_0 hemizygous regenerants from 8 independent events were produced. We screened the T_1 progenies from 5 out of the 8 independent events for roGFP2 fluorescence with a confocal laser scanning microscope and selected lines with 3:1 segregation of positive:negative fluorescence. T_2 progenies of positive-fluorescent plants were further screened for 100% fluorescence expression to obtain homozygous transgenics. This procedure resulted in selecting two independent lines (5-3#39 and 2-1#1). We conducted all reported experiments in homozygous T_3 progenies of these lines.

Excitation scan of young barley leaves

Leaf discs were transferred into the wells of a 96-well plate containing 200 µL imaging buffer (10 mM MES, 5 mM KCl, 10 mM $CaCl_2$, 10 mM $MgCl_2$ pH 5.8). For reduction and oxidation of Grx1-roGFP2 the imaging buffer was supplemented with 1.5 M H_2O_2, 5 mM 2,2'-dipyridyl disulfide (DPS) or 10 mM dithiothreitol (DTT) to obtain total reduction and oxidation of the sensor. Leaf discs were vacuum infiltrated for 10 min and further incubated for 30 min. Fluorescence spectra were recorded with a plate reader (Clariostar®, BMG) with excitation wavelengths from 386-495 nm and emission set to 530/40 nm. Fluorescence was normalized over the fluorescence intensity at the isosbestic point (IP) of roGFP2 at 425 nm.

Confocal laser scanning microscopy of Grx1-roGFP2

Confocal laser scanning microscopy of Grx1-roGFP2 in barley roots and leaves was conducted with a LSM780 (Axio Observer.Z1, Carl Zeiss, Oberkochen, Germany) using a 25x (Plan-Apochromat 25x/0.8) or 40x (C-Apochromat 40x/1.2W) objective by exciting roGFP2 at 405 nm (diode laser, 3%) and 488 nm (argon laser (1.5 %) and collecting roGFP2 fluorescence between 508 and 535 nm. Autofluorescence was detected at 430 to 470 nm after excitation at 405 nm. Ratio calculations and further image analysis was performed in a MATLAB-based ratio software (RRA) (Fricker 2016). Where indicated, regions of interest were set to nuclei as shown in **Suppl. Fig. 1**. Oxidation degree of roGFP2 (OxD) was calculated according to Schwarzländer *et al.* (2008).

Glutathione detection in barley roots

After 96 h of stress treatment (see above), roots were incubated in 100 µM MCB (monochlorobimane) for exactly 30 min to label glutathione and subsequently transferred to a 50 µM propidium iodide (PI) solution for 5 min to label cell walls and prove cell viability (Meyer

bioRxiv preprint doi: https://doi.org/10.1101/2022.12.22.521445; this version posted December 22, 2022. The copyright holder for this preprint (which was not certified by peer review) is the author/funder, who has granted bioRxiv a license to display the preprint in perpetuity. It is made available under aCC-BY-NC-ND 4.0 International license.

et al. 2001). After the labelling procedure, residual dyes were washed out in deionised water. Fluorescence was imaged after excitation at 405 nm at emission wavelengths of 449-613 nm (MCB) and after 543 nm excitation with emission wavelengths of 613-704 nm (PI). Confocal z-stacks were taken with identical settings with the confocal laser scanning microscope covering 270 µm of root tissue in 10 µm slices/image. Gain and laser settings were kept constant throughout the imaging process. Only roots showing no severe cell damage indicated by PI staining were further analysed in ImageJ as 8-bit images of maximum intensity projections of the z-stacks. The mean pixel intensity was extracted of the area of the root tip in each image and blotted as boxplot using GraphPad Prism 9.

Glutathione reductase activity assay in barley root extracts

Flash-frozen and pulverized (TissueLyser (Qiagen) for 1.5 min, 30000 Hz) root material was dissolved in 100 µL of 100 mM K_2HPO_4/KH_2PO_4 at pH 7.5 supplemented with 0.5 mM EDTA and 0.1% of Plant Protease Inhibitor Cocktail P9599 (Sigma). Samples were vortexed and centrifuged at 20.000 x g 5 min at 4°C. The supernatant was transferred into a new tube and the centrifugation step was repeated. Protein concentration was determined in a Bradford assay (Bradford 1976). Extract containing 5 µg of protein was used in a total assay volume of 250 µL for the DTNB (5,5′-dithiobis(2-nitrobenzoic acid))-based GR activity assay (Smith *et al.* 1988; Marty *et al.* 2009), together with 1 mM EDTA, 750 µM DTNB, 1 mM GSSG in 100 mM K_2HPO_4/KH_2PO_4 at pH 7.5. TNB absorbance was followed at 412 nm using a plate reader (Clariostar®, BMG). After 5 min of measuring background activity, NADPH was added to a final concentration of 200 µM. Glutathione reductase activity was calculated via the increase of A_{412nm}/min and the molar extinction coefficient of TNB.

RESULTS

Generation of stable barley lines expressing cytosolic Grx1-roGFP2

We generated barley (cv. Golden Promise Fast) lines constitutively expressing Grx1-roGFP2 under the control of the maize ubiquitin promotor (*ZmUbi*), including the 5'UTR intron. Two independent lines originating from shoots from different calli were chosen based on consistent GFP fluorescence (5-3 #39 and 2-1 #1) and brought to homozygosity. In the chosen homozygous lines, we observed Grx1-roGFP2 signal, independent of tissue type or developmental stage (**Suppl. Fig. 1**). No phenotypic difference in growth was observed between barley expressing the sensor and the Golden Promise Fast background.

bioRxiv preprint doi: https://doi.org/10.1101/2022.12.22.521445; this version posted December 22, 2022. The copyright holder for this preprint (which was not certified by peer review) is the author/funder, who has granted bioRxiv a license to display the preprint in perpetuity. It is made available under aCC-BY-NC-ND 4.0 International license.

The epidermal layer of barley leaves showed the typical sensor fluorescence signal in the nucleus and cytosol **(Fig. 1A)**. High autofluorescence signal was detected after excitation at 405 nm in guard cells and in vacuoles of mesophyll cells, as well as in the wall of root cells.

Cytosolic Grx1-roGFP2 reacts to oxidising and reducing agents in barley shoots and roots

To assess if the sensor is responsive to exogenously induced reduction or oxidation, leaf discs of 7-day-old barley plants were exposed to oxidising and reducing agents. We observed a roGFP2-typical *in planta* excitation spectrum after excitation of the leaf discs at 386 to 495 nm (**Fig. 1B**). Reduction of the sensor with DTT lead to a higher excitation peak while oxidation with H_2O_2 or DPS lead to a lower excitation peak in the spectral range above the isosbestic point (IP) at 425 nm. Below the IP, the influence of sensor oxidation or reduction on *in vivo* excitation spectra was only low, resulting in a minor contribution to 405/488 ratio changes. The *in vivo* spectroscopic dynamic range (δ) of Grx1-roGFP2 was calculated to be around 2- to -3-fold (405/488) (×2.79 2-1 #1; ×2.65 5-3 #39). Untreated barley leaves showed a similar spectral signal as the DTT-treated leaves, suggesting a largely reduced sensor under physiological conditions. Furthermore, the sensor did not behave significantly different between the two independent lines.

We further determined the *in vivo* dynamic range of Grx1-roGFP2 in barley plants based on confocal microscopy. As the nuclear roGFP2 signal in root and leaf tissue was not affected by interfering autofluorescence signals we used nuclear regions of interest during image analysis to minimize cell wall and vacuole fluorescence interference (**Fig. 2, Suppl. Figs. 2 and 3**). We calibrated Grx1-roGFP2 in root and leaf tissue of young barley seedlings and observed tissue-dependent differences (**Suppl. Fig. 2**). While the calibration of line 5-3 #39 and line 2-1 #1 in leaves resulted in a dynamic range of δ = 1.3-1.5, calibration of the root tissue resulted in a dynamic range of δ = 2.3-2.7 depending on the used oxidizing agent. Furthermore, the physiological state of Grx1-roGFP2 in roots revealed a higher 405/488 nm ratio of 0.93 ± 0.50 (2-1 #1) and 1.05 ± 0.61 (5-3 #39) compared to leaves with a ratio of 0.63 ± 0.27 (2-1 #1) and 0.60 ± 0.18 (5-3 #39), suggesting a slightly more oxidized sensor in roots than in leaves.

Cytosolic E_{GSH} reacts only slowly and mildly to severe growth-impairing osmotic and salt stress

A recent transcriptomic study (Osthoff *et al.* 2019) showed that barley seedlings treated with a combination of salt and osmotic stress in a paper roll system upregulate transcript encoding the cytosolic isoform of glutathione reductase (GR1; HORVU6Hr1G089780) after 24 h of

bioRxiv preprint doi: https://doi.org/10.1101/2022.12.22.521445; this version posted December 22, 2022. The copyright holder for this preprint (which was not certified by peer review) is the author/funder, who has granted bioRxiv a license to display the preprint in perpetuity. It is made available under aCC-BY-NC-ND 4.0 International license.

stress exposure. As the expression of the most important enzyme for maintaining a highly reduced cytosolic glutathione redox status was affected under these conditions and the used paper roll system allows for soil-free imaging of barley plants, we chose the same experimental conditions for barley expressing Grx1-roGFP2 to assess potential effects of this stress treatment on the cytosolic E_{GSH}.

As reported by Osthoff *et al.* (2019), barley seedlings treated with a combined stress of 150 mM NaCl and a water potential of -0.8 MPa (adjusted using PEG8000) showed a decrease in root growth (**Fig. 3**). While the mean root growth of barley grown for 7 days in ½ strength Hoagland solution showed root lengths between 57.47 ± 22.05 mm (mean of 5-3 #39 and 2-1 #1, control), root growth decreased significantly after a combined salt and osmotic stress for 96 h to 34.7 ± 14.81 mm (mean of 5-3 #39 and 2-1 #1, 150 mM NaCl, -0.8 MPa PEG8000).

Next, we followed the redox state of the Grx1-roGFP2 sensor at 24 h, 48 h and 96 h after the start of the stress (Osthoff *et al.* 2019). Grx1-roGFP2 redox state was read out via confocal laser scanning microscopy and quantified via ratio image analysis of nuclei as regions of interest (ROIs). We found that cytosolic E_{GSH} is maintained during the first 48 After 96 ha significant but small oxidative shift in the 405/488 nm ratio between stressed (1.05) and non-stressed (0.86) plants (**Fig. 4, Suppl. Figs. 4, 5, 6**). The measured difference in 405/488 nm ratio corresponds to only a 3% shift in degree of sensor oxidation.

Investigating the molecular basis for E_{GSH} robustness under stress

According to the Nernst equation, E_{GSH} is dependent on both the total concentration of GSH and the amount of glutathione disulfide (GSSG). Thus, a less negative local E_{GSH} as measured via roGFP2 redox state could be caused by either increased GSSG levels or decreased total glutathione content in the cytosol. Glutathione reductase recycles GSSG back to GSH, using NADPH as electron donor. As the K_m of this important enzyme is in the nanomolar range, [GSSG] would only rise if enzymatic capacity of GR is not sufficient to reduce GSSG immediately or if there is a shortage of NADPH. Transcriptomic analyses of Osthoff *et al.* (2019) identified the transcripts of both barley GR isoforms as differentially upregulated after 24 h of combined salt and osmotic stress (GR1: HORVU6Hr1G089780 $\log_2$FC 1.3; GR2: HORVU4Hr1G073930 $\log_2$FC 1.5). In contrast, transcripts encoding barley orthologs of the two proteins involved in GSH biosynthesis (GSH1 HORVU1Hr1G015590 and GSH2 HORVU5Hr1G027100) were not differentially expressed under those conditions (Osthoff *et al.* 2019).

Thus, we used an enzymatic assay for GR activity in plant extracts to test if total GR activity is increased in response to the same stress treatment. We did not find significantly reduced or

bioRxiv preprint doi: https://doi.org/10.1101/2022.12.22.521445; this version posted December 22, 2022. The copyright holder for this preprint (which was not certified by peer review) is the author/funder, who has granted bioRxiv a license to display the preprint in perpetuity. It is made available under aCC-BY-NC-ND 4.0 International license.

increased total GR activity in the 96 h stress treatment samples (**Fig. 5 A**). The GR activity of the 2-1 #1 line under control and stress conditions remained constant with values of 105.5 ± 36.4 and 105.9 ± 39.8 nmol TNB/min/mg protein, similar to the 5-3 #39 line with a slightly lower measured GR activity of 98.9 ± 46.7 and 92.3 ± 43 nmol TNB/min/mg protein. To compensate for possible differences in the individual measurements, we normalized the measured activities after stress treatment with those of the corresponding control treatment (**Fig. 5 B**). The resulting normalized ratio values of 1.1 ± 0.5 (2-1 #1) and 1.0 ± 0.6 (5-3 #39) did not show significant differences in response to the stress treatment and maintained a high variance.

We additionally tested if the stress treatment modifies the total glutathione content after 96 h (**Fig. 6**). emitting fluorescence at 449-613 nm after excitation at 405 nm; Haugland *et al.* 1996). MCB-stained roots of stressed (150 mM NaCl, -0.8 MPa PEG8000, 96 h) and unstressed seedlings were imaged with a confocal laser scanning microscope. , excluding a large increase in glutathione content after stress treatment

DISCUSSION

In this study we generated and characterised two independent transgenic barley (*Hordeum vulgare*, cv. Golden Promise Fast) lines expressing the genetically encoded biosensor Grx1-roGFP2 under the control of the *Zea mays* Ubiquitin promoter including the 5' UTR intron (Christensen & Quail 1996). As expected, the biosensor was constitutively expressed and localised to the cytosol and nucleus. The fluorescence intensity was sufficiently high for ratiometric sensor read-out in all examined tissues. As we observed high autofluorescence after excitation with UV light (405 nm) in the apoplast and sometimes the vacuole and cell walls, we preferably calculated 405/488 nm ratios from regions of interest set to nuclei. Using this approach, we determined that the *in vivo* dynamic range of cytosolic Grx1-roGFP is c. 1.3 - 1.5 in leaves and c. 2.3 - 2.7 in roots. The previously reported *in vitro* dynamic range of roGFP2 was c. 8.2 - 9.2 (405/488 nm) (Schwarzländer *et al.* 2008; Aller *et al.* 2013) while *in vivo* samples often displayed decreased dynamic ranges of c. 5 in confocal microscopy or c. 3 in plate reader-based sensor read-out (Ugalde *et al.* 2021, 2022). This difference in dynamic range between *in vitro* and *in vivo* sensor read-out can be explained by interference of plant compounds that overlay the changes in sensor absorption in the UV range (below the isosbestic point at c. 425 nm). This is also the case for barley, where the change in roGFP2 excitation in the UV range between fully reduced and fully oxidized plant samples is very small (**Fig. 1B**). Thus, the 405/488 sensor ratio displays a lower dynamic range *in vivo* than *in vitro*. The observed differences in calibration between leaf samples and root samples (**Fig. 2**) could be attributed to insufficient penetration of the oxidants H_2O_2 and DPS into barley leaves. However, within each tissue sensor oxidation caused by 1.5 M H_2O_2 or 5 mM DPS were not

bioRxiv preprint doi: https://doi.org/10.1101/2022.12.22.521445; this version posted December 22, 2022. The copyright holder for this preprint (which was not certified by peer review) is the author/funder, who has granted bioRxiv a license to display the preprint in perpetuity. It is made available under aCC-BY-NC-ND 4.0 International license.

significantly different. Usually, lower concentrations of H_2O_2 (10-100 mM) are used for *in vivo* roGFP2 sensor calibration but were not effective in barley (this study) and potato (Hipsch *et al.* 2021). Generally, it is very important to identify the optimal conditions for sensor calibration that allow both determination of the 405/488 nm ratio values for 0% and 100% roGFP oxidation (OxD), especially when mV values for the glutathione redox potential are to be calculated (reviewed in Müller-Schüssele et *al*. 2021, Schwarzländer, *et al.* 2021). Using the sensor calibration in roots and the untreated (physiological) root samples, we calculated that the cytosolic E_{GSH} of the barley cytosol is c. -308 to -320 mV assuming a pH of 7.2 (**Suppl. Fig. 2**). This is close to the cytosolic E_{GSH} in *A. thaliana*, which was measured as c. -320 to -310 mV (Meyer *et al.* 2007; Schwarzländer *et al.* 2008; Aller *et al.* 2013). This E_{GSH} in the barley cytosol results in mostly reduced Grx1-roGFP2, supporting the suitability of Grx1-roGFP2 to sense oxidative changes in this compartment.

We also observed a small, but statistically significant difference in the 405/488 nm sensor ratio between barley roots and leaves (**Fig. 2, Suppl. Fig. 2**), which suggests a slightly more reduced physiological steady state of Grx1-roGFP2 in leaves than in roots, corresponding to a 5-10 mV difference. However, we cannot rule out that read-out of roGFP2 excitation ratios differs slightly between these organs due to tissue-specific differences in wavelength penetration or autofluorescence.

Many molecules in plants emit fluorescence after excitation in the UV range such as chlorophyll, lignin or alkaloids (Donaldson, 2020). We detected high levels of autofluorescence in barley leaves and roots excited with 405 nm. Since cells may contain multiple autofluorescent compounds, we cannot narrow down the exact source of autofluorescence in these tissues after excitation with 405 nm. Barley tissues are rich in phenolic compounds such as the phenylpropanoid ferulic acid (4-hydroxy-3-methoxy-cinnamicacid) with concentrations ranging from 359-624 µg/g dry weight (Hernanz et al., 2001; Bonoli et al., 2004).

By applying stress to the generated reporter lines, we observed shorter seminal root lengths after 96 h (4 days) of combined salt and osmotic stress comparable to Osthoff *et al.* (2019). We therefore used this time point to asses shifts in the cytosolic glutathione redox potential. We first monitored the roGFP2 redox state 24 h, 48 h and 96 h after combined stress treatment and where able to detect significant but small changes in the roGFP2 oxidation degree after 96 h. The measured shift in roGFP2 405/488 nm ratio corresponds to a 3% shift in degree of oxidation, implying a + 2.1 mV shift from -314 mV (control 96 h) to -311.9 mV (150 mM NaCl, -0.8 MPa PEG8000) (pH 7.2, calibration values of 2-1 #1 root).

Water deficit and salt stress caused upregulation of transcripts related to the response to an oxidative challenge (Osthoff *et al.* 2019). Several enzymes involved in the response to

bioRxiv preprint doi: https://doi.org/10.1101/2022.12.22.521445; this version posted December 22, 2022. The copyright holder for this preprint (which was not certified by peer review) is the author/funder, who has granted bioRxiv a license to display the preprint in perpetuity. It is made available under aCC-BY-NC-ND 4.0 International license.

oxidative stress draw electrons from the glutathione pool, generating local GSSG. The highest flux of electrons can arguably be expected from DHAR, which re-reduces dehydroascorbate to ascorbate in the ascorbate/glutathione cycle that scavenges H_2O_2 (Foyer & Noctor 2011). As we detected only a slight oxidative response of Grx1-roGFP2 after 96 h of combined water deficit and salt stress, the cytosolic E_{GSH} in barley seems highly robust against oxidative changes. Possible reasons could be that (1) GSH does not serve as electron donor to mitigate these stress conditions or (2) GSH serves as electron donor and generates GSSG but compensatory mechanisms keep E_{GSH} constant. According to the Nernst equation, E_{GSH} could be kept constant via an increase in total GSH or removal of GSSG. To test these scenarios, we assessed total glutathione content and total glutathione reductase activity, but we found no changes in these parameters under the tested stress conditions. However, it should be noted that our imaging-based approach is limited regarding the investigated tissue type and that the enzyme activity-based approach can only assess total glutathione reductase activity (i.e. GR1 and GR2). Thus, we cannot completely rule out an increase in activity of cytosolic GR1 under osmotic and salt stress. Another, untested possibility is an efficient export of GSSG from the cytosol, e.g. to the vacuole (Morgan *et al.* 2013; Marty *et al.* 2019).

We created our reporter lines in the transformable background Golden Promise Fast, which has shown resilience under drought stress (Gol *et al.* 2021). Our lines in this background showed reductions in root growth under combined salt and osmotic stress, similarly to the German spring barley cultivar Scarlett (Osthoff *et al.* 2019), indicating that Golden Promise Fast does respond to these abiotic stresses. However, it is formally possible that the robust redox state displayed by Golden Promise Fast under our combined stress treatments are a particularity of this genetic background. Thus, it may be of interest to introgress the reporter in other cultivars and study its response to similar stresses.

In conclusion, we generated barley reporter lines that allow to monitor the cytosolic E_{GSH} via Grx1-roGFP2 oxidation state and that can be used to further investigate stress tolerance in barley. To further dissect if the high robustness of cytosolic E_{GSH} correlates with high stress resilience further investigations will be required, such as genetic analyses of different redox enzyme mutants.

In general, the glutathione-dependent redox system is viewed as a house-keeping redox system and E_{GSH} as a relatively constant parameter in the plant cytosol. Given the robustness of $E_{GSH,}$ it may be tempting to propose that this parameter could be a strong predictor of irreversible damage and imminent cell death. In this regard, E_{GSH} reporter lines would be interesting resources to screen for higher stress resilience.

bioRxiv preprint doi: https://doi.org/10.1101/2022.12.22.521445; this version posted December 22, 2022. The copyright holder for this preprint (which was not certified by peer review) is the author/funder, who has granted bioRxiv a license to display the preprint in perpetuity. It is made available under aCC-BY-NC-ND 4.0 International license.

Conflict of Interest

The authors declare that they have no conflicts of interest.

Author Contributions

FB, IA, AJM and SJMS designed the research. FB, AK and HT performed experiments and analysed data. SJMS, MS, AJM, FH and IA supervised the research and provided resources.

FB and SJMS wrote the manuscript with contributions from all authors. All authors approved the manuscript before submission.

Acknowledgements

We thank Alexa Brox and Maria Homagk (Chemical Signalling, INRES, University of Bonn) for assistance in cloning, barley cultivation and stress treatments, and Edelgard Wendeler (MPIPZ) for her technical support for the generation of the transgenic lines.

This work was supported by the DFG-funded Research Training Group GRK2064: “Water use efficiency and drought stress responses: From Arabidopsis to Barley” (AJM, .MS, FAB and SJM), and the Max Planck Society (IFA).

Literature

Aller I., Rouhier N., Meyer A.J. (2013) Development of roGFP2-derived redox probes for measurement of the glutathione redox potential in the cytosol of severely glutathione-deficient *rml1* seedlings. Frontiers in Plant Science **4**:506.

Amanda D., Frey F.P., Neumann U., Przybyl M., Šimura J., Zhang Y., Chen Z., Gallavotti A., Fernie A.R., Ljung K., Acosta I.F. (2022) Auxin boosts energy generation pathways to fuel pollen maturation in barley. Current Biology **32**:1798-1811.e8.

Bangash S.A.K., Müller-Schüssele S.J., Solbach D., Jansen M., Fiorani F., Schwarzländer M., Kopriva S., Meyer A.J. (2019) Low-glutathione mutants are impaired in growth but do not show an increased sensitivity to moderate water deficit. PloS One **14**:e0220589.

Bradford M.M. (1976) A rapid and sensitive method for the quantitation of microgram quantities of protein utilizing the principle of protein-dye binding. Analytical Biochemistry **72**:248–254.

Christensen A.H., Quail P.H. (1996) Ubiquitin promoter-based vectors for high-level expression of selectable and/or screenable marker genes in monocotyledonous plants. Transgenic Research **5**:213–218.

Dawson I.K., Russell J., Powell W., Steffenson B., Thomas W.T.B., Waugh R. (2015) Barley: a translational model for adaptation to climate change. New Phytologist **206**:913–931.

Foyer C.H., Noctor G. (2011) Ascorbate and glutathione: the heart of the redox hub. Plant Physiology **155**:2–18.

bioRxiv preprint doi: https://doi.org/10.1101/2022.12.22.521445; this version posted December 22, 2022. The copyright holder for this preprint (which was not certified by peer review) is the author/funder, who has granted bioRxiv a license to display the preprint in perpetuity. It is made available under aCC-BY-NC-ND 4.0 International license.

403 Fricker M.D. (2016) Quantitative redox imaging software. Antioxidants & Redox Signaling
404 **24**:752–762.

405 Giridhar M., Meier B., Imani J., Kogel K.-H., Peiter E., Vothknecht U.C., Chigri F. (2022)
406 Comparative analysis of stress-induced calcium signals in the crop species barley and
407 the model plant *Arabidopsis thaliana*. BMC Plant Biology **22**:447.

408 Gol L., Haraldsson E.B., von Korff M. (2021) Ppd-H1 integrates drought stress signals to
409 control spike development and flowering time in barley (M. Jones, Ed.). Journal of
410 Experimental Botany **72**:122–136.

411 Gutscher M., Pauleau A.-L., Marty L., Brach T., Wabnitz G.H., Samstag Y., Meyer A.J., Dick
412 T.P. (2008) Real-time imaging of the intracellular glutathione redox potential. Nature
413 Methods **5**:553–559.

414 Haugland R.P., Spence M.T.Z., Johnson I.D. (1996) Handbook of fluorescent probes and
415 research chemicals, 6th ed. Molecular Probes, Eugene, OR, USA (4849 Pitchford Ave.,
416 Eugene 97402).

417 Hoagland D.R, Arnon D.I. The water-culture method for growing plants without soil. College of
418 Agriculture, University of California, 1938

419 Himmelbach A., Zierold U., Hensel G., Riechen J., Douchkov D., Schweizer P., Kumlehn J.
420 (2007) A set of modular binary vectors for transformation of cereals. Plant Physiology
421 **145**:1192–1200.

422 Hipsch M., Lampl N., Zelinger E., Barda O., Waiger D., Rosenwasser S. (2021) Sensing stress
423 responses in potato with whole-plant redox imaging. Plant Physiology **187**:618–631.

424 Imani J., Li L., Schäfer P., Kogel K.-H. (2011) STARTS - A stable root transformation system
425 for rapid functional analyses of proteins of the monocot model plant barley: Stable
426 barley root transformation system. The Plant Journal **67**:726–735.

427 Kirschner G.K., Stahl Y., Imani J., von Korff M., Simon R. (2018) Fluorescent reporter lines for
428 auxin and cytokinin signalling in barley (*Hordeum vulgare*) (X. Li, Ed.). PLOS ONE
429 **13**:e0196086.

430 Kreszies T., Shellakkutti N., Osthoff A., Yu P., Baldauf J.A., Zeisler-Diehl V.V., Ranathunge K.,
431 Hochholdinger F., Schreiber L. (2019) Osmotic stress enhances suberization of
432 apoplastic barriers in barley seminal roots: analysis of chemical, transcriptomic and
433 physiological responses. New Phytologist **221**:180–194.

434 Marty L., Bausewein D., Müller C., Bangash S.A.K., Moseler A., Schwarzländer M., Müller-
435 Schüssele S.J., Zechmann B., Riondet C., Balk J., Wirtz M., Hell R., Reichheld J.-P.,
436 Meyer A.J. (2019) Arabidopsis glutathione reductase 2 is indispensable in plastids,
437 while mitochondrial glutathione is safeguarded by additional reduction and transport
438 systems. The New Phytologist **224**:1569–1584.

439 Marty L., Siala W., Schwarzlander M., Fricker M.D., Wirtz M., Sweetlove L.J., Meyer Y., Meyer
440 A.J., Reichheld J.-P., Hell R. (2009) The NADPH-dependent thioredoxin system
441 constitutes a functional backup for cytosolic glutathione reductase in Arabidopsis.
442 Proceedings of the National Academy of Sciences **106**:9109–9114.

443 Mascher M., Gundlach H., Himmelbach A., Beier S., Twardziok S.O., Wicker T., Radchuk V.,
444 Dockter C., Hedley P.E., Russell J., Bayer M., Ramsay L., Liu H., Haberer G., Zhang
445 X.-Q., Zhang Q., Barrero R.A., Li L., Taudien S., Groth M., Felder M., Hastie A.,

bioRxiv preprint doi: https://doi.org/10.1101/2022.12.22.521445; this version posted December 22, 2022. The copyright holder for this preprint (which was not certified by peer review) is the author/funder, who has granted bioRxiv a license to display the preprint in perpetuity. It is made available under aCC-BY-NC-ND 4.0 International license.

Šimková H., Staňková H., Vrána J., Chan S., Muñoz-Amatriaín M., Ounit R., Wanamaker S., Bolser D., Colmsee C., Schmutzer T., Aliyeva-Schnorr L., Grasso S., Tanskanen J., Chailyan A., Sampath D., Heavens D., Clissold L., Cao S., Chapman B., Dai F., Han Y., Li H., Li X., Lin C., McCooke J.K., Tan C., Wang P., Wang S., Yin S., Zhou G., Poland J.A., Bellgard M.I., Borisjuk L., Houben A., Doležel J., Ayling S., Lonardi S., Kersey P., Langridge P., Muehlbauer G.J., Clark M.D., Caccamo M., Schulman A.H., Mayer K.F.X., Platzer M., Close T.J., Scholz U., Hansson M., Zhang G., Braumann I., Spannagl M., Li C., Waugh R., Stein N. (2017) A chromosome conformation capture ordered sequence of the barley genome. Nature **544**:427–433.

Meyer A.J., Brach T., Marty L., Kreye S., Rouhier N., Jacquot J.-P., Hell R. (2007) Redox-sensitive GFP in *Arabidopsis thaliana* is a quantitative biosensor for the redox potential of the cellular glutathione redox buffer. The Plant Journal **52**:973–986.

Meyer A.J., Dreyer A., Ugalde J.M., Feitosa-Araujo E., Dietz K.-J., Schwarzländer M. (2021) Shifting paradigms and novel players in Cys-based redox regulation and ROS signaling in plants - and where to go next. Biological Chemistry **402**:399–423.

Meyer A.J., May M.J., Fricker M. (2001) Quantitative *in vivo* measurement of glutathione in Arabidopsis cells: *In vivo* measurement of glutathione. The Plant Journal **27**:67–78.

Morgan B., Ezeriņa D., Amoako T.N.E., Riemer J., Seedorf M., Dick T.P. (2013) Multiple glutathione disulfide removal pathways mediate cytosolic redox homeostasis. Nature Chemical Biology **9**:119–125.

Müller-Schüssele S.J., Bohle F., Rossi J., Trost P., Meyer A.J., Zaffagnini M. (2021) Plasticity in plastid redox networks: evolution of glutathione-dependent redox cascades and glutathionylation sites. BMC Plant Biology **21**:322.

Müller-Schüssele S.J., Schwarzländer M., Meyer A.J. (2021) Live monitoring of plant redox and energy physiology with genetically encoded biosensors. Plant Physiology **186**:93–109.

Müller-Schüssele S.J., Wang R., Gütle D.D., Romer J., Rodriguez-Franco M., Scholz M., Buchert F., Lüth V.M., Kopriva S., Dörmann P., Schwarzländer M., Reski R., Hippler M., Meyer A.J. (2020) Chloroplasts require glutathione reductase to balance reactive oxygen species and maintain efficient photosynthesis. The Plant Journal **103**:1140–1154.

Munns R., James R.A., Läuchli A. (2006) Approaches to increasing the salt tolerance of wheat and other cereals. Journal of Experimental Botany **57**:1025–1043.

Muzammil S., Shrestha A., Dadshani S., Pillen K., Siddique S., Léon J., Naz A.A. (2018) An ancestral allele of *pyrroline-5-carboxylate synthase1* promotes proline accumulation and drought adaptation in cultivated barley. Plant Physiology **178**:771–782.

Newton A.C., Flavell A.J., George T.S., Leat P., Mullholland B., Ramsay L., Revoredo-Giha C., Russell J., Steffenson B.J., Swanston J.S., Thomas W.T.B., Waugh R., White P.J., Bingham I.J. (2011) Crops that feed the world 4. Barley: a resilient crop? Strengths and weaknesses in the context of food security. Food Security **3**:141–178.

Osthoff A., Donà dalle Rose P., Baldauf J.A., Piepho H.-P., Hochholdinger F. (2019) Transcriptomic reprogramming of barley seminal roots by combined water deficit and salt stress. BMC Genomics **20**:325.

Rey P., Tarrago L. (2018) Physiological roles of plant methionine sulfoxide reductases in redox homeostasis and signaling. Antioxidants **7**:114.

bioRxiv preprint doi: https://doi.org/10.1101/2022.12.22.521445; this version posted December 22, 2022. The copyright holder for this preprint (which was not certified by peer review) is the author/funder, who has granted bioRxiv a license to display the preprint in perpetuity. It is made available under aCC-BY-NC-ND 4.0 International license.

491 Schwarzländer M., Dick T.P., Meyer A.J., Morgan B. (2016) Dissecting redox biology using
492 fluorescent protein sensors. Antioxidants & Redox Signaling **24**:680–712.

493 Schwarzländer M., Fricker M.D., MüLler C., Marty L., Brach T., Novak J., Sweetlove L.J., Hell
494 R., Meyer A.J. (2008) Confocal imaging of glutathione redox potential in living plant
495 cells. Journal of Microscopy **231**:299–316.

496 Schwarzländer M., Fricker M.D., Sweetlove L.J. (2009) Monitoring the *in vivo* redox state of
497 plant mitochondria: Effect of respiratory inhibitors, abiotic stress and assessment of
498 recovery from oxidative challenge. Biochimica et Biophysica Acta (BBA) -
499 Bioenergetics **1787**:468–475.

500 Smith I.K., Vierheller T.L., Thorne C.A. (1988) Assay of glutathione reductase in crude tissue
501 homogenates using 5,5′-dithiobis(2-nitrobenzoic acid). Analytical Biochemistry
502 **175**:408–413.

503 Ugalde J.M., Fecker L., Schwarzländer M., Müller-Schüssele S.J., Meyer A.J. (2022) Live
504 monitoring of ROS-induced cytosolic redox changes with roGFP2-based sensors in
505 plants. In: Mhamdi A (ed) Reactive Oxygen Species in Plants. Springer US, New York,
506 NY, pp 65–85.

507 Ugalde J.M., Fuchs P., Nietzel T., Cutolo E.A., Homagk M., Vothknecht U.C., Holuigue L.,
508 Schwarzländer M., Müller-Schüssele S.J., Meyer A.J. (2021) Chloroplast-derived
509 photo-oxidative stress causes changes in H_2O_2 and E_{GSH} in other subcellular
510 compartments. Plant Physiology **186**:125–141.

511 Wagner S., Steinbeck J., Fuchs P., Lichtenauer S., Elsässer M., Schippers J.H.M., Nietzel T.,
512 Ruberti C., Van Aken O., Meyer A.J., Van Dongen J.T., Schmidt R.R., Schwarzländer
513 M. (2019) Multiparametric real-time sensing of cytosolic physiology links hypoxia
514 responses to mitochondrial electron transport. New Phytologist **224**:1668–1684.

515 Watanabe K., Breier U., Hensel G., Kumlehn J., Schubert I., Reiss B. (2016) Stable gene
516 replacement in barley by targeted double-strand break induction. Journal of
517 Experimental Botany **67**:1433–1445.

518

519

bioRxiv preprint doi: https://doi.org/10.1101/2022.12.22.521445; this version posted December 22, 2022. The copyright holder for this preprint (which was not certified by peer review) is the author/funder, who has granted bioRxiv a license to display the preprint in perpetuity. It is made available under aCC-BY-NC-ND 4.0 International license.

FIGURES

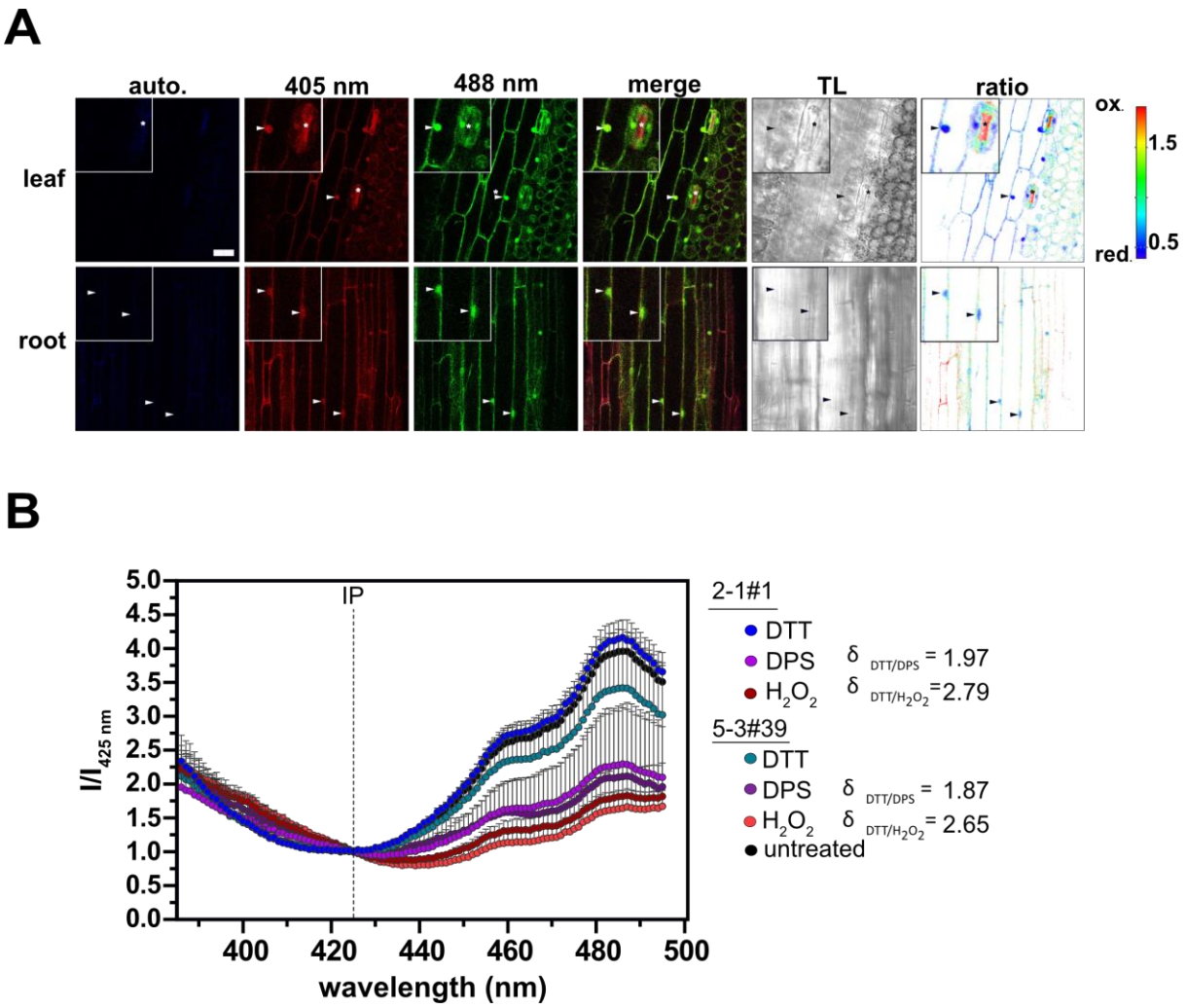

Figure 1: Grx1-roGFP2 expression in barley leaf and root tissue

A Confocal microscopy images of roGFP2 (405 nm and 488 nm excitation; 508-535 nm emission) and autofluorescence (auto, 405 nm excitation, 430-470 nm emission). The merge image displays the overlay of 405 and 488 intensities. TL displays the transmitted light image. Arrowheads indicate nucleus- and cytosol-localized sensor signal, and the asterisks show regions of high autofluorescence. Scale bar = 40 µm. **B** Excitation scan (386-495 nm; emission: 530-40 nm) of barley leaf discs treated with 10 mM DTT, 5 mM DPS or 1.5 M H_2O_2. Fluorescence was normalized over the fluorescence intensity at the isosbestic point (IP) of roGFP2 at 425 nm. Significance between genotypes and treatments of the 405 and 488 nm peak intensity was tested with a Two-way ANOVA and Tukey's post hoc test with $\alpha<0.05$. No significant differences were observed between the lines within one treatment while peak intensities of 488 nm were significantly different in reducing (DTT) and oxidizing (H_2O_2 and DPS) treatments.

bioRxiv preprint doi: https://doi.org/10.1101/2022.12.22.521445; this version posted December 22, 2022. The copyright holder for this preprint (which was not certified by peer review) is the author/funder, who has granted bioRxiv a license to display the preprint in perpetuity. It is made available under aCC-BY-NC-ND 4.0 International license.

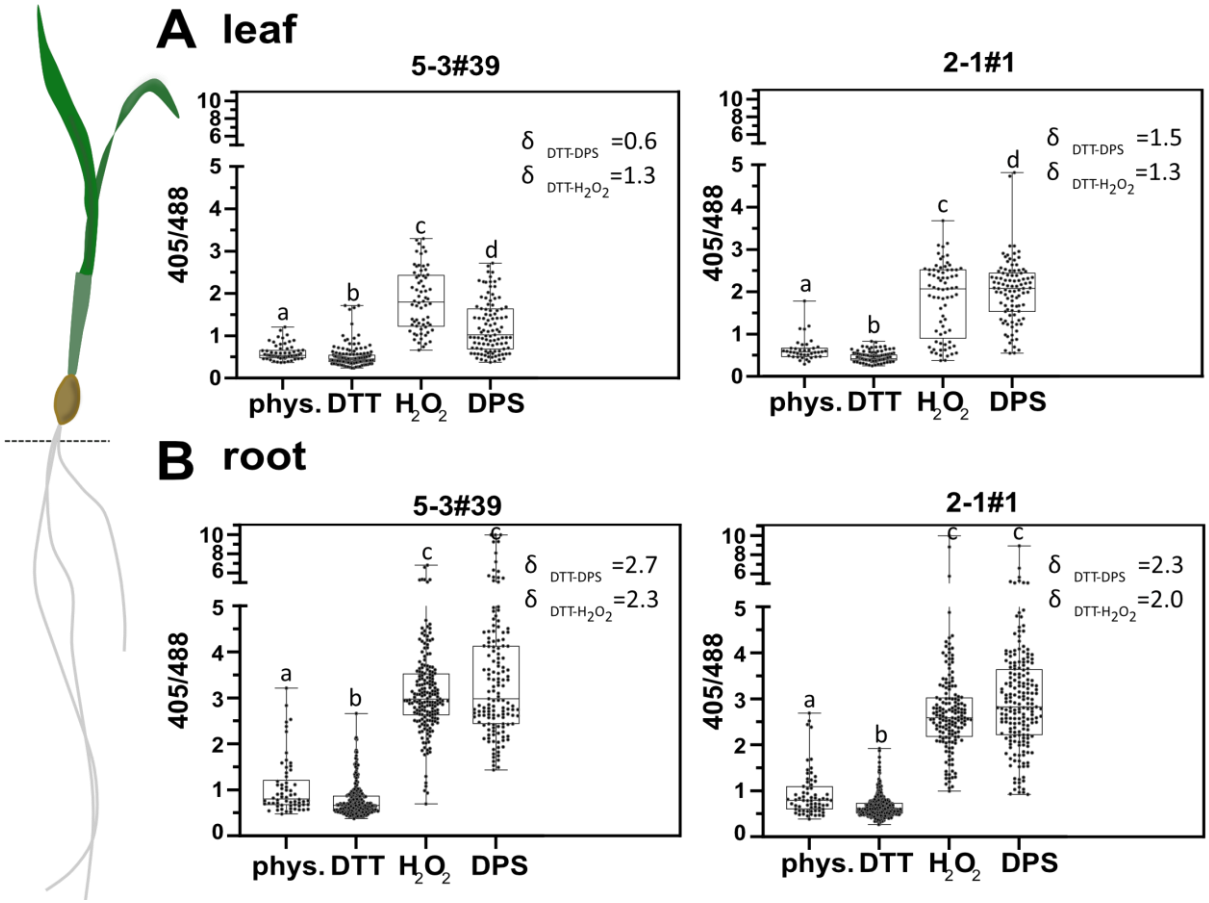

Figure 2: Grx1-roGFP2 sensor calibration in barley leaf and root tissue

Box plots of Grx1-roGFP2 signal ratios (405/408) calculated from fluorescence intensities in nuclei of leaf (**A**) and root (**B**) tissue treated with 10 mM DTT, 5 mM DPS or 1.5 M H_2O_2 and imaged via confocal microscopy. A one-way ANOVA and Tukey's multiple comparison test was conducted on log transformed ratio values. Significantly different treatments ($p < 0,0001$) are indicated by different letters. Boxes display 25 to 75 percentiles with whiskers showing min to max values. The middle line indicates the median and dots represent the data of every nucleus obtained from 2 to 5 seedlings per treatment.

bioRxiv preprint doi: https://doi.org/10.1101/2022.12.22.521445; this version posted December 22, 2022. The copyright holder for this preprint (which was not certified by peer review) is the author/funder, who has granted bioRxiv a license to display the preprint in perpetuity. It is made available under aCC-BY-NC-ND 4.0 International license.

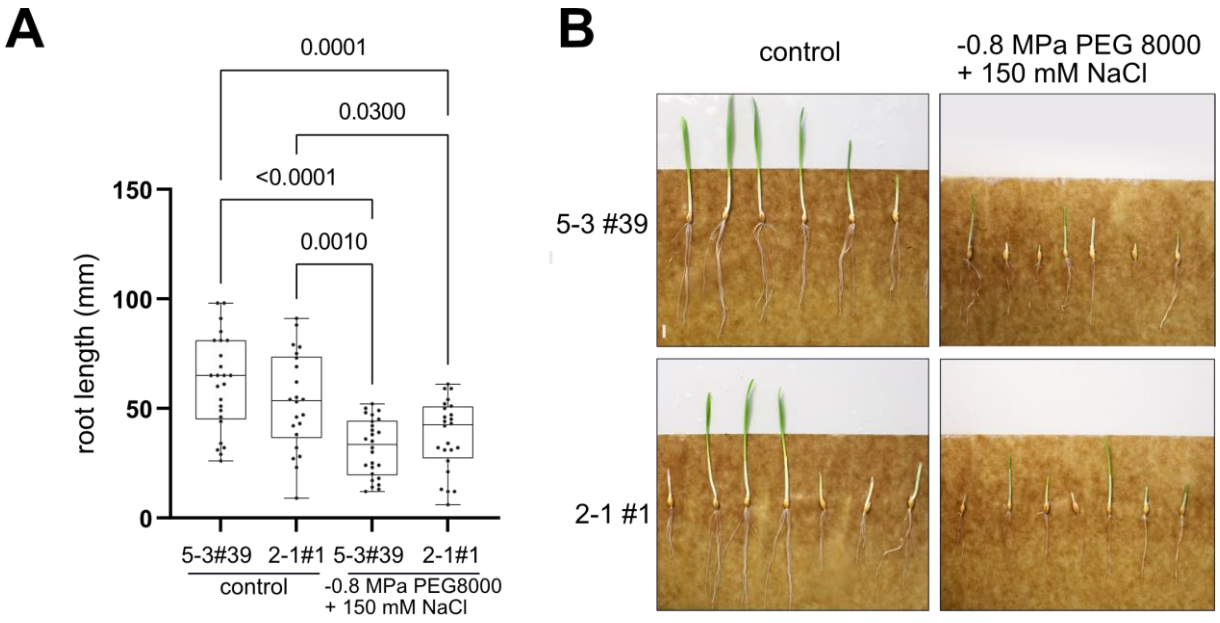

Figure 3: Effect of combined osmotic and salt stress on barley seedling root growth

A Root length of 7-day old barley plants after 96 h of combined osmotic and salt stress. Boxes display 25 to 75 percentiles with whiskers showing min to max values. The median is indicated by the horizontal line. Dots show individual root lengths measured of 21-26 individual seedlings. **B** Example images of Grx1-roGFP2 sensor lines under control and stress conditions, 96 h after beginning of the stress.

bioRxiv preprint doi: https://doi.org/10.1101/2022.12.22.521445; this version posted December 22, 2022. The copyright holder for this preprint (which was not certified by peer review) is the author/funder, who has granted bioRxiv a license to display the preprint in perpetuity. It is made available under aCC-BY-NC-ND 4.0 International license.

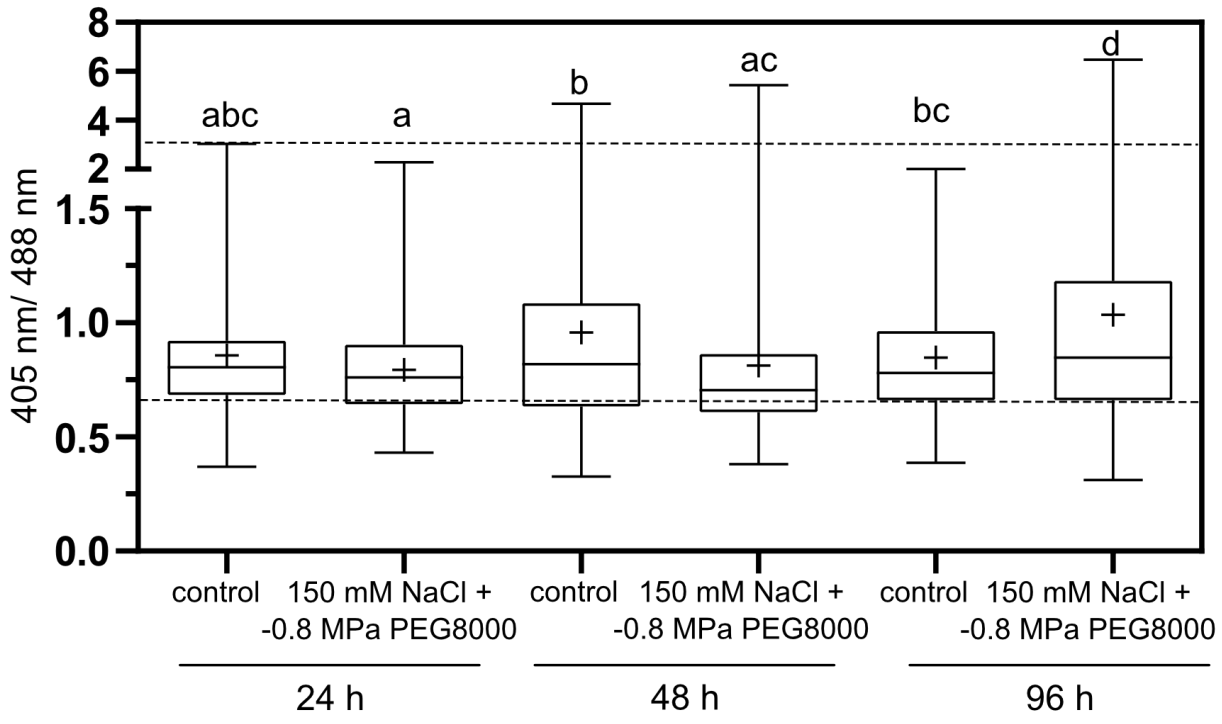

547

548 **Figure 4: roGFP2 ration in roots of barley seedlings after 24, 48 or 96 h of combined osmotic and salt stress**

549 Box plots of roGFP2 nuclear signal ratio (405/488). Boxes display 25 to 75 percentiles with whiskers showing min
550 to max values. The median is displayed as horizontal line and the mean is indicated with the '+' sign. Dotted lines
551 indicate 100 % oxidation and reduction of the sensor (calibration with line 2-1 #1 root values, see **Fig. 2**). Two-way
552 ANOVA was conducted on log-transformed values with $\alpha = 0.05$, different letters indicate significantly different
553 categories. Between 170-256 nuclei were analysed from 3-5 seedlings per line and treatment.

bioRxiv preprint doi: https://doi.org/10.1101/2022.12.22.521445; this version posted December 22, 2022. The copyright holder for this preprint (which was not certified by peer review) is the author/funder, who has granted bioRxiv a license to display the preprint in perpetuity. It is made available under aCC-BY-NC-ND 4.0 International license.

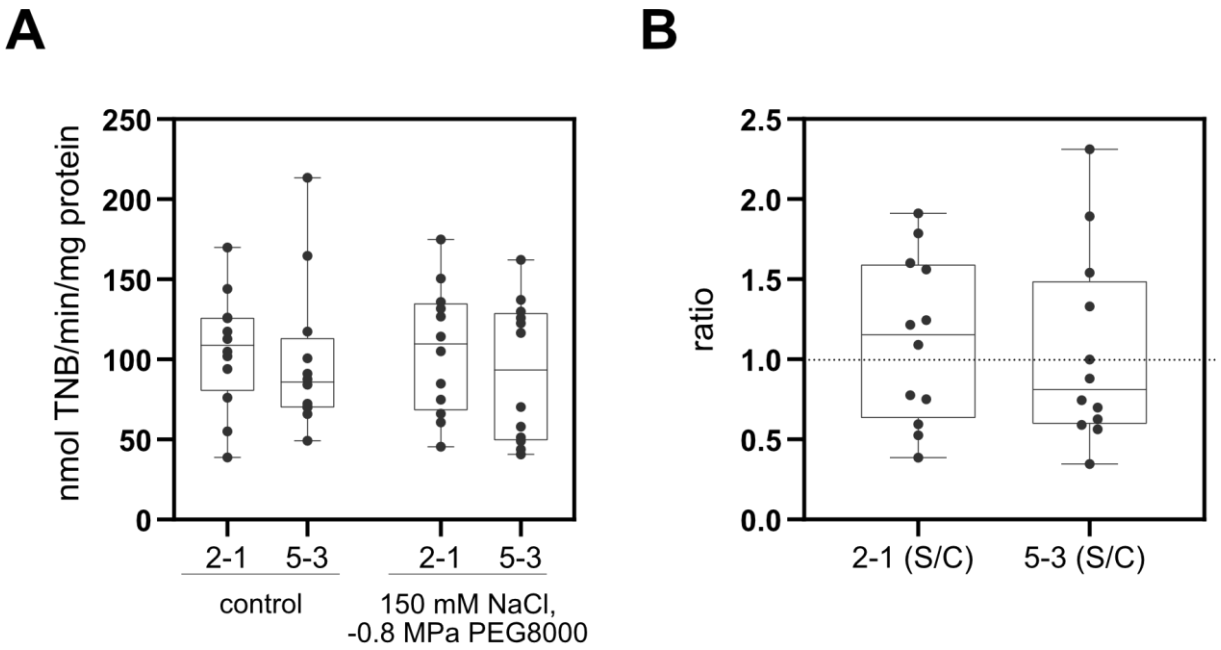

554

555 **Figure 5: DTNB – based glutathione reductase assay in barley roots after osmotic and salt stress**

556 **A** Absolute GR activity under control and 96 h of stress conditions displayed as box plots with boxes displaying 25
557 to 75 percentiles and whiskers showing min to max. Median is shown as horizontal line. Individual GR activities of
558 12 biological replicates for each line and condition are shown as dots. **B** GR activity in stressed samples was divided
559 by the corresponding control activity. A Two-way ANOVA (A) and T-test (B) was conducted on data sets A and B
560 with $\alpha = 0.05$ and no significant differences were observed.

bioRxiv preprint doi: https://doi.org/10.1101/2022.12.22.521445; this version posted December 22, 2022. The copyright holder for this preprint (which was not certified by peer review) is the author/funder, who has granted bioRxiv a license to display the preprint in perpetuity. It is made available under aCC-BY-NC-ND 4.0 International license.

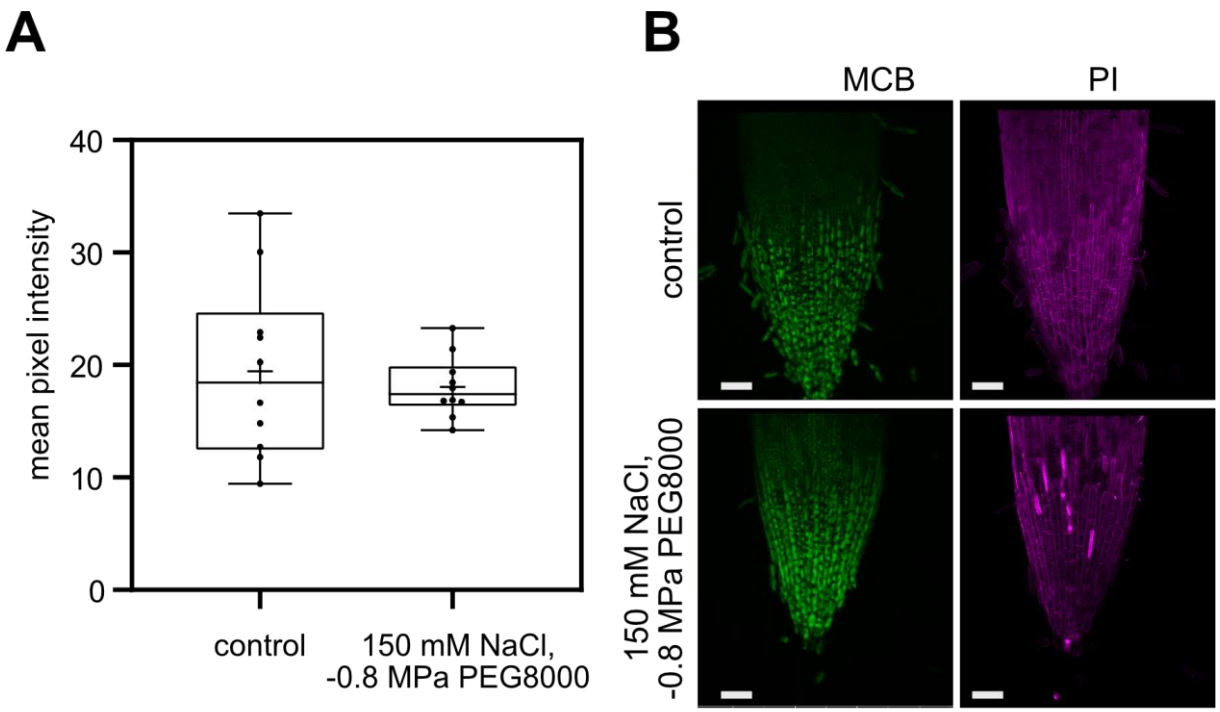

561

562 **Figure 6: *In situ* detection of total glutathione and cell damage in stressed barley root tips (96 h).**

563 **A** Mean pixel intensities of root tips stained with MCB were extracted with ImageJ (8-bit,0-255 display range). Boxes
564 display 25 to 75 percentiles with whiskers showing min to max values, the median is displayed as constant line.
565 The mean of all data points is shown as '+' (n = 10). No significant differences were detected (T-test). **B** Maximum
566 intensity projection of barley root tips stained with monochlorobimane (MCB) (excitation: 405 nm, emission: 449-
567 613 nm) and propidium iodide (PI, excitation: 543 nm, emission: 613-704 nm). Scale bar = 100 µm.

Supplemental Figures

Bohle *et al.*, High robustness of cytosolic glutathione redox potential under combined salt and osmotic stress in barley as revealed by the biosensor Grx1-roGFP2

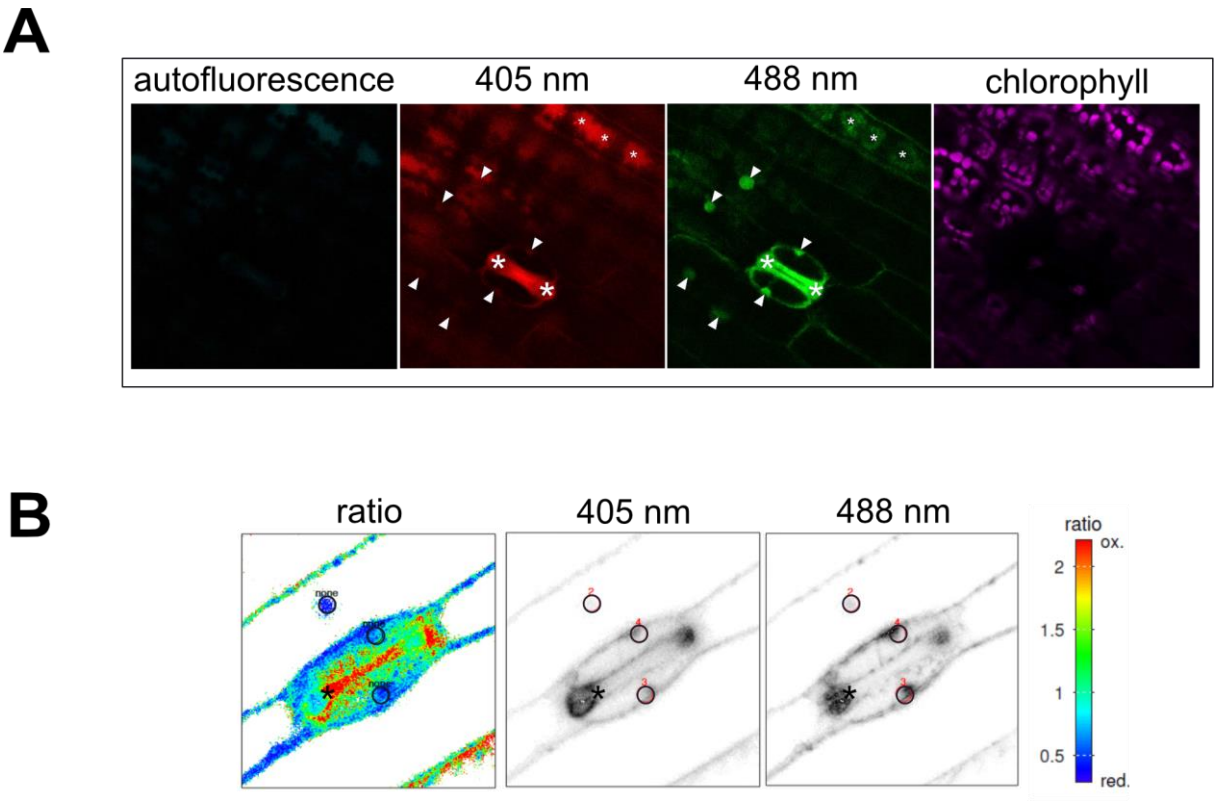

Supplemental Figure 1: Screening and analysis of Grx1-roGFP2 signal in barley

A Localisation and fluorescence signal of Grx1-roGFP2 in barley leaves. White arrowheads indicate specific roGFP2 signal, asterisks show positions of high autofluorescence signal. **B** Regions of interest (ROI, black circles) set in nuclei for ratio calculation with the RRA software in the Grx1-roGFP2 channels (405 nm, 488 nm) and the false coloured ratio image (ratio). Black asterisks show autofluorescence signal, seen as red false colouring in the ratio image.

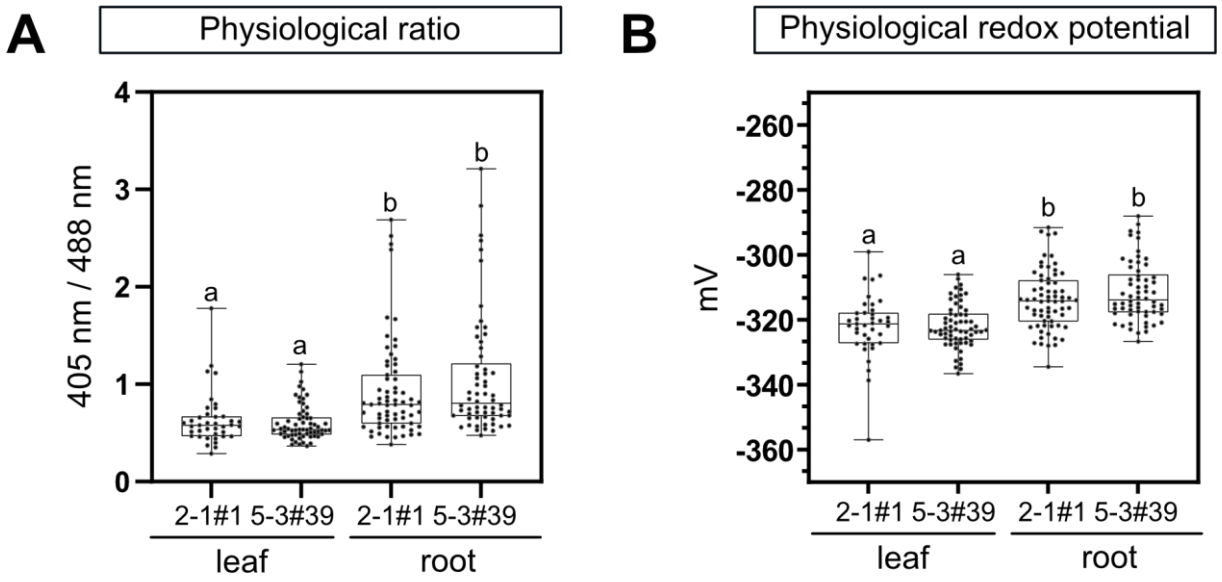

Supplemental Figure 2: Physiological glutathione redox potential as indicated by Grx1-roGFP2 in barely root and leaf tissue

A Box plots of Grx1-roGFP2 signal ratios (405/488) under physiological conditions (same data as in **Fig. 2**, but with a different scale in the y-axis to facilitate visualization). **B** The redox potential of each ratio point depicted in A was translated into mV by setting the calibration of line 2-1 #1 (DTT and DPS root values) as 100 % oxidized and reduced for a pH of 7.2 (Schwarzländer et al. 2008). Box plot features and statistics are as described in **Fig. 2 A**.

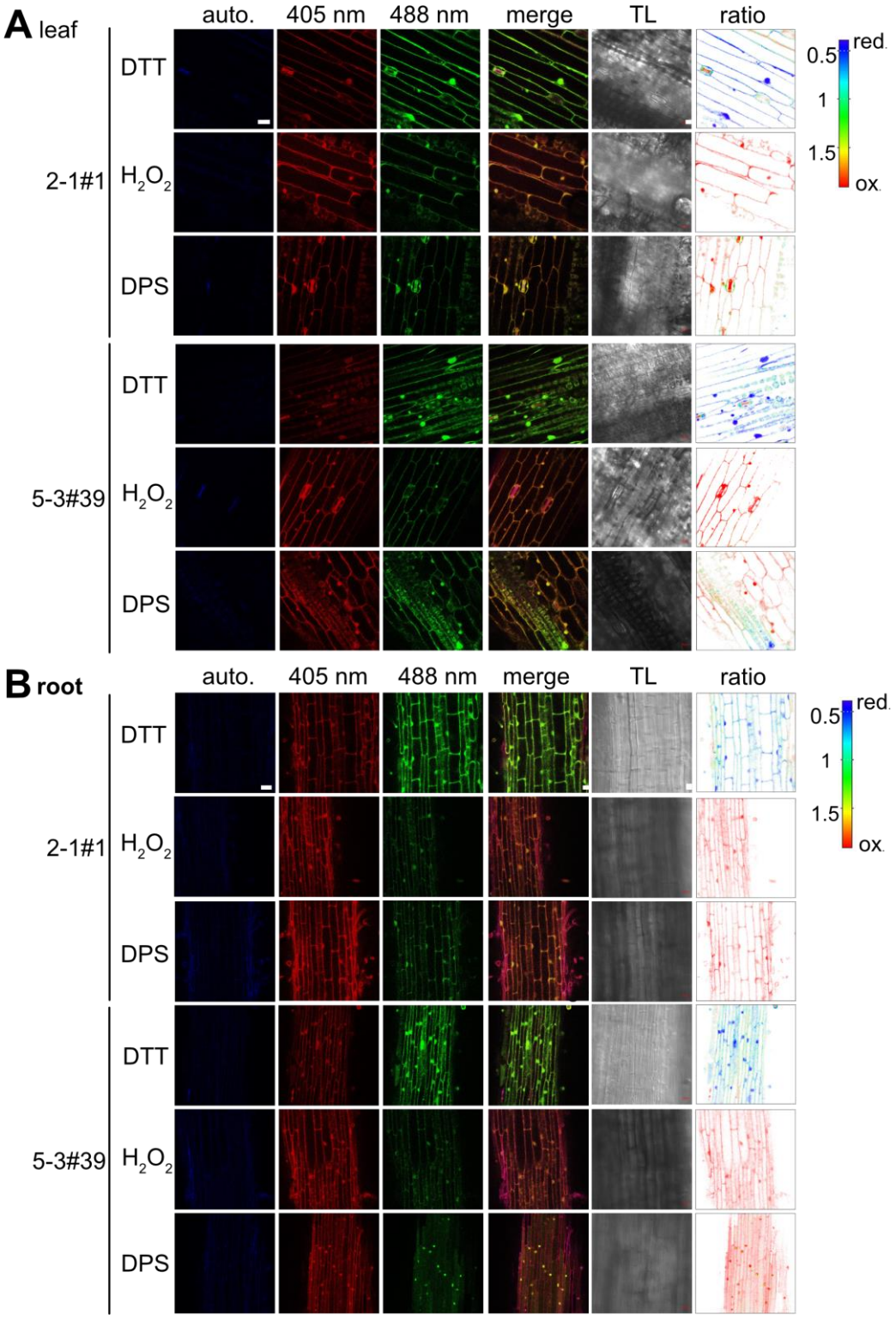

Supplemental Figure 3: Calibration of barley root and leaf tissue

Representative examples of the type of confocal microscopy images used to collect the data in **Fig. 2** for **A** leaf and **B** root tissues. Confocal laser scanning microscopy of barley seedlings treated with 10 mM DTT or 1.5 M H_2O_2 or 5 mM DPS for 30 min. roGFP2 was excited at 405 and 488 nm while emission was set to 508-535 nm. Autofluorescence was collected after excitation at 405 nm and emission between 430 to 470 nm. Overlay of channels 405 and 488 are shown as 'merge'. Transmitted light (TL). Ratios were calculated with the ratio imaging software RRA and are false color coded. Scale bar = 40 µm.

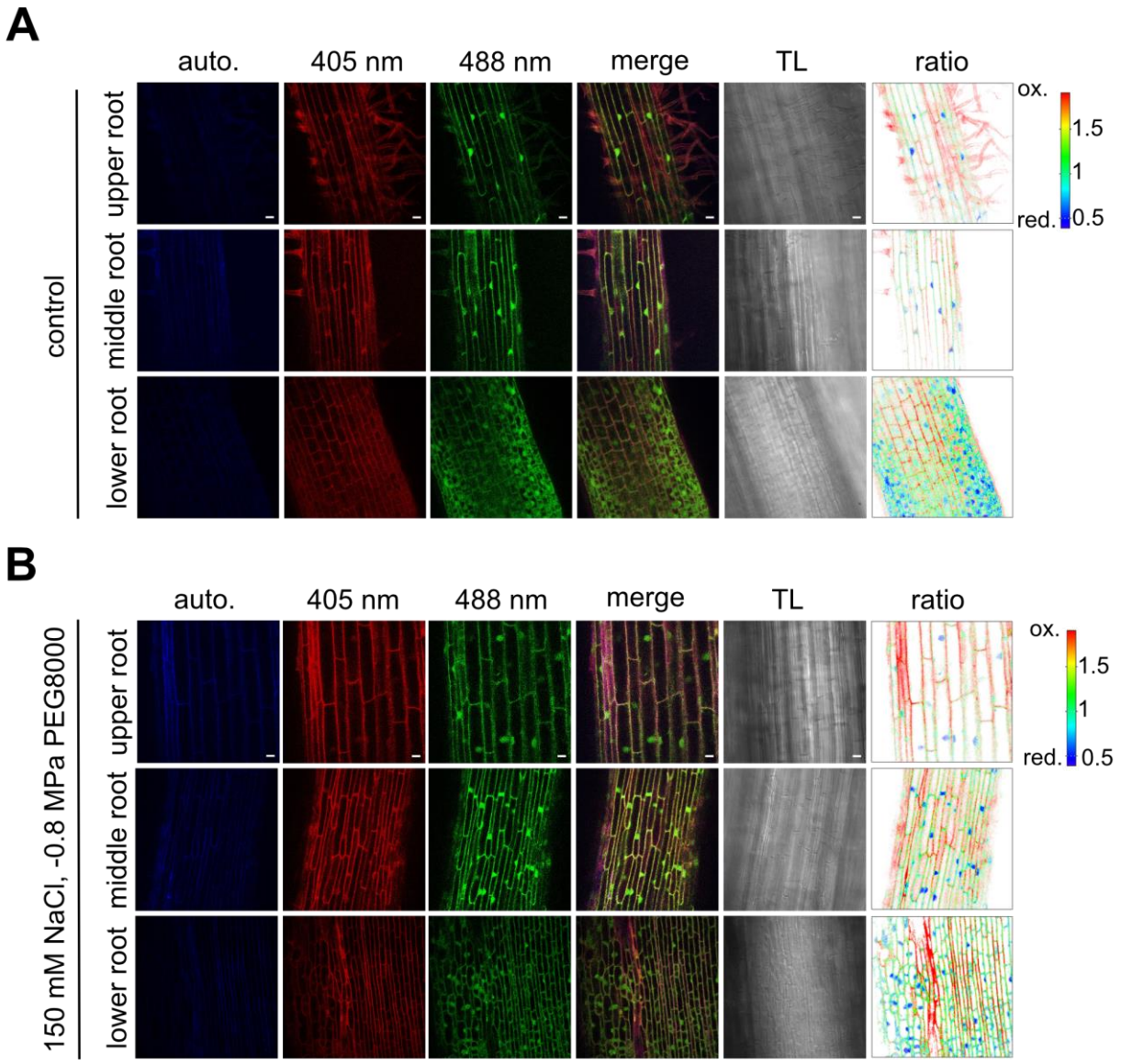

Supplemental Figure 4: Grx1-roGFP2 ratio after 24 h of combined stress treatment

Representative examples of the type of confocal microscopy images used to collect the data in **Fig.4** for **A** control and **B** stressed samples treated with 150 mM NaCl and -0.8 MPa PEG800 for 24 h. roGFP2 was excited at 405 and 488 nm and emission set to 508-535 nm. Autofluorescence was collected after excitation at 405 nm and emission set to 430 to 470 nm. Overlay of channels 405 and 488 are shown as 'merge'. Transmitted light (TL). Ratios were calculated with the ratio imaging software RRA and are false color coded. Scale bar = 40 µm.

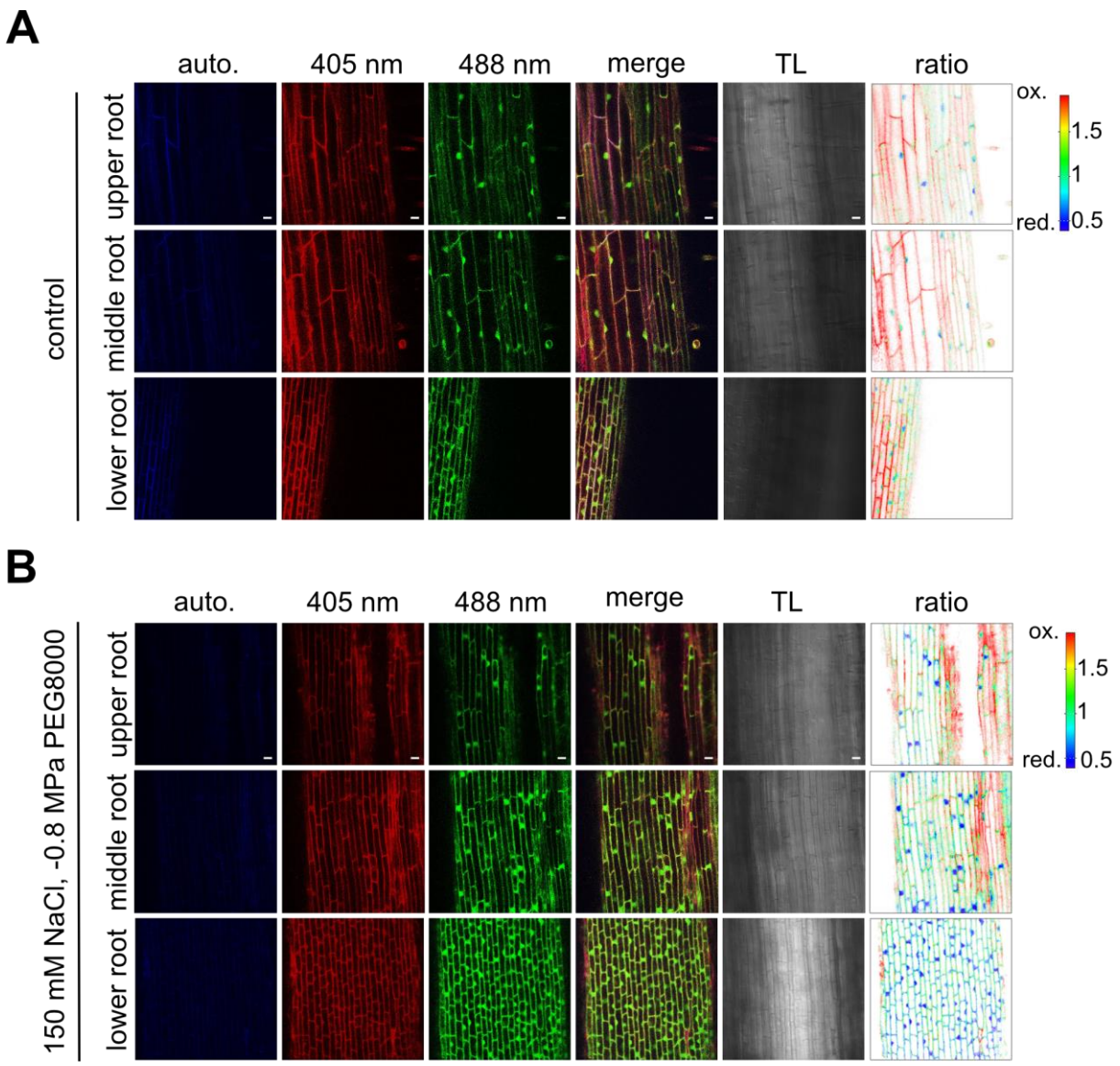

Supplemental Figure 5: Grx1-roGFP2 ratio after 48 h of combined stress treatment

Representative examples of the type of confocal microscopy images used to collect the data in **Fig.4** for **A** control and **B** stressed samples treated with 150 mM NaCl and -0.8 MPa PEG800 for 48 h. roGFP2 was excited at 405 and 488 nm and emission set to 508-535 nm. Autofluorescence was collected after excitation at 405 nm and emission set to 430 to 470 nm. Overlay of channels 405 and 488 are shown as 'merge'. Transmitted light (TL). Ratios were calculated with the ratio imaging software RRA and are false color coded. Scale bar = 40 µm.

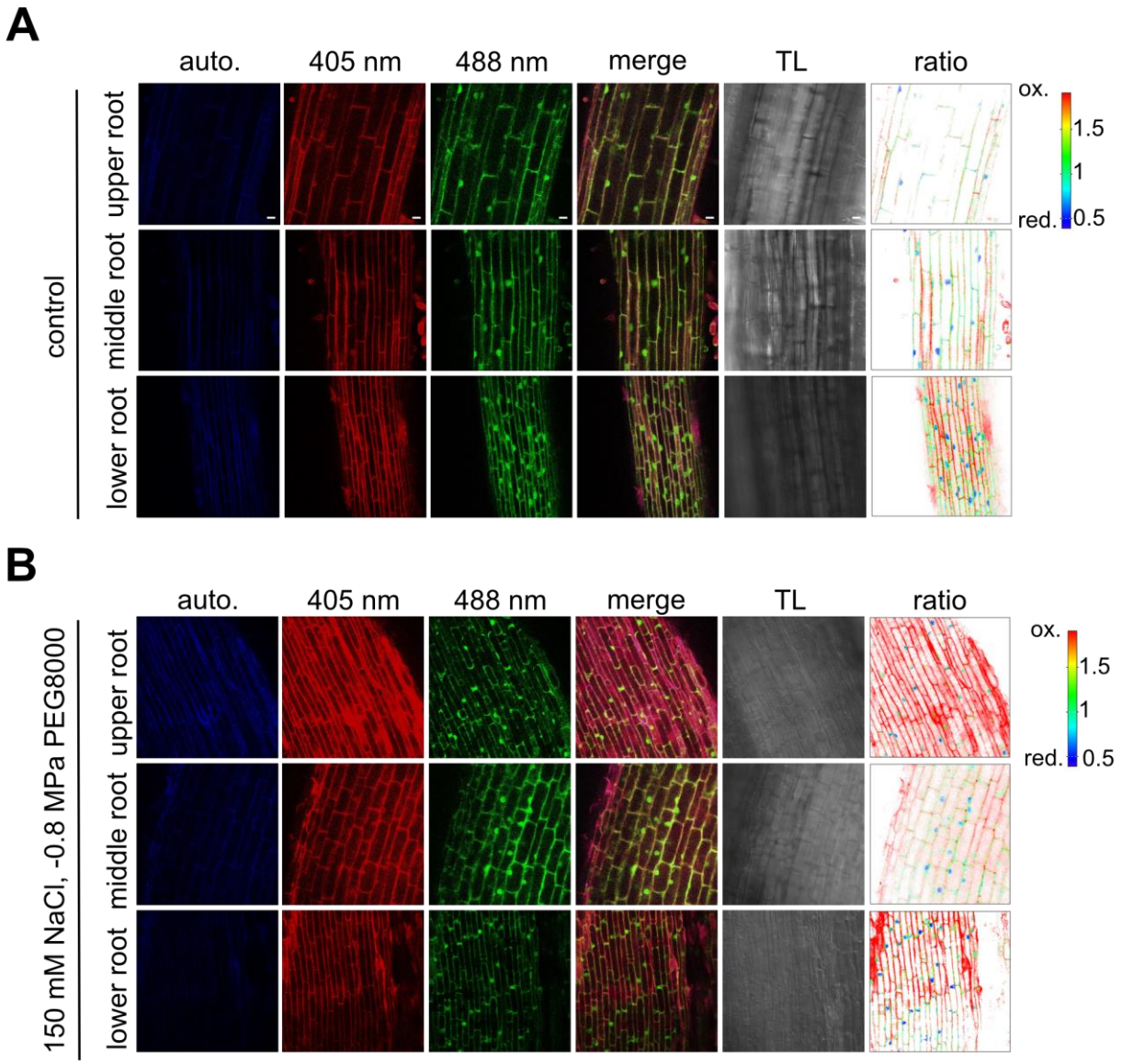

Supplemental Figure 6: Grx1-roGFP2 ratio after 96 h of combined stress treatment

Representative examples of the type of confocal microscopy images used to collect the data in **Fig.4** for **A** control and **B** stressed samples treated with 150 mM NaCl and -0.8 MPa PEG800 for 96 h. roGFP2 was excited at 405 and 488 nm and emission set to 508-535 nm. Autofluorescence was collected after excitation at 405 nm and emission set to 430 to 470 nm. Overlay of channels 405 and 488 are shown as 'merge'. Transmitted light (TL). Ratios were calculated with the ratio imaging software RRA and are false color coded. Scale bar = 40 µm.

6.3. Associated Results

Additional experiments were performed with the aim to induce a detectable shift in the cytosolic E_{GSH} of *Hordeum vulgare* (var. Golden Promise Fast) expressing Grx1-roGFP2. Faralli *et al.* 2015 found that under elevated temperatures applied for 30 min (>45°C) and additional growth on salt-supplemented media (200 mM NaCl) barley (*Hordeum vulgare* L.) was not able to survive.

We added a third stress after 96 h of the osmotic (-0.8 MPa PEG8000) and salt (150 mM NaCl) treatments already described in section 6.2 by subjecting the barley plants to 48°C for 0, 1, and 2 h, respectively and measured roGFP2 oxidation state immediately after heat stress. Hoagland solution with and without salt and PEG8000 was preheated at 48°C. Barley grown in paper-rolls were transferred to the heated solution for 1 or 2 h and subsequently imaged with the CLSM.

6.3.1 Osmotic, salt and heat stress treatment of barley

The addition of a heat shock at 48°C for 1 or 2 h did not lead to a difference in 405 nm/488 nm ratio change. We detected a larger spread of roGFP2 ratio values for line 5-3 #39. However, this scatter occurred with and without heat application for 1 or 2 h (Figure 52). Ratios showed similar ranges in root and shoot tissue. We were able to detect growth impairments in form of shoot reduction and smaller roots after osmotic, salt and heat treatments (Figure 53). However, an overall heterogeneity of barley growth was detected as well under control (non-stressed) conditions as seen for the growth of 2-1 #1 (Figure 53; RT, control).

The obtained results do not alter or lead to changes in the statements made in section 6.2.

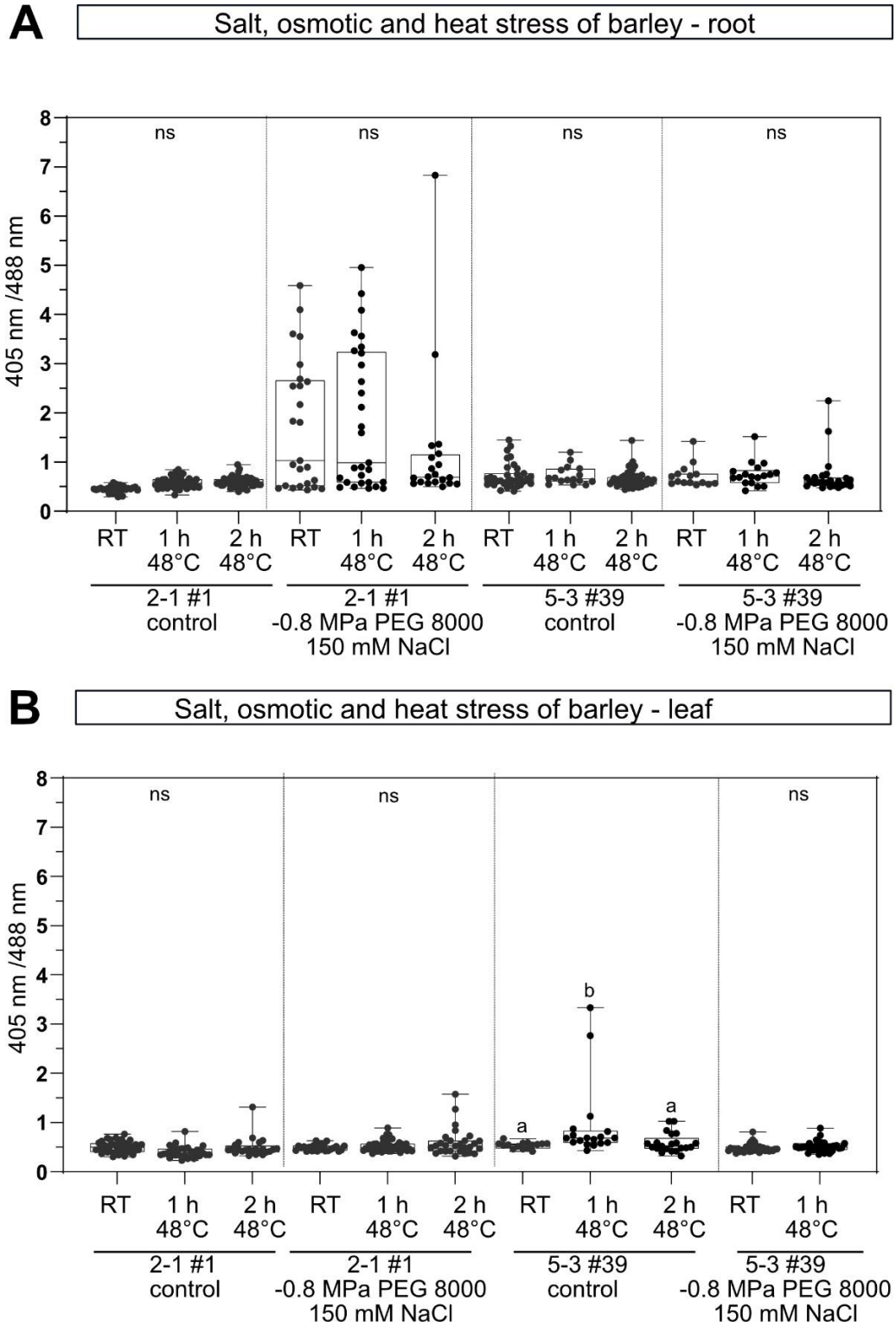

Figure 52: Osmotic, salt and heat stress of barley expressing Grx1-roGFP2

Grx1-roGFP2 nuclear signal upon a combined osmotic, salt (150 mM) and heat stress. Barley was subjected to 96 h of growth on Hoagland solution containing 150 mM salt and an osmotic potential -0.8 MPa adjusted with PEG8000. Boxplots display min to max values with boxes indicating 25-75 percentiles. The median is indicated by a horizontal line. Dots represent single measured nuclei intensities (nuclei n= 14-57). Intensities were extracted from confocal images using RRA imaging software. Significance of ratio change depending of treatment was tested via one-way ANOVA with Tukey's multiple comparison analysis (α=0.05). Differing lowercase letters depict significance, ns = non significant.

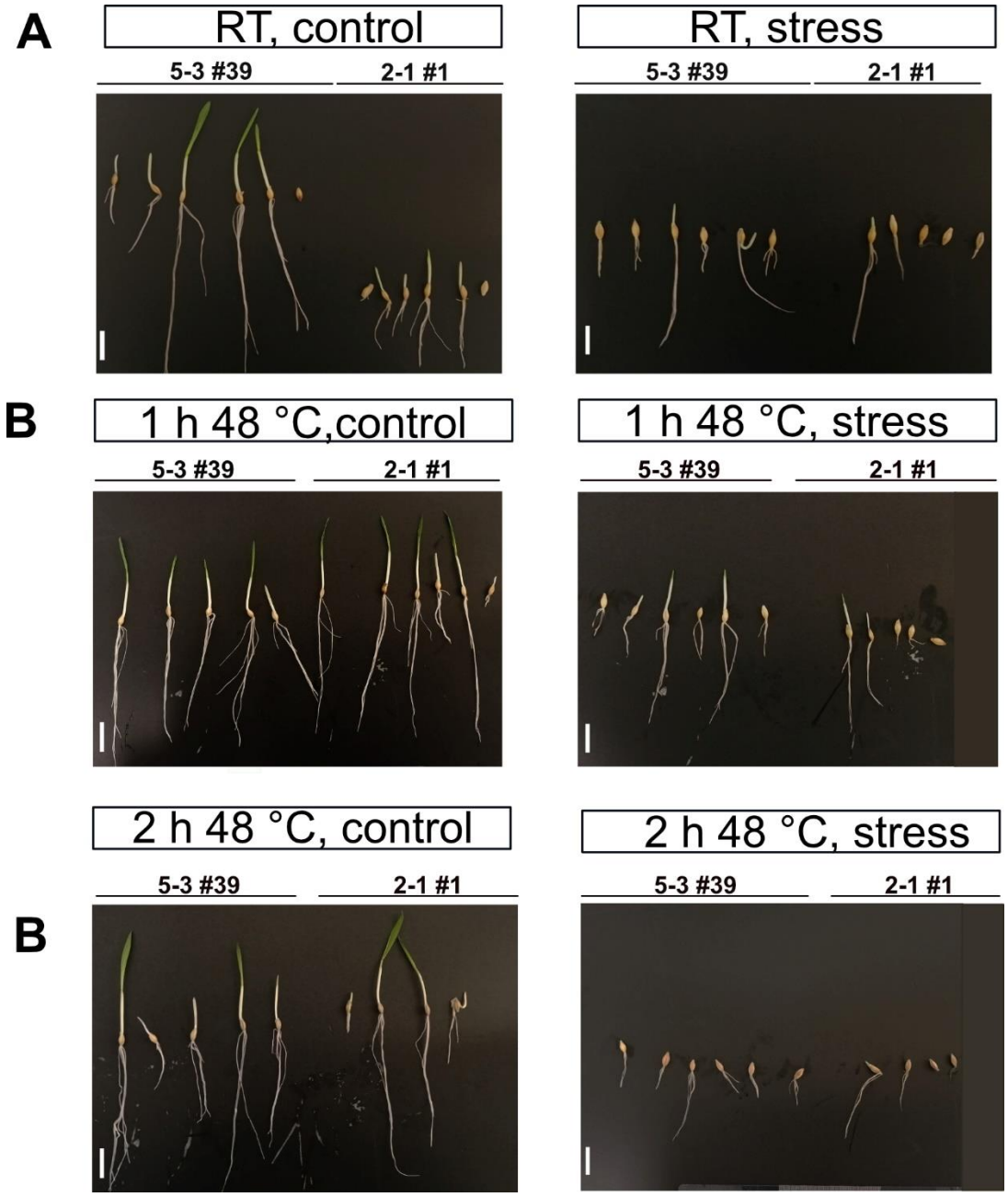

Figure 53: Phenotypic images of barley seedlings after 96 h of osmotic and salt stress combined with 1-2 h of elevated temperature

7-day old barley seedlings expressing Grx1-roGFP2 treated for 96 h with 150 mM NaCl and -0.8 MPa osmotic potential (adjusted by PEG8000) combined with 1 or 2 h treatment 48°C. Barley was incubated at room temperature (22-25°C;RT) as control. **A** 96 h salt and osmotic stress, without additional heat treatment. **B** 96 h salt and osmotic stress, with 1 h treatment at 48°C. **C** 96 h salt and osmotic stress, with 2 h treatment at 48°C. Scale bar = 4 cm. Seedlings were used for monitoring E_{GSH}

7. Conclusion and Outlook

Based on the results obtained in this study, this work has contributed to expand the current understanding of protein *S*-glutathionylation *in vivo* and *in vitro* and provided a starting point for future research. This work provides resources for analyzing redox processes by the introduction of the genetically encoded biosensors GRX1-roGFP2 in the model crop *H. vulgare* Especially for crop science, the introduction of the GRX1-roGFP2 sensor in *H. vulgare* will support future work linked to redox research and stress resilience in crop plants. First characterization of GRX1-roGFP2 in *H. vulgare* revealed a highly robust cytosolic E_{GSH}, even after severe osmotic and salt stress treatments. Furthermore, the introduction of the thioredoxin sensor CROST2 in *A. thaliana* and *P. patens* has the potential to enable research questions regarding a potential crosstalk between the plastidial glutathione and thioredoxin system. Here, first experiments with CROST2 in mutants with impaired stromal E_{GSH} (*miao*) showed a non-significant but observable trend to faster sensor oxidation in light to dark transitions, paving the way for future experiments regarding the thioredoxin and glutathione system crosstalk.

Furthermore, this work contributes to an integrated understanding of protein *S*-(de)glutathionylation:

- by summarizing plastid-localized target proteins via literature screening in combination with phylogenetic reconstruction of GSH-dependent redox networks in plastids from algae to flowering plants. Here, GRXs and GR showed the formation of evolutionary ancient clades, suggesting an important and conserved function within the GSH-dependent network.
- by mapping the influence of GSH:GSSG ratio and E_{GSH} on oxidation of roGFP2 *in vitro*. Plate reader-based *in vitro* experiments with roGFP2 revealed that under constant E_{GSH} the GSH:GSSG ratio has a significant effect on the rate of GRX-dependent and independent disulfide formation. A lower GSH:GSSG ratio (5.25) with a high concentration of reduced glutathione in the mM range showed slower oxidation kinetics. The GRX-catalyzed reduction of glutathionylated roGFFP2 to reduced roGFP2 was excluded as source of slowed down oxidation kinetics based on *At*GRXS15, a GRX only catalyzing the oxidative half reaction. However, the reduction of the roGFP2 intramolecular disulfide by GSH has not been shown to be GRX dependent so far and

may increase in the GSH:GSSG ratios with higher concentrations of reduced glutathione, competing with the GRX catalyzed oxidation reaction and leading to overall slowed down oxidation kinetics. Thus, at constant E_{GSH} and in presence of class I GRX, lower GSSG concentrations within a GSH:GSSG ratio are sufficient to drive oxidation kinetics, while higher GSSG concentrations are required in the absence of GRX.

The glutathionylation target roGFP2-C204S, a roGFP2 cysteine mutant, is unable to form an intramolecular disulfide. It also shows a loss of the roGFP2-specific fluorescence-based ratiometric read-out. An SDS-PAGE and MPEG-Mal induced size-shift based approach to differentiate between glutathionylated and non-glutathionylated roGFP2-C204S revealed difficulties in the MPEG-Mal labelling of the monocysteinic roGFP2 variant. As the control treatment with roGFP2 and MPEG-Mal was successful in all tested conditions, the reason for inefficient labeling may rather be specific to properties of Cys147 in roGFP2-C204S. To successfully utilize the here developed read-out technique of roGFP2-C204S, the reduced controls must successfully result in 100% MPEG-Mal labelling.

- by analyzing class I GRX function in the stroma. GRXC5/S12, MSRB1, DHAR, GSTI/L and PRXIIE require GSH for reduction. Inefficient GSH regeneration observed in the *P. patens* knock-out mutant of organellar GR (Δ*gr1*) results in a dwarfed and stress-sensitive phenotype. The knock-out of GRXC5 (Δ*grxc5*), the only plastidial class I GRX in *P. patens*, revealed a WT-like phenotype. Thus, stromal class I GRX malfunction can be excluded as source for the dwarfed and stress-sensitive Δ*gr1* phenotype. Future experiments based on a reverse genetic approach can target the plastidial enzymes MSRB1, PRXIIE, DHAR and GSTI/L and generate knock-out mutants. Phenotypic characterization of the respective knock-out mutants will provide information on whether the respective enzyme dysfunction is the cause of the Δ*gr1* phenotype. Interestingly, GSH-dependent roGFP2 reduction after oxidative stress was significantly impaired in Δ*grxc5,* concluding, that in plastids of Δ*grxc5* the cysteine redox state of roGFP2 is kinetically uncoupled from the stromal E_{GSH}. A remaining open question is the effect of inefficient deglutathionylation on plastidial *S*-glutathionylation target proteins in Δ*grxc5,* since no impact on photosynthetic performance, non-photochemical quenching or respiration (CO_2 release and uptake) was observed.

However, with the Δ*grxc5* mutant in *P. patens*, we have provided a first tool to study the effect of a complete loss of class I GRX activity within an organelle. This allows further research of class I GRX function *in vivo* without interference from redundant isoforms as is often the case in higher plants.

- by monitoring total *S*-glutathionylation levels after oxidative challenge in combination with GR and GRX mutants. *In vivo* experiments exploring the effect of less reducing E_{GSH} in GR mutants such as Δ*gr1* (*P. patens*), *gr1-1* (*A. thaliana*) or in the class I GRX mutant (Δ*grxc5*) on the level of protein *S*-glutathionylation, did not reveal a consistent increase in steady-state protein *S*-glutathionylation levels. Furthermore, the WT-like *S*-glutathionylation level under oxidative stress conditions of Δ*grxc5* demonstrates, that class I GRX activity in the plastid stroma was not necessary for *S*-glutathionylation *in vivo* within the tested conditions. Identifying physiological stresses triggering *S*-glutathionylation may offer new insights in the mechanisms of protein (de)glutathionylation and are more relatable to *in vivo* conditions.

ACKNOWLEDGEMENT

Ich möchte mich bei all den lieben Menschen bedanken, die mich auf meinem Weg unterstützt und begleitet haben. Zuerst möchte ich mich bei meiner Betreuerin **Stefanie Müller-Schüssele** bedanken. Liebe Steffi, vielen Dank für deine wirklich hervorragende wissenschaftliche Betreuung und Begleitung. Ich habe mich persönlich immer sehr gut aufgehoben und unterstützt gefühlt und konnte besonders von deiner gut organisierten Arbeitsweise viel lernen. Danke für die wirklich schöne Arbeitsatmosphäre! Danke auch an meinen „zweiten" Erstbetreuer **Andreas Meyer** für die vielen inspirierenden wissenschaftlichen Diskussionen und Möglichkeiten die sich während meiner Doktorandenzeit ergeben haben. Vielen Dank **Markus Schwarzländer** an die Betreuung aus der Ferne, deinen wissenschaftlichen Input und für deine Unterstützung! Ich bedanke mich bei meinen Zweitgutachter Peter Dörmann und den beiden Promotionskommissionsmitgliedern **Lukas Schreiber** und **Sigurd Höger** für ihre Zeit. Vielen Dank **Anna-Lena**, **Alina** und **Maria** für die Kaffee (oder Tee) Pausen, die Kuchen oder Schokoladenstücke, die aufbauenden Worte und die gegenseitige Unterstützung. Mit euch an der Seite waren manche Hürden nicht mehr ganz so unbesiegbar und vor allem mit viel mehr Spaß verbunden! Danke liebe **Anna** für die Motivation zum Sport als Ausgleich, das Korrekturlesen der Arbeit und dein offenes Ohr. Danke lieber **José** für die Story time beim Mittagstisch und dass du immer mit einem offenen Ohr und individuellen Lösungsansätzen zur Seite standest. Danke lieber **Luca**, liebe **Michelle**, **Alexa**, **Annika**, ich habe die Zeit mit euch als Freunde und Kollegen sehr genossen und hätte es mir nicht anders wünschen können! Mein Dank gilt auch den weiteren Mitgliedern der **Chemical Signalling** und **Crop Functional Genomics** Arbeitsgruppe, es hat sich immer eher wie eine große Arbeitsgruppe angefühlt, was ein sehr schönes Miteinander war. Danke an **Frau Jessen**, **Frau Kreitz, Frau Skamel** für all die Hilfe und den Durchblick bei allen bürokratischen Angelegenheiten. Vielen Dank an die **Arbeitsgruppe molekulare Botanik**, insbesondere **Tamy und Julian**, die mich nicht nur durch Döner-Dienstage und Döner-Donnerstag, auch in einer fremden Stadt immer gut mit Essen verpflegt haben! Von tiefstem Herzen möchte ich mich bei meiner **Familie (A,D,F,F,T,T,K,L,B,J,S,C,F)** bedanken, die mich zu jeder Zeit unterstützt! Ich bin sehr dankbar, dass ich euch an meiner Seite weiß! Zu guter Letzt möchte ich mich bei all meinen **Freunden** bedanken, die mich unterstützt, abgelenkt, zugehört und geduldig mit mir waren! Schön, dass es euch gibt!

REFERENCES

Aller I., Rouhier N., Meyer A.J. (2013) Development of roGFP2-derived redox probes for measurement of the glutathione redox potential in the cytosol of severely glutathione-deficient *rml1* seedlings. Frontiers in Plant Science **4**

Alvarez B. (2022) Redox chemistry and biology of thiols. Academic Press, London, UK.

Alvarez B., Salinas G. (2022) Basic concepts of thiol chemistry and biology. In: Redox Chemistry and Biology of Thiols. Elsevier, pp 1–18.

Amanda D., Frey F.P., Neumann U., Przybyl M., Šimura J., Zhang Y., Chen Z., Gallavotti A., Fernie A.R., Ljung K., Acosta I.F. (2022) Auxin boosts energy generation pathways to fuel pollen maturation in barley. Current Biology **32**:1798-1811.e8.

Anderson L.E., Ringenberg M.R., Carol A.A. (2004) Cytosolic glyceraldehyde-3-P dehydrogenase and the B subunit of the chloroplast enzyme are present in the pea leaf nucleus. Protoplasma **223**:33–43.

Apel K., Hirt H. (2004) Reactive oxygen species: Metabolism, oxidative stress, and signal transduction. Annual Review of Plant Biology **55**:373–399.

Arnaud D., Deeks M.J., Smirnoff N. (2022) Organelle-targeted biosensors reveal distinct oxidative events during pattern-triggered immune responses. Plant Physiology

Arnér E.S.J., Holmgren A. (2000) Physiological functions of thioredoxin and thioredoxin reductase: Thioredoxin and thioredoxin reductase. European Journal of Biochemistry **267**:6102–6109.

Baker L.M.S., Poole L.B. (2003) Catalytic mechanism of thiol peroxidase from *Escherichia coli*. Journal of Biological Chemistry **278**:9203–9211.

Ball L., Accotto G.-P., Bechtold U., Creissen G., Funck D., Jimenez A., Kular B., Leyland N., Mejia-Carranza J., Reynolds H., Karpinski S., Mullineaux P.M. (2004) Evidence for a direct link between glutathione biosynthesis and stress defense gene expression in Arabidopsis. The Plant Cell **16**:2448–2462.

Bangash S.A.K., Müller-Schüssele S.J., Solbach D., Jansen M., Fiorani F., Schwarzländer M., Kopriva S., Meyer A.J. (2019) Low-glutathione mutants are impaired in growth but do not show an increased sensitivity to moderate water deficit. PloS One **14**:e0220589.

Banks J.A., Nishiyama T., Hasebe M., Bowman J.L., Gribskov M., dePamphilis C., Albert V.A., Aono N., Aoyama T., Ambrose B.A., Ashton N.W., Axtell M.J., Barker E., Barker M.S., Bennetzen J.L., Bonawitz N.D., Chapple C., Cheng C., Correa L.G.G., Dacre M., DeBarry J., Dreyer I., Elias M., Engstrom E.M., Estelle M., Feng L., Finet C., Floyd S.K., Frommer W.B., Fujita T., Gramzow L., Gutensohn M., Harholt J., Hattori M., Heyl A., Hirai T., Hiwatashi Y., Ishikawa M., Iwata M., Karol K.G., Koehler B., Kolukisaoglu U., Kubo M., Kurata T., Lalonde S., Li K., Li Y., Litt A., Lyons E., Manning G., Maruyama T., Michael T.P., Mikami K., Miyazaki S., Morinaga S., Murata T., Mueller-Roeber B., Nelson D.R., Obara M., Oguri Y., Olmstead R.G., Onodera N., Petersen B.L., Pils B., Prigge M.,

Rensing S.A., Riaño-Pachón D.M., Roberts A.W., Sato Y., Scheller H.V., Schulz B., Schulz C., Shakirov E.V., Shibagaki N., Shinohara N., Shippen D.E., Sørensen I., Sotooka R., Sugimoto N., Sugita M., Sumikawa N., Tanurdzic M., Theißen G., Ulvskov P., Wakazuki S., Weng J., Willats W.W.G.T., Wipf D., Wolf P.G., Yang L., Zimmer A.D., Zhu Q., Mitros T., Hellsten U., Loqué D., Otillar R., Salamov A., Schmutz J., Shapiro H., Lindquist E., Lucas S., Rokhsar D., Grigoriev I.V. (2011) The Selaginella genome identifies genetic changes associated with the evolution of vascular plants. Science **332**:960–963.

Bedhomme M., Adamo M., Marchand C.H., Couturier J., Rouhier N., Lemaire S.D., Zaffagnini M., Trost P. (2012) Glutathionylation of cytosolic glyceraldehyde-3-phosphate dehydrogenase from the model plant *Arabidopsis thaliana* is reversed by both glutaredoxins and thioredoxins *in vitro*. Biochemical Journal **445**:337–347.

Bedhomme M., Zaffagnini M., Marchand C.H., Gao X.-H., Moslonka-Lefebvre M., Michelet L., Decottignies P., Lemaire S.D. (2009) Regulation by glutathionylation of isocitrate lyase from *Chlamydomonas reinhardtii*. Journal of Biological Chemistry **284**:36282–36291.

Begas P., Liedgens L., Moseler A., Meyer A.J., Deponte M. (2017) Glutaredoxin catalysis requires two distinct glutathione interaction sites. Nature Communications **8**:14835.

Begas P., Staudacher V., Deponte M. (2015) Systematic re-evaluation of the bis(2-hydroxyethyl)disulfide (HEDS) assay reveals an alternative mechanism and activity of glutaredoxins. Chemical Science **6**:3788–3796.

Belin C., Bashandy T., Cela J., Delorme-Hinoux V., Riondet C., Reichheld J.P. (2015) A comprehensive study of thiol reduction gene expression under stress conditions in *Arabidopsis thaliana*: Arabidopsis redoxins gene expression. Plant, Cell & Environment **38**:299–314.

Berndt C., Hudemann C., Hanschmann E.-M., Axelsson R., Holmgren A., Lillig C.H. (2007) How does iron–sulfur cluster coordination regulate the activity of human glutaredoxin 2? Antioxidants & Redox Signaling **9**:151–157.

Bertani G. (1951) Studies on lysogenesis: The mode of phage liberation by lysogenic *Escherichia coli*. Journal of Bacteriology **62**:293–300.

Biesecker G., Ieuan Harris J., Thierry J.C., Walker J.E., Wonacott A.J. (1977) Sequence and structure of D-glyceraldehyde 3-phosphate dehydrogenase from *Bacillus stearothermophilus*. Nature **266**:328–333.

Biteau B., Labarre J., Toledano M.B. (2003) ATP-dependent reduction of cysteine–sulphinic acid by *S. cerevisiae* sulphiredoxin. Nature **425**:980–984.

Bohle F., Meyer A.J., Mueller-Schuessele S.J. (2023) Quantification of redox-sensitive GFP cysteine redox state via gel-based read-out. In: Sharma M (ed) Fluorescent Proteins. Springer US, New York, NY, pp 259–268.

de Bont L., Jacquot J.-P., Rouhier N. (2022) Thiol-based redox control in chloroplasts. In: Redox Chemistry and Biology of Thiols. Elsevier, pp 507–532.

Bowman J.L., Kohchi T., Yamato K.T., Jenkins J., Shu S., Ishizaki K., Yamaoka S., Nishihama R., Nakamura Y., Berger F., Adam C., Aki S.S., Althoff F., Araki T., Arteaga-Vazquez M.A., Balasubrmanian S., Barry K., Bauer D., Boehm C.R., Briginshaw L., Caballero-Perez J., Catarino B., Chen F., Chiyoda S., Chovatia M., Davies K.M., Delmans M., Demura T., Dierschke T., Dolan L., Dorantes-Acosta A.E., Eklund D.M., Florent S.N., Flores-Sandoval E., Fujiyama A., Fukuzawa H., Galik B., Grimanelli D., Grimwood J., Grossniklaus U., Hamada T., Haseloff J., Hetherington A.J., Higo A., Hirakawa Y., Hundley H.N., Ikeda Y., Inoue K., Inoue S., Ishida S., Jia Q., Kakita M., Kanazawa T., Kawai Y., Kawashima T., Kennedy M., Kinose K., Kinoshita T., Kohara Y., Koide E., Komatsu K., Kopischke S., Kubo M., Kyozuka J., Lagercrantz U., Lin S.-S., Lindquist E., Lipzen A.M., Lu C.-W., De Luna E., Martienssen R.A., Minamino N., Mizutani M., Mizutani M., Mochizuki N., Monte I., Mosher R., Nagasaki H., Nakagami H., Naramoto S., Nishitani K., Ohtani M., Okamoto T., Okumura M., Phillips J., Pollak B., Reinders A., Rövekamp M., Sano R., Sawa S., Schmid M.W., Shirakawa M., Solano R., Spunde A., Suetsugu N., Sugano S., Sugiyama A., Sun R., Suzuki Y., Takenaka M., Takezawa D., Tomogane H., Tsuzuki M., Ueda T., Umeda M., Ward J.M., Watanabe Y., Yazaki K., Yokoyama R., Yoshitake Y., Yotsui I., Zachgo S., Schmutz J. (2017) Insights into land plant evolution garnered from the *Marchantia polymorpha* genome. Cell **171**:287-304.e15.

Brandes H.K., Larimer F.W., Hartman F.C. (1996) The molecular pathway for the regulation of phosphoribulokinase by thioredoxin f. Journal of Biological Chemistry **271**:3333–3335.

Buchanan B.B. (1991) Regulation of CO_2 assimilation in oxygenic photosynthesis: The ferredoxin/thioredoxin system. Archives of Biochemistry and Biophysics **288**:1–9.

Buchanan B.B., Balmer Y. (2005) Redox regulation: A broadening horizon. Annual Review of Plant Biology **56**:187–220.

Cairns N.G., Pasternak M., Wachter A., Cobbett C.S., Meyer A.J. (2006) Maturation of Arabidopsis seeds is dependent on glutathione biosynthesis within the embryo. Plant Physiology **141**:446–455.

Calderón A., Lázaro-Payo A., Iglesias-Baena I., Camejo D., Lázaro J.J., Sevilla F., Jiménez A. (2017) Glutathionylation of Pea chloroplast 2-Cys Prx and mitochondrial Prx IIF affects their structure and peroxidase activity and sulfiredoxin deglutathionylates only the 2-Cys Prx. Frontiers in Plant Science **8**:118.

Can B., Kulaksiz Erkmen G., Dalmizrak O., Ogus I.H., Ozer N. (2010) Purification and characterisation of rat kidney glutathione reductase. The Protein Journal **29**:250–256.

Chardonnet S., Sakr S., Cassier-Chauvat C., Le Maréchal P., Chauvat F., Lemaire S.D., Decottignies P. (2015) First proteomic study of *S*-glutathionylation in cyanobacteria. Journal of Proteome Research **14**:59–71.

de Chaumont F., Dallongeville S., Chenouard N., Hervé N., Pop S., Provoost T., Meas-Yedid V., Pankajakshan P., Lecomte T., Le Montagner Y., Lagache T., Dufour A., Olivo-Marin J.-C. (2012) Icy: an open bioimage informatics platform for extended reproducible research. Nature Methods **9**:690–696.

Clough S.J., Bent A.F. (1998) Floral dip: a simplified method for Agrobacterium-mediated transformation of *Arabidopsis thaliana*. The Plant Journal **16**:735–743.

Cobbett C.S., May M.J., Howden R., Rolls B. (1998) The glutathione-deficient, cadmium-sensitive mutant, cad2-1, of *Arabidopsis thaliana* is deficient in gamma-glutamylcysteine synthetase. The Plant Journal **16**:73–78.

Couturier J., Chibani K., Jacquot J.-P., Rouhier N. (2013) Cysteine–based redox regulation and signaling in plants. Frontiers in Plant Science **4**

Couturier J., Jacquot J.-P., Rouhier N. (2009) Evolution and diversity of glutaredoxins in photosynthetic organisms. Cellular and Molecular Life Sciences **66**:2539–2557.

Couturier J., Jacquot J.-P., Rouhier N. (2013) Toward a refined classification of class I dithiol glutaredoxins from poplar: biochemical basis for the definition of two subclasses. Frontiers in Plant Science **4**

Couturier J., Koh C.S., Zaffagnini M., Winger A.M., Gualberto J.M., Corbier C., Decottignies P., Jacquot J.-P., Lemaire S.D., Didierjean C., Rouhier N. (2009) Structure-function relationship of the chloroplastic glutaredoxin S12 with an atypical WCSYS active site. Journal of Biological Chemistry **284**:9299–9310.

Couturier J., Ströher E., Albetel A.-N., Roret T., Muthuramalingam M., Tarrago L., Seidel T., Tsan P., Jacquot J.-P., Johnson M.K., Dietz K.-J., Didierjean C., Rouhier N. (2011) Arabidopsis chloroplastic glutaredoxin C5 as a model to explore molecular determinants for iron-sulfur cluster binding into glutaredoxins. Journal of Biological Chemistry **286**:27515–27527.

Cox J., Mann M. (2008) MaxQuant enables high peptide identification rates, individualized p.p.b.-range mass accuracies and proteome-wide protein quantification. Nature Biotechnology **26**:1367–1372.

Cuypers A., Karen S., Jos R., Kelly O., Els K., Tony R., Nele H., Nathalie V., Suzy V.S., Frank V.B., Yves G., Jan C., Jaco V. (2011) The cellular redox state as a modulator in cadmium and copper responses in *Arabidopsis thaliana* seedlings. Journal of Plant Physiology **168**:309–316.

Cuypers A., Plusquin M., Remans T., Jozefczak M., Keunen E., Gielen H., Opdenakker K., Nair A.R., Munters E., Artois T.J., Nawrot T., Vangronsveld J., Smeets K. (2010) Cadmium stress: an oxidative challenge. BioMetals **23**:927–940.

Dalle-Donne I., Rossi R., Colombo G., Giustarini D., Milzani A. (2009) Protein *S*-glutathionylation: a regulatory device from bacteria to humans. Trends in Biochemical Sciences **34**:85–96.

Dard A., Weiss A., Bariat L., Picault N., Pontvianne F., Riondet C., Reichheld J.-P. (2022) *Glutathione-mediated plant response to high-temperature*. Plant Biology.

Dawson I.K., Russell J., Powell W., Steffenson B., Thomas W.T.B., Waugh R. (2015) Barley: a translational model for adaptation to climate change. New Phytologist **206**:913–931.

Deponte M. (2017) The incomplete glutathione puzzle: Just guessing at numbers and figures? Antioxidants & Redox Signaling **27**:1130–1161.

Deponte M. (2022) Glutathione and glutathione-dependent enzymes. In: Redox Chemistry and Biology of Thiols. Elsevier, pp 241–275.

Dietz K.-J. (2003) Plant peroxiredoxins. Annual Review of Plant Biology **54**:93–107.

Dietz K.-J. (2011) Peroxiredoxins in plants and cyanobacteria. Antioxidants & Redox Signaling **15**:1129–1159.

Dietz K.-J., Turkan I., Krieger-Liszkay A. (2016) Redox- and reactive oxygen species-dependent signaling into and out of the photosynthesizing chloroplast. Plant Physiology **171**:1541–1550.

Dixon D.P., Cummins I., Cole D.J., Edwards R. (1998) Glutathione-mediated detoxification systems in plants. Current Opinion in Plant Biology **1**:258–266.

Dixon D.P., Fordham-Skelton A.P., Edwards R. (2005) Redox regulation of a soybean tyrosine-specific protein phosphatase. Biochemistry **44**:7696–7703.

Dixon D.P., Skipsey M., Grundy N.M., Edwards R. (2005) Stress-induced protein *S* -glutathionylation in Arabidopsis. Plant Physiology **138**:2233–2244.

Draculic T., Dawes I.W., Grant C.M. (2000) A single glutaredoxin or thioredoxin gene is essential for viability in the yeast *Saccharomyces cerevisiae*. Molecular Microbiology **36**:1167–1174.

Dreyer A., Treffon P., Basiry D., Jozefowicz A.M., Matros A., Mock H.-P., Dietz K.-J. (2021) Function and regulation of chloroplast peroxiredoxin IIE. Antioxidants **10**:152.

Edwards K., Johnstone C., Thompson C. (1991) A simple and rapid method for the preparation of plant genomic DNA for PCR analysis. Nucleic Acids Research **19**:1349–1349.

Eklund H., Cambillau C., Sjöberg B.M., Holmgren A., Jörnvall H., Höög J.O., Brändén C.I. (1984) Conformational and functional similarities between glutaredoxin and thioredoxins. The EMBO Journal **3**:1443–1449.

Ellis R.J. (1979) The most abundant protein in the world. Trends in Biochemical Sciences **4**:241–244.

Elsässer M., Feitosa-Araujo E., Lichtenauer S., Wagner S., Fuchs P., Giese J., Kotnik F., Hippler M., Meyer A.J., Maurino V.G., Finkemeier I., Schallenberg-Rüdinger M., Schwarzländer M. (2020) Photosynthetic activity triggers pH and NAD redox signatures across different plant cell compartments. Biorxiv.

Falz A.-L., Müller-Schüssele S.J. (2019) Physcomitrella as a model system for plant cell biology and organelle-organelle communication. Current Opinion in Plant Biology **52**:7–13.

Faralli M., Lektemur C., Rosellini D., Gürel F. (2015) Effects of heat shock and salinity on barley growth and stress-related gene transcription. Biologia plantarum **59**:537–546.

Foyer C.H. (2018) Reactive oxygen species, oxidative signaling and the regulation of photosynthesis. Environmental and Experimental Botany **154**:134–142.

Foyer C.H., Noctor G. (2011) Ascorbate and glutathione: The heart of the redox hub. Plant Physiology **155**:2–18.

Foyer C.H., Shigeoka S. (2011) Understanding oxidative stress and antioxidant functions to enhance photosynthesis. Plant Physiology **155**:93–100.

Frand A.R., Cuozzo J.W., Kaiser C.A. (2000) Pathways for protein disulphide bond formation. Trends in Cell Biology **10**:203–210.

Fricker M.D. (2016) Quantitative redox imaging software. Antioxidants & Redox Signaling **24**:752–762.

Fricker M.D., May M., Meyer A.J., Sheard N., White N.S. (2000) Measurement of glutathione levels in intact roots of Arabidopsis. Journal of Microscopy **198**:162–173.

Gama F., Bréhélin C., Gelhaye E., Meyer Y., Jacquot J.-P., Rey P., Rouhier N. (2008) Functional analysis and expression characteristics of chloroplastic Prx IIE. Physiologia Plantarum **133**:599–610.

Gao X.-H., Bedhomme M., Michelet L., Zaffagnini M., Lemaire S.D. (2009) Glutathionylation in photosynthetic organisms. In: Advances in Botanical Research. Elsevier, pp 363–403.

Geck M.K., Larimer F.W., Hartman F.C. (1996) Identification of residues of spinach thioredoxin f that influence interactions with target enzymes. Journal of Biological Chemistry **271**:24736–24740.

Gelhaye E., Rouhier N., Navrot N., Jacquot J.P. (2005) The plant thioredoxin system. Cellular and Molecular Life Sciences **62**:24–35.

Giridhar M., Meier B., Imani J., Kogel K.-H., Peiter E., Vothknecht U.C., Chigri F. (2022) Comparative analysis of stress-induced calcium signals in the crop species barley and the model plant *Arabidopsis thaliana*. BMC plant biology **22**:447.

Glaser E., Soll J. (2004) Targeting signals and import machinery of plastids and plant mitochondria. In: Daniell H, Chase C (eds) Molecular Biology and Biotechnology of Plant Organelles. Springer Netherlands, Dordrecht, pp 385–417.

Gol L., Haraldsson E.B., von Korff M. (2021) Ppd-H1 integrates drought stress signals to control spike development and flowering time in barley (M. Jones, Ed.). Journal of Experimental Botany **72**:122–136.

Goodstein D.M., Shu S., Howson R., Neupane R., Hayes R.D., Fazo J., Mitros T., Dirks W., Hellsten U., Putnam N., Rokhsar D.S. (2012) Phytozome: A comparative platform for green plant genomics. Nucleic Acids Research **40**:D1178–D1186.

Gupta V., Carroll K.S. (2014) Sulfenic acid chemistry, detection and cellular lifetime. Biochimica et Biophysica Acta (BBA) - General Subjects **1840**:847–875.

Gutscher M., Pauleau A.-L., Marty L., Brach T., Wabnitz G.H., Samstag Y., Meyer A.J., Dick T.P. (2008) Real-time imaging of the intracellular glutathione redox potential. Nature Methods **5**:553–559.

Halliwell B. (1999) Antioxidant defence mechanisms: From the beginning to the end (of the beginning). Free Radical Research **31**:261–272.

Halliwell B., Foyer C.H. (1978) Properties and physiological function of a glutathione reductase purified from spinach leaves by affinity chromatography. Planta **139**:9–17.

Hancock J.T., Henson D., Nyirenda M., Desikan R., Harrison J., Lewis M., Hughes J., Neill S.J. (2005) Proteomic identification of glyceraldehyde 3-phosphate dehydrogenase as an inhibitory target of hydrogen peroxide in Arabidopsis. Plant Physiology and Biochemistry **43**:828–835.

Hanson G.T., Aggeler R., Oglesbee D., Cannon M., Capaldi R.A., Tsien R.Y., Remington S.J. (2004) Investigating mitochondrial redox potential with redox-sensitive green fluorescent protein indicators. Journal of Biological Chemistry **279**:13044–13053.

Hara M.R., Agrawal N., Kim S.F., Cascio M.B., Fujimuro M., Ozeki Y., Takahashi M., Cheah J.H., Tankou S.K., Hester L.D., Ferris C.D., Hayward S.D., Snyder S.H., Sawa A. (2005) *S*-nitrosylated GAPDH initiates apoptotic cell death by nuclear translocation following Siah1 binding. Nature Cell Biology **7**:665–674.

Hell R., Bergmann L. (1988) Glutathione synthetase in tobacco suspension cultures: catalytic properties and localization. Physiologia Plantarum **72**:70–76.

Hiner A.N.P., Rodríguez-López J.N., Arnao M.B., Raven E.L., García-Cánovas F., Acosta M. (2000) Kinetic study of the inactivation of ascorbate peroxidase by hydrogen peroxide. Biochemical Journal **348**:321–328.

Hipsch M., Lampl N., Zelinger E., Barda O., Waiger D., Rosenwasser S. (2021) Sensing stress responses in potato with whole-plant redox imaging. Plant Physiology **187**:618–631.

Holtgrefe S., Gohlke J., Starmann J., Druce S., Klocke S., Altmann B., Wojtera J., Lindermayr C., Scheibe R. (2008) Regulation of plant cytosolic glyceraldehyde 3-phosphate dehydrogenase isoforms by thiol modifications. Physiologia Plantarum **133**:211–228.

Horstmann V., Huether C.M., Jost W., Reski R., Decker E.L. (2004) Quantitative promoter analysis in *Physcomitrella patens* : a set of plant vectors activating gene expression within three orders of magnitude. BMC Biotechnology **4**:13.

Howden R., Goldsbrough P.B., Andersen C.R., Cobbett C.S. (1995) Cadmium-sensitive, *cad1* mutants of *Arabidopsis thaliana* are phytochelatin deficient. Plant Physiology **107**:1059–1066.

Huang J., Willems P., Wei B., Tian C., Ferreira R.B., Bodra N., Martínez Gache S.A., Wahni K., Liu K., Vertommen D., Gevaert K., Carroll K.S., Van Montagu M., Yang J., Van Breusegem F., Messens J. (2019) Mining for protein S-sulfenylation in Arabidopsis

uncovers redox-sensitive sites. Proceedings of the National Academy of Sciences **116**:21256–21261.

Johansson C., Lillig C.H., Holmgren A. (2004) Human mitochondrial glutaredoxin reduces S-glutathionylated proteins with high affinity accepting electrons from either glutathione or thioredoxin reductase. Journal of Biological Chemistry **279**:7537–7543.

Jozefczak M., Remans T., Vangronsveld J., Cuypers A. (2012) Glutathione is a key player in metal-induced oxidative stress defenses. International Journal of Molecular Sciences **13**:3145–3175.

Kataya A.R.A., Reumann S. (2010) Arabidopsis glutathione reductase 1 is dually targeted to peroxisomes and the cytosol. Plant Signaling & Behavior **5**:171–175.

Kirschner G.K., Stahl Y., Imani J., von Korff M., Simon R. (2018) Fluorescent reporter lines for auxin and cytokinin signalling in barley (*Hordeum vulgare*) (X. Li, Ed.). PLOS ONE **13**:e0196086.

Koornneef M., Meinke D. (2010) The development of Arabidopsis as a model plant. The Plant Journal **61**:909–921.

Laugier E., Tarrago L., Vieira Dos Santos C., Eymery F., Havaux M., Rey P. (2009) *Arabidopsis thaliana* plastidial methionine sulfoxide reductases B, MSRBs, account for most leaf peptide MSR activity and are essential for growth under environmental constraints through a role in the preservation of photosystem antennae: Role of plastidial methionine sulfoxide reductases B. The Plant Journal **61**:271–282.

Lazo G.R., Stein P.A., Ludwig R.A. (1991) A DNA transformation–competent arabidopsis genomic library in agrobacterium. Bio/Technology **9**:963–967.

Li S. (2014) Redox modulation matters: Emerging functions for glutaredoxins in plant development and stress responses. Plants **3**:559–582.

Li F.-W., Brouwer P., Carretero-Paulet L., Cheng S., de Vries J., Delaux P.-M., Eily A., Koppers N., Kuo L.-Y., Li Z., Simenc M., Small I., Wafula E., Angarita S., Barker M.S., Bräutigam A., dePamphilis C., Gould S., Hosmani P.S., Huang Y.-M., Huettel B., Kato Y., Liu X., Maere S., McDowell R., Mueller L.A., Nierop K.G.J., Rensing S.A., Robison T., Rothfels C.J., Sigel E.M., Song Y., Timilsena P.R., Van de Peer Y., Wang H., Wilhelmsson P.K.I., Wolf P.G., Xu X., Der J.P., Schluepmann H., Wong G.K.-S., Pryer K.M. (2018) Fern genomes elucidate land plant evolution and cyanobacterial symbioses. Nature Plants **4**:460–472.

Li F.-W., Nishiyama T., Waller M., Frangedakis E., Keller J., Li Z., Fernandez-Pozo N., Barker M.S., Bennett T., Blázquez M.A., Cheng S., Cuming A.C., de Vries J., de Vries S., Delaux P.-M., Diop I.S., Harrison C.J., Hauser D., Hernández-García J., Kirbis A., Meeks J.C., Monte I., Mutte S.K., Neubauer A., Quandt D., Robison T., Shimamura M., Rensing S.A., Villarreal J.C., Weijers D., Wicke S., Wong G.K.-S., Sakakibara K., Szövényi P. (2020) Anthoceros genomes illuminate the origin of land plants and the unique biology of hornworts. Nature Plants **6**:259–272.

Liebthal M., Maynard D., Dietz K.-J. (2018) Peroxiredoxins and redox signaling in plants. Antioxidants & Redox Signaling **28**:609–624.

Liedgens L., Zimmermann J., Wäschenbach L., Geissel F., Laporte H., Gohlke H., Morgan B., Deponte M. (2020) Quantitative assessment of the determinant structural differences between redox-active and inactive glutaredoxins. Nature Communications **11**:1725.

Little C., O'brien P.J. (1969) Mechanism of peroxide-inactivation of the sulphydryl enzyme glyceraldehyde-3-Phosphate dehydrogenase. European Journal of Biochemistry **10**:533–538.

Liu X., Chai J., Ou X., Li M., Liu Z. (2019) Structural insights into substrate selectivity, catalytic mechanism, and redox regulation of rice photosystem II core phosphatase. Molecular Plant **12**:86–98.

Liu Y.-J., Han X.-M., Ren L.-L., Yang H.-L., Zeng Q.-Y. (2013) Functional divergence of the glutathione *S* -transferase supergene family in *Physcomitrella patens* reveals complex patterns of large gene family evolution in land plants. Plant Physiology **161**:773–786.

Luikenhuis S., Perrone G., Dawes I.W., Grant C.M. (1998) The Yeast *Saccharomyces cerevisiae* contains two glutaredoxin genes that are required for protection against reactive oxygen species. Molecular Biology of the Cell **9**:1081–1091.

Lyons T.W., Reinhard C.T., Planavsky N.J. (2014) The rise of oxygen in Earth's early ocean and atmosphere. Nature **506**:307–315.

Manevich Y., Feinstein S.I., Fisher A.B. (2004) Activation of the antioxidant enzyme 1-CYS peroxiredoxin requires glutathionylation mediated by heterodimerization with πGST. Proceedings of the National Academy of Sciences **101**:3780–3785.

Manta B., Hugo M., Ortiz C., Ferrer-Sueta G., Trujillo M., Denicola A. (2009) The peroxidase and peroxynitrite reductase activity of human erythrocyte peroxiredoxin 2. Archives of Biochemistry and Biophysics **484**:146–154.

Marotta R., Del Giudice A., Gurrieri L., Fanti S., Swuec P., Galantini L., Falini G., Trost P., Fermani S., Sparla F. (2022) Unravelling the regulation pathway of photosynthetic AB-GAPDH. Acta Crystallographica Section D Structural Biology **78**:1399–1411.

Martin J.L. (1995) Thioredoxin —a fold for all reasons. Structure **3**:245–250.

Marty L., Bausewein D., Müller C., Bangash S.A.K., Moseler A., Schwarzländer M., Müller-Schüssele S.J., Zechmann B., Riondet C., Balk J., Wirtz M., Hell R., Reichheld J., Meyer A.J. (2019) Arabidopsis glutathione reductase 2 is indispensable in plastids, while mitochondrial glutathione is safeguarded by additional reduction and transport systems. New Phytologist **224**:1569–1584.

Marty L., Siala W., Schwarzlander M., Fricker M.D., Wirtz M., Sweetlove L.J., Meyer Y., Meyer A.J., Reichheld J.-P., Hell R. (2009) The NADPH-dependent thioredoxin system constitutes a functional backup for cytosolic glutathione reductase in Arabidopsis. Proceedings of the National Academy of Sciences **106**:9109–9114.

Mascher M., Gundlach H., Himmelbach A., Beier S., Twardziok S.O., Wicker T., Radchuk V., Dockter C., Hedley P.E., Russell J., Bayer M., Ramsay L., Liu H., Haberer G., Zhang X.-Q., Zhang Q., Barrero R.A., Li L., Taudien S., Groth M., Felder M., Hastie A., Šimková H., Staňková H., Vrána J., Chan S., Muñoz-Amatriaín M., Ounit R., Wanamaker S., Bolser D., Colmsee C., Schmutzer T., Aliyeva-Schnorr L., Grasso S., Tanskanen J., Chailyan A., Sampath D., Heavens D., Clissold L., Cao S., Chapman B., Dai F., Han Y., Li H., Li X., Lin C., McCooke J.K., Tan C., Wang P., Wang S., Yin S., Zhou G., Poland J.A., Bellgard M.I., Borisjuk L., Houben A., Doležel J., Ayling S., Lonardi S., Kersey P., Langridge P., Muehlbauer G.J., Clark M.D., Caccamo M., Schulman A.H., Mayer K.F.X., Platzer M., Close T.J., Scholz U., Hansson M., Zhang G., Braumann I., Spannagl M., Li C., Waugh R., Stein N. (2017) A chromosome conformation capture ordered sequence of the barley genome. Nature **544**:427–433.

Mehler A.H. (1951) Studies on reactions of illuminated chloroplasts. II. Stimulation and inhibition of the reaction with molecular oxygen. Archives of Biochemistry and Biophysics **34**:339–351.

Meyer A.J. (2008) The integration of glutathione homeostasis and redox signaling. Journal of Plant Physiology **165**:1390–1403.

Meyer A.J., Brach T., Marty L., Kreye S., Rouhier N., Jacquot J.-P., Hell R. (2007) Redox-sensitive GFP in *Arabidopsis thaliana* is a quantitative biosensor for the redox potential of the cellular glutathione redox buffer. The Plant Journal **52**:973–986.

Meyer A.J., Dick T.P. (2010) Fluorescent protein-based redox probes. Antioxidants & Redox Signaling **13**:621–650.

Meyer A.J., Dreyer A., Ugalde J.M., Feitosa-Araujo E., Dietz K.-J., Schwarzländer M. (2021) Shifting paradigms and novel players in Cys-based redox regulation and ROS signaling in plants - and where to go next. Biological Chemistry **402**:399–423.

Meyer A.J., Hell R. (2005) Glutathione homeostasis and redox-regulation by sulfhydryl groups. Photosynthesis Research **86**:435–457.

Mhamdi A., Queval G., Chaouch S., Vanderauwera S., Van Breusegem F., Noctor G. (2010) Catalase function in plants: a focus on Arabidopsis mutants as stress-mimic models. Journal of Experimental Botany **61**:4197–4220.

Michelet L., Zaffagnini M., Lemaire D. (2009) Thioredoxins and related proteins. In: The Chlamydomonas Sourcebook. Elsevier, pp 401–443.

Michelet L., Zaffagnini M., Marchand C., Collin V., Decottignies P., Tsan P., Lancelin J.-M., Trost P., Miginiac-Maslow M., Noctor G., Lemaire S.D. (2005) Glutathionylation of chloroplast thioredoxin f is a redox signaling mechanism in plants. Proceedings of the National Academy of Sciences **102**:16478–16483.

Michelet L., Zaffagnini M., Morisse S., Sparla F., Pérez-Pérez M.E., Francia F., Danon A., Marchand C.H., Fermani S., Trost P., Lemaire S.D. (2013) Redox regulation of the Calvin–Benson cycle: something old, something new. Frontiers in Plant Science **4**

Michelet L., Zaffagnini M., Vanacker H., Le Maréchal P., Marchand C., Schroda M., Lemaire S.D., Decottignies P. (2008) *In vivo* targets of *S*-thiolation in *Chlamydomonas reinhardtii*. Journal of Biological Chemistry **283**:21571–21578.

Mieyal J.J., Gallogly M.M., Qanungo S., Sabens E.A., Shelton M.D. (2008) Molecular mechanisms and clinical implications of reversible protein *S* -glutathionylation. Antioxidants & Redox Signaling **10**:1941–1988.

Mittler R. (2002) Oxidative stress, antioxidants and stress tolerance. Trends in Plant Science **7**:405–410.

Mittler R., Vanderauwera S., Gollery M., Van Breusegem F. (2004) Reactive oxygen gene network of plants. Trends in Plant Science **9**:490–498.

Mittler R., Zandalinas S.I., Fichman Y., Van Breusegem F. (2022) Reactive oxygen species signalling in plant stress responses. Nature Reviews Molecular Cell Biology **23**:663–679.

Mittler R., Zilinskas B.A. (1991) Purification and characterization of Pea cytosolic ascorbate peroxidase. Plant Physiology **97**:962–968.

Møller I.M., Jensen P.E., Hansson A. (2007) Oxidative modifications to cellular components in plants. Annual Review of Plant Biology **58**:459–481.

Moreno J., Garcia-Murria M.J., Marin-Navarro J. (2008) Redox modulation of Rubisco conformation and activity through its cysteine residues. Journal of Experimental Botany **59**:1605–1614.

Moreno-García B., López-Calcagno P.E., Raines C.A., Sweetlove L.J. (2022) Suppression of metabolite shuttles for export of chloroplast and mitochondrial ATP and NADPH increases the cytosolic NADH:NAD+ ratio in tobacco leaves in the dark. Journal of Plant Physiology **268**:153578.

Morgan B., Schwarzländer M. (2016) Fluoreszierende Proteinsensoren für die Redoxregulation in lebenden Zellen. BIOspektrum **22**:260–263.

Mortimer C.E., Müller U. (Eds) (2015) Chemie: Das Basiswissen der Chemie, 12th edn. Georg Thieme Verlag, Stuttgart.

Moseler A., Aller I., Wagner S., Nietzel T., Przybyla-Toscano J., Mühlenhoff U., Lill R., Berndt C., Rouhier N., Schwarzländer M., Meyer A.J. (2015) The mitochondrial monothiol glutaredoxin S15 is essential for iron-sulfur protein maturation in *Arabidopsis thaliana*. Proceedings of the National Academy of Sciences **112**:13735–13740.

Müller S.J., Gütle D.D., Jacquot J.-P., Reski R. (2016) Can mosses serve as model organisms for forest research? Annals of Forest Science **73**:135–146.

Müller-Schüssele S.J., Bohle F., Rossi J., Trost P., Meyer A.J., Zaffagnini M. (2021) Plasticity in plastid redox networks: evolution of glutathione-dependent redox cascades and glutathionylation sites. BMC Plant Biology **21**:322.

Müller-Schüssele S.J., Schwarzländer M., Meyer A.J. (2021) Live monitoring of plant redox and energy physiology with genetically encoded biosensors. Plant Physiology **186**:93–109.

Müller-Schüssele S.J., Wang R., Gütle D.D., Romer J., Rodriguez-Franco M., Scholz M., Buchert F., Lüth V.M., Kopriva S., Dörmann P., Schwarzländer M., Reski R., Hippler M., Meyer A.J. (2020) Chloroplasts require glutathione reductase to balance reactive oxygen species and maintain efficient photosynthesis. The Plant Journal **103**:1140–1154.

Nagy P. (2013) Kinetics and mechanisms of thiol–disulfide exchange covering direct substitution and thiol oxidation-mediated pathways. Antioxidants & Redox Signaling **18**:1623–1641.

Nietzel T., Elsässer M., Ruberti C., Steinbeck J., Ugalde J.M., Fuchs P., Wagner S., Ostermann L., Moseler A., Lemke P., Fricker M.D., Müller-Schüssele S.J., Moerschbacher B.M., Costa A., Meyer A.J., Schwarzländer M. (2018) The fluorescent protein sensor roGFP2-Orp1 monitors *in vivo* H_2O_2 and thiol redox integration and elucidates intracellular H_2O_2 dynamics during elicitor-induced oxidative burst in Arabidopsis. The New Phytologist

Nishiyama T., Sakayama H., de Vries J., Buschmann H., Saint-Marcoux D., Ullrich K.K., Haas F.B., Vanderstraeten L., Becker D., Lang D., Vosolsobě S., Rombauts S., Wilhelmsson P.K.I., Janitza P., Kern R., Heyl A., Rümpler F., Villalobos L.I.A.C., Clay J.M., Skokan R., Toyoda A., Suzuki Y., Kagoshima H., Schijlen E., Tajeshwar N., Catarino B., Hetherington A.J., Saltykova A., Bonnot C., Breuninger H., Symeonidi A., Radhakrishnan G.V., Van Nieuwerburgh F., Deforce D., Chang C., Karol K.G., Hedrich R., Ulvskov P., Glöckner G., Delwiche C.F., Petrášek J., Van de Peer Y., Friml J., Beilby M., Dolan L., Kohara Y., Sugano S., Fujiyama A., Delaux P.-M., Quint M., Theißen G., Hagemann M., Harholt J., Dunand C., Zachgo S., Langdale J., Maumus F., Van Der Straeten D., Gould S.B., Rensing S.A. (2018) The chara genome: Secondary complexity and implications for plant terrestrialization. Cell **174**:448-464.e24.

Noctor G., Foyer C.H. (1998) Ascorbate and glutathione: Keeping active oxygen under control. Annual Review of Plant Physiology and Plant Molecular Biology **49**:249–279.

Noctor G., Mhamdi A., Chaouch S., Han Y., Neukermans J., Marquez-Garcia B., Queval G., Foyer C.H. (2012) Glutathione in plants: an integrated overview: Glutathione status and functions. Plant, Cell & Environment **35**:454–484.

Noguera-Mazon V., Lemoine J., Walker O., Rouhier N., Salvador A., Jacquot J.-P., Lancelin J.-M., Krimm I. (2006) Glutathionylation induces the dissociation of 1-Cys D-peroxiredoxin non-covalent homodimer. Journal of Biological Chemistry **281**:31736–31742.

Noshi M., Hatanaka R., Tanabe N., Terai Y., Maruta T., Shigeoka S. (2016) Redox regulation of ascorbate and glutathione by a chloroplastic dehydroascorbate reductase is required for high-light stress tolerance in Arabidopsis. Bioscience, Biotechnology, and Biochemistry **80**:870–877.

Ogawa K., Tasaka Y., Mino M., Tanaka Y., Iwabuchi M. (2001) Association of glutathione with flowering in *Arabidopsis thaliana*. Plant and Cell Physiology **42**:524–530.

Ojeda V., Pérez-Ruiz J.M., Cejudo F.J. (2018) 2-Cys peroxiredoxins participate in the oxidation of chloroplast enzymes in the dark. Molecular Plant **11**:1377–1388.

Osthoff A., Donà dalle Rose P., Baldauf J.A., Piepho H.-P., Hochholdinger F. (2019) Transcriptomic reprogramming of barley seminal roots by combined water deficit and salt stress. BMC Genomics **20**:325.

Pasternak M., Lim B., Wirtz M., Hell R., Cobbett C.S., Meyer A.J. (2007) Restricting glutathione biosynthesis to the cytosol is sufficient for normal plant development: Compartmentation of glutathione biosynthesis. The Plant Journal **53**:999–1012.

Peltoniemi M.J., Karala A.-R., Jurvansuu J.K., Kinnula V.L., Ruddock L.W. (2006) Insights into deglutathionylation reactions. Journal of Biological Chemistry **281**:33107–33114.

Peñarrubia L., Moreno J. (1990) Increased susceptibility of ribulose-1,5-bisphosphate carboxylase/oxygenase to proteolytic degradation caused by oxidative treatments. Archives of Biochemistry and Biophysics **281**:319–323.

Poole L.B., Karplus P.A., Claiborne A. (2004) Protein sulfenic acids in redox signaling. Annual Review of Pharmacology and Toxicology **44**:325–347.

Puthiyaveetil S., Woodiwiss T., Knoerdel R., Zia A., Wood M., Hoehner R., Kirchhoff H. (2014) Significance of the photosystem II core phosphatase PBCP for plant viability and protein repair in thylakoid membranes. Plant and Cell Physiology **55**:1245–1254.

Rabenstein D.L., Millis K.K. (1995) Nuclear magnetic resonance study of the thioltransferase-catalyzed glutathione/glutathione disulfide interchange reaction. Biochimica et Biophysica Acta (BBA) - Protein Structure and Molecular Enzymology **1249**:29–36.

Rahantaniaina M.-S., Li S., Chatel-Innocenti G., Tuzet A., Issakidis-Bourguet E., Mhamdi A., Noctor G. (2017) Cytosolic and chloroplastic DHARs cooperate in oxidative stress-driven activation of the salicylic acid pathway. Plant Physiology **174**:956–971.

Rajeevkumar S., Anunanthini P., Sathishkumar R. (2015) Epigenetic silencing in transgenic plants. Frontiers in Plant Science **6**

Raven J.A. (2013) Rubisco: still the most abundant protein of Earth? New Phytologist **198**:1–3.

Reddie K.G., Carroll K.S. (2008) Expanding the functional diversity of proteins through cysteine oxidation. Current Opinion in Chemical Biology **12**:746–754.

Reichheld J.-P., Bashandy T., Siala W., Riondet C., Delorme V., Meyer A., Meyer Y. (2009) Redundancy and crosstalk Within the thioredoxin and glutathione pathways: A new development in plants. In: Botanical Research. Elsevier, pp 254–276.

Rensing S.A., Lang D., Zimmer A.D., Terry A., Salamov A., Shapiro H., Nishiyama T., Perroud P.-F., Lindquist E.A., Kamisugi Y., Tanahashi T., Sakakibara K., Fujita T., Oishi K., Shin-I T., Kuroki Y., Toyoda A., Suzuki Y., Hashimoto S.-I., Yamaguchi K., Sugano S., Kohara Y., Fujiyama A., Anterola A., Aoki S., Ashton N., Barbazuk W.B., Barker E., Bennetzen J.L., Blankenship R., Cho S.H., Dutcher S.K., Estelle M., Fawcett J.A., Gundlach H., Hanada

K., Heyl A., Hicks K.A., Hughes J., Lohr M., Mayer K., Melkozernov A., Murata T., Nelson D.R., Pils B., Prigge M., Reiss B., Renner T., Rombauts S., Rushton P.J., Sanderfoot A., Schween G., Shiu S.-H., Stueber K., Theodoulou F.L., Tu H., Van de Peer Y., Verrier P.J., Waters E., Wood A., Yang L., Cove D., Cuming A.C., Hasebe M., Lucas S., Mishler B.D., Reski R., Grigoriev I.V., Quatrano R.S., Boore J.L. (2008) The Physcomitrella genome reveals evolutionary insights into the conquest of land by plants. Science (New York, NY) **319**:64–69.

Reski R., Abel W.O. (1985) Induction of budding on chloronemata and caulonemata of the moss, *Physcomitrella patens*, using isopentenyladenine. Planta **165**:354–358.

Rey P., Bécuwe N., Barrault M.-B., Rumeau D., Havaux M., Biteau B., Toledano M.B. (2007) The *Arabidopsis thaliana* sulfiredoxin is a plastidic cysteine-sulfinic acid reductase involved in the photooxidative stress response: Reduction of overoxidized peroxiredoxin by sulfiredoxin. The Plant Journal **49**:505–514.

Rey P., Tarrago L. (2018a) Physiological Roles of Plant Methionine Sulfoxide Reductases in Redox Homeostasis and Signaling. Antioxidants **7**:114.

Rey P., Tarrago L. (2018b) Physiological roles of plant methionine sulfoxide reductases in redox homeostasis and signaling. Antioxidants **7**:114.

Riondet C., Desouris J.P., Montoya J.G., Chartier Y., Meyer Y., Reichheld J.-P. (2012) A dicotyledon-specific glutaredoxin GRXC1 family with dimer-dependent redox regulation is functionally redundant with GRXC2: A dicotyledon-specific glutaredoxin. Plant, Cell & Environment **35**:360–373.

Romero-Puertas M.C., Laxa M., Mattè A., Zaninotto F., Finkemeier I., Jones A.M.E., Perazzolli M., Vandelle E., Dietz K.-J., Delledonne M. (2008) S-nitrosylation of peroxiredoxin II E promotes peroxynitrite-mediated tyrosine nitration. The Plant Cell **19**:4120–4130.

Roni Md.S., Sakil Md.A., Aktar M.M., Takatsuka C., Mukae K., Inoue-Aono Y., Moriyasu Y. (2022) Hydrogen peroxide mediates premature senescence caused by darkness and inorganic nitrogen starvation in *Physcomitrium patens*. Plants **11**:2280.

Ronquist F., Huelsenbeck J.P. (2003) MrBayes 3: Bayesian phylogenetic inference under mixed models. Bioinformatics **19**:1572–1574.

Roret T., Zhang B., Moseler A., Dhalleine T., Gao X.-H., Couturier J., Lemaire S.D., Didierjean C., Johnson M.K., Rouhier N. (2021) Atypical iron-sulfur cluster binding, redox activity and structural properties of *Chlamydomonas reinhardtii* glutaredoxin 2. Antioxidants **10**:803.

Rouhier N. (2010) Plant glutaredoxins: pivotal players in redox biology and iron–sulphur centre assembly. New Phytologist **186**:365–372.

Rouhier N., Gelhaye E., Jacquot J.-P. (2002) Exploring the active site of plant glutaredoxin by site-directed mutagenesis. FEBS Letters **511**:145–149.

Rouhier N., Lemaire S.D., Jacquot J.-P. (2008) The role of glutathione in photosynthetic organisms: Emerging functions for glutaredoxins and glutathionylation. Annual Review of Plant Biology **59**:143–166.

Rouhier N., Unno H., Bandyopadhyay S., Masip L., Kim S.-K., Hirasawa M., Gualberto J.M., Lattard V., Kusunoki M., Knaff D.B., Georgiou G., Hase T., Johnson M.K., Jacquot J.-P. (2007) Functional, structural, and spectroscopic characterization of a glutathione-ligated [2Fe–2S] cluster in poplar glutaredoxin C1. Proceedings of the National Academy of Sciences **104**:7379–7384.

Rouhier N., Villarejo A., Srivastava M., Gelhaye E., Keech O., Droux M., Finkemeier I., Samuelsson G., Dietz K.J., Jacquot J.-P., Wingsle G. (2005) Identification of plant glutaredoxin targets. Antioxidants & Redox Signaling **7**:919–929.

Schaefer D.G., Zryd J.-P. (1997) Efficient gene targeting in the moss *Physcomitrella patens*. The Plant Journal **11**:1195–1206.

Schafer F.Q., Buettner G.R. (2001) Redox environment of the cell as viewed through the redox state of the glutathione disulfide/glutathione couple. Free Radical Biology and Medicine **30**:1191–1212.

Schneider C.A., Rasband W.S., Eliceiri K.W. (2012) NIH Image to ImageJ: 25 years of image analysis. Nature Methods **9**:671–675.

Schubert D., Lechtenberg B., Forsbach A., Gils M., Bahadur S., Schmidt R. (2004) Silencing in Arabidopsis T-DNA transformants: The predominant role of a gene-specific RNA sensing mechanism versus position effects. The Plant Cell **16**:2561–2572.

Schürmann P., Jacquot J.-P. (2000) Plant thioredoxin systems revisited. Annual Review of Plant Physiology and Plant Molecular Biology **51**:371–400.

Schurmann P., Maeda K., Tsugita A. (1981) Isomers in thioredoxins of spinach chloroplasts. European Journal of Biochemistry **116**:37–45.

Schwarzländer M., Dick T.P., Meyer A.J., Morgan B. (2016) Dissecting redox biology using fluorescent protein sensors. Antioxidants & Redox Signaling **24**:680–712.

Schwarzländer M., Fricker M.D., MüLler C., Marty L., Brach T., Novak J., Sweetlove L.J., Hell R., Meyer A.J. (2008) Confocal imaging of glutathione redox potential in living plant cells. Journal of Microscopy **231**:299–316.

Schwarzländer M., Fricker M.D., Sweetlove L.J. (2009) Monitoring the *in vivo* redox state of plant mitochondria: Effect of respiratory inhibitors, abiotic stress and assessment of recovery from oxidative challenge. Biochimica et Biophysica Acta (BBA) - Bioenergetics **1787**:468–475.

Sessions A.L., Doughty D.M., Welander P.V., Summons R.E., Newman D.K. (2009) The continuing puzzle of the great oxidation event. Current Biology **19**:R567–R574.

Sharma S.S., Dietz K.-J. (2009) The relationship between metal toxicity and cellular redox imbalance. Trends in Plant Science **14**:43–50.

Sirover M.A. (2011) On the functional diversity of glyceraldehyde-3-phosphate dehydrogenase: Biochemical mechanisms and regulatory control. Biochimica et Biophysica Acta (BBA) - General Subjects **1810**:741–751.

Sirover M.A. (2012) Subcellular dynamics of multifunctional protein regulation: Mechanisms of GAPDH intracellular translocation. Journal of Cellular Biochemistry **113**:2193–2200.

Soulie J.-M., Meunier J.-C., Pradel J., Ricard J. (1981) Molecular properties of chloroplastic thioredoxin f and the photoregulation of the activity of fructose 1,6-bisphosphatase. European Journal of Biochemistry **119**:497–502.

Spaniol B., Lang J., Venn B., Schake L., Sommer F., Mustas M., Geimer S., Wollman F.-A., Choquet Y., Mühlhaus T., Schroda M. (2022) Complexome profiling on the Chlamydomonas *lpa2* mutant reveals insights into PSII biogenesis and new PSII associated proteins (H. Griffiths, Ed.). Journal of Experimental Botany **73**:245–262.

Sparla F., Pupillo P., Trost P. (2002) The C-terminal extension of glyceraldehyde-3-phosphate dehydrogenase subunit B acts as an autoinhibitory domain regulated by thioredoxins and nicotinamide adenine dinucleotide. Journal of Biological Chemistry **277**:44946–44952.

Sugiura K., Yokochi Y., Fu N., Fukaya Y., Yoshida K., Mihara S., Hisabori T. (2019) The thioredoxin (Trx) redox state sensor protein can visualize Trx activities in the light/dark response in chloroplasts. Journal of Biological Chemistry **294**:12091–12098.

Taiz L., Zeiger E., Møller I.M., Murphy A.S. (2015) *Plant physiology and development*, Sixth edition. Sinauer Associates, Inc., Publishers, Sunderland, Massachusetts.

Tenaud M., Jacquot J.P. (1987) In vitro Thiol-dependent Redox Regulation of Purified Ribulose-1,5-bisphosphate Carboxylase. Journal of Plant Physiology **130**:315–326.

The Arabidopsis Genome Initiative (2000) Analysis of the genome sequence of the flowering plant *Arabidopsis thaliana*. Nature **408**:796–815.

The International Brachypodium Initiative (2010) Genome sequencing and analysis of the model grass *Brachypodium distachyon* . Nature **463**:763–768.

Trifinopoulos J., Nguyen L.-T., von Haeseler A., Minh B.Q. (2016) W-IQ-TREE: A fast online phylogenetic tool for maximum likelihood analysis. Nucleic Acids Research **44**:W232–W235.

Trnka D., Engelke A.D., Gellert M., Moseler A., Hossain M.F., Lindenberg T.T., Pedroletti L., Odermatt B., de Souza J.V., Bronowska A.K., Dick T.P., Mühlenhoff U., Meyer A.J., Berndt C., Lillig C.H. (2020) Molecular basis for the distinct functions of redox-active and FeS-transfering glutaredoxins. Nature Communications **11**:3445.

Turell L., Botti H., Carballal S., Ferrer-Sueta G., Souza J.M., Durán R., Freeman B.A., Radi R., Alvarez B. (2008) Reactivity of sulfenic acid in human serum albumin. Biochemistry **47**:358–367.

Tzafrir I., Pena-Muralla R., Dickerman A., Berg M., Rogers R., Hutchens S., Sweeney T.C., McElver J., Aux G., Patton D., Meinke D. (2004) Identification of genes required for embryo development in Arabidopsis. Plant Physiology **135**:1206–1220.

Ugalde J.M., Fecker L., Schwarzländer M., Müller-Schüssele S.J., Meyer A.J. (2022) Live monitoring of ROS-induced cytosolic redox changes with roGFP2-based sensors in plants. In: Mhamdi A (ed) Reactive Oxygen Species in Plants. Springer US, New York, NY, pp 65–85.

Ugalde J.M., Fuchs P., Nietzel T., Cutolo E.A., Homagk M., Vothknecht U.C., Holuigue L., Schwarzländer M., Müller-Schüssele S.J., Meyer A.J. (2021) Chloroplast-derived photo-oxidative stress causes changes in H_2O_2 and E_{GSH} in other subcellular compartments. Plant Physiology **186**:125–141.

Ugalde J.M., Lamig L., Herrera-Vásquez A., Fuchs P., Homagk M., Kopriva S., Müller-Schüssele S.J., Holuigue L., Meyer A.J. (2021) A dual role for glutathione transferase U7 in plant growth and protection from methyl viologen-induced oxidative stress. Plant Physiology **187**:2451–2468.

Ugalde J.M., Schlößer M., Dongois A., Martinière A., Meyer A.J. (2021) The latest HyPe(r) in plant H_2O_2 biosensing. Plant Physiology **187**:480–484.

Vaseghi M.-J., Chibani K., Telman W., Liebthal M.F., Gerken M., Schnitzer H., Mueller S.M., Dietz K.-J. (2018) The chloroplast 2-cysteine peroxiredoxin functions as thioredoxin oxidase in redox regulation of chloroplast metabolism. eLife **7**:e38194.

Vernoux T., Wilson R.C., Seeley K.A., Reichheld J.-P., Muroy S., Brown S., Maughan S.C., Cobbett C.S., Van Montagu M., Inzé D., May M.J., Sung Z.R. (2000) The *ROOT MERISTEMLESS1* / *CADMIUM SENSITIVE2* gene defines a glutathione-dependent pathway involved in initiation and maintenance of cell division during postembryonic root development. The Plant Cell **12**:97–109.

Vescovi M., Zaffagnini M., Festa M., Trost P., Lo Schiavo F., Costa A. (2013) Nuclear accumulation of cytosolic glyceraldehyde-3-phosphate dehydrogenase in cadmium-stressed arabidopsis roots. Plant Physiology **162**:333–346.

Vlamis-Gardikas A., Holmgren A. (2002) Thioredoxin and glutaredoxin isoforms. In: Methods in Enzymology. Elsevier, pp 286–296.

Wachter A., Wolf S., Steininger H., Bogs J., Rausch T. (2004) Differential targeting of GSH1 and GSH2 is achieved by multiple transcription initiation: implications for the compartmentation of glutathione biosynthesis in the Brassicaceae: Differential targeting of GSH1 and GSH2. The Plant Journal **41**:15–30.

Wagner S., Steinbeck J., Fuchs P., Lichtenauer S., Elsässer M., Schippers J.H.M., Nietzel T., Ruberti C., Van Aken O., Meyer A.J., Van Dongen J.T., Schmidt R.R., Schwarzländer M. (2019) Multiparametric real-time sensing of cytosolic physiology links hypoxia responses to mitochondrial electron transport. New Phytologist **224**:1668–1684.

Winterbourn C.C., Metodiewa D. (1999) Reactivity of biologically important thiol compounds with superoxide and hydrogen peroxide. Free Radical Biology and Medicine **27**:322–328.

Wirtz M., Hell R. (2003) Production of cysteine for bacterial and plant biotechnology: application of cysteine feedback-insensitive isoforms of serine acetyltransferase. Amino Acids **24**:195–203.

Wolosiuk R.A., Buchanan B.B. (1977) Thioredoxin and glutathione regulate photosynthesis in chloroplasts. Nature **266**:565–567.

Yoshida K., Hara A., Sugiura K., Fukaya Y., Hisabori T. (2018) Thioredoxin-like2/2-Cys peroxiredoxin redox cascade supports oxidative thiol modulation in chloroplasts. Proceedings of the National Academy of Sciences **115**

Yu X., Pasternak T., Eiblmeier M., Ditengou F., Kochersperger P., Sun J., Wang H., Rennenberg H., Teale W., Paponov I., Zhou W., Li C., Li X., Palme K. (2013) Plastid-Localized Glutathione Reductase2-regulated glutathione redox status is essential for Arabidopsis root apical meristem maintenance. The Plant Cell **25**:4451–4468.

Zaffagnini M., Bedhomme M., Groni H., Marchand C.H., Puppo C., Gontero B., Cassier-Chauvat C., Decottignies P., Lemaire S.D. (2012) Glutathionylation in the photosynthetic model organism *Chlamydomonas reinhardtii*: A proteomic survey. Molecular & Cellular Proteomics **11**:M111.014142.

Zaffagnini M., Bedhomme M., Marchand C.H., Couturier J., Gao X.-H., Rouhier N., Trost P., Lemaire S.D. (2012) Glutaredoxin S12: Unique properties for redox signaling. Antioxidants & Redox Signaling **16**:17–32.

Zaffagnini M., Bedhomme M., Marchand C.H., Morisse S., Trost P., Lemaire S.D. (2012) Redox regulation in photosynthetic organisms: Focus on glutathionylation. Antioxidants & Redox Signaling **16**:567–586.

Zaffagnini M., Fermani S., Costa A., Lemaire S.D., Trost P. (2013) Plant cytoplasmic GAPDH: Redox post-translational modifications and moonlighting properties. Frontiers in Plant Science **4**

Zaffagnini M., Fermani S., Marchand C.H., Costa A., Sparla F., Rouhier N., Geigenberger P., Lemaire S.D., Trost P. (2019) Redox homeostasis in photosynthetic organisms: Novel and established thiol-based molecular mechanisms. Antioxidants & Redox Signaling **31**:155–210.

Zaffagnini M., Marchand C.H., Malferrari M., Murail S., Bonacchi S., Genovese D., Montalti M., Venturoli G., Falini G., Baaden M., Lemaire S.D., Fermani S., Trost P. (2019) Glutathionylation primes soluble glyceraldehyde-3-phosphate dehydrogenase for late collapse into insoluble aggregates. Proceedings of the National Academy of Sciences **116**:26057–26065.

Zaffagnini M., Michelet L., Marchand C., Sparla F., Decottignies P., Le Maréchal P., Miginiac-Maslow M., Noctor G., Trost P., Lemaire S.D. (2007) The thioredoxin-independent

isoform of chloroplastic glyceraldehyde-3-phosphate dehydrogenase is selectively regulated by glutathionylation. The FEBS journal **274**:212–226.

Zimmermann J., Oestreicher J., Hess S., Herrmann J.M., Deponte M., Morgan B. (2020) One cysteine is enough: A monothiol GRX can functionally replace all cytosolic TRX and dithiol GRX. Redox Biology **36**:101598.

APPENDIX

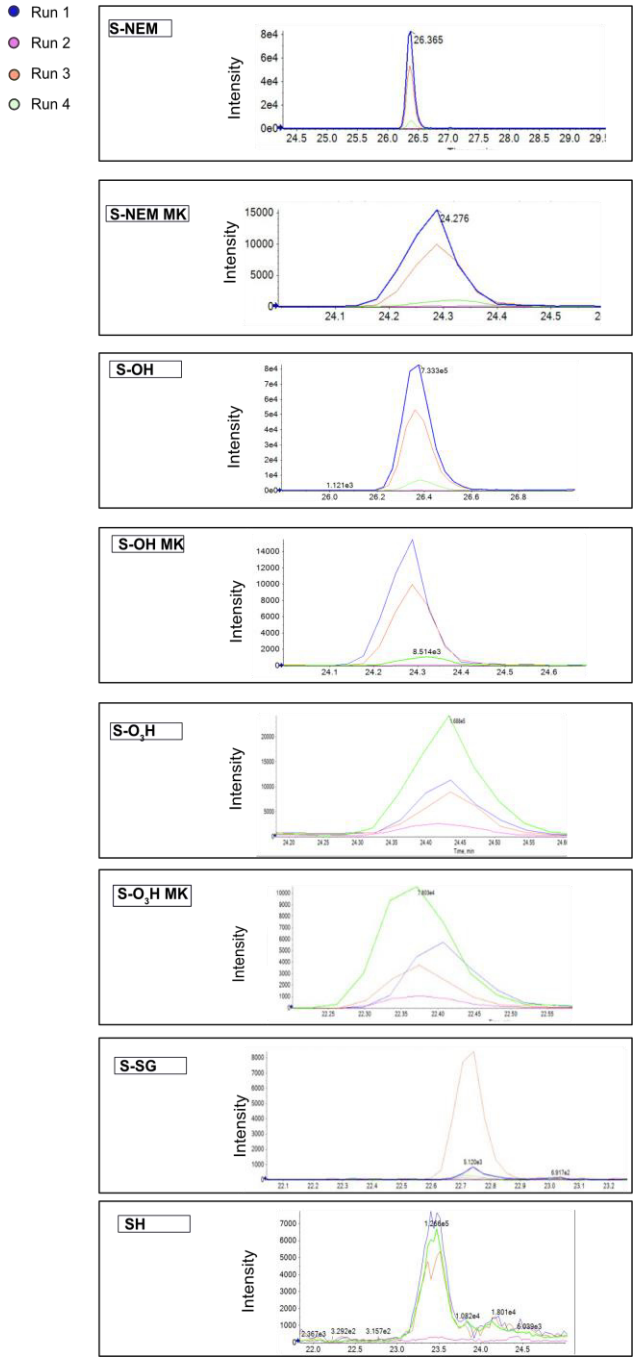

Supplemental Figure 1 Intensity peaks of MS/MS runs 1,2,3,4 divided by detected cysteine modifications.

Peaks of intensity of each modification detected in the MS/MS in the peptide sequence of roGFP2-C204S LEYNYNCHNVYIMADK and LEYNYNCHNVYIMADKQK (missed lysin (K) cleavage (MK)) are shown for all the modification (SNEM, SOH, SO_3H, SSG ,SH) detected in the Runs. In each graph, Run 1 (blue) contains the sample of roGFP2-C204S treated with DTT. run 2 (pink) contained the upper band of roGFP2-C204S treated with H_2O_2, run 3 (orange) contains the band of roGFP2_c204S treated with 40 µM GSSG and 1 µM GRXC1, run 4 (green) contains the lower band of roGFP2-C204S treated with H_2O_2. X-axis shows the time, y-axis shows the intensity detected.

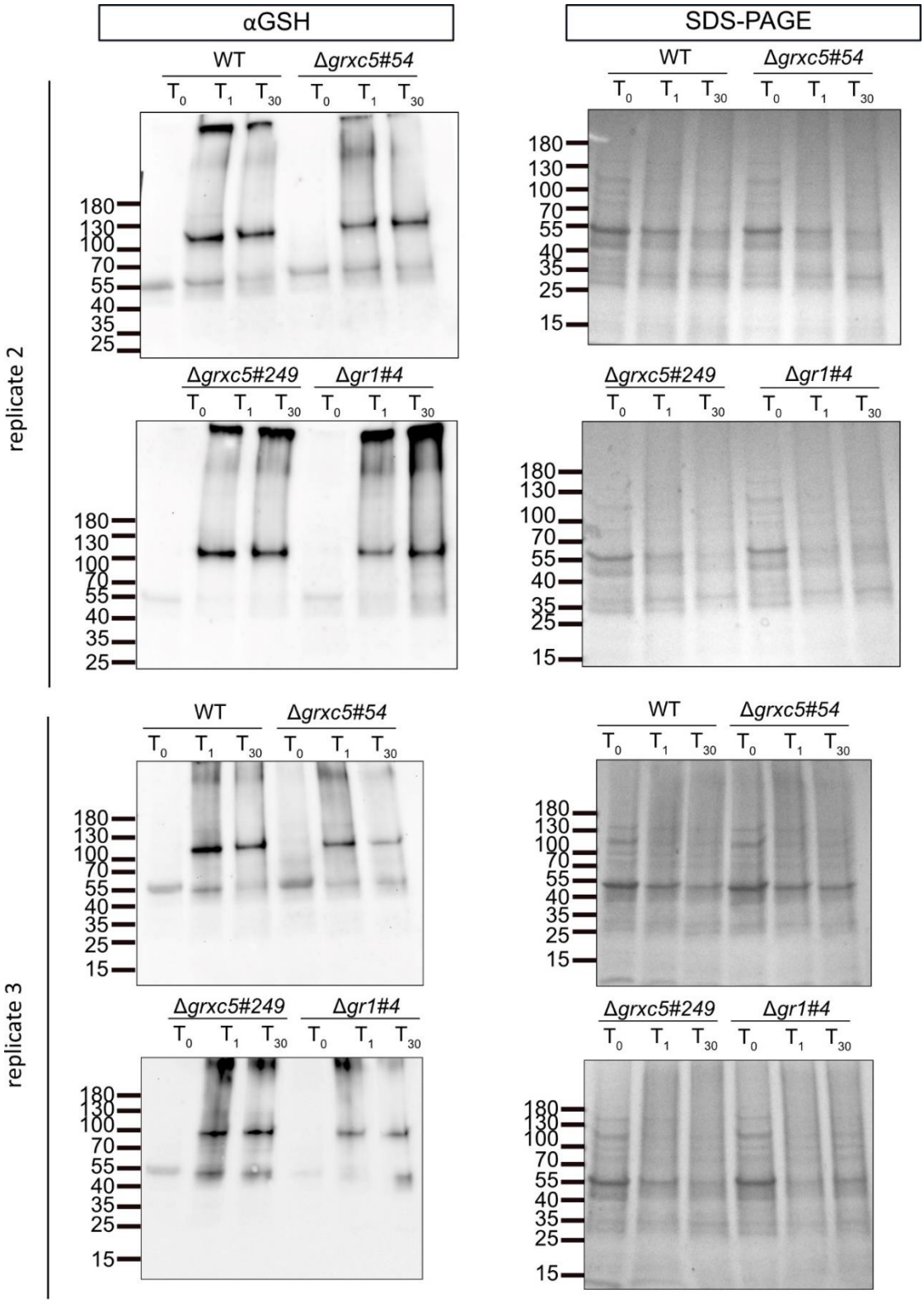

Supplemental Figure 2: Detection of glutathionylated proteins (αGSH) in protonema extract treated with H_2O_2

immunoblots with αGSH (ThermoFisher) of proteins extracted from *P. patens* protonema tissue treated with 10 mM H_2O_2 and harvested at different time points (T_0, T_1, T_{30}). Proteins were extracted in the presence of 20 mM NEM and 10 µg total protein was loaded onto a 4-20% gradient SDS-PAGE as loading control.

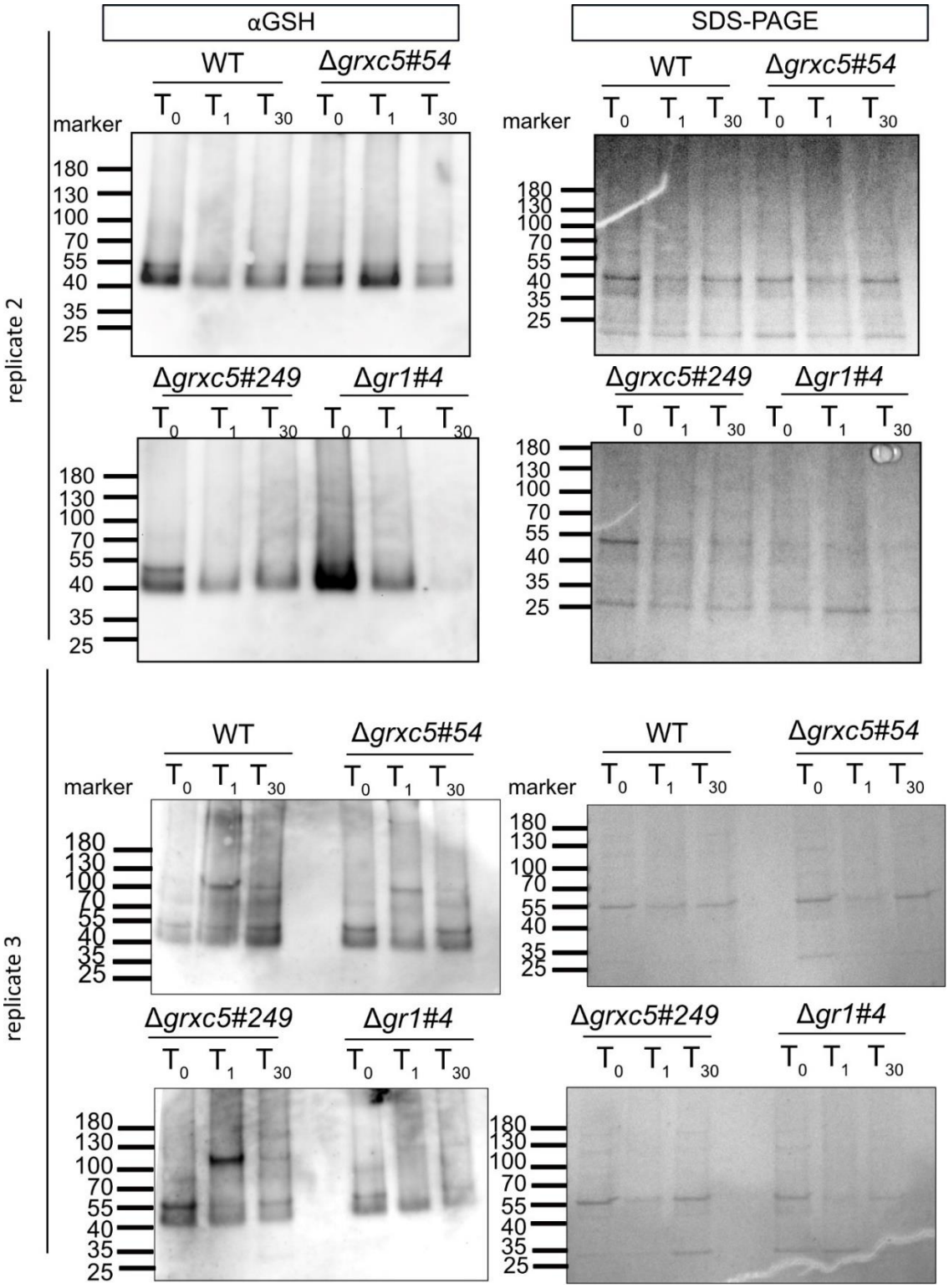

Supplemental Figure 3: Detection of glutathionylated proteins in gametophore extract treated with H_2O_2 in falcon tubes

Western blot of glutathionylated proteins extracted from *P. patens* gametophore tissue treated with 10 mM H_2O_2 and harvested at different time points (T_0, T_1, T_{30}). Proteins were extracted in the presence of 20 mM NEM and 5 µg total protein was loaded onto a 4-20% gradient SDS-PAGE as loading control.

ABBREVIATIONS

A	assimilation rate
ΔA	change of assimilation rate over time
ANOVA	analysis of variance
At	*Arabidopsis thaliana*
App	apparent
β-ME	β-mercaptoethanol
c	concentration
Cad	cadmium
CaMV35S	cauliflower mosaic virus 35S promoter
cDNA	complementary DNA
CLSM	confocal laser scanning microscopy
Col-0	Colombia zero
Cys	cysteine
δ	dynamic range
DPS	2,2'-dipyridyldisulfide
DTT	1,4-dithiothreitol
$E^{0'}$	midpoint potential
E_{GSH}	glutathione redox potential
EtOH	ethanol
FTR	ferredoxin dependent thioredoxin reductase
GFP	green fluorescent protein
GR	glutathione reductase
GRX	glutaredoxin
GSH	reduced glutathione
GSSG	glutathione disulfide
H_2O_2	hydrogen peroxide
HED	bis(2-hydroxyethyl)disulfide
I	intensity
kDa	kilo Dalton

k_{cat}	rate constant
K_m	Michaelis constant
MeOH	methanol
MPEG-Mal	Methoxy polyethylene glycol maleimide
n	sample size
NADPH	nicotinamide adenine dinucleotide phosphate
ns	non significant
NEM	*N*-ethylmaleimide
NPQ	non-photochemical quenching
NTR	NADPH-dependent thioredoxin reductase
OD	optical density
Ox	oxidized
OxD	oxidation degree
p	probability value
PAR	photosynthetically active radiation
pKa	-log10 of the acid dissociation constant
Pp	*Physcomitrium patens*
PRX	peroxiredoxin
RBCL	RuBisCO large subunit
roGFP2	reduction-oxidation sensitive GFP2
ROS	reactive oxygen species
TCEP	tris(2-carboxyethyl)phosphine
TKTP	transketolase targeting peptide
Tris	2-amino-2-(hydroxymethyl)propane-1,3-diol
TRX	thioredoxin
WT	wild type
v/v	volume per volume
w/v	weight per volume
YFP	yellow fluorescent protein

LIST OF FIGURES

LIST OF TABLES

ATTACHED PUBLICATIONS

Bohle F, Meyer AJ, Mueller-Schüssele SJ. Quantification of redox-sensitive GFP cysteine redox state via gel-based read-out. Methods Mol Biol. 2023;2564:259-268. doi: 10.1007/978-1-0716-2667-2_13. PMID: 36107347

Reproduced with permission from Springer Nature.

Chapter 13

Quantification of Redox-Sensitive GFP Cysteine Redox State via Gel-Based Read-Out

Finja Bohle, Andreas J. Meyer, and Stefanie J. Mueller-Schuessele

Abstract

To date, fluorescent protein biosensors are widely used in research. In vivo, they can be applied to dynamically monitor several physiological parameters in various subcellular compartments. Redox-sensitive green fluorescent protein 2 (roGFP2) senses the glutathione redox potential via a disulfide bridge formed between neighboring beta-strands of its beta-barrel structure. As changes in redox state affect both excitation maxima of roGFP2 oppositely, sensor responses are ratiometric. The reaction mechanism of roGFP2 is well characterized and involves an intermediate *S*-glutathionylation step. Thus, roGFP2 is also used in enzymatic in vitro assays, e.g., assessing glutaredoxin kinetics. In addition to the fluorescent read-out, the roGFP2 redox state can also be determined by differential migration on a non-reducing SDS-PAGE. This read-out mode may be beneficial in some applications, e.g., if mass-spectrometric analysis of posttranslational cysteine modifications is desired. Here, we describe a protocol for gel-based fluorescent read-out of the roGFP2 redox state, as well as modification of free cysteines by maleimide-based reagents.

Key words Fluorescent biosensor, Redox-sensitive GFP, Cysteine modification, *S*-glutathionylation, MPEG-Mal

1 Introduction

Redox-sensitive green fluorescent protein (roGFP)-based biosensors constitute a family of fluorescent proteins that sense redox dynamics via redox-dependent changes of their excitation spectrum [1–4]. Based on optical and biophysical properties, the variant roGFP2 has developed into the most frequently used roGFP [5–7]. As the absorption of light changes in opposite directions below and above the isosbestic point of the excitation spectrum (c. 425 nm for roGFP2 [2]), the sensor redox state can be read out ratiometrically by quantifying green fluorescence intensities occurring after excitation with UV light compared to blue light (e.g., the 405/488 nm ratio when using laser excitation [8]). On the molecular level, changes in absorption are caused by ionization shifts of the chromophore in response to structural constraints on

Mayank Sharma (ed.), *Fluorescent Proteins: Methods and Protocols*, Methods in Molecular Biology, vol. 2564,
https://doi.org/10.1007/978-1-0716-2667-2_13,
© The Author(s), under exclusive license to Springer Science+Business Media, LLC, part of Springer Nature 2023

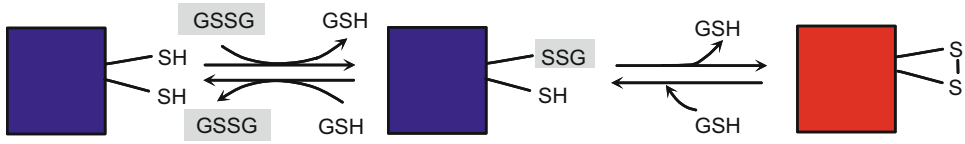

Fig. 1 Schematic overview of roGFP2 oxidation/reduction via *S*-glutathionylation. The thiol group (-SH) of Cys147 in roGFP2 can be *S*-glutathionylated (-SSG) upon reaction of the thiolate anion (S^-) with oxidized glutathione (glutathione disulfide, GSSG). This *S*-glutathionylation on Cys147 is effectively resolved by the thiol group of Cys204 from the neighboring beta-strand, resulting in a disulfide bridge between Cys204 and Cys147. This disulfide formation results in changes of the absorption properties of the chromophore

the protein beta-barrel. These redox-dependent structural constraints are created by formation and reduction of a disulfide bridge between two neighboring beta-strands on the outer surface of the beta-barrel [1] (for review, *see* [7]).

Further investigations of roGFP2 properties have shown that disulfide formation occurs via an *S*-glutathionylation intermediate (*see* Fig. 1) and that roGFP2 equilibrates with the glutathione redox potential (E_{GSH}) (for review, *see* [9, 10]). This equilibration can be kinetically accelerated by the action of class I glutaredoxins (GRX), small thiol oxidases that mediate protein (de)glutathionylation [11, 12]. The linear response of roGFP2 is limited to approximately +/− 30 mV around its midpoint potential with a consensus value of −280 mV (for review, *see* [7]). As a protein biosensor, roGFP2 was consequently used to reveal the E_{GSH} dynamics of various cell compartments in vivo using confocal microscopy set-ups or parallel multiplexing in fluorescence plate-reader set-ups [5, 6, 13, 14]. For detailed protocols regarding in vivo experiments using roGFP2-based redox sensors, please *see* [8].

Many redox relays occurring in vivo can be recreated in vitro with purified proteins and buffer solutions with specific redox potentials. Thus, roGFP2 has also been used in biochemical assays, e.g., to characterize GRX properties [11, 15, 16]. As the oxidation state of roGFP2 can be monitored and quantified via changes of its ratiometric fluorescence read-out, reaction kinetics can be followed in real-time using a fluorescence plate reader-based set-up. Figure 2 shows an oxidation assay where reduced roGFP2 is oxidized in the presence of a class I GRX after addition of GSSG or in a GSH/GSSG buffer with a specific E_{GSH}. For the demonstrative purpose, an E_{GSH} near the midpoint potential of roGFP2 was chosen, resulting in 50% oxidation and 50% reduction of the sensor.

Some applications, such as further analysis via mass spectrometry, may require a gel-based read-out of roGFP2 redox state. This is feasible, as the migration behavior of the reduced and oxidized sensors differs in non-reducing SDS-PAGE (sodium dodecyl-sulfate polyacrylamide gel electrophoresis).

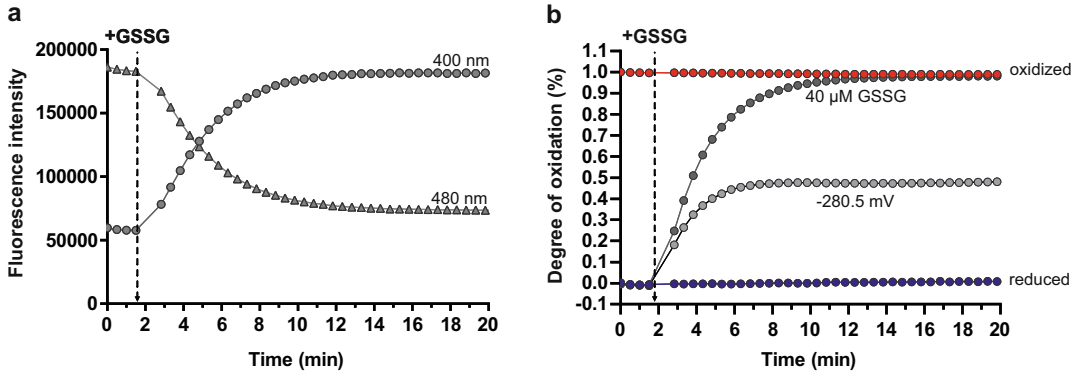

Fig. 2 Oxidation assay of roGFP2 with 40 µM GSSG. (**a**) 1 µM of pre-reduced roGFP2 was oxidized with 40 µM GSSG and the fluorescence intensity was followed at 520–10 nm after excitation with 400–10 nm (circle) and 480–16 nm (triangle) using the CLARIOstar plate-reader (BMG). Fluorescence after excitation at 400 nm increases while fluorescence after excitation at 480 nm decreases, leading to an increase of the 400/480 ratio. (**b**) 1 µM roGFP2 was oxidized with 10 mM H_2O_2 (red circle) or reduced with 10 mM DTT (blue circle). After reduction, roGFP2 was treated with 40 µM GSSG and 1 µM *At*GRXC1 (dark grey) or 6.6 mM GSH and 0.04 µM GSSG (redox potential of −280.5 mV) and 1 µM *At*GRXC1 (light grey). Individual fluorescence intensities were followed, the ratio after excitation at 400 and 480 nm calculated and transformed into the degree of roGFP2 oxidation (%) (for review, *see* [7])

This chapter gives an example of the gel-based read-out of the redox state of roGFP2, including the modification of reduced cysteines with either NEM or MPEG-Maleimide (MPEG-Mal). We further detail how a roGFP2 assay with a specific redox potential of the buffer can be realized. These methods can also be transferred to other roGFP variants.

2 Materials

2.1 Affinity-Purified Proteins

For appropriate protocols for protein purification, *see*, e.g., [17].

1. roGFP2 [1].
2. *At*GRXC1 (At5g63030) or other class I glutaredoxin [9, 12].

2.2 Prereduction or Oxidation of Purified roGFP2

1. Zeba™ spin-desalting columns, molecular weight cutoff 7 kDa, 0.5 mL.
2. KPE buffer 1: 100 mM potassium phosphate buffer, pH 7.4, 0.5 mM ethylenediaminetetraacetic acid (EDTA).
3. 100 µL of 20 µM roGFP2 in KPE buffer 1.
4. 1 M dithiothreitol (DTT) stock in KPE buffer 1.
5. 1 M hydrogen peroxide (H_2O_2) stock in KPE buffer 1 (*see* **Note 1**).

2.3 Glutathionylation of roGPF2 Using GSH/GSSG Buffers with a Specific E_{GSH}

For a glutathione redox potential (E_{GSH}) of −280 mV at pH 7.4 (*see* **Note 2**):

1. KP buffer 2: 200 mM potassium phosphate buffer, pH 7.4.
2. 160 mM reduced glutathione (GSH) stock in KP buffer 2 (*see* **Note 3**).
3. 10 mM glutathione disulfide (GSSG) stock in KP buffer 2.
4. 10 μM class I glutaredoxin, e.g., *Arabidopsis thaliana* GRXC1 in KPE buffer 1 (*see* **Note 4**).

2.4 Labelling of Reduced Thiol Groups

1. 100 mM *N*-ethylmaleimide (NEM) stock in KPE buffer 1.
2. 20 mM methoxypolyethylene glycol maleimide 5000 (MPEG-Mal; PEG average M_n 5000, Sigma-Aldrich CAS: 99126-64-4) in KPE buffer 1.

2.5 SDS-Polyacrylamide Gel Components and Gel Imaging

1. 5× non-reducing loading buffer: 10% sodium dodecyl sulfate (SDS), 50% glycerol, 0.02% bromophenol blue, and 0.3125 M Tris–HCl, pH 6.8.
2. 10× SDS running buffer: 30.0 g of Tris–HCl, 144 g of glycine, 10 g of SDS, volume adjust to 1 L with H_2O.
3. E.g., Mini-PROTEAN TGX precast gel, 10% (Bio-Rad).
4. E.g., PageRuler™ prestained protein ladder, 10 to 180 kDa.
5. UV light table or fluorescence imager.
6. ImageJ Software (version 1.53n7 was used here).

3 Methods

3.1 Preparation of Protein Solutions

1. Determine protein amount of affinity-purified proteins, e.g., by Bradford assay (*see* **Note 5**).
2. Dilute roGFP2 in KPE buffer 1 to 20 μM in 99 μL.
3. Dilute *At*GRXC1 in KPE buffer 1 to 10 μM in 100 μL.

3.2 Prereduction or Oxidation of Purified roGFP2

1. For complete sensor reduction, add 1 μL 1 M DTT (final c = 10 mM) to 99 μL of 20 μM roGFP2 to obtain a final volume of 100 μL. Alternatively, a final concentration of 10 mM tris(2-carboxyethyl)phosphine (TCEP) can be used. Incubate for 30 min at room temperature.
2. For complete sensor oxidation, add 1 μL 1 M H_2O_2 (final c = 10 mM) to 99 μL of 20 μM roGFP2 to obtain a final volume of 100 μL. Incubate for 30 min at room temperature.
3. Use Zeba™ spin-desalting columns to remove DTT, TCEP, or H_2O_2 from the samples according to the user manual. After desalting, use KPE buffer 1 and a volume of 100 μL to

re-buffer your protein. Proceed immediately with the next steps to minimize reoxidation of the pre-reduced roGFP2.

3.3 Equilibration of GSH:GSSG Redox Buffer to a Redox Potential of −280.5 mV

1. For calculation of a specific redox potential, e.g., −280.5 mV (*see* **Note 6**), use the Nernst equation (Eq. 1) with R = 8.315 J K^{-1} mol^{-1}, T = 298.15 K, z = 2, F = 96.485 C mol^{-1} (= 96,485 J V^{-1} mol^{-1}), and E_0' = −240 mV at pH 7 [6]. For KPE buffer 1 with a pH of 7.4, the pH-adjusted redox potential of glutathione (E_0'^{pH}) would be equal to −251.8 mV following Eq. 2 [1, 5]

$$E_{GSH} = E_0'^{pH} - \frac{2.303RT}{zF} \log_{10} \frac{[GSH]^2}{[GSSG]}, \quad (1)$$

$$E_0'^{pH} = E_0' - 29.5\,mV \times (pH - 7), \quad (2)$$

2. To determine the concentration of GSH and GSSG to adjust a specific E_{GSH}, Eq. 1 is modified and solved by inserting the concentration of GSSG (use unit M) from which the concentration of GSH can be calculated:

$$-280.5\,mV = -251\,mV - \frac{2.303RT}{zF} \log_{10} \frac{[GSH]^2}{[GSSG]}$$

$$-280.5\,mV = -251\,mV - 29.5\,mV \times \log_{10} \frac{[GSH]^2}{[GSSG]}$$

$$-29.5\,mV = -29.5\,mV \times \log_{10} \frac{[GSH]^2}{[GSSG]}$$

$$\log_{10} \frac{[GSH]^2}{[GSSG]} = 1$$

$$10 = \frac{[GSH]^2}{[GSSG]}$$

$$[GSH] = \sqrt{10 * [GSSG]}$$

3. Various concentrations are possible for a specific E_{GSH}, resulting in different ratios of GSH to GSSG, and a different total amount of glutathione in the buffer (*see* **Note 7**) (Table 1).

Table 1
Example concentrations of GSSG and GSH to adjust a GSH/GSSG mixture to −280.5 mV

If [GSSG] is set to	GSH concentration is calculated according to [GSSG]
0.0004 M	0.063 M
0.0000399 M	0.0199 M
0.0000044 M	0.0066633 M

3.4 In Vitro Treatment of roGFP2 to Modify Free Cysteines

1. Add 25 μL of 20 μM reduced and desalted roGFP2 to 75 μL of KPE buffer 1 for the fully reduced control. Add 25 μL of 20 μM oxidized and desalted roGFP2 to 75 μL of KPE buffer 1 for the fully oxidized control. Mix by pipetting up and down. The final volume is 100 μL.
2. The pipetting order of the assay samples should be in the following order: start with preparing the buffer, add the glutathione solutions, add the GRX, and as a final step, add roGFP2, so that the starting point of the assay is kept as simultaneous as possible.
3. For an assay reaching 100% roGFP2 oxidation (*see* Fig. 2), add 10 μL of 0.4 mM GSSG to 10 μL of 10μM *At*GRXC1 (final concentration = 1 μM). Add KPE buffer 1 until a volume of 75 μL is reached.
4. Mix 13.32 μL of 50 mM GSH with 4.4 μL of 0.1 mM GSSG to obtain a redox potential of −280.5 mV (*see* Fig. 2). Add 10 μl of 10 μM *At*GRXC1 (final concentration of 1 μM). Add KPE buffer 1 until a total volume of 75 μL is reached.
5. Add 25 μL of reduced and desalted roGFP2 (5 μM final concentration) to all assay samples, reaching the final volume of 100 μL per sample. Mix by pipetting up and down, and incubate the samples for ~1 h at room temperature (25 °C) (*see* **Note 8**).

3.5 Blocking of Free Thiol Groups with NEM or MPEG-Mal

1. Take 15 μL of the samples (containing 5 μM roGFP2), and incubate them with 5 μL of NEM (100 mM) or MPEG-Mal (20 mM) to obtain final concentrations of 3 μM roGFP2 with 20 mM NEM and 4 mM MPEG-Mal (in a total volume of 25 μL after the addition of loading-dye (*see* **step 3**).
2. Mix by pipetting up and down. Incubate the samples with the MPEG-Mal or NEM for 1–2 h at 21 °C under shaking in a thermomixer.
3. Add 5 μL 5× non-reducing loading dye to obtain a volume of 25 μL (*see* **Note 9**).

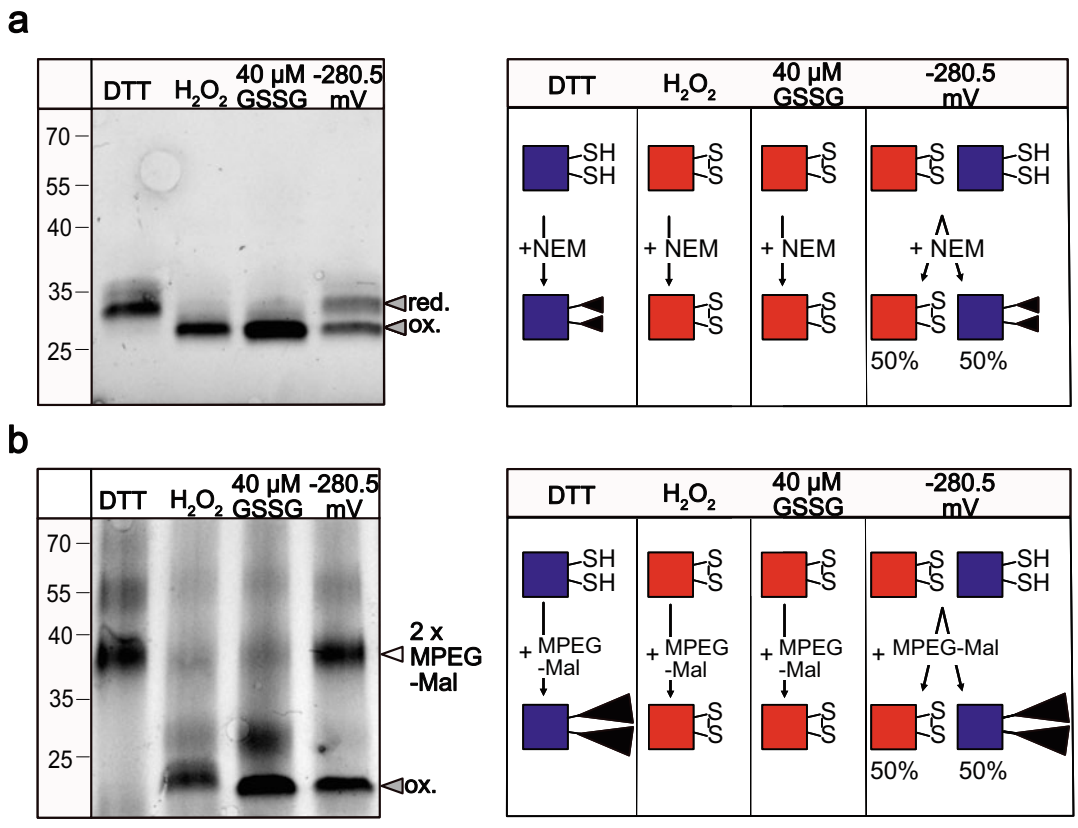

Fig. 3 roGFP2 gel-based read-out of oxidation assay. (**a**) Left panel: roGFP2 was pre-reduced with 10 mM DTT before oxidation with 40 µM GSSG +1 µM *At*GRXC1 (40 µM GSSG) or 6.6 mM GSH + 40 µM GSSG +1 µM *At*GRXC1 (glutathione buffer with $E_{GSH} = -280.5$ mV at pH 7.4). Reduced cysteines were blocked with 20 mM NEM before the gel run to avoid reoxidation. 2.1 µg roGFP2 (MW = 28 kDa) (5 µL of 3 µM roGFP2) were loaded on a 10% SDS-PAGE. Right panel: schematic overview of redox states in A. (**b**) Left panel: free cysteines were labeled with 4 mM MPEG-Mal (adding c. 5 kDa for each reduced cysteine). 2.1 µg roGFP2 were loaded on a 10% SDS-PAGE. Right panel: schematic overview of redox states in B (*see* **Note 10**)

3.6 Gel-Based Size Shift Read-Out of roGFP2 Redox State

1. Perform SDS-PAGE, e.g., using a Mini-PROTEAN TGX precast gel (10%) loading up to 30 µL of your sample. Add your protein ladder of choice (prestained). Fill up your chamber with 1× SDS running buffer, and let the gel run for up to 1 h at 120 V or until the running front reaches the end of your gel.
2. Take the gel out of the cast and shortly wash it in water before proceeding to gel imaging.
3. Detect fluorescent protein bands under UV light (or blue light with GFP filter settings in a fluorescence imager) (Fig. 3). Use a prestained marker to identify the sizes of your protein: Take a photo of the gel to overlay the marker for analysis.

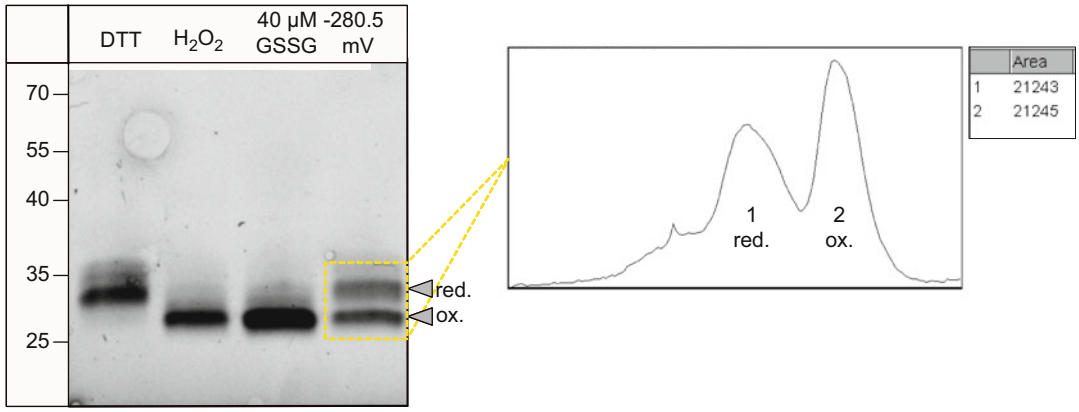

Fig. 4 Analyzing gel band intensities with ImageJ. The image of the protein gel is opened in ImageJ and bands of interest are selected (*see* Fig. 3a, lane 4). The selection (yellow) will be plotted as intensity curves and the area below the curves calculated. In this example, a roGFP2 oxidation assay using a GSH/GSSG redox buffer with −280.5 mV leads to c. 50% oxidation of roGFP2 (which has a midpoint potential of −280 mV)

3.7 Quantification of Band Intensities by ImageJ

1. Analysis of roGFP2 redox state from gel images can be performed using software such as ImageJ, quantifying band intensities of the reduced and oxidized forms that show a different migration behavior on a nonreducing SDS-PAGE (*see* Figs. 3 and 4).
2. Open the gel image in ImageJ. Select bands of interest via the selection rectangle tool (*see* **Note 11**).
3. Select: analyze →gel→plot lanes to plot intensities of selected bands. Use the wand (tracing) tool to obtain the values in a table. Subsequently, you can calculate the ratio and percentage of oxidation using the obtained intensity values.

4 Notes

1. Calculating the molar concentration of a 30% hydrogen peroxide solution using the density (ρ): exact numbers might vary depending on the supplier. Check the technical data sheets for exact values.

   H_2O_2 Roth (30% (w/w)): ρ = 1.1 g/mL, MW = 34.01 g/mol

$$1\,\text{L} = 1100\,\text{g}$$

$$1100\,\text{g} \times 0.3 = 330\,\text{g}$$

$$\frac{330\,\text{g}}{34.01\,\text{g/mol}} = 9.7\,\text{mol/L}$$

2. Depending on the calculated redox potential and glutathione ratios, concentrations of GSH and GSSG stock solutions can be upscaled or downscaled depending on the required concentration. Be aware of the GSH and GSSG solubilities in aqueous solution as provided by the manufacturer's instructions. (GSH: 100 g/L (= 320 mM) (Roth), GSSG: ~100 mM (Abcam)).
3. Use an appropriate buffer as basis for the stock solution, and control the pH before using it.
4. Any GRX that can glutathionylate/deglutathionylate proteins (generally class I GRX) can be used. Depending on the GRX, reaction times may have to be adjusted.
5. Any method determining the protein concentration is suitable.
6. A redox potential of −280.5 mV was chosen as an example due to the midpoint redox potential of roGFP2 at −280 mV. Around 50% of roGFP2 are oxidized at −280 mV.
7. Use molar concentrations (mol/L) for calculations in the Nernst equation. GSSG concentrations might be too low to accurately pipet (do not go lower than 1 μL). As an alternative, either change the redox potential, or decide for a different concentration.
8. If using roGFP2 you can follow the oxidation state with a fluorescence plate-reader. The assay can be stopped when all samples reached a plateau. The reaction kinetics depend on the activity and concentration of the used GRX, as well as the roGFP2 concentration. For the conditions described in this protocol, a plateau is reached after approximately 30 min.
9. Do not boil the samples or add a reductant prior to loading. Boiling the samples containing roGFP2 will prevent a UV-based read-out, as it causes denaturation of the protein. The UV-based read-out offers the advantage that denatured or degraded fluorescent protein is not visible, in contrast to protein staining methods.
10. MPEG-Mal can lead to smears in lanes [18] and changes the running behavior of bands. The apparent protein sizes on non-reducing gels do not correspond to the known molecular weights.
11. Do not use a high contrast for intensity calculation in ImageJ. Differences might be masked due to oversaturation.

Acknowledgments

This work was supported by the Deutsche Forschungsgemeinschaft (DFG) through the Research Training Group GRK 2064 "Water use efficiency and drought stress responses: From Arabidopsis to Barley" (F.B., A.J.M., S.J.M.-S.).

References

1. Hanson GT, Aggeler R, Oglesbee D et al (2004) Investigating mitochondrial redox potential with redox-sensitive green fluorescent protein indicators. J Biol Chem 279: 13044–13053. https://doi.org/10.1074/jbc.M312846200
2. Aller I, Rouhier N, Meyer AJ (2013) Development of roGFP2-derived redox probes for measurement of the glutathione redox potential in the cytosol of severely glutathione-deficient rml1 seedlings. Front Plant Sci 4: 506. https://doi.org/10.3389/fpls.2013.00506
3. Cannon MB, Remington SJ (2006) Re-engineering redox-sensitive green fluorescent protein for improved response rate. Protein Sci 15:45–57. https://doi.org/10.1110/ps.051734306
4. Lohman JR, Remington SJ (2008) Development of a family of redox-sensitive green fluorescent protein indicators for use in relatively oxidizing subcellular environments. Biochemistry 47:8678–8688. https://doi.org/10.1021/bi800498g
5. Schwarzländer M, Fricker MD, MüLler C et al (2008) Confocal imaging of glutathione redox potential in living plant cells. J Microsc 231: 299–316. https://doi.org/10.1111/j.1365-2818.2008.02030.x
6. Meyer AJ, Brach T, Marty L et al (2007) Redox-sensitive GFP in Arabidopsis thaliana is a quantitative biosensor for the redox potential of the cellular glutathione redox buffer. Plant J 52:973–986. https://doi.org/10.1111/j.1365-313X.2007.03280.x
7. Müller-Schüssele SJ, Schwarzländer M, Meyer AJ (2021) Live monitoring of plant redox and energy physiology with genetically encoded biosensors. Plant Physiol 186:93–109. https://doi.org/10.1093/plphys/kiab019
8. Ugalde JM, Fecker L, Schwarzländer M, et al (2022) Live monitoring of ROS-induced cytosolic redox changes with roGFP2-based sensors in plants. In: Mhamdi A (ed) Reactive Oxygen Species in Plants. Springer US, New York, NY, pp 65–85. https://doi.org/10.1007/978-1-0716-2469-2_5
9. Meyer AJ, Dick TP (2010) Fluorescent protein-based redox probes. Antioxid Redox Signal 13:621–650. https://doi.org/10.1089/ars.2009.2948
10. Schwarzländer M, Dick TP, Meyer AJ, Morgan B (2016) Dissecting redox biology using fluorescent protein sensors. Antioxid Redox Signal 24:680–712. https://doi.org/10.1089/ars.2015.6266
11. Begas P, Liedgens L, Moseler A et al (2017) Glutaredoxin catalysis requires two distinct glutathione interaction sites. Nat Commun 8: 14835. https://doi.org/10.1038/ncomms14835
12. Fernandes AP, Holmgren A (2004) Glutaredoxins: glutathione-dependent redox enzymes with functions far beyond a simple thioredoxin backup system. Antioxid Redox Signal 6: 63–74. https://doi.org/10.1089/152308604771978354
13. Wagner S, Steinbeck J, Fuchs P et al (2019) Multiparametric real-time sensing of cytosolic physiology links hypoxia responses to mitochondrial electron transport. New Phytol 224: 1668–1684. https://doi.org/10.1111/nph.16093
14. Rosenwasser S, Rot I, Meyer AJ et al (2010) A fluorometer-based method for monitoring oxidation of redox-sensitive GFP (roGFP) during development and extended dark stress. Physiol Plant 138:493–502. https://doi.org/10.1111/j.1399-3054.2009.01334.x
15. Trnka D, Engelke AD, Gellert M et al (2020) Molecular basis for the distinct functions of redox-active and FeS-transfering glutaredoxins. Nat Commun 11:3445. https://doi.org/10.1038/s41467-020-17323-0
16. Liedgens L, Zimmermann J, Wäschenbach L et al (2020) Quantitative assessment of the determinant structural differences between redox-active and inactive glutaredoxins. Nat Commun 11:1725. https://doi.org/10.1038/s41467-020-15441-3
17. Loughran ST, Bree RT, Walls D (2017) Purification of polyhistidine-tagged proteins. In: Walls D, Loughran ST (eds) Protein chromatography. Springer, New York, pp 275–303
18. Zheng CY, Ma G, Su Z (2007) Native PAGE eliminates the problem of PEG–SDS interaction in SDS-PAGE and provides an alternative to HPLC in characterization of protein PEGylation. Electrophoresis 28:2801–2807. https://doi.org/10.1002/elps.200600807

SUPPLEMENTARY PROTOCOL INFORMATION

1. HED ASSAY

Material:

- GRX (freshly isolated on the same day, in Tris-HCL pH 7.9)
- GR (stock 1,3 mg/ml; can be calculated from manufacturer, (GR, *Saccharomyces cerevisiae*, Sigma CAS-9001-48-3, Nr. G3664 Concentration and activity is written on the vial (u/mg protein and ml)).
- NADPH (10 mM in Tris-HCL pH 7.9 ? check concentration using the molar extinction coefficient of NADPH. The molar extinction coefficient for NADH or NADPH at 340 nm is 6.22 l/mmol/cm.
- GSH (50 mM in Tris-HCL pH 7.9) in 100 mM Tris pH 7.9
- HED (100 mM in Tris-HCL pH 7.9) bis(2-hydroxyethyl) disulfide, Alfa Aesar L11800
- Nanodrop 2000c/spectrophotometer
- 1 ml plastic cuvettes (Polystyrol, Sarstedt, REF 67.742) or any other cuvette allowing measurements at 340 nm.
- 100 mM Tris, 1 mM EDTA pH 7.9

Procedure:

Before starting. Check for the optimal concentration of your GRX. Perform the HED assay (see below) using 1 mM GSH and 0.7 mM HED with various concentrations of your GRX (varying from 10-50 nM) and go for the concentration where your GRX shows a linear activity (example in Supplemental Figure. 4: below 30 nM). Perform a Bradford assay after every freeze and thaw cycle to be sure about your enzyme concentration!

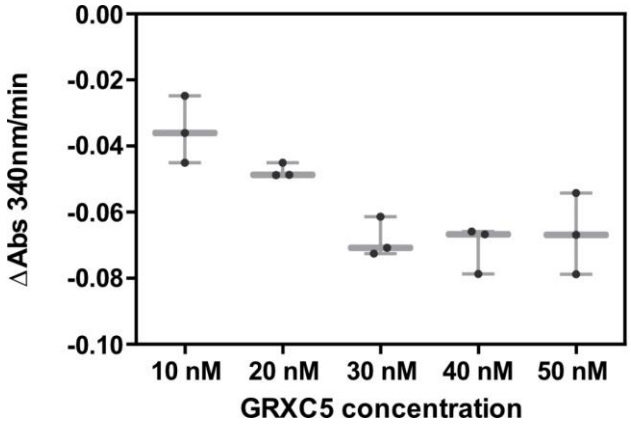

Supplemental Figure 4: HED assay: Determining the linear activity of GRXC5

HED assay performed with varying concentrations of *Pp*GRXC5 to determine the linear activity of *Pp*GRXC5.

NOTE 1 Check NADPH stock concentration in the nanodrop 2000c by using the NADPH coefficient (molar extinction coefficient for NADH or NADPH at 340 nm is 6.22 l/mmol/cm). **NOTE 2** If performing experiments via the Nanodrop 2000c: Open the Nanodrop 2000c kinetic editor. Set the program to measure at 340 nm every 2 sec for 1 min.

Pipette into a **1 ml** cuvette to a final concentration:

Tris-HCL pH 7.9 = 100 mM

NADPH = 0.2 mM

GSH = 1 mM (or var. from 0.5-5 mM, use the same stock)

HED = 0.7 mM (or var. from 0.3-2 mM, use the same stock)

As soon as you added HED and GSH**, incubate for exactly 3 min**! Important! Within the three minutes, the spontaneous reaction of GSH with HED leads to the formation of glutathionylated ß-ME (ß-ME-SSG). To ensure that ß-ME-SSG concentrations are comparable between the experiments, the time for the spontaneous reaction has to be kept constant. Then add GR (to a final concentration of 6 µg/mL) and GRX (final c = x nM), mix with a pipette. Your final volume here is 1 mL.

Exemplary volumes (adjust to your stock concentrations) to obtain your final concentrations in 1 mL of assay:

10 µL of a 20 mM NADPH stock in 1 mL assay

20 µL of a 50 mM GSH stock in 1 mL assay

10 µL of a 70 mM HED stock in 1 mL assay

Adjust with Tris-HCL to 1000 µL by subtracting the volume of later added GR (-4.6 µL of 1.3 mg/mL stock) and (-10 µL of x µM stock) GRX. As soon as you added HED and GSH**, incubate for exactly 3 min**! Important! Then add GR and GRX:

+ GR 4.6 µL of 1.3 mg/mL in 1 mL assay

+ 10 µL GRX at your concentration e.g. 20 nM in 1 mL assay (typical GRX stock concentration 10 µM, diluted in Tris-HCL pH 7.9)

Mix everything quickly with a 1000 µL pipette by pipetting up and down. Place the cuvette in the nanodrop and press “measure”.

NOTE 3 The steps should be done as consistent and fast as possible!

NOTE 4 For each concentration of GSH/HED prepare a background activity cuvette, adding buffer (Tris-HCL pH 7.9) instead of GRX. It is important to measure the background activity on the same day and with the same stock concentrations than your sample cuvettes.
Save the measurement points of the Nanodrop by copying it to the clipboard (nanodrop cannot directly perform the excel export of the kinetic values) and import it into Excel.

Analysis

To analyze your data you can use Excel to calculate the slopes and you can use Prism/GraphPad or any other program able to do Michaelis Menten kinetics. You want to blot concentrations of your substrates tested (either HED or GSH) against the reaction velocity. Slope calculation will be performed on the first minute (hole measurement). Your values of the Nanodrop are absorbance at 340 nm. To calculate the delta absorbance /s, you divide the absorbance values by the time. (Values will be negative, since curve NADPH is decreasing). Change the values into positive ones (*-1). Dividing it by the NADPH extinction coefficient in a 1 ml cuvette will give you mM NADPH/s. To get µM NADPH/s multiply by 1000. If you want to transform your data into turnover rate (k_{cat}) s^{-1} divide µM NADPH/s with the concentration in µM of your GRX. Use the µM NADPH/s values to copy into the Prism file. Let the software calculate your apparent K_m, V_{max} and k_{cat} values. **NOTE5:** Your increasing concentrations of HED or GSH should lead to a flattening of the curve (‘form a plateau’). If the plateau is reached in lower concentrations adjust to smaller concentrations to test the activity. If the plateau is not reached with the highest concentration of HED or GSH, increase the concentration.